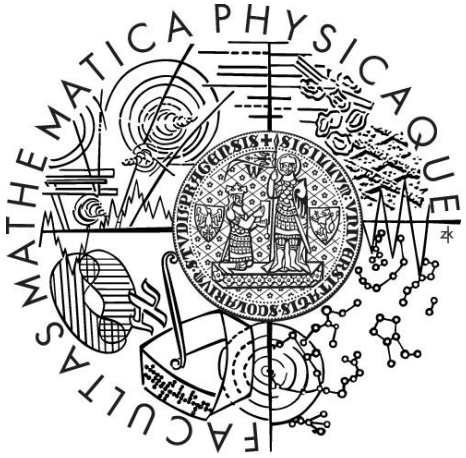
Charles University in Prague
Faculty of Mathematics and Physics

DOCTORAL THESIS



Petra Suková

Chaotic Motion around Black Holes

Institute of Theoretical Physics

Supervisor of the doctoral thesis: doc. RNDr. Oldřich Semerák, DSc.
Study programme: Physics
Specialization: Theoretical Physics,
Astronomy and Astrophysics

Prague 2013

I am indebted to my supervisor doc. Oldřich Semerák for numerous pieces of advice and patient guidance during writing the thesis. I am also grateful to Miroslav Žáček who kindly provided me his numerical code. I would like to thank Ladislav Šubr and David Heyrovský for hints and consultations and my husband Karel Tůma for numerous discussions and technical support.

I acknowledge support of grants GAUK-86508, GAUK-428011, SVV-265301 and GACR-205/09/H033.

To my parents.

I declare that I carried out this doctoral thesis independently, and only with the cited sources, literature and other professional sources.

I understand that my work relates to the rights and obligations under the Act No. 121/2000 Coll., the Copyright Act, as amended, in particular the fact that the Charles University in Prague has the right to conclude a license agreement on the use of this work as a school work pursuant to Section 60 paragraph 1 of the Copyright Act.

In ..... date ..... signature of the author

Název práce: Chaos v pohybu kolem černých děr

Autor: Petra Suková

Katedra: Ústav teoretické fyziky

Vedoucí disertační práce: doc. RNDr. Oldřich Semerák, Dr., DSc.

Abstrakt: Dynamické systémy v obecné relativitě, představující nelineární teorii popisující vývoj prostoročasu, jsou náchylnější ke vzniku chaotického chování než jejich odpovídající newtonské protějšky. V této práci studujeme dynamiku časupodobných geodetik ve statických a axiálně symetrických prostoročasech zadaných pomocí přesných řešení Einsteinových rovnic, která popisují pole superpozice Schwarzschildovy černé díry a tenkého hmotného disku nebo prstence. Odhalíme vznik a ústup chaotického chování geodetického toku se změnou parametrů systému, tedy relativní hmotnosti disku nebo prstence a poloze jeho vnitřního okraje a energii a momentu hybnosti testovací částice za pomoci (i) Poincarého řezů, (ii) spektrální analýzy časových řad dynamických proměnných, (iii) dvou rekurenčních metod pro analýzu časových řad, tzv. rekurenční analýzy a výpočtu váženého průměru směrových vektorů a (iv) výpočtu Ljapunovových exponentů a podobných koeficientů, které kvantifikují míru rozbíhavosti blízkých trajektorií. Zaměříme se také na tzv. „sticky“ trajektorie, jejichž segmety vykazují různé stupně chaotičnosti. Pro krátké seznámení s klasickými chaotickými systémy, které jsou dokonce disipativní, použijeme některé tyto metody také na studium pohybu třídy mechanických oscilátorů popsaných nestandardními konstitutivními vztahy.

Klíčová slova: obecná relativita, černé díry v astrofyzice, chaos, geodetický pohyb

Title: Chaotic Motion around Black Holes

Author: Petra Suková

Department: Institute of Theoretical Physics

Supervisor: doc. RNDr. Oldřich Semerák, Dr., DSc.

Abstract: As a non-linear theory of space-time, general relativity deals with interesting dynamical systems which can be expected more prone to chaos than their Newtonian counter-parts. In this thesis, we study the dynamics of time-like geodesics in the static and axisymmetric field of a Schwarzschild black hole surrounded, in a concentric way, by a massive thin disc or ring. We reveal the rise (and/or decline) of geodesic chaos in dependence on parameters of the system (the disc/ring mass and position and the test-particle energy and angular momentum), (i) on Poincaré sections, (ii) on time series of position and their power spectra, (iii) by applying two simple yet powerful recurrence methods, and (iv) by computing Lyapunov exponents and two other related quantifiers of orbital divergence. We mainly focus on "sticky" orbits whose different parts show different degrees of chaoticity and which offer the best possibility to test and compare different methods. We also add a treatment of classical but dissipative system, namely the evolution of a class of mechanical oscillators described by non-standard constitutive relations.

Keywords: general relativity, black holes in astrophysics, chaos, geodesic motion

Contents

Introduction **3**

1 Chaos in nonlinear dynamics **5**
1.1 Concept of chaos in conservative systems 6
1.2 Weakly non-integrable systems: KAM theory 7
1.3 Period doubling bifurcation 9
1.4 Few basic facts about chaos in dissipative systems 11

2 Diagnosis and classification of chaos within the framework of General Relativity **13**
2.1 Principles of basic methods 13
2.2 Poincaré surface of section 14
2.3 Lyapunov exponents and related indices 15
2.4 Latitudinal action approximating the missing conserved quantity . 19
2.5 Time series and their power spectra 19
2.6 Phase space recurrences 20
2.6.1 Phase space reconstruction 20
2.6.2 Recurrence analysis 21
2.6.3 Weighted average of directional vectors 26

3 Motion of test particles in Weyl spacetimes **29**
3.1 Schwarzschild black hole 30
3.2 Family of inverted Morgan-Morgan discs 31
3.3 Family of discs with power-law density profile 34
3.4 Bach-Weyl ring 35
3.5 Motion of the test particles in Weyl fields 36
3.6 Numerical integration of the equation of motion 37

4 Results **41**
4.1 Methods for dynamical systems with given equation of motion . . 41
4.1.1 Poincaré surfaces of section 42
4.1.2 Lyapunov exponents 45
4.1.3 FLI and MEGNO 48
4.1.4 Latitudinal action 62
4.2 Time series analysis 62
4.2.1 Power spectra 63
4.2.2 Weighted average of directional vectors 63
4.2.3 Recurrence analysis 67

5 Class of mechanical oscillators described by a non-standard constitutive relations **71**
5.1 Introduction 71
5.2 A spring with a non-standard cubic constitutive relation 74
5.3 A non-standard Duffing oscillator 74
5.4 Rigid-elastic spring with linear dasphot 78
5.5 Bingham fluid 82

Conclusions **87**

Bibliography **92**

List of Figures **93**

List of Notations **95**

Attachments **97**

A Free motion around black holes with discs: between integrability and chaos – I **99**

B Free motion around black holes with discs: between integrability and chaos – II **131**

C Free motion around black holes with discs: between integrability and chaos – III **155**

D Geodesic chaos around black holes with discs **175**

E Chaotic geodesic motion around a black hole and disc **179**

F Recurrence of geodesics in a black-hole–disc field **185**

G Geodesic chaos in perturbed black-hole fields **191**

Introduction

With the improvement of various telescopes and probes the strong gravity regime near the black holes has come under intense study recently. Most if not all of the known large galaxies are thought to be occupied by a supermassive black hole in their center. Some of these black holes are probably going through very intense accretion epoch which turns them into a very powerful and persistent source of radiation within the whole electromagnetic spectrum, called the active galactic nuclei (AGN). Due to the extraordinary amount of energy emanating from AGNs, they are among the most distant visible objects in the universe and as such they are used to put constraints on the cosmological models (see e.g. [3]). Because the accretion is the underlying engine for these powerful jets, the behaviour and motion of matter near the ultra compact objects needs to be understood sufficiently in order to explain and describe these extremely bright sources properly. However, the accretion models usually assume the accreting disc to be composed of test matter only, thus the gravitational field of the black hole is not influenced by this additional matter.

Also the center of our Galaxy, even though it is not very active, is endowed with the black hole comprising millions of solar masses. As the nearest supermassive black hole the Sagittarius A* (Sgr A*) has the biggest angular diameter on the sky which allows us to resolve the innermost accretion region. Sgr A* is surrounded by several stars (S-stars) moving so close, that we can observe their whole orbits in real time. This was first announced in 2008 for the S2 star with the orbital period about 15 and half years and the pericenter only 17 light hours (or 3000 M) from the black hole [12]. Also a cloud of gas G2 weighting more than three Earth's masses has been observed on the orbit which will probably takes it only about 25 light hours (4400M) from the black hole during this year (see [16]). The subsequent evolution of the cloud is uncertain, one possible scenario is the breakage of the cloud and its consequent accretion onto the black hole. This would significantly brighten the Sgr A*'s emission and bring more information about the accretion process. Hence, the galactic center of our own Galaxy is an excellent probe of motion in the strong gravity regime.

Also for the other close compact objects the spectral analysis of the emitted light together with its time variability provides information about the properties of the black hole and their vicinity (e.g. the measurement of the black hole spin, quasi-periodic oscillations, time lags etc., [15],[5],[40], etc.).

In all the examples mentioned above the understanding of the motion in strong gravity field plays a fundamental role, from which every conclusion comes out. Taking into account only the test particle motion described by the geodesic equations, still the system is highly non-linear. Hence, the question of onset of chaos, the most typical behaviour of non-linear systems, arises.

During the last decades there has been strong outburst of study of chaotic motion in the frame of general relativity (GR). Even though the general relativistic systems are natural stage for the chaos to emerge due to high non-linearity of the Einstein equations, the diagnosis and classification of chaotic behaviour within GR proved to be very cumbersome task. Because some of the classical approach is based on non-invariant ideas, their applications directly within the

general relativity is questionable or even impossible.

Laying down the theoretical background for the chaos theory in the general relativistic framework is of crucial importance, because all the real physical processes happen in the space time (described by GR) no matter how strong the field is. Thus also the chaotic behaviour should in principle be described in the context of GR. Among the main issues belong the choice of the time coordinate in which we follow the evolution of the system and the correct measuring and renormalisation of the deviation vector in the phase space. Some of the new fundamentals have been built during the last years in the literature which take into account the need of invariant description.

The aim of this thesis is bringing new approaches in this field and describing the onset of chaos induced purely by the gravitational effect of the additional matter surrounding the accreting black hole, when the system is assumed to be the superposition of the static black hole and a static thin disc or ring. Different methods of classification and quantification the chaotic behaviour will be used and compared.

1. Chaos in nonlinear dynamics

"Chaos: When the present determines the future, but the approximate present does not approximately determine the future."

Edward Lorenz, 2005[1]

During the last century the theory of chaos was one of the most developing segments of physics. What was firstly considered as "weird" behaviour of some special systems was gradually recognised as the universal property of general nonlinear dynamical systems. Main development came with the improving computer capabilities, which bring not only new tools for the research but also the need for more advanced theoretical analysis of chaotic systems.

The extensive numerical simulations of nonlinear systems revealed the fundamental difficulties which are hard or impossible to overcome. The brokers all around the world fight their everyday struggle with the unpredictable complex evolution on financial market. The other well known example is the weather forecast – the so called "butterfly effect" prevents us to predict the weather more than few days in advance. Actually, half century ago Lorenz published his famous paper *Deterministic nonperiodic flow* ([29]) and he estimated the maximal time for a meaningful forecast to about two weeks, *no matter how accurate our measurement would be* (because we are never able to completely describe the current state of the atmosphere). Now, fifty years later during which an outstanding revolution in the computer science took part (which could be hardly forseen at that time) we are far from achieving the accurate weather forecast for two weeks.

Mentioned only two examples among many others we demonstrate how much the chaotic dynamics has significant influence on our every day lives in many different ways. The theory of nonlinear dynamical systems, or the chaos theory, thus comprise essential ideas and processes, which are common for extremely wide field of science.

When dealing with the chaotic behaviour, there is a substantial difference between the conservative and dissipative systems. In this thesis we will mainly examine the former represented by the geodesic flow, although we will also give a short example of the latter when applying our methods on classical dissipative systems – the class of mechanical oscillators with non-standard constitutive relations.

The theoretical background for the chaos theory in conservative Hamiltonian systems is the so-called KAM theory (Kolmogorov-Arnold-Moser theory), which was developed in the middle of the last century (during the years 1954 – 1963), although the problem with small divisors was first encountered in his work by Henri Poincaré. The KAM theory deals with the weakly non-integrable systems, that are initially integrable Hamiltonians which undergo a small non-integrable perturbation, and states conditions for the appearance of chaos in some regions of the phase space. A short summary of its results are given in Section 1.2.

[1] according to [8]

In dissipative systems the subsets of phase space where the orbits converge to, *the attractors*, play a fundamental role. In chaotic case their topology is complex and their dimension is non-integer. All the initial conditions whose evolution converge to one particular attractor are denoted as the basins of attraction of this attractor. In the chaotic regime the boundary between different basins of attraction is very complicated, in fact it is fractal, thus self-similar on all scales. In Section 1.4 we present a brief introduction in this topic.

But first of all we need to know what does it mean when we denote some system as chaotic. Unfortunately, even the *definition* of chaos is not clear and could be treated in different ways. In the next section we will give a definition valid for motion in bounded region of the phase space and independent of the form of the time coordinate, published in [55].

1.1 Concept of chaos in conservative systems

When studying the properties of non-linear dynamical system we have to start with the definition of chaotic motion itself. Although the problem of chaos is intrinsic for many different dynamical systems, there is not some clear (mathematical) definition of chaos, which would hold for all cases. Usually it is said that the motion is chaotic, when it is sensitive to initial conditions, hence when one of the Lyapunov exponents is positive. However such a definition is not sufficient, because there are simple dynamical systems with positive Lyapunov exponent, which in our understanding do not correspond to chaos (a very simple example is the system described by the equation ($\dot{x} = x$)).

Here we adopt a geometrical definition published in [55] which holds for conservative systems with bounded phase space endowed with metrisable topology.

Let us consider a phase space $\mathcal{P}$ with given metric g. Let us consider a dynamical system $(\mathcal{P}, \varphi_t)$, where φ_t is a map induced by the dynamical flow $\varphi_t : \mathcal{P} \to \mathcal{P}$ and for all $x \in \mathcal{P}$ the point $\varphi_t(x)$ is the image of the point x's evolution after time t. Such a dynamical system is chaotic if it contains a future chaotic invariant subset Λ, satisfying the conditions

- a) Λ is a compact set invariant with respect to the map φ_t:

$$\varphi_t(\Lambda) \subset \Lambda \qquad \forall t \in \mathcal{R}, \qquad t > 0.$$

- b) Λ is topologically transitive:

$$\exists T > 0 \quad \forall U, V \subset \varphi_T(\Lambda) \quad \exists t > 0, s > 0 : \varphi_t(U) \cap \varphi_s(V) \neq \emptyset.$$

- c) The flow in Λ is sensitive to initial conditions:

$$\exists \delta \quad \forall x \in \Lambda, \forall U \subset \Lambda \quad \exists y \in U, t > 0 : g[\varphi_t(x), \varphi_t(y)] > \delta.$$

  where U is an open neighbourhood of x and δ is a fixed constant.

The first condition means that the motion is constrained to the set Λ for all the time in the future and can not escape. The second condition is also sometimes called the *mixing* property, because it states that the evolution of any

two potentially initially distinct small subsets after some time will immingle these sets together. The last condition expresses the divergence of nearby trajectories.

Although this definition of chaos is applicable only in some situations, it brings quite a clear idea of the properties of chaotic motion, which could come in handy also in other systems. During our study we encounter both the cases, which do or do not meet the requirements of this definition.

1.2 Weakly non-integrable systems: KAM theory

The KAM theory concerns the situation of *nearly integrable hamiltonian systems*, when the system which is known to be integrable is exposed to a small perturbation. A conservative system with dimension N, which could be described by its Hamiltonian

$$H = H(q_i, p_i, t), \tag{1.1}$$

where q_i, p_i are the position in the configuration space and the conjugate momenta, respectively, which represent the coordinates in the $2N$-dimensional phase space, is called separable in case that the function (1.1) could be written in the form

$$H = \sum_{i}^{N} H_i(Q_i, P_i), \tag{1.2}$$

where Q_i, P_i are some canonical conjugated coordinates obtained by a canonical transformation of the original coordinates q_i, p_i.

For some of the Hamiltonians we can find a special coordinates J_i, w_i called the "action – angle coordinates", in which the Hamiltonian has a special form

$$H = \sum_{i=1}^{N} \alpha_i(J_i). \tag{1.3}$$

System described by such Hamiltonian are said to be integrable. The phase orbits of these systems are confined on the surface of the N-dimensional so-called invariant tori, whose axes are given by the values of the actions J_i and the cyclic angle coordinates w_i run along the torus.

Now suppose that the Hamiltonian of the integrable system with a small perturbation could be written in the form

$$H = H_0(\boldsymbol{J}) + \varepsilon H_1(\boldsymbol{J}, \boldsymbol{w}), \tag{1.4}$$

where $\varepsilon \ll 1$ and $\boldsymbol{J}, \boldsymbol{w}$ are the action – angle variables of the unperturbed Hamiltonian H_0. The additional term causes that the total Hamiltonian H is non-integrable. When trying to solve the dynamics of the new system and find new action – angle variables $\bar{J}, \bar{\boldsymbol{w}}$ (see e.g. [39]) we find out that the contribution of H_1 is proportional to the inverse of $\boldsymbol{m} \cdot \boldsymbol{\omega} = \sum_i^N m_i \omega_i$, where $\boldsymbol{m}$ is a vector of integers and $\boldsymbol{\omega}$ is the vector of frequencies of the unperturbed system H_0, thus $\boldsymbol{\omega} = \frac{\mathrm{d}\boldsymbol{w}}{\mathrm{d}t} = \frac{\partial H_0}{\partial \bar{\boldsymbol{J}}}$. This means that the more resonant the frequencies are the bigger is the influence of the perturbation. Realising that the irrational ratio between the frequencies means that the orbit is quasiperiodical and that it eventually

covers the whole surface of the torus, while the resonant frequencies (meaning that the ratio of the frequencies could be written in the form k/l, where k and l are small integers) leads to periodical motion (in 2D case the orbit turns k-times around the coordinates w_1 and l-times around w_2), it turns out that the higher periodic orbits of the unperturbed system bring its sensitivity to the perturbation. The conclusion of KAM theory states that for orbits with initial conditions sufficiently far from the resonance the invariant torus survives the perturbation only being deformed. In order to be "sufficiently far" from the resonance the initial conditions have to satisfy

$$|\boldsymbol{m}.\boldsymbol{\omega}| \geq \gamma |\boldsymbol{m}|^{-\tau}, \tag{1.5}$$

where γ and τ depend on the dimension N, the strength of the perturbation ε, number of derivatives of H_1 and the nonlinearity of H_0. The union of all the surviving tori (KAM tori), denoted as the Kolmogorov set, has a non-zero measure in phase space, which goes to 1 as $1 - \mathcal{O}(\sqrt{\varepsilon})$ when the strength of the perturbation goes to zero.

For those orbits which are not sufficiently far away from the resonance the KAM statement does not hold, the respective tori break under the perturbation and the motion is not confined on the N-dimensional surface any more, in other words the orbit fills in a non-zero volume in the phase space. If the dimension $N = 2$, then the invariant tori divide the phase space into non-connected domains, in particular they separate different stochastic regions and confine the chaotic trajectories into smaller layers with only bounded change of action. The chaotic orbits undergo changes of action in the order $\mathcal{O}(1)$ after the last invariant torus is destroyed due to the perturbation. For higher dimension there is a possibility for the chaotic trajectories to "get around" the regions with persisting KAM tori and to diffuse into very distant positions in the phase space meaning a substantial change of action. This feature is called Arnold diffusion or Arnold web (for chaos in higher dimension see [28]) referring to the idea of chaotic trajectories intermeshing between the chains of regular islands.

The periodic orbits are thus of particular importance for the chaos in Hamiltonian systems. In the vicinity of the stable periodic orbit the equations of motion can be locally linearized into the form of harmonic oscillator librating around the periodic orbit. The region, where such behaviour with the same topological features occurs, is a periodic island. Different periodic islands are separated by a separatrix, which is a special trajectory connecting the stable and unstable manifold of one or two unstable periodic orbits. Because the separatrix belongs to the unstable manifold, it originates near the unstable periodic orbit for $t = -\infty$ and it approaches another (or the same) periodic orbit in the future $t = +\infty$. Near the separatrix the frequency of the motion goes to zero, which leads to multiple occurence of resonances, accompanied by the formation of new higher period islands and the respective new separatrices, which affect the orbits. When the strength of the perturbation is high enough, the invariant tori near the separatrix break and a stochastic layer called also the resonant separatrix chaotic layer emerges.

The topological features of the phase space thus change significantly with the strength of the perturbation. These characteristics could be observed in the 2D case on the well-known Poincaré surface of section, which we introduce in

Section 2.2, in higher dimension the situation is more complicated and other methods have to be used. These methods lie more in the individual and local properties of the chaotic trajectories than in the global topology of the phase space.

One of the most apparent properties of chaotic orbits is the sensitive dependence of the motion on initial conditions which is closely related to the exponential divergence of nearby trajectories. In the system with more possible outputs (e.g. a system of two black holes, where the particle can either A) fall into the first black hole or B) fall into the second black hole or C) escape to infinity) this idea could be clarified with the following. In the chaotic regime in any arbitrary small neighbourhood of any point which is the initial condition of trajectory ending in the output A we can find some points whose future image heads into output B or C. The set of initial conditions leading to the output A, which is an analogue of attractors existing in disipative systems, is called the basin of attraction of the output A. For chaotic systems the basins of attraction have an fractal boundary, within which the sensitive dependence of initial condition holds.

In conservative systems with bounded phase space, i.e. there is no output of orbits, the sensitive dependence of initial conditions is expressed by the locally exponential divergence of nearby trajectories holding until the distance of the two orbits is comparable with some typical length of the whole phase space. The well known example of this behaviour is the chaotic motion of the double pendulum. When slightly changing the initial conditions after some time the trajectories differ significantly, but due to the constant length of the two arms of the pendulum, the distance of the trajectories can not grow unconstrained.

How to recognize this type of behaviour either from the known equations of motion or from a given set of (potentially experimental) data we describe closely in Sections 2.6.2, 2.6.3 and 2.3.

1.3 Period doubling bifurcation

We have to emphasize here one fundamental process which is common for many different (conservative and dissipative, continuous or discrete) systems in some way. That is the period doubling bifurcation. In this section we shall give only short introduction, the detailed description (concerning chaos in both dissipative and conservative systems in general) is given in [39] and [1].

At first we have to define the term bifurcation. Suppose we have a dynamical system, which depends on one scalar quantity, which we call a parameter. This could be for example a mass ratio of components of the system, the friction coefficient or an amplitude of the driving force. Then the bifurcation is the qualitative change of the system properties at some value of the parameter. This may be the change of stable periodic orbit to unstable one or creating periodic orbit with higher period etc.

The period doubling bifurcation is one type of the general bifurcations, during which the period one stable orbit turns to unstable and another stable period two orbit appears, when the parameter r achieves critical value r_{c1}. Increasing the parameter further to another value r_{c2} leads to another bifurcation, when the period two orbit becomes unstable and period four stable orbit occurs. For $r = r_{c3}$, which is closer to r_{c2} than r_{c2} to r_{c1}, the same happens to the periodic

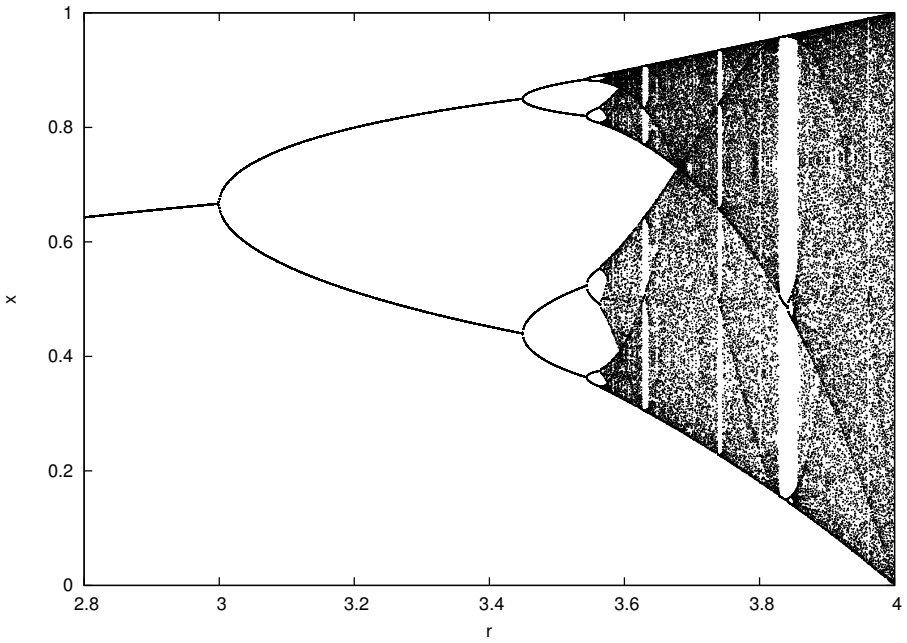


Figure 1.1: Bifurcation diagram of logistic map.

four orbit. The successive bifurcations occur with decreasing parameter's step and at some point r_{chaos} an infinite number of unstable periodic orbits exists and the system transits to chaotic regime.

We can demonstrate this process in case of the simple 1D discrete dissipative system by means of the *bifurcation diagram*. A typical example is the so-called logistic map given by the relation

$$x_{n+1} = r x_n (1 - x_n), \tag{1.6}$$

where r is the parameter governing the evolution. For $r \in [0, 4]$ the interval $x \in [0, 1]$ is mapped onto itself.

For discrete map we can construct the bifurcation diagram in that way, that we plot all possible values x as a function of r (after the transient regime). Continuous systems could be represented as discrete maps using the Poincaré map (the map, which evolves one point in Poincaré surface of section into the next one), therefore the bifurcation diagram could be constructed for them too. In Chapter 5 we construct the bifurcation diagram by plotting all the maxima of the curve $x(t)$ (or $F_s(t)$) against the amplitude of the driving force A.

The p-periodic orbits (or fixed points in the corresponding map) appear at the bifurcation diagram as p distinct points. The period doubling bifurcation is the position in the bifurcation diagram, where the line denoting the changing position of the periodic orbit with the changing parameter splits into two lines. This is due to the fact, that the lower periodic orbit becomes unstable and the new double periodic orbit emerges, which is stable (thus in the numerical computation the trajectories will approach the stable higher periodic orbit). The example for the logistic map is given in Figure 1.1, where we iterated the map 1500 times and then we recorded next 150 values and plotted them against r.

Very interesting fact about this process is its universality. In very different systems the same pattern could be found. In fact, for every one-dimensional map the ratio between the successive bifurcation intervals

$$\delta' = \lim_{n\to\infty} \frac{r_{c(n-1)} - r_{c(n-2)}}{r_{c(n)} - r_{c(n-1)}} \tag{1.7}$$

is *the same constant*, which is called the Feigenbaum constant $\delta' \approx 4.669201....$ This is remarkable result, which brings more connection between dynamical systems in different field of physics.

What is more, the period doubling bifurcation occurs also in the weakly integrable Hamiltonian (conservative) systems, which we described in Section 1.2. This is related to the resonant tori of the unperturbed system. For systems with two degrees of freedom, the resonant tori have rational ratio between the two frequencies describing the motion on the tori ω_1/ω_2. Under the perturbation these tori break and are replaced by equal number of elliptic and hyperbolic fixed points (in the view of the Poincaré map or its multiples, that is the map which evolves one point in the surface of section into next point). Around the elliptic points, the situation is self-similar to the whole picture with their own islands; some of them are also resonant, so the situation repeats. The elliptic fixed points with the increasing strength of the perturbation change to hyperbollic ones along with creating the double periodic elliptic orbit. In this way, the period doubling bifurcation expresses itself in the conservative systems. Also for Hamiltonian period doubling bifurcation the universal numbers govern the evolution, but in this case, the values are different than the Feigenbaum constant.

1.4 Few basic facts about chaos in dissipative systems

The dissipative processes during the evolution of dissipative systems lead to the loss of energy, which is why the phase space volume is not conserved. Because we are interested in the topological properties of phase space trajectories when studying chaotic motion, this is a crucial difference for us. In such systems only the presence of driving force ensures the continuation of the motion, otherwise it would eventually stop. For the long term evolution the form of the driving force is determining and the information about the exact initial position is lost due to the dissipation. The regime, where it has not yet happened, is called the transient state, after that the established motion occurs.

A fundamental concept in the frame of dissipative chaotic systems is the attractor. Attractor is a region in phase space, towards which the evolution of the system tends. It could be a single point in case of a stable focus (e.g. in case of motion of bead inside a well the friction causes the loss of energy and the bead settles in the minimum of the well for some range of initial conditions) or a finite set of points, a manifold with higher dimension or a very complex object with fractal structure and non-integer dimension, called a *strange attractor*. The latter case holds for the chaotic dynamics.

Even though the dissipative system forgets about its origin, the exact initial condition are crucial for its fate in case, when there are more different attractors

for the same global parameters. The subset of points in the phase space which tend to a particular attractor is called a basin of attraction of this attractor. Fulfilling the "butterfly effect" or in other words the sensitive dependence on initial conditions, two nearby initial condition could evolve towards different attractors, even though after the transient time the motion is governed by the driving force. This behaviour mirrors in the topology of the boundary between different basins of attraction, namely the boundary is also fractal with non-integer dimension.

There are some methods for studying the dynamical systems, which lies in computing this dimension. We plot several maps of basins of attractor in Sections 5.4 and 5.5.

2. Diagnosis and classification of chaos within the framework of General Relativity

After the complicated properties of nonlinear systems have been recognized in various physical and mathematical situations, new methods for their classification have been developed. Some of these methods are tailored to application in specific situations, others are usable in wide range of problems.

General relativity as a theory of gravity, within which the configuration space itself is described by a nonlinear system of equations, represents a part of physics, where particular attention should be paid to the possible chaotic behaviour. However, as it was shown by many authors (e.g. [18],[36],[43]) the treatment of such research within the general relativistic frame has to be taken very cautiously, which is caused mainly by the fact, that the time coordinate has no special status among the other coordinates.

Because within the classical physics the time and space are treated differently in its very foundations, it is often very complicated or even impossible to transfer the ideas about chaos from other physical branches into relativistic systems. In addition to this also the choice of appropriate norm in the phase space is questionable and has to be dealt with.

Despite the fact, that some classical ways of *classification* of chaotic behaviour could not be used straightforwardly in general relativity, we will show, that the basic features of conservative nonlinear systems hold (which is certainly true for weak gravitational field). In this thesis we will seek to present suitable methods which bring reasonable results for the geodesic flow in the field of black hole surrounded by additional matter and hopefully also in other similar situations.

2.1 Principles of basic methods

The appearance of chaotic behaviour ensures high degree of complexity of the motion and as such many different properties of orbits could be discovered. The consequence of the complexity is the existence of many fundamentally different approaches to study the of dynamical systems. As we have shown in Section 1.4, there are two different embodiments of chaos which differ qualitatively in their manifestations. One takes part in the conservative systems, the other in the dissipative systems. Therefore there are two large sets of methods dealing with the conservative and dissipative dynamics, respectively. However, some techniques are suitable for both types.

Another distinction is based on the input information needed by the procedures. We can find analytic approaches to the complex dynamical system, which stem from the mathematical description of the motion and are often designed to study properties of certain orbits only. This includes e.g. investigating the form of quantities similar to effective potential, which take different shapes in different regions of phase space (number of minima and maxima or saddle points, number of possible escapes from the system etc., see [9], [50]) or the Melnikov method,

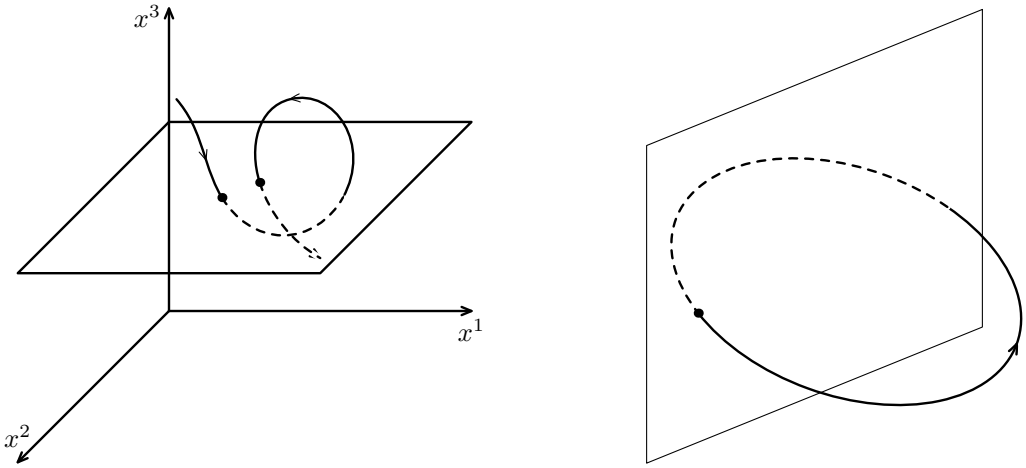


Figure 2.1: The illustration of construction of the Poincareś surface of section (left) and the example of the surface of section of the periodic orbit (right).

which lies in estimating the influence of a perturbation on the homoclinic orbit present in the unperturbed system (details are described in [4]).

Other methods use the analytical form of the equations of motion and they numerically find the phase space orbits together with other needed quantities. In this category we can include the Poincaré surfaces of section described in Section 2.2, computation of latitudinal action (Section 2.4) or determination of Lyapunov exponents and similar indices (Section 2.3). Also the construction of the bifurcation diagram or the map of the basins of attractors proceed in similar way.

At last there is a range of methods suitable for processing the experimental data, namely those which do not require the knowledge of the exact form of the underlying dynamical equations but which rather handle the measured time series of different dynamical variables. The most basic technique of that kind is the spectral analysis (Section 2.5), among others we will describe the process of reconstruction the phase space from the partial data (Section 2.6.1), the recurrence analysis (Section 2.6.2) or the evaluation of the averaged directional vectors in the reconstruced phase space (Section 2.6.3).

2.2 Poincaré surface of section

Poincaré surface of section, in other words also the first recurrence map, is a well known method of picturing the global properties of phase space suitable for analyzing the near integrable systems introduced in Section 1.2 in the low-dimensional case (especially 2D).

We will consider an autonomous Hamiltonian system with two degrees of freedom. The Hamiltonian in this case equals to a constant E, the phase trajectories are thus confined to a three-dimensional surface embedded into the four-dimensional phase space, which is described by the coordinates x_1, x_2, p_1, p_2. Due to the integral of motion E we can eliminate one of the variables (e.g. $p_2 = f(x_1, x_2, p_1, E)$).

Now we choose some two-dimensional surface $\mathcal{S}$ in the phase space, transversal to the flow (e.g. the plane x_2), and we will follow some orbit during its evolution in the phase space. Whenever the orbit crosses the surface $\mathcal{S}$ in a given direction, we plot a dot on this surface.

If there exists another quantity which is conserved along the trajectories, then the Hamiltonian is integrable as we have seen in the preceding section and the motion is restricted to the two-dimensional surfaces of the invariant tori nested within each other. Indeed, another of the remaining coordinates can be eliminated and expressed as a function of the other two and the value of the second constant of motion C, e.g. $p_2 = h(x_1, x_2, C, E)$. Thus, such orbit plots an one-dimensional curve in the surface $\mathcal{S} : x_2 = \text{const}$ (or only several points in case of periodic orbits). On the other hand, the chaotic motion is not confined on the two-dimensional surface of any torus, therefore it fills a non-zero area on the surface $\mathcal{S}$.

The process of generating the points in the surface $\mathcal{S}$ from the flow induce a map $P : \mathcal{S} \to \mathcal{S}$ with lower dimension, in which the properties of the flow are encoded. In this map, called the Poincaré's map, the position in the phase space, not an constant amount of time, decides when to plot a point.

For systems with two degrees of freedom the Poincaré's surface of section method is excellent for picturing the global topological properties of the phase space. However due to the existence of Arnold diffusion and the problematic imaging of higher-dimensional objects, this method is not suitable for systems with more degrees of freedom if the motion in some of the dimensions is not trivial.

In our case, thanks to the existence of two integrals of motion (see Section 3.5), the motion in the direction t and ϕ is completely given by the value of energy $\mathcal{E}$ and angular momentum ℓ and the metric. The motion thus has effectively only two degrees of freedom and that along with the condition of the normalization of the four velocity makes the Poincaré surface of section useful for the analysis. We start our analysis of the system using this method to gain an overview of the evolution of the phase space and furthermore we use the surfaces of section endowed with some additional information for our next analysis. The results are given in Chapter 4, especially in the Section 4.1.1.

The substantial point to realize is that this method could be used only for dynamical system with a known equation of motion, when we are able to follow the whole phase trajectory, thus mainly for theoretical studies. We can not use it for examination of the experimental data. The same statement holds also for the computing the various Lyapunov-like exponents, described in Section 2.3.

2.3 Lyapunov exponents and related indices

One of the basic (though not necessarily "sufficient") symptoms of chaos is a quick divergence of phase trajectories in certain directions — the well-known sensitive dependence on initial conditions. The rate of this tendency can be quantified by several coefficients whose main purpose is to distinguish between polynomial and exponential divergence. The basic from these coefficients are the Lyapunov exponents.

Unfortunately, their computation involves following the rate of divergence of

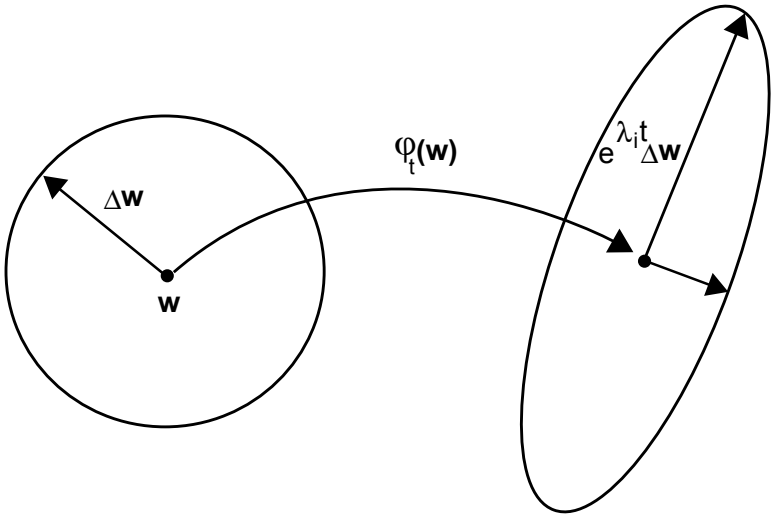


Figure 2.2: The illustration of the meaning of Lyapunov exponents. We evolve a given point in phase space $\mathbf{w}$ of a dynamical system, which is described by the flow φ_t. After a time t the sphere of nearby trajectories deforms into an ellipse with the semiaxes length is given by the Lyapunov exponents.

nearby orbits (or the rate of increase of the deviation vector obtained as a solution of variational equations) which is accompanied by the necessary renormalizations. This of course brings the issue of choosing the time coordinate, which plays quite different role than the other coordinates. Hence, the very idea of Lyapunov exponent is not covariant and it has been shown in literature that their exact value is not invariant [43]. However some of the statements about the system based on such coefficients are invariant, as was shown e.g. in [37]. In our case, due to the symmetries of the system, there is a preferred global time, which assigns some meaning to those indices. We will show that also the proper time τ is a suitable choice for these computations.

Lyapunov characteristic exponents (LCE) are in general numerically computed in two different ways, namely solving the variational equations along with the equations of motion or following two different orbits and their separation. Variational approach is surely more accurate and realiable but in case of relativistic systems the equations are complicated to derive and to integrate along with the dynamical system. In this sense, the two-particle method is much more convenient. It has been shown though in the literature that in the relativistic framework also this approach is somehow questionable. In our analysis we will follow the procedure proposed by Wu and Huang in 2006.

Spectrum of LCE describes the rate of diverging of points in the neighbourhood of a given trajectory. In fact they represent the deformation of a sphere of initial condition equally distant from a given point $\mathbf{w}$ in phase space by an small amount $\mathbf{\Delta w}$. The evolution of such points deforms the original sphere into an ellipsoid, whose semiaxes are given as $e^{\lambda_i t}|\mathbf{\Delta w}|$, where λ_i are the LCE in the direction of the i-th axis, see Figure 2.2. From the spectrum of all LCE, the maximal LCE (mLCE) is the most important for identifying chaotic motion, for which it is a positive number. Therefore, luckily, we do not have to compute the

whole spectrum and we can avoid the Gramm-Schmidt orthonormalization process. This is provided by the fact, that for a randomly selected nearby trajectory, the separation vector has a nonzero component in the direction corresponding to the mLCE and after a short time this component outweighs the others. Thus for two nearby orbits $\mathbf{w}(t)$ and $\mathbf{w}'(\mathrm{t})$ mLCE is given by a limit

$$\lambda_{\max} = \lim_{t\to\infty} \frac{1}{t} \ln \frac{\|\boldsymbol{\Delta}\mathbf{w}(t)\|}{\|\boldsymbol{\Delta}\mathbf{w}(0)\|}, \tag{2.1}$$

where $\|\boldsymbol{\Delta}\mathbf{w}(t)\| = \|\mathbf{w}(t) - \mathbf{w}'(t)\|$ is the norm of the deviation vector in the phase space.

From the form of equation (2.1) it is obvious that the quantity $\lambda_{\max}$ is coordinate dependent. In [53] authors argued that one should examine whether the proper distance between the orbit and its neighbour grows exponentially with proper time rather than the coordinate quantities. They also showed that one need to take into account only the distance in the configuration space to successfully distinguish between regular and chaotic orbits, which simplifies the computation.

Furthermore in [54] they showed that the projection of the displacement vector on a certain time hyper-surface is not necessary, hence the most convenient way how to compute the corresponding mLCE is given by the relation

$$\tilde{\lambda}_{\max} = \lim_{\tau\to\infty} \frac{1}{\tau} \ln \frac{|\Delta\mathbf{x}(\tau)|}{|\Delta\mathbf{x}(0)|}, \tag{2.2}$$

$$|\Delta\mathbf{x}(\tau)| = \sqrt{|g_{\mu\nu}\Delta\mathbf{x}^{\mu}(\tau)\mathbf{x}^{\nu}(\tau)|}, \tag{2.3}$$

where proper time τ is the independent integration variable and $\Delta\mathbf{x}$ is the deviation vector in the configuration space. The difference between (2.1) and (2.2) beside using proper time is also another vector space in which the norm of the deviation vector is computed. This norm corresponds to the proper distance of the two neighbours when they are close enough. To hold this condition during the integration the separation vector needs to be renormalized once it attains some critical value. Together with this renormalization, the velocity deviation vector needs to be renormalize by the same factor $(|\boldsymbol{\Delta}\mathbf{x}(0)|/|\boldsymbol{\Delta}\mathbf{x}(\tau)|)$.

This relativistic modification of mLCE definition has similar properties as the classical one, namely one bothersome feature, which is a very slow convergence to the final value. For weakly chaotic orbits we need to integrate for a very long time to prove the chaotic nature of the motion. Therefore a lot of different coefficients was proposed in the literature which aim to overcome this issue and reveal the orbit's character in significantly shorter integration time.

A direct application of definition (2.2) and the very idea of exponential versus polynomial growth of the deviation vector leads to the definition of Fast Lyapunov Index (FLI) (see [21]). This index is related to norm of the separation vector by the relation

$$\mathrm{FLI}(t) = \log_{10} \frac{\|\boldsymbol{\Delta}\mathbf{w}(t)\|}{\|\boldsymbol{\Delta}\mathbf{w}(0)\|}. \tag{2.4}$$

In accordance with what was said about the norm of the deviation vector earlier we replace this expression with another one living only in the configuration

space

$$\mathrm{FLI}(\tau) = \log_{10} \frac{|\mathbf{\Delta x}(\tau)|}{|\mathbf{\Delta x}(0)|}. \tag{2.5}$$

The value of $\mathrm{FLI}(\tau)$ grows much more faster for chaotic trajectories. This trend is visible earlier than $\tilde{\lambda}_{\max}$ converges to its final value. If we compute $\mathrm{FLI}(\tau_{\max})$ for a set of initial condition, the values for chaotic orbits will be much higher than the ones for regular orbits. Hence choosing the appropriate treshold, which depends on the total integration time and on properties of our system, we can distinguish the regular and chaotic regions in the phase space. Moreover the more chaotic the trajectory is (the higher mLCE it has), the higher value of $\mathrm{FLI}(\tau_{\max})$ it achieves. The degree of chaoticity of different stochastic layers in phase space thus could be compared by the value of $\mathrm{FLI}(\tau_{\max})$, even though its numerical value has not an invariant meaning.

In spite of these benefits still one disadvantage of FLI remains, which is its time-dependent nature. The difference between chaotic and regular motion is encoded in the distinct rate of FLI's grow not in distinct values of the latter. Hence for examination of some dynamical system we need to know the values of $\mathrm{FLI}(\tau_{\max})$ for some regular and chaotic orbit, whose behaviour has to be revealed by another method.

For an extensive automatic survey of a dynamical system through a wide range of parameters the analysis could be significantly simplified, if some Lyapunov-like exponent with time independent output could be implemented. Quantity with desired properties was introduced in [7] for the length of the deviation vector computed from the variational equations $\boldsymbol{\delta}(t)$ and its derivative $\dot{\boldsymbol{\delta}}(t)$, namely the mean exponential growth factor of nearby orbits (MEGNO), which is given by

$$Y(t) = \frac{2}{T} \int_0^T \frac{\|\dot{\boldsymbol{\delta}}(t)\|}{\|\boldsymbol{\delta}(t)\|} t \, \mathrm{d}t. \tag{2.6}$$

As was shown by the authors, the value of MEGNO tends to 2 with an additional bounded oscillating term for regular orbits and grows linearly for chaotic ones with the slope corresponding to the mLCE. For t long enough the values are clearly separated for both regimes.

Having this in mind we can take an advantage from the results of [33], where an analytic relation between FLI and MEGNO was proposed [1]. The relation in question combines the actual value of FLI and its time average in the following way

$$Y(\tau) = 2(\mathrm{FLI}(\tau) - \overline{\mathrm{FLI}}(\tau)) \ln(10), \tag{2.7}$$

where we adopt the factor $\ln(10)$ due to our definition of FLI and we use the proper time τ. The time average is given by

$$\overline{\mathrm{FLI}}(\tau) = \frac{1}{\tau} \int_0^\tau \mathrm{FLI}(s) \mathrm{d}s. \tag{2.8}$$

[1] While comparing these two papers be cautious about the different definition of FLI, using the decadic logarithm in the former and natural logarithm in the latter.

Because the actual value of MEGNO oscillates with the same frequency as FLI, we can compute its time average in the same way

$$\overline{Y}(\tau) = \frac{1}{\tau}\int_0^\tau \mathrm{Y}(s)\mathrm{d}s, \tag{2.9}$$

in order to get rid of the oscillations.

The average MEGNO $\overline{\mathrm{Y}}(\tau)$ behaves smoothly and for τ long enough clearly distinguishes between regular and chaotic motion, therefore it is the most suitable indicator for automatic computations and could be easily determined from the course of FLI. Furthermore, as was mentioned in [7], the asymptotic of MEGNO for large τ is linear $Y(\tau) \approx \lambda_{\max}\tau$ for chaotic orbits. Thus computing the linear regression of the course of MEGNO we can estimate the value of mLCE.

The results are summarized in Section 4.1.2 and 4.1.3.

2.4 Latitudinal action approximating the missing conserved quantity

Because the regular motion is confined on the surface of an invariant torus, there has to be some quantity, which is conserved during the motion. If we could find this quantity, we would prove the regularity of the motion. Unfortunately, finding this quantity is generally very complicated task. However, we can compute quantity called the latitudinal action, defined by the relation

$$J_\theta = \frac{1}{l}\int \sqrt{g_{\theta\theta}u^\theta u^\theta}\mathrm{d}\tau, \tag{2.10}$$

where l is the length of one orbital cycle of the particle (in our case it is the part of the trajectory between two successive passages through the equatorial plane in the same direction).

The properties of this quantity was shown in [51] quite in detail for the motion of charged test particles moving in the electromagnetic field around a rotating black hole. As they have shown, this is *not* the conserved quantity, however it is some approximation of it, showing very different behaviour for the chaotic and regular motion in the following.

When the orbit is regular then the value of the latitudinal action oscillates around a constant value during the whole duration of the motion.

On the contrary, for the chaotic orbit we can not find any mean value holding during the evolution, the value of the latitudinal action varies wildly and unexpectedly. Only when the chaotic motion is captured for some time near the regular island, the value behaves periodically and similarly to the regular motion.

Numerical results are presented in Section 4.1.4.

2.5 Time series and their power spectra

When we turn our attention to the possible processing of experimental data, which means some time series of a measured values, the first thing which comes to mind is to compute a power spectrum. In analogy with the astronomical observation

we choose the vertical coordinate $z = r\cos\theta$ which denotes the position out of the equatorial plane.

The spectrum is thus given by the Fourier transformation

$$z(\omega) = \lim_{T\to\infty} \int_0^T z(t) \mathrm{e}^{\mathrm{i}\omega t} \mathrm{d}t, \tag{2.11}$$

$$P(\omega) = |z(\omega)|^2. \tag{2.12}$$

Regular motion (periodic or quasiperiodic) is determined by a finite number of characteristic frequencies ($\omega = 2\pi f$) describing the motion around the invariant torus. This frequencies and their harmonics are visible in the spectrum as distinct peaks, the rest of spectrum (especially in the low frequencies) is a smooth curve.

The irregular character of the chaotic trajectories is reflected by the noisy shape of spectrum whose amplitude oscillates in the whole frequency range. Two different types of spectra could be found, as was shown e.g. by [26] for motion of spinning test particles around a Schwarzschild black hole. Spectra of the first kind are produced by strong chaotic trajectories moving in the big chaotic layers and could be identified by "white noise" in the low frequencies.

The other type of spectrum is characterized by $1/f$ course in the low frequencies. Such spectrum is produced by chaotic orbits, which are trapped around periodic islands for a longer time, switching between them abruptly. This behaviour is called a sticky motion.

In Section 4.2.1 our results are discussed.

2.6 Phase space recurrences

A lot of information about the dynamical system is hidden in the path of the orbit through the phase space. In a geometrical point of view a dynamical system is represented by vector field on the phase space inducing the flow emerging from the initial conditions. Therefore looking at the evolution of the nearby phase trajectories could tell us whether the vector field varies widely on small scales or not, in other words whether the evolution of the system depends strongly on the initial conditions. Thus, the recurrences or the comebacks of the orbit to some region in phase space are worth to watch.

We will now introduce two different methods which in some way quantify the recurrences in the system, namely the recurrence analysis in Section 2.6.2 and the computation of the weighted average of the directional vectors in Section 2.6.3.

Thanks to the technique of reconstructing the phase space from only partially known trajectory (often from the course of one particular coordinate), these methods could be used for studying the properties of observed (astronomical) systems. This procedure is briefly described in Section 2.6.1.

2.6.1 Phase space reconstruction

Usually the whole phase space trajectory could not been obtained from the experiment, especially for the astronomical observations. Therefore we need to somehow reconstruct the path of the particle in the phase space. Fortunately, there is a procedure, called time-delay embedding procedure, which is used within

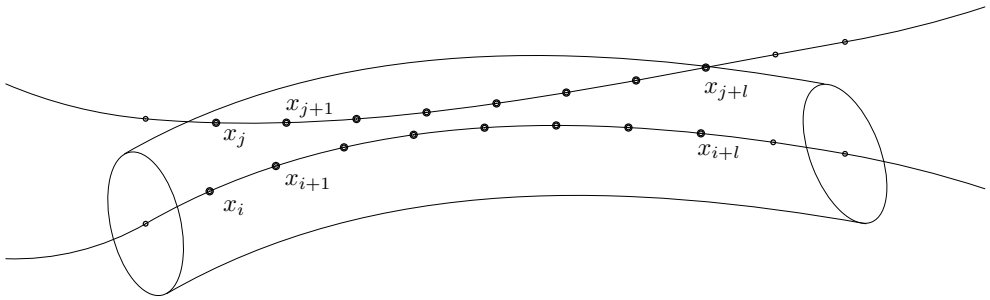


Figure 2.3: An illustration of the origin of the diagonal line in the recurrence plot. On the picture two different parts of the trajectory are depicted, whose distance at the times t_i and t_j is lower than the threshold ε. Within the time $l\Delta t$ the parts move similarly in the way that the pair of points x_{i+k} and x_{j+k} are closer then ε. The line ends when the successive points of the segments move away from each other.

wide field of applications, including the higher dimensional dissipative systems with strange attractors ([24],[13],[6],[10]).

Let's assume that we have only a single variable time series, in our case we adopt the time series of the position above and below the equatorial plane, the coordinate $z(\tau) = r(\tau)\cos\theta(\tau)$. The information about the velocity of the particle is encoded in the differences between the values of the series.

We reconstruct the phase space by shifting the time series by a constant time interval $\Delta\tau$ d-times obtaining the $d+1$-dimensional phase space $\mathbf{w}' = [z(\tau), z(\tau - \Delta\tau), \ldots, z(\tau - d\Delta\tau)]$. When applied to a dissipative system for uncovering the strange attractor, the choice of the embedding dimension d is crucial, because d has to be bigger than the dimension of the attractor (which is non-integer for chaotic trajectories) but not too much in order not to loose the properties of the attractor. Also the choice of the time lag $\Delta\tau$ is a subtle issue, when we want to truly reveal the properties of the attractor. For inappropriate value of $\Delta\tau$ the resulting structure will be deformed and squeezed. The value corresponding to the minimum of the mutual information function was suggested in [20] for the best resolution of the attractor.

Because we consider a conservative system in a low dimension, we do not want to find some non-integer attractor, but rather to simulate the phase space orbits. Therefore we choose $d = 2$ and we obtain the 3D embedding of the particle's orbit, which can be described by a vector $\mathbf{w}' = [z(\tau), z(\tau - \Delta\tau), z(\tau - 2\Delta\tau)]$. As we will show in Section 2.6.3, we will not look for the best choice of the delay $\Delta\tau$ but we will rather follow the dependence of the resulting quantifier (the average of the directional vectors) on the delay and we will show that this behaviour is different for regular and chaotic trajectories.

2.6.2 Recurrence analysis

Recurrence analysis is a powerful tool for discovering the traces of chaos which are hidden in the time evolution of some dynamical quantity. Since 1987, when Eckmann et al. [11] invented the recurrence plots (RP), this method has been used to analyse the behaviour of nonlinear dynamical systems very wide-ranging

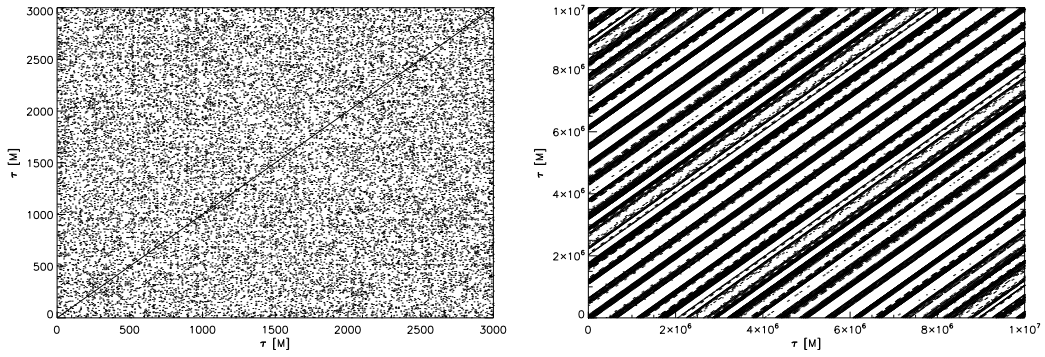


Figure 2.4: Recurrence plot for a random data series (left) and a regular trajectory (right).

fields of study, including physics, mathematics, financial markets and medicine. Very recently this method was also used for detecting chaos in relativistic system of charge particle moving around a magnetised rotating black hole [25].

The key feature for RP is the fact, that the patterns of recurrences of the motion are different for random, chaotic and regular trajectories. The recurrences are encoded in the recurrence matrix

$$\mathbf{R}_{i,j}(\varepsilon) = \Theta(\varepsilon - \parallel \vec{x}_i - \vec{x}_j \parallel), \qquad i,j = 1,...,N, \tag{2.13}$$

where $\vec{x}_i = \vec{x}(t_i)$ are (N) points of the phase trajectory sampled with the constant time step $t_i = i\Delta t$, ε denotes a chosen threshold and Θ is the Heaviside step function. If we do not know the phase space trajectory in all dimensions, we can perform the same calculation either only with the coordinates available or we can first reconstruct the missing information using the time-delay procedure described in Section 2.6.1.

Looking at the definition (2.13) it is obvious, that the recurrence matrix consists of 0's and 1's only, when 1 is in case, that the i-th point is inside the ε-neighbourhood of the j-th point. In spite of the very simple construction of the recurrence matrix, it contains a lot of information about the motion, as we will see hereafter.

The matrix could be visualised in the RP easily, namely plotting a dot at the coordinates i, j for which the matrix element $\mathbf{R}_{i,j}(\varepsilon) = 1$. The resulting plot contains structures which reflect the underlying dynamic and reveal long diagonal line for regular motion and randomly scattered points for random processes. According to the definition the diagonal lines in the recurrence plot mean a series of dots with the coordinates $i, j; i+1, j+1; i+2, j+2, \ldots, i+l, j+l$, where l is the length of the diagonal line. Thus, the distance between two points $\vec{x}(t_i)$ and $\vec{x}(t_j)$ is smaller than ε as well as is the distance between the pairs $\vec{x}(t_{i+1})$ and $\vec{x}(t_{j+1})$, $\vec{x}(t_{i+2})$ and $\vec{x}(t_{j+2})$, $\ldots$, $\vec{x}(t_{i+l})$ and $\vec{x}(t_{j+l})$. Hence the diagonal line in the RP arises in the case, that the trajectory at a time t_j behaves similarly like it did at another time t_i, see Figure 2.3 for better idea. If there exist long diagonal lines in the RP we can also say that the evolution of the orbit does not strongly depend on initial conditions, because when it starts with slightly different initial condition (the points $\vec{x}(t_i)$ and $\vec{x}(t_j)$ are close) then it behaves similarly for a long time $t = l\Delta t$ and the two parts of the trajectory do not diverge quickly. Therefore the diagonal lines are typical for the regular motion.

Completely different looks the RP of a random time series, where are only solitary points scattered across the plot. Such RP plot does not contain any dynamical structures. This feature is helpful for experimental physicists whose one big challenge is to identify a signal (coming from some deterministic dynamical system) among the noise in the data. The examples of RP's for the random and regular trajectory is given in Figure 2.4.

In the case of the chaotic trajectories, the diagonal lines are the shorter the bigger the Lyapunov exponent is (see Section 2.3), thus the more chaotically the trajectory behaves. Also more vertical structures or lines with different slope appear which is a consequence of a change of rate of the dynamical processes and of a "frozen" motion in some part of the phase space.

The RP's by themselves are not very suitable for a deeper analysis, because the evaluation of the structures in the plot is attitudinal. However, we can compute some statistical characteristics of the recurrence matrix which reveal the differences between the three regimes of motion. These quantities called the RQA quantifiers could be derived from the matrix and help us to find chaos in very effective way without the necessity to actually look at the resulting RP's (for very detailed summary see [31]).

The simplest among the RQA quantifiers is the ratio of the recurrence points ($\mathbf{R}_{i,j}(\varepsilon) = 1$) within all points of the matrix, called recurrence rate. We adopt the notation introduced in [31], hence we can write the definition of recurrence rate in the following form

$$RR(\varepsilon) = \frac{1}{N^2} \sum_{i,j=1}^{N} R_{i,j}(\varepsilon). \tag{2.14}$$

The recurrence rate is an increasing function of the threshold ε.

As we have mentioned earlier the structures of diagonal lines in the RP are significant for different regimes of motion. Therefore we need to somehow enumerate their occurrence in the RP. For this purpose we introduce the most important quantifier, namely the histogram of diagonal lines of a certain prescribed length l,

$$P(\varepsilon, l) = \sum_{i,j=1}^{N} (1 - R_{i-1,j-1}(\varepsilon))(1 - R_{i+l,j+l}(\varepsilon)) \prod_{k=0}^{l-1} R_{i+k,j+k}(\varepsilon), \tag{2.15}$$

which for given ε denotes the number of diagonal lines with length l.

On the basis of (2.15) several further quantities could be defined:

$$DET = \sum_{l=l_{min}}^{N} lP(l) / \sum_{l=1}^{N} lP(l), \tag{2.16}$$

$$L_{\max} = \max(\{l_i\}_{i=1}^{N}), \tag{2.17}$$

$$DIV = \frac{1}{L_{\max}}. \tag{2.18}$$

Thus, DET gives the ratio between all recurrence points and those of them which lie at a diagonal line longer than $l_{\min}$. The choice of $l_{\min}$ ensures the elimination of the so called "sojourn points", that result from the tangential motion, i. e. when ε is high enough to capture more successive points of the

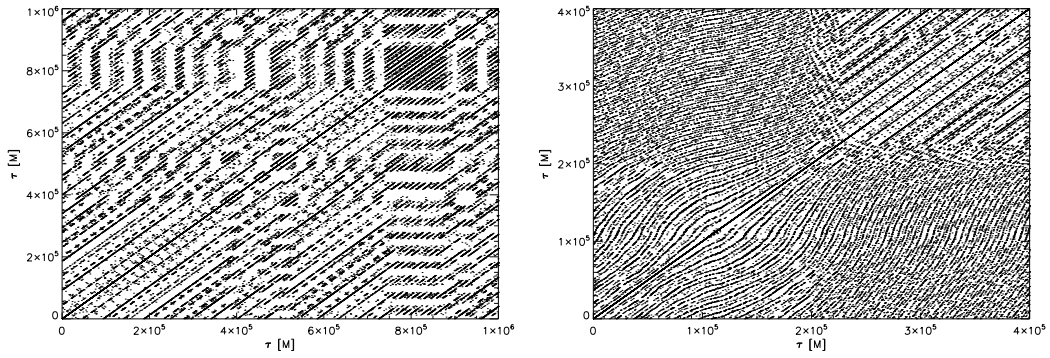


Figure 2.5: Recurrence plots for two different chaotic trajectories.

trajectory into the ε-neighbourhood. When ε is small enough, the appropriate choice is $l_{\min} = 2$, which separates the randomly scattered points from the points composing the diagonal lines. Consequently for random data DET will be very small, in contrast to high values for regular motion.

Unlike the random data series, the difference between regular and chaotic motion lies more in the number of *long* diagonal lines. We introduced quantifiers dealing with the longer lines, namely $L_{\max}$ stands for the length of the longest diagonal line and $DIV = 1/L_{\max}$ is the inverse of this value. Having in mind the idea of the diagonal lines in RP we can claim, that the length of the longest diagonal line (along with the value of DIV) is related to the mLCE of the system (see 2.3), the threshold ε and the "density" of the orbit in the phase space . This is given by the fact that two different orbits diverge exponentially with the coefficient $\lambda_{\max}$ and their separation s will reach ε after the time $t = (\ln(\varepsilon/s_0))/\lambda_{\max}$, where s_0 is the initial separation. For given ε the longest diagonal line thus depends on $\lambda_{\max}$ and on the smallest separation of two different points in RP.

Furthermore, in [31] authors showed that the Rényi entropy of second order K_2 (or the correlation entropy) is related to the occurrence of diagonal lines with the length l.

For a trajectory $\mathbf{x}(t)$ with N points sampled with the constant time step Δt moving in the phase space divided into boxes of the size ε the entropy is defined by the relation

$$K_2 = -\lim_{\Delta t\to 0}\lim_{\varepsilon\to 0}\lim_{l\to\infty}\frac{1}{l\Delta t}\ln\sum_{i_1,\ldots,i_l} p^2_{i_1,\ldots,i_l}(\varepsilon), \tag{2.19}$$

where $p_{i_1,\ldots,i_j}$ is the probability, that the first point $\mathbf{x}(1\Delta t)$ is inside the i_1-box, the second point $\mathbf{x}(2\Delta t)$ is inside the box i_2 and so on to the last point $\mathbf{x}(l\Delta t)$, which should be inside the box i_l. We sum the squares of this probability through all combination of boxes i_j, thus we are interested in cases where there are *two* pieces of the trajectory, whose first point is in the box i_1, the second point $\mathbf{x}(2\Delta t)$ is inside the box i_2 etc. Under some assumptions (e.g. the ergodicity of the system) this corresponds to the occurrence of the diagonal line such that the l successive points of the trajectory lies in the boxes i_1,...i_l. The probability in relation (2.19) thus could be rewritten using the probability $p_t(\varepsilon, l)$ of finding a diagonal line of

the length l at the time t

$$p^2_{i_1,\ldots,i_l}(\varepsilon) \approx \frac{1}{N}\sum_{t=1}^{N} p_t(\varepsilon, l). \tag{2.20}$$

It follows that we can estimate the correlation entropy from the relation

$$K_2(\varepsilon, l) = -\frac{1}{l\Delta t}\ln(p_c(\varepsilon, l)), \tag{2.21}$$

where $(p_c(\varepsilon, l))$ is the probability of finding a diagonal line of at least length l. This probability in the case of the analysed finite segment of the trajectory is derived from the cumulative histogram of diagonal lines. Plotting the logarithm of the cumulative histogram $\ln(p_c(\varepsilon, l))$ against l for large l yields a straight line with the slope $-K_2(\varepsilon)\Delta t$.

At the same time the correlation entropy gives the lower estimate of the sum of positive Lyapunov exponents, hence we are able to constrain their value from the time series of one dynamical variable when we compute the linear regression on the $\ln p_c(\varepsilon, l)$ versus l plot.

Similarly, the histogram of vertical lines can be introduced,

$$P(\varepsilon, v) = \sum_{i,j=1}^{N}(1 - R_{i,j}(\varepsilon))(1 - R_{i,j+v}(\varepsilon))\prod_{k=0}^{v-1} R_{i,j+k}(\varepsilon), \tag{2.22}$$

along with the measure of vertical structures

$$LAM = \sum_{v=v_{\min}}^{N} vP(v) / \sum_{v=1}^{N} vP(v), \tag{2.23}$$

which reveals the laminar states of the motion and trapping time

$$TT = \sum_{v=v_{\min}}^{N} vP(v) / \sum_{v_{\min}}^{N} P(v), \tag{2.24}$$

which reveals the average length of the vertical lines.

From the probabilities that some chosen diagonal/vertical line has length l/v, $p(l) = P(l)/N_L$ and $p(v) = P(v)/N_V$, where N_L and N_V are the total numbers of diagonal/vertical lines, one can compute the Shannon entropies

$$ENTR = -\sum_{l=l_{min}}^{N} p(l)\ln p(l); \quad VENTR = -\sum_{v=v_{min}}^{N} p(v)\ln p(v).$$

Finally, we can compute the recurrence times given by differences between serial numbers of the consecutive recurrence points in one column $\vec{x}_{j_{k+1}}$, $\vec{x}_{j_k}$ multiplied by the respective proper-time step, $\{T_k = (j_{k+1} - j_k)\Delta\tau\}$. The mean of T_k is called the recurrence time of the first type, $T1$. In this set there are also the recurrence points called (*sojourn points*) which we mentioned earlier. It is desirable to discard these points from the set in order to make the statistics only over the real recurrences, after which we get the recurrence times of the second type $T_k^{(2)}$ and the mean value $T2$.

When we change some parameters of the motion (e.g. the energy of the particle or the relative mass of the external source), the dynamics could change its character abruptly from regular to chaotic and vice versa which causes changes in the recurrence patterns of the trajectory. This fact is reflected by the values of the quantifiers, so they are able to reveal changes in the dynamics.

We apply this method on the geodesic flow in the studied spacetimes (see 4.2.3) and on the mechanical oscillators (Chapter 5).

2.6.3 Weighted average of directional vectors

Another method of post-processing the measured time series of some dynamical variable is computing the weighted average of directional vectors (WADV) in the reconstructed phase space. This procedure was introduced by Kaplan in 1992 [24] in order to distinguish between deterministic and random experimental data. Similarly as for the recurrence analysis the input needed for this method is the time series (with constant time step) of one dynamical variable. The keypoint of this method is also similar as the RP's, that is considering the recurrences in the phase space. However, within this method we do not take into account the position in the phase space only but also the direction of the time evolution of the orbit.

The input of our analysis is the vertical position $z(\tau) = r(\tau)\cos\theta(\tau)$. We will start with the time-delay reconstruction, described in Section 2.6.1, with $d = 2$. The resulting 3D phase orbit is included in a cube with length of the side $L = z_{\max} - z_{\min}$. We divide this cube into m^3 boxes with the side $l = L/m$. We follow the phase space orbit moving through these boxes and every time it crosses the boundary of a j-th box, we construct a unit vector pointing in the direction of the passage (connecting the point where the trajectory enters the box with the point where the trajectory leaves the box). After processing the whole trajectory in this way in each box we sum all the unit vectors and divide the norm of the resulting vector $|\mathbf{V}_j|$ by the number of passages through the box n_j. The length of the vector $|\mathbf{V}_j|$ is computed using the standard euclidean norm.

If the unit vectors in one box point in approximately the same direction, then after the normalization on the number of the vectors inside the box the resulting vector's length will be close to unity. When the unit vectors have very different directions, their vector sum's norm will be significantly lower than n_j (for illustration see Figure 2.6).

Because the evolution for an autonomous dynamical system is given only by the position in the phase space, the orbits should evolve in the same way at nearby locations (e.g. inside one box). Hence, for some suitable value of the time lag $\Delta\tau$ the values of $|\mathbf{V}_j/n_j|$ remain close to one with growing n for deterministic systems while it decreases with n as the average displacement per step for a random walk in a 3D space for random processes, given by

$$\bar{R}^3_{n_j} = \frac{4}{(6\pi)^{1/2}} n_j^{-\frac{1}{2}}. \tag{2.25}$$

In our case all the orbits are driven by a deterministic process, alias the equations of motion, thus there could be found such value of $\Delta\tau$ for which the norm $|\mathbf{V}_j/n_j|$ does not fall down with growing n_j. But instead of studying the

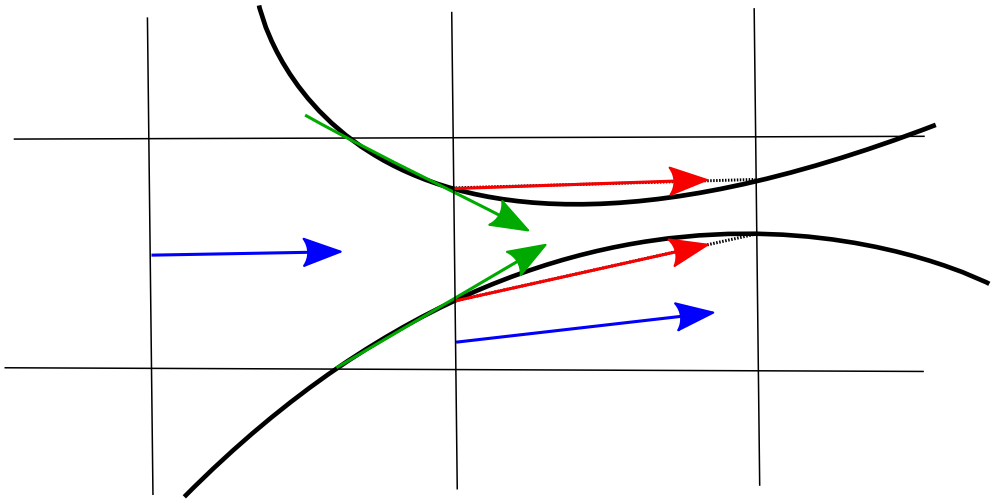


Figure 2.6: Illustration for computation of WADV

dependence on n we compute the weighted average through all boxes

$$\bar{\Lambda}(\Delta\tau) = \Big\langle \frac{(\mathbf{V}_j/n_j)^2 - (R^3_{n_j})^2}{1 - (R^3_{n_j})^2} \Big\rangle, \tag{2.26}$$

and look at the dependence of this quantity on the chosen $\Delta\tau$. For regular trajectories it remains close to one for almost all values of $\Delta\tau$ except for some particular values connected with the orbital period of the motion. This is caused by the fact, that the regular trajectory behaves similarly during the whole evolution. So no matter how far in the past we "look" with the choice of $\Delta\tau$ we still get a phase trajectory which at similar places proceeds in similar direction.

On the other hand for chaotic trajectories the deterministic connection between the points fades away quickly with the growing time lag because of the strong dependence on initial condition and exponential diverging in the chaotic layer. Hence, when there are two nearby points in one box, their position in far history could be completely different. Therefore when we reconstruct the phase orbit with big time delay, the resulting direction within one box could differ significantly. Thus, the value $\bar{\Lambda}(\Delta\tau)$ decreases with growing $\Delta\tau$ more quickly for the very chaotic orbits and less quickly for the weakly chaotic orbits.

The summary of our results concerning the computation of WADV is given in Section 4.2.2.

3. Motion of test particles in Weyl spacetimes

Following our astrophysical motivation we strive to study the motion of time-like test particles near galactic centre, where a super-massive black hole is surrounded by an accretion disc and a distant massive torus of dust. Our aim is to observe the effect of this additional matter on the geodesic flow, which could be substantial due to the nonlinearity of general relativity. However for observing the nonlinearity of the theory itself we need to examine an exact solution of the Einstein equations to get rid of the artificial effects of various approximative solutions (see e.g. [23]). As a consequence we are forced to significantly simplify our physical model, in particular we have to exclude rotation from our system, because no explicit exact solution is known describing such a complicated process as the accretion. On that account we will focus on motion of geodesic test particles in static axi-symmetric spacetimes.

The special class of solutions with these symmetries is described by a metric in the Weyl form

$$\mathrm{d}s^2 = -\mathrm{e}^{2\nu(\rho,z)}\mathrm{d}t^2 + \rho^2\mathrm{e}^{-2\nu(\rho,z)}\mathrm{d}\phi^2 + \mathrm{e}^{2\lambda(\rho,z)-2\nu(\rho,z)}(\mathrm{d}\rho^2 + \mathrm{d}z^2), \tag{3.1}$$

where ρ, z and ϕ are the Weyl's cylindrical-type coordinates (ϕ stands for the angle around the symmetry axis z). We set $c = 1$ and $G = 1$, the signature of the metric is $(-+++)$. Due to the symmetries we postulate on our system the metric functions ν a λ are functions of the coordinates ρ and z only.

This special form of the metric leads to a significant simplification of the Einstein equations

$$\frac{\partial^2\nu}{\partial\rho^2} + \frac{1}{\rho}\frac{\partial\nu}{\partial\rho} + \frac{\partial^2\nu}{\partial z^2} = 0, \tag{3.2}$$

$$\frac{1}{\rho}\frac{\partial\lambda}{\partial\rho} - \left(\frac{\partial\nu}{\partial\rho}\right)^2 + \left(\frac{\partial\nu}{\partial z}\right)^2 = 0, \tag{3.3}$$

$$\frac{1}{\rho}\frac{\partial\lambda}{\partial z} - 2\frac{\partial\nu}{\partial\rho}\frac{\partial\nu}{\partial z} = 0. \tag{3.4}$$

First equation (3.2) is the Laplace equation for the metric function ν, which is also called potential, and from the second (3.3) and third equation (3.4) it follows that the function λ could be computed as a line integral in a vacuum region from the symmetry axis to the point in configuration space (ρ, z) from the derivatives of ν

$$\lambda = \int_{\mathrm{axis}}^{(\rho,z)} \rho\left(\left(\left(\frac{\partial\nu}{\partial\rho}\right)^2 - \left(\frac{\partial\nu}{\partial z}\right)^2\right)\mathrm{d}\rho + 2\frac{\partial\nu}{\partial\rho}\frac{\partial\nu}{\partial z}\mathrm{d}z\right). \tag{3.5}$$

From the properties of the Laplace equation the sum of two solutions is also a solution, namely we can add the solution ν_{Schw} describing the space-time of a simple Schwarzschild black hole and another solution ν_{ext} corresponding to the external source of field (disc or ring in our case) to obtain the solution as the superposition of these two sources ν

$$\nu = \nu_{\mathrm{Schw}} + \nu_{\mathrm{ext}}. \tag{3.6}$$

Having the function ν, the function λ is given by

$$\begin{aligned}\lambda &= \lambda_{\mathrm{Schw}} + \lambda_{\mathrm{ext}} + 2\int_{\mathrm{axis}}^{\rho,z} \rho[(\nu_{\mathrm{Schw},\rho}\nu_{\mathrm{ext},\rho} - \nu_{\mathrm{Schw},z}\nu_{\mathrm{ext},z})\mathrm{d}\rho + \\ &+(\nu_{\mathrm{Schw},\rho}\nu_{\mathrm{ext},z} + \nu_{\mathrm{Schw},z}\nu_{\mathrm{ext},\rho})\mathrm{d}z]. \end{aligned} \tag{3.7}$$

Usually when superposing two non-trivial sources it is not possible to express the line integral as an analytic function, but we are able to numerically find λ and to follow the motion of test particles.

The equation (3.2) could be solved using the oblate spheroidal coordinates

$$z = bxy, \qquad \rho^2 = b(x^2+1)(1-y^2), \qquad x \geq 0, -1 \leq y \leq 1. \tag{3.8}$$

with the inverse relation

$$x = \frac{\sqrt{2}|z|}{\sqrt{\sqrt{(\rho^2 - b^2 + z^2)^2 + 4b^2z^2} - (\rho^2 - b^2 + z^2)}}, \tag{3.9}$$

$$y = \frac{z}{bx}. \tag{3.10}$$

In these coordinates the obtained solution is product of the Legendre polynomials and Legendre functions of the second kind.

Another suitable coordinate systems are the Schwarzschild coordinates (r, θ) introduced by the relation

$$\rho = \sqrt{r(r-2M)}\sin(\theta), \tag{3.11}$$

$$z = (r-M)\cos(\theta). \tag{3.12}$$

We will present some of the result (e.g. the Poincare's surfaces of section etc.) in these coordinates.

As was shown in [47] the potential of a massive thin disc lying in the equatorial plane is given by an integral

$$\nu_{ext}(\rho, z) = -4\int_b^\infty \frac{w(\rho')\rho'}{\sqrt{(\rho+\rho')^2 + z^2}} K\left(\frac{2\sqrt{\rho\rho'}}{\sqrt{(\rho+\rho')^2+z^2}}\right)\mathrm{d}\rho', \tag{3.13}$$

where K stands for the complete elliptic integral of the first kind. In the equatorial plane this simplifies into

$$\nu_{ext}(\rho, 0) = -4\int_b^\infty \frac{w(\rho')\rho'}{\sqrt{(\rho+\rho')^2}} K\left(\frac{2\sqrt{\rho\rho'}}{\sqrt{(\rho+\rho')^2}}\right)\mathrm{d}\rho'. \tag{3.14}$$

3.1 Schwarzschild black hole

In case of the Schwarzschild black hole the metric is in the form (3.1), where ν and λ are given by

$$\begin{aligned}\nu_{\mathrm{Schw}} &= \frac{1}{2}\ln\left(1 - \frac{2M}{r}\right), \\ \lambda_{\mathrm{Schw}} &= \frac{1}{2}\ln\frac{r(r-2M)}{(r-M)^2 - M^2\cos^2(\theta)}, \end{aligned} \tag{3.15}$$

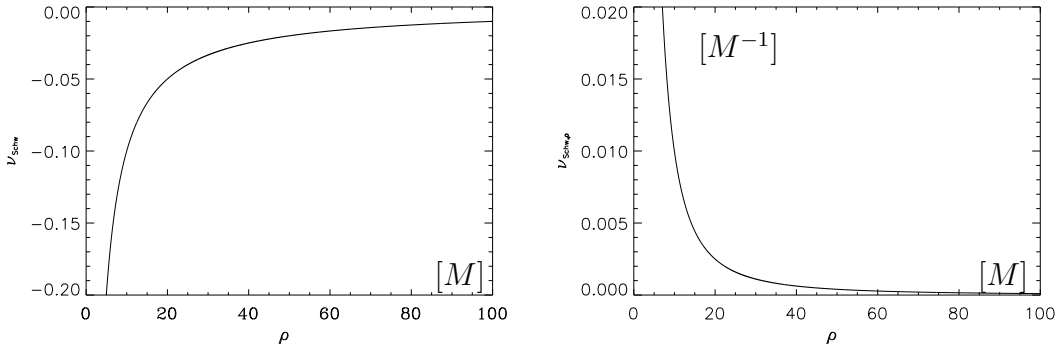


Figure 3.1: The potential $\nu_{\rm schw}$ of the Schwarzschild black hole and its derivative $\nu_{,\rho}$ in the equatorial plane $\theta = \pi/2$, $\nu_{,z} = 0$.

where (t, r, θ, ϕ) are Schwarzschild's coordinates (3.11), which are suitable for the spherical symmetry. Hovewer for the superposition with another axially symmetric source we need to rewrite (3.16) in terms of Weyl's coordinates

$$\begin{aligned} \nu_{\rm Schw} &= \frac{1}{2}\ln\frac{d_1+d_2-2M}{d_1+d_2+2M}, \\ \lambda_{\rm Schw} &= \frac{1}{2}\ln\frac{(d_1+d_2)^2-4M^2}{4\Sigma}, \end{aligned} \tag{3.16}$$

where $d_{1,2} = \sqrt{\rho^2+(z\mp M)^2}$, $\Sigma = d_1 d_2 = \sqrt{(\rho^2+z^2+M^2)^2-4z^2M^2}$.

3.2 Family of inverted Morgan-Morgan discs

When thinking about the possible additional source of perturbation to the field of the black hole the accretion disc formed from the matter in the neighbourhood inspiraling slowly down to the centre comes first to the mind. The physics in the accretion disc is very complicated, because the matter closest to the black hole have to loose its angular momentum through various viscous turbulent processes in favour of the outer part of the disc. Thus it is impossible to describe the disc properly by an exact solution of Einstein equations. For the purpose of this thesis, which is the study of the non-linear effects of general relativity itself, we are forced to employ some simplified exact model of the disc.

First model stems from the solution which was published in 1969 by Morgan and Morgan [35] and which describes the family of finite massive thin discs with the the outer rim b and the mass $\mathcal{M}$, centered at the coordinates' origin. The density profile of these discs is given by

$$w^{(m)}_{\rm MM}(\rho \le b) = \frac{(2m+1)\mathcal{M}}{2\pi b^2}\left(1-\frac{\rho^2}{b^2}\right)^{m-\frac{1}{2}}, \tag{3.17}$$

where m is nonnegative integer.

This spacetime is vacuum everywhere, the disc's matter is encoded in the jump of the derivatives of the potential when going through the disc, which is placed in the equatorial plane.

The potential ν of the m-th member of the family is expressed in the oblate coordinates (3.8) by the sum of Legendre polynomials P_n and Legendre functions

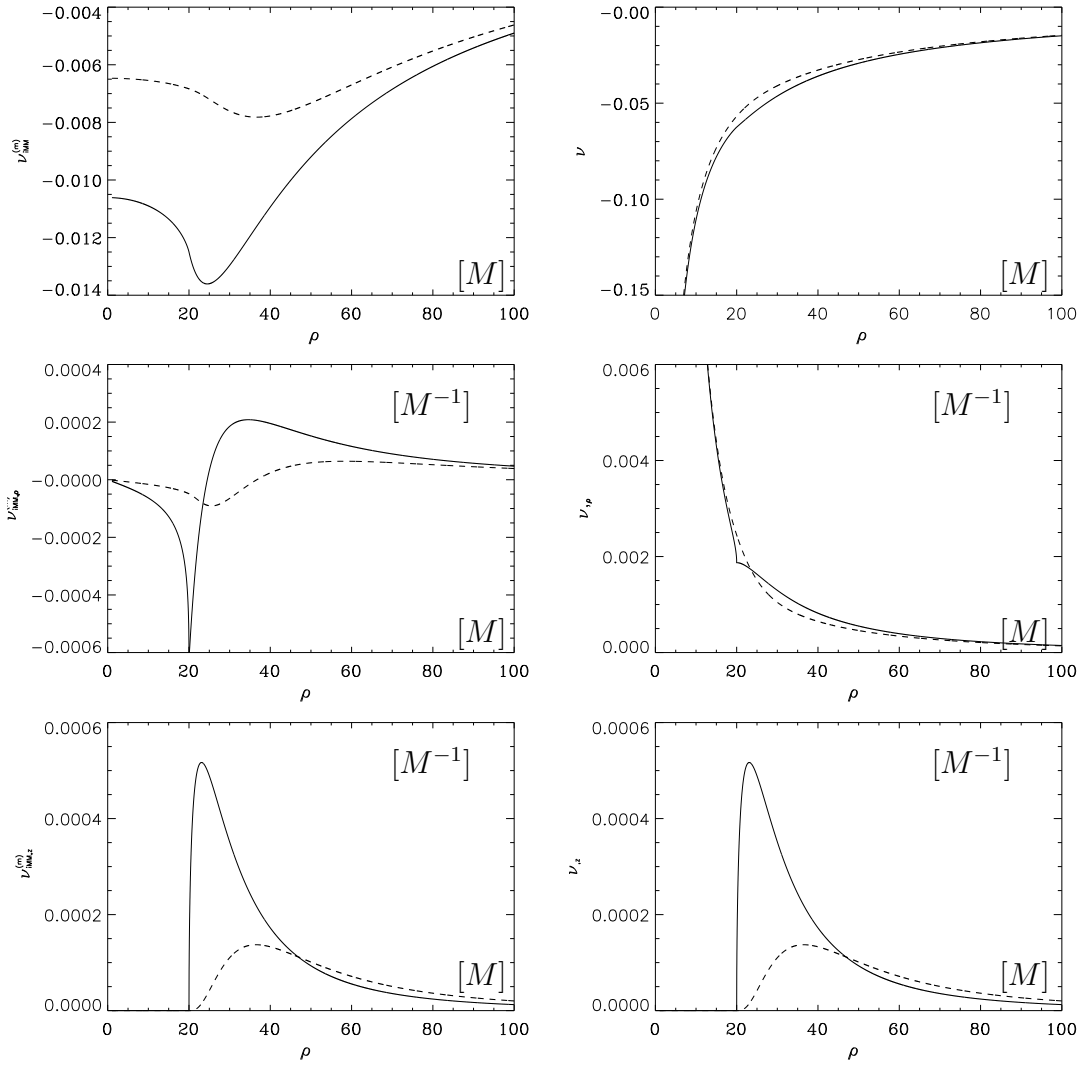


Figure 3.2: The potential ν and its derivatives ν_ρ, ν_z in equatorial plane for the inverted Morgan-Morgan discs, $\mathcal{M} = 0.5M$, $b = 20M$ (left); the superposed potential of Schwarzschild black hole and the discs (right). first iMM disc ($m = 1$) is plotted by solid line, the fourth iMM disc ($m = 4$) is plotted by dashed line.

of the second kind Q_n,

$$\nu_{\mathrm{MM}}^{(m)} = -\frac{\mathcal{M}}{b}(2m+1)!\sum_{n=0}^{m} C_{2n}^{(m)} iQ_{2n}(ix)P_{2n}(y). \tag{3.18}$$

The coefficients are defined for $(n \leq m)$ by the relation

$$C_{2n}^{(m)} = \frac{(-1)^n(4n+1)(2n)!(m+n)!}{(n!)^2(m-n)!(2m+2n+1)!}. \tag{3.19}$$

The Laplace equation (3.2) is invariant with respect to the Kelvin transformation of coordinates

$$\rho \to \frac{b^2\rho}{\rho^2+z^2}, \qquad z \to \frac{b^2 z}{\rho^2+z^2} \tag{3.20}$$

in Weyl coordinates, which means

$$x \to \frac{y}{\sqrt{x^2+1-y^2}}, \qquad y \to \frac{x}{\sqrt{x^2+1-y^2}} \tag{3.21}$$

in oblate spheroidal coordinates. Therefore we can invert the spacetime with the Morgan-Morgan disc with respect to the outer rim b to obtain a solution which describes the infinite annular disc, which has an inner rim b (inside the radius b is an empty "hole"). Because the original solid disc is stretched through the rim into infinity, the inverted disc is infinite in the sense, that the density is nonzero for arbitrary high radius, but the total mass remains finite. Also, for the same reasons, the density peak is placed quite near the inner rim, which is physically reliable in the case of the accretion disc.

After the inversion the radial density is given by

$$w_{\mathrm{iMM}}^{(m)} = \frac{2^{2m}(m!)^2\mathcal{M}b}{(2m)!\pi^2\rho^3}\left(1-\frac{b^2}{\rho^2}\right)^{m-\frac{1}{2}} \tag{3.22}$$

and the potential (see [27])

$$\nu_{\mathrm{ext}} = \nu_{\mathrm{iMM}}^{(m)} = \frac{2^{2m+1}(m!)^2}{\pi(2m+1)!}\frac{\nu_{\mathrm{MM}}^{(m)}\left(\frac{|y|}{\sqrt{x^2+1-y^2}}, \frac{x}{\sqrt{x^2+1-y^2}}\right)}{\sqrt{x^2+1-y^2}}. \tag{3.23}$$

The jump of the normal derivative of the potential in the equatorial plane, which is caused by the disc presence, is given in terms of the density as follows

$$\left(\frac{\partial \nu_{\mathrm{iMM}}^{(m)}}{\partial z}\right)_{z\to 0^{\pm}} = \pm 2\pi w_{\mathrm{iMM}}^{(m)}. \tag{3.24}$$

We will study the influence on geodesic flow of two different members of this family, namely the first inverted Morgan-Morgan disc (1. iMM disc) with $m = 1$ and the fourth first inverted Morgan-Morgan disc (4. iMM disc) with $m = 4$. According to the shape of the density profile (see [44]) and the course of the potential function ν (see Figure 3.2) we expect the 1. iMM disc would have larger influence on the motion, because there is more matter concentrated close to the inner rim, which will create deeper potential well.

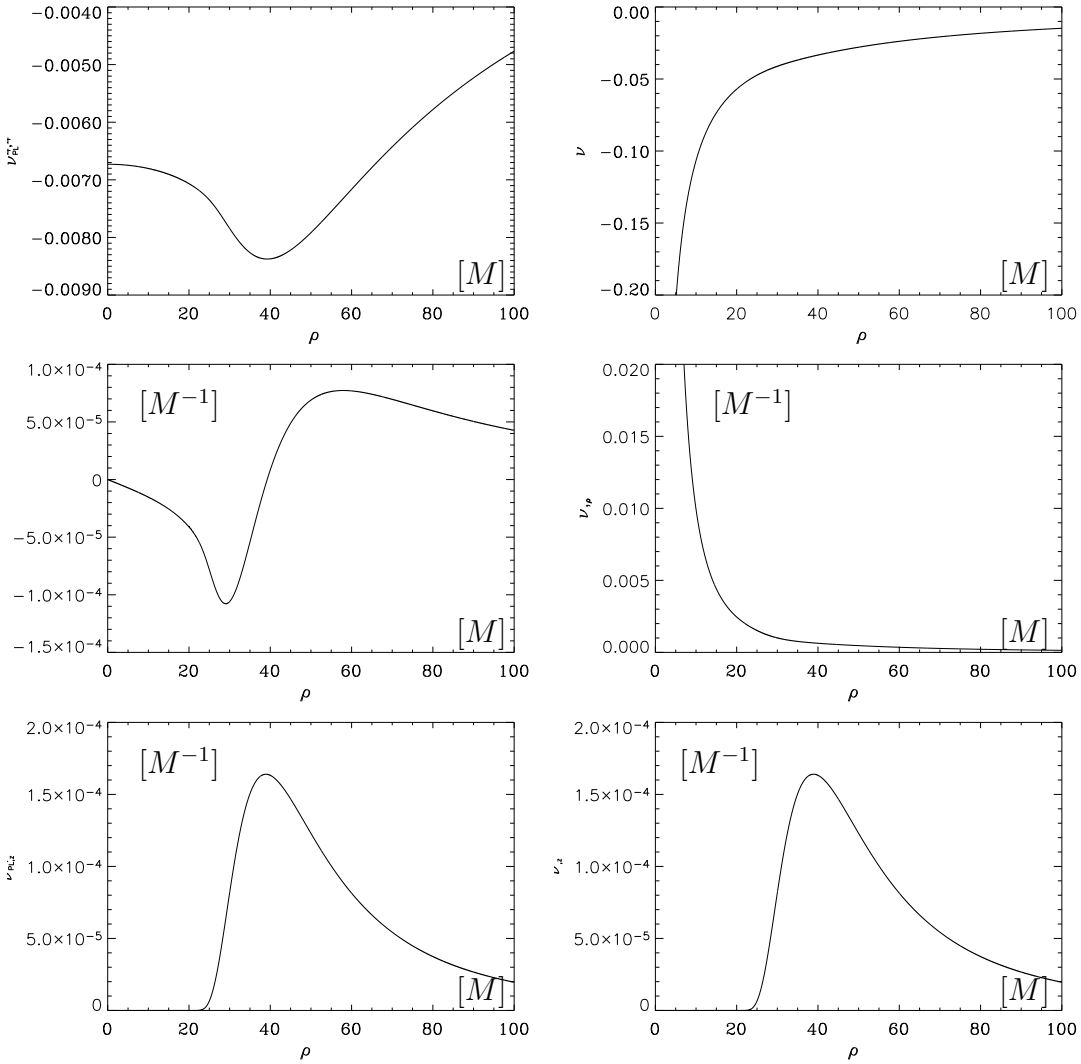


Figure 3.3: The potential ν and its derivatives ν_ρ, ν_z in equatorial plane for the disc with power-law profile with $m = 4$, $n = 4$, $\mathcal{M} = 0.5M$, $b = 20M$ (left); the superposed potential of Schwarzschild black hole and the discs and the derivatives (right).

3.3 Family of discs with power-law density profile

Another model of a family of thin annular discs with finite total mass $\mathcal{M}$ is described by the solution published in 2004 in [47]. This family has a power-law density profile in the Weyl radius ρ

$$w^{(m,n)}(\rho) = \frac{(1+\frac{1}{n})_m}{m!}\frac{\mathcal{M}b}{2\pi\rho^3}\left(1-\frac{b^n}{\rho^n}\right)^m, \tag{3.25}$$

where $(a)_m = (a+m-1)(a+m-2)\dots(a) = \Gamma(a+m)/\Gamma(a)$ is the so called Pochhammer symbol, m and n are integers.

The potential could be expressed for n even for $\sqrt{\rho^2+z^2} < b$ (inside the inner

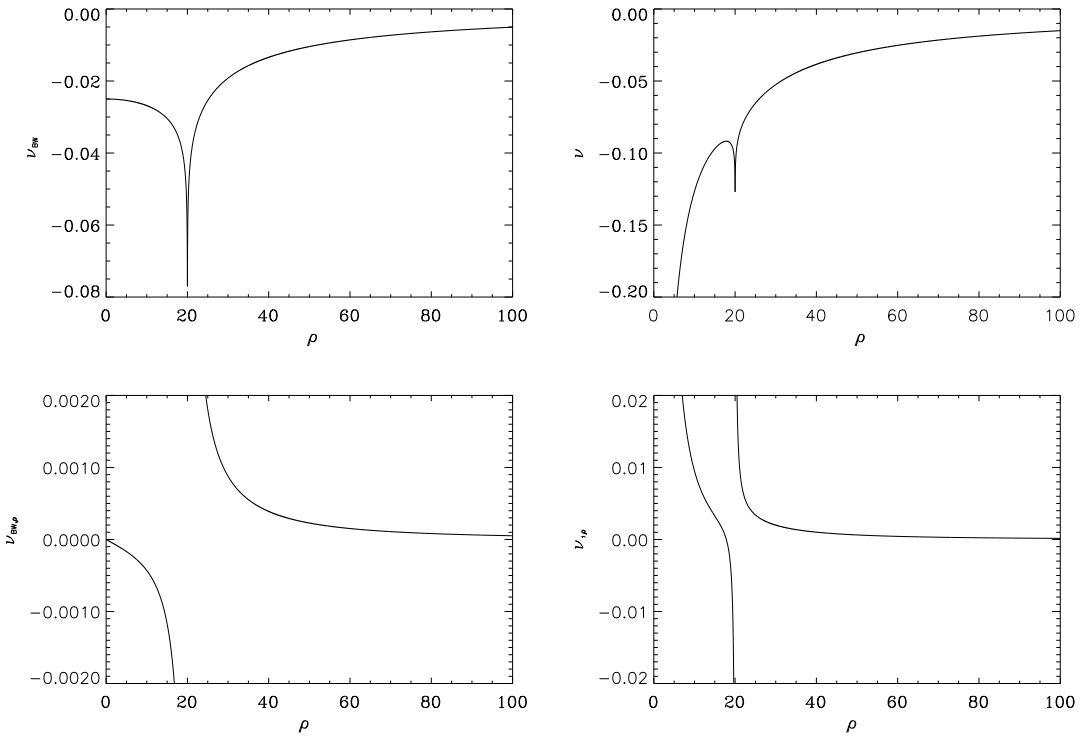


Figure 3.4: The potential $\nu_{\rm BW}$ and its derivatives $\nu_{{\rm BW},\rho}$, $\nu_{{\rm BW},z}$ in equatorial plane for the Bach-Weyl ring with $\mathcal{M} = 0.5M$, $b = 20M$ (left); the superposed potential of Schwarzschild black hole and the ring(right).

rim) in the form

$$\nu_{\rm ext} = \nu_{\rm pl}^{(m,n)}(\rho, z) = -\frac{(1+\frac{1}{n})_m}{n}\frac{\mathcal{M}}{b}\sum_{j=0}^{\infty}\frac{P_{2j}(0)P_{2j}(\frac{z}{\sqrt{\rho^2+z^2}})(\rho^2+z^2)^j}{(\frac{2+2j}{n})_{m+1}b^{2j}}. \qquad (3.26)$$

For $\sqrt{\rho^2+z^2} > b$ the relation is a little bit more complicated

$$\begin{aligned}\nu_{\rm ext} = \nu_{\rm pl}^{(m,n)}(\rho, z) \quad &= \quad -\frac{(1+\frac{1}{n})_m}{\sqrt{\rho^2+z^2}}\mathcal{M}\left(\sum_{j=0}^{\infty}\frac{P_{2j}(0)P_{2j}(\frac{z}{\sqrt{\rho^2+z^2}})b^{2j}}{n(\frac{1-2j}{n})_{m+1}(\rho^2+z^2)^j}\right. \qquad (3.27)\\ &\left. +\sum_{k=0}^{m}\frac{(-1)^k Q_{kn+1}(0)P_{kn+1}(\frac{|z|}{\sqrt{\rho^2+z^2}})b^{kn+1}}{k!(m-k)!(\rho^2+z^2)^{\frac{kn+1}{2}}}\right).\end{aligned}$$

$P(x)$ and $Q(x)$ are the Legendre polynomials and the Legendre function of the second kind, respectively.

In this thesis we will consider the case $m = 4, n = 4$ which will be denoted as (4,4)-th disc.

3.4 Bach-Weyl ring

Beside an accretion disc there can be also a torus consisting of gas and dust in the vicinity of super-massive black holes in the center of galaxies. In our Galaxy

there are probably two toroidal massive structures, one of them is at a distance around few parsecs ($1.5 \div 3pc$) with the total mass estimate $1\% \div 30\%$ of the mass of the black hole M_G (there are several estimates in the literature, see e.g. [14], [38], [34]), the other is placed at 60 up to 90 parsecs with a total mass $7M_G$ (see [17]). The simplest way how to describe these structures is the model of a thin massive ring with the mass $\mathcal{M}$ placed at the radius b, which in 1992 published Bach and Weyl in [2]. In this case the potential is given by means of the complete elliptic integral of the first kind $K(k) \equiv \int_0^{\pi/2} \frac{\mathrm{d}\phi}{\sqrt{1-k^2\sin^2\phi}}$

$$\begin{aligned} \nu_{\mathrm{ext}} = \nu_{\mathrm{BW}} &= -\frac{2\mathcal{M}K(k)}{\pi l_2}, \\ \lambda_{\mathrm{ext}} = \lambda_{\mathrm{BW}} &= \frac{(M)^2k^4}{4\pi^2b^2\rho}[(\rho+b)(-K^2+4k'^2K\dot{K}+4k^2k'^2\dot{K}^2) - \\ &\quad -4\rho k^2k'^2(k'^2+2)\dot{K}^2], \end{aligned} \tag{3.28}$$

where $\dot{K} \equiv \frac{\mathrm{d}K}{\mathrm{d}(k^2)}$, $k'^2 = \frac{(l_1)^2}{(l_2)^2}$, $k^2 = 1-k'^2 = \frac{4b\rho}{(l_2)^2}$, $l_{1,2} \equiv \sqrt{(\rho \mp b)^2+z^2}$.

Because the Bach-Weyl ring is only one dimensional source of field, we can expect that its influence on the motion would be bigger than the two-dimensional disc with the same mass, which we can see also on the course of the potential in Figure 3.4

3.5 Motion of the test particles in Weyl fields

In the superposed field described in the preceding Sections we will follow motion of the test particle, which could represent the motion of one star around a supermassive black hole in the galactic centre. It is governed by the geodesic equation

$$\frac{\mathrm{d}u^\nu}{\mathrm{d}\tau} + \Gamma^\nu_{\sigma\mu}u^\mu u^\sigma = 0, \tag{3.29}$$

where Christoffel's symbols $\Gamma^\nu_{\sigma\mu}$ are given in terms of the derivatives of the metric by a relation

$$\Gamma^\nu_{\sigma\mu} = \frac{1}{2}g^{\nu\alpha}(g_{\alpha\sigma,\mu} + g_{\mu\alpha,\sigma} - g_{\sigma\mu,\alpha}). \tag{3.30}$$

As was shown above, the metric of static and axially symmetric spacetimes could be written in the Weyl form (3.1), which is independent on the variables t and ϕ. Noether's theorem thus ensures the existence of two integrals of geodesic motion, which is the energy per unit mass $-u_t \equiv \mathcal{E}$ and the projection of the angular momentum into the symmetry axis per unit mass $u_\phi \equiv \ell$. Also the rest mass of the test particle is conserved during the motion, $m = -g^{\mu\nu}p_\mu p_\nu$. The motion of the particle is a 4-dimensional problem, thus if no other integral of motion exists, the motion could be chaotic.

Inserting the metric form (3.1) into the geodesic equations (3.30) and (3.29) and using the definition of the constants of motion we can write the equation of motion for the test particle in Weyl coordinates in the form

$$
\begin{aligned}
\frac{\mathrm{d}u^\rho}{\mathrm{d}\tau} &= -\frac{\mathcal{E}^2\nu_{,\rho}}{e^{2\lambda}} - \frac{\ell^2 e^{4\nu}\nu_{,z}}{\rho^3 e^{2\lambda}}(1-\rho\nu_{,\rho}) \\
&\quad +(\nu_{,\rho}-\lambda_{,\rho})[(u^\rho)^2-(u^z)^2] + 2(\nu_{,z}-\lambda_{,z})u^\rho u^z, \qquad (3.31)\\
\frac{\mathrm{d}u^z}{\mathrm{d}\tau} &= -\frac{\mathcal{E}^2\nu_{,z}}{e^{2\lambda}} - \frac{\ell^2 e^{4\nu}\nu_{,z}}{\rho^2 e^{2\lambda}} - (\nu_{,z}-\lambda_{,z})[(u^\rho)^2-(u^z)^2] + 2(\nu_{,\rho}-\lambda_{,\rho})u^\rho u^z, \\
\frac{\mathrm{d}u^t}{\mathrm{d}\tau} &= -\frac{2\mathcal{E}}{e^{2\nu}}(\nu_{,\rho}u^\rho + \nu_{,z}u^z), \\
\frac{\mathrm{d}u^\phi}{\mathrm{d}\tau} &= \frac{2e^{2\nu}\ell}{\rho^3}[\rho(\nu_{,\rho}u^\rho + \nu_{,z}u^z) - u^\rho],
\end{aligned}
$$

where

$$\mathcal{E} = -g_{tt}u^t, \qquad (3.32)$$

$$\ell = g_{\phi\phi}u^\phi. \qquad (3.33)$$

Because the motion in the t and ϕ direction is completely given by the relations (3.32) and (3.33), our situation is similar to the 2D systems. Together with the fact that the normalization of the four-velocity is conserved along the motion, the situation is similar to the autonomous Hamiltonian systems (where the energy is conserved) and the Poincaré's surface of section could be used for studying the motion.

3.6 Numerical integration of the equation of motion

We follow the motion of the test particles by solving the equations of motion (3.29), which we rewrite to an set of 8 equations of the first order. We do not take advantage of the form of the equations obtained in (3.31) after inserting the metric, we rather compute the whole geodesic equation with all the Christoffel's symbols computed from the metric. In this way we do not use the fact, that the normalization of four-velocity, the energy and the angular momentum is conserved along the trajectory, so we can independently control the accuracy of our computation by checking their values based on the actual four-velocity.

To obtain the geodesic we need to know the values of metric functions ν and λ and their derivatives. While we have an analytic relation for the former (differing with the type of external source we adopt), the latter has to be computed numerically using the relation (3.5). The value of $\lambda(\rho, z)$ of course depends only on the position in the plane ρ, z not on the curve along which the integral is computed. Therefore for the sake of shorter CPU time, at the beginning of the computation we determine the value of λ at a initial position of the test particle and then we compute λ along the trajectory as a ninth equation of our set of equations.

For this computation we adapt a program package `gravitacek` written by M. Žáček for integrating geodesics in the field of the superposition of the static black hole with the first inverted Morgan-Morgan disc or the Bach-Weyl ring. We add the field of the fourth iMM disc and of the disc with power-law density profile. The equations are solved using the Runge-Kutta method of the six order with the adaptive time step. The step size is controlled by checking the absolute and

relative error between the result obtained with one step of the length $2h$ and two consecutive steps of the length h. When the errors do not meet the values we demand, we halve the time step to $h/2$ and repeat the computation.

We are able to follow the motion of test particles in the field of the black hole superposed with the first inverted Morgan-Morgan disc or Bach-Weyl ring for thousands of cycles around the centre with the cumulative error in the normalization of the four-velocity $g_{\mu\nu}u^\mu u^\nu = -1 \pm 10^{-14}$, similarly for the errors in energy and angular momentum. Fourth inverted Morgan-Morgan disc yields errors about one order higher. Worse situation is in the case of the disc with power-law density profile, where the relations (3.26) and (3.27), respectively, contain an infinite sum of Legendre polynomials and Legendre function of the second kind. Not only this fact leads to more complicated computational procedure, but also brings the necessity of truncating the summation at some point. In order to achieve a reasonable CPU time needed for the integration, we choose the threshold in such way, that the total error in the normalization is about 10^{-10}.

The Poincaré surfaces of section are computed on the equatorial plane $\theta = \pi/2$. Due to the reflection symmetry of the system for this surface we can record the passages through the plane in both directions and obtain more points in shorter time. The map of the phase space is constructed from tens to hundreds of particular orbits with the same global parameters $\mathcal{E}, \ell, \mathcal{M}, b$ but different initial conditions. We launch the particles from the equatorial plane, the constant of motion $\mathcal{E}$ and ℓ together with the metric functions on the given position determines two components of the four-velocity u^t and u^ϕ according to relations (3.32) and (3.33). At given position we can compute the maximal value of u^ρ from the normalization of four-velocity if we set $u^z = 0$. This computation gives the shape of the curve of zero velocity (CZV) bounding the accessible lobe of the particle. We usually plot the CZV on the surface of section with red or purple.

We distribute the initial conditions across the accessible lobe with launching several particles at a given radius ρ increasing their u^ρ by a constant step modified by a small random value. Similarly we increase the radius ρ until we reach the end of the lobe.

The computed trajectory is recorded in the Schwarzschild coordinates t, r, θ, ϕ with constant proper time step $\Delta\tau$ together with the values of actual $\mathcal{E}$ and ℓ for the check of accuracy. This information is sufficient for computing the power spectra and the WADV for the orbits, for the latter quite fine resolution is needed (at least 100 points for one orbital period or more). For the Poincaré surfaces of section we record the r and u^r position whenever during the integration the coordinate z changes the sign. For recurrence analysis we record the position and velocity in the "cartesian-like coordinates"

$$x = r\sin\theta\cos\phi, \tag{3.34}$$

$$y = r\sin\theta\sin\phi, \tag{3.35}$$

$$z = r\cos\theta, \tag{3.36}$$

suitable for using the simple euclidean norm in the cartesian coordinates. Still before we analyse the recurrences in the trajectory we renormalize all the coordinates separately to have zero mean and unit standard deviation to overcome the different ranges for the coordinates, otherwise the coordinates would have

different impact on the results. For processing the recurrence analysis on the prepared data sets we use the code `Commandline recurrence plots` written by N. Marwan [30]. We computed the RP's from six columns of data x, y, z, u^x, u^y, u^z and also from only one column z using the possibility of reconstruction of the phase space by the time-delay procedure, which is incorporated in the software. Both this approaches give similar results.

The computation of the Lyapunov exponents (and FLI) is implemented using the two-particle method. That means, that we simultaneously initiate two neighbouring particle, whose radial position differ by the amount $\Delta\rho = 10^{-9}M^{-1}$, and we renormalize their distance, when it exceeds $10^{-1}M^{-1}$. This values hold for most of the calculation of particles moving very close to the black hole. For the astrophysical case, when we simulate the motion of stars in the galactic center surrounded by the massive distant ring (that means that the particles move at the distances ranging from few thousands M to several millions M), we increase both the values, the initial distance ranging from $10^{-5}M^{-1} \div 10^{-2}M^{-1}$ and the threshold for the renormalization in the order $10M \div 100M$. This has to be done because too small ratio between the distance $\Delta\rho$ and some typical value of ρ would lead to overestimation of the rate of divergence due to the rounding errors, which was already mentioned in [52]. When the initial distance is undervalued, than the distance grow rapidly to some reasonable value whether the motion is regular or not.

The norm of the deviation between the two particles is computed *in the configuration space only* after certain proper time step (if the proper time of the two particles differ, we "push forward" the particle which is behind) using their proper distance. The velocity of the neighbour is then renormalized by the same factor as the distance.

The MEGNO is then computed from the time evolution of FLI according to the relation (2.7). With the obtained values of different quantifiers (e.g. FLI, MEGNO or DIV) we can colour the points in the surface of section of the correspondent orbit. By this way we obtain coloured maps of the phase space revealing different chaotic and regular layers. For the MEGNO based maps we set a threshold $\delta = 4$ for distinguishing between regular and chaotic motion and increase all the values higher than δ by a constant value (typically 200) in order to change significantly the colour tone of the chaotic orbits. Thanks to this we can visually easily distinguish also the weakly chaotic and regular orbits.

4. Results

The main aim of this thesis is to present the consequences of the nonlinearity of the Einstein equations encoded in the geodesic flow of test particles. We are interested in real physical situations taking part around stellar or super massive compact objects which are the neutron stars and black holes. Therefore we did not include only a simple model for testing the possible chaotic behaviour, but we picked out the most reliable *exact* solutions describing a typical situation near black holes, namely the matter forming an accretion disc or a distant dust torus. The studied systems are described in details in Chapter 3.

We are also interested not only in the onset of chaos itself but also in different ways of obtaining important information about the motion and their effectiveness. We are using different methods suitable for theoretical exploration of dynamical systems or for practical examination of experimental data sets. The former could be used for detailed study of dynamical systems which we are able to compute the trajectories and possibly also some other quantities of, i.e. we know the equations of motion. Their outcomes are summarized in Section 4.1. The latter use the information about the system encoded in the time series of some dynamical quantity, such as the time evolution of one coordinates, *without* necessity of knowing the underlying dynamical equations. These methods have practical importance for the investigation of real astrophysical processes, like the motion of observed stars in the galactic center. For this type of analysis see Section 4.2. The theoretical background is given in Chapter 2.

To confirm our results obtained by the used methods we also studied a classical system consisting of a spring and a dashpot characterized by a non-standard constitutive relations in the similar way. These systems are dissipative because of the presence of the dashpot which bring along some new phenomena not observed in the Hamiltonian case. A short introduction into the chaos in dissipative systems is given in Section 1.4, the studied systems and the results are described in Chapter 5.

4.1 Methods for dynamical systems with given equation of motion

At the beginning of our study we want to capture the global properties of the phase space and estimate the parameters range where the chaotic motion manifests if there is any. Having the equation of motion of our test particles we adopt the Poincaré surface of section to trace the regular islands, their separatrices and stochastic layers. Mostly we examine the space time of the superposition of the initially Schwarzschild black hole with the first inverted Morgan-Morgan disc (see Section 3.2) because for this source the computations consume the least computer time. For comparison we also give examples of space times with the fourth inverted Morgan-Morgan disc, with the (4,4)-th disc with power-law density profile and with Bach-Weyl ring.

We focus on the geodesic particles with two parameters (the constants of motion energy $\mathcal{E}$ and angular momentum ℓ per unit mass) orbiting the black hole

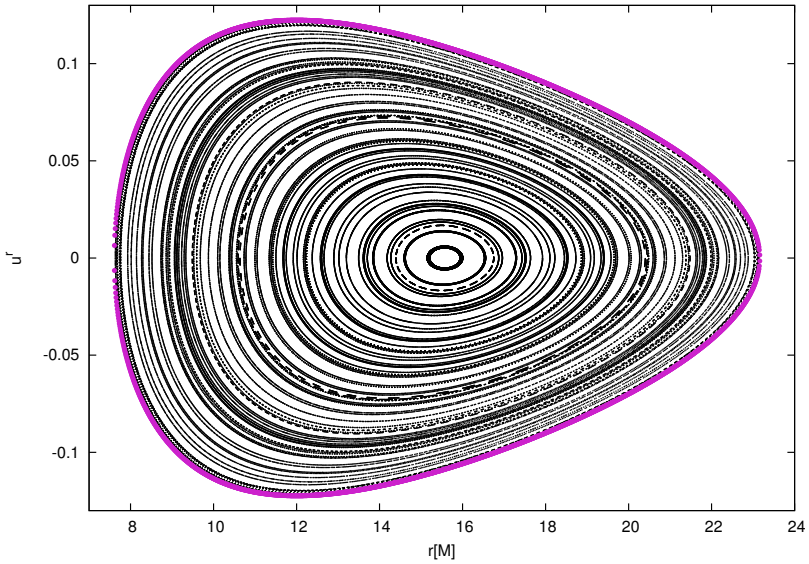


Figure 4.1: Poincaré surface of section for motion of test particles with $\mathcal{E} = 0.97$ and $\ell = 4$ around a Schwarzschild black hole without any other additional source.

on quite low radii, between $r = 3M$ to approximately $r = 50M$ which is only few times the Schwarzschild radius. Around the black hole we place a disc or ring with the inner rim ranging from few M to about $30M$ and with varying relative mass $\mathcal{M}$ from a fraction of the mass of the black hole M to comparable values. We consider bounded orbits with energy $\mathcal{E} < 1$. Such particles can exist only in a finite region in the phase space bounded by a surface of zero velocity, which intersects the surface of section along the curve of zero velocity (CZV). If the angular momentum is high enough the potential barrier prohibits the particles from falling into the black hole and the CVZ outlines a closed accessible lobe in the phase space. Such configuration satisfies the requirements needed for the chaos definition presented in the Section 1.1.

4.1.1 Poincaré surfaces of section

In Figure 4.1 we give a typical surface of section for the test geodesic motion around a simple Schwarzschild black hole, which is known to be completely integrable. For construction of all the Poincaré surface of section we choose the equatorial plane $z = 0$, where we can plot the passages in both direction due to the reflection symmetry of the system. The CZV circumscribing the lobe is plotted with magenta. The motion is purely regular, librating around a periodic orbit in the centre of the accessible lobe, hence forming the primary island which is folliated into the invariant tori by the value of action. Their surfaces are after some time covered with the quasiperiodic trajectories. Hereafter we will study the differences of the phase space topology from this typical case caused by the presence of additional matter around the black hole.

The first finding which follow from the obtained surfaces of section is the fact, that the global topological properties of the phase space strongly depend on all the parameters describing the motion in the superposed field. We compute a

several series of surfaces of section with changing one of the parameters $\mathcal{M}$, b, $\mathcal{E}$ and ℓ, keeping the others constant. The results were published in paper *Free motion around black holes with discs: between integrability and chaos – I*, which is attached in Appendix A [45].

In Figure A.4 (the Figure 4 in the Appendix A) the series of Poincaré surfaces for various mass of the first inverted Morgan-Morgan disc is plotted. Although the value range is quite short, $\mathcal{M} \in [0.1 \div 2]M$, the topology of the phase space undergoes significant transmutation. For lower mass of the disc the motion is completely regular and very similar to the unperturbed case in Figure 4.1, the presence of the disc only affects the size of the accessible lobe, in other words it lessens the potential near the black hole and enables motion of particles with lower energy.

When the mass $\mathcal{M}$ is high enough new stable higher periodic orbits appear and form their own islands. At this moment also new unstable periodic orbits arise at the points where the separatrices cross. For higher mass of the disc thin stochastic layers grow up along the separatrices. These layers are first visible in Fig. 4 for $\mathcal{M} = 0.46M$ and they are densely covered by dots creating a black region in contrast to the regular orbits forming a closed curves. It is typical that the biggest stochastic layer forms near the edge of the lobe, another very thin chaotic layer also encloses the island with period 7.

Increasing the mass further, the potential barrier around the black hole lowers and could be overcome by the particles. That leads to the escape of particles from the stochastic layer into the black hole. The part of the phase space which enables this escape is significantly lighter in the presented plots, because we map the surface with different initial condition quite uniformly (see Section 3.6 for details).

In that case, obviously, the presumptions of the chaos definition presented in Section 1.1 do not hold because the motion is not bounded in a finite volume of phase space. Since the particles could escape from the system we can not construct a future invariant set for $\tau \to \infty$. But the visible features of the parts of the orbits, we can follow before this happen, do not change, the chaotic behaviour clearly have validity also locally (including time). Thus there should be given another definition (and description) of chaotic motion which also comprehends such cases.

With the increasing strength of the perturbation many of the invariant tori break and the chaotic layers merge together to form a big "chaotic sea". Within the primary island also new periodic islands appear and tend to the outer region. For $\mathcal{M} = 0.9M$, the motion is very chaotic and dissimilar to the unperturbed case. The motion is highly affected by the presence of the disc, the primary island is small and surrounded by few higher periodic islands. For $\mathcal{M} = 1.1M$ the primary island is broken completely giving rise to an unstable periodic orbit at its place and a period two islands above and below the zero radial velocity line. However such configuration holds only for a small range of $\mathcal{M}$ and soon the primary island emerge again.

This first encounter with our system proves that the dynamics evolves according to the KAM theory also for the comparable mass of the disc with respect to the central black hole. The two dimensional nature of the disc makes it weaker source of the field than the black hole even when the total mass of the disc is

greater than the total mass of the black hole. During our survey we did not obtain any surface of section with completely chaotic motion, some regular islands persist in every configuration.

On the next Figure (Figure A.5) a series with changing position of the inner rim of the disc is presented, where the position on the rim r_{disc} is given in Schwarzschild coordinates (3.11). When the disc is placed close to the black hole, which is supposed for the accretion disc to reach the ISCO, most of the matter of disc is below the orbits, because the maximum of the density of inverted Morgan-Morgan disc is near the inner rim especially for the first iMM disc. Accordingly on the first plot we can see a big primary island of regular motion above the density maximum. There is a chaotic layer near the edge of the lobe, but the potential barrier is not high enough and these particles escape into the black hole quite soon. Moving the rim further from the black hole causes more changes of the motion, chaotic motion which does not escape onto the centre appears, many different periodic islands arise. The changes of topology proceed in rather different manner, another kind of structures appears. Within this range of r_{disc} the motion of particles is again highly sensitive to the exact position of the inner rim. For r_{disc} higher than $22M$ the motion is regular again.

Similarly to the case with changing mass proceed the change of energy depicted in Figure A.6. This similarity arises from the fact that the more massive disc lowers the potential in the region, thus enlarges the accessible lobe of the particle and effectively imitates increasing of energy. Interesting point of this survey is the fact that the higher energy means the higher chaos only within a range of lower energies, in contrary for high energy the motion returns to regular regime in a substantial part of the phase space.

The last parameter of our system is the angular momentum ℓ. Realising that the higher angular momentum means that the motion is more concentrated in the azimuthal direction and this part of the evolution is completely driven by the relation (3.33), we come to a conclusion that increasing the angular momentum while keeping the energy and other parameters constant leads to suppressing chaos. At the same time this process also makes it difficult for the particles to fall into the black hole and thus enables the existence of future invariant chaotic set. During our computations we have seen both this effects of angular momentum.

With these surveys we mapped the influence of the parameters on the motion. We observed a substantial effect of the additional source within certain range of parameters. The next question is whether the exact form (namely the density profile) of the additional source is significant for the perturbation. Therefore we compute similar plots also for the other sources, namely the fourth inverted Morgan-Morgan disc and the (4,4)-th disc with the power-law density profile.

The results for the fourth inverted Morgan-Morgan disc are given in Figures 7 and 8 of Appendix A. The difference between this two additional sources is very small, the latter has only slightly wider shape of the density profile with smaller peak. Indeed, the topologies of the geodesic flow in this two systems are comparable and the evolution proceeds in similar way. However we can notice that in order to obtain a similar topology, the total mass of the fourth iMM disc has to be higher than the mass of the first iMM disc, we can say that the fourth disc is weaker perturbation.

In case of the power-law disc, depicted in Figure A.9, the situation looks

very similar to Figure 4, but we have to notice that the energy of the particles is set to bigger value. Again, this source proves to be weaker than first iMM disc, but otherwise the topological properties of the phase space are quite similar. Comparing this three types of source we can conclude, that the exact density (and thus field) profile is not crucial and all three forms of the disc lead to analogous behaviour which is predicted by the KAM theory (see Section 1.2).

Another situation occurs in the system of the black hole surrounded by the Bach-Weyl ring. In Figure 10 of Appendix A several plots with increasing mass of the ring is given and the mass of the ring is notably smaller than the mass of the black hole, namely it changes in the range $\mathcal{M} \in [0.001 \div 0.04]M$. Despite low mass of the ring the motion is significantly influenced by its presence, many resonant islands occur and the phase space topology is considerably dissimilar to the disc case. The particles feel the ring presence everywhere in the phase space. On the second part of this Figure higher masses are considered ($\mathcal{M} \in [0.07 \div 1.1]M$). Here, when the orbits are captured in the region above the ring, they behave regularly feeling only the centre more massive. The rest of the phase space shows dominantly chaotic behaviour and many of the higher period islands disappear for the more massive rings.

From what was said above we can conclude that the more singular additional source causes stronger perturbation. This holds for the disc with different density profiles as two dimensional sources and especially for the ring as one dimensional source. We have also observed that the response of the dynamic is not linear with respect to the change of the parameters. In some parameter ranges the topology changes wildly with many emerging and disappearing islands together with their thin stochastic layers along their separatrices, in the phase space evolves quite smoothly and slowly.

In this Section we used the capability of Poincaré surface of section and we described the phase space of the particles quite in detail. However, as we will show later, we can combine the Poincaré surface of section with other methods to display more information about the system.

4.1.2 Lyapunov exponents

After quite detailed survey of the main global topological properties of the phase space of geodesic test particles we focus more on individual trajectories and their features, which could be described by many different quantifiers. At first we will compute the relativistic counterpart of the classical maximal Lyapunov exponent. As we have mentioned in Section 2.3 its computation has to be treated cautiously and the obtained value has to be interpreted carefully. We adopt the procedure proposed by [54] for this task, however in our case there is a preferred time coordinate related to the symmetry of the system, which makes the interpretation more natural.

For obtaining the value of mLCE we plot the values of the so called time-dependent maximal Lyapunov exponent $\tilde{\lambda}_{\max}(\tau)$ in the log-log scale. For regular orbits, which have the theoretical value $\tilde{\lambda}_{\max}(\tau \to \infty) = 0$, the time-dependent value approaches zero decreasing linearly in the log-log scale. The chaotic orbits initially behave similarly and after the final value is reached the curve saturates and remains constant. Therefore in order to distinguish between these two regime

we have to compute for long time enough not only to reach the final value but also to recognise its convergence. Bearing in mind that we observe the course of $\tilde{\lambda}_{\max}(\tau)$ in log-log scale, the total integration time has to be significantly larger than the time when the final value is reached.

We choose several regular and chaotic orbits and compute their evolution for a very long time $\tau_{\max} = 10^7 M$, corresponding to several tens of thousands of orbital cycles around the central black hole. The Poincaré surfaces of section together with the course of $\tilde{\lambda}_{\max}$ for these six trajectories are given in Figures C.1 and C.2.

In Figure C.1 all the orbits belong to the same phase space (i. e. they have the same parameters) and they differ by the initial conditions only. We present one regular orbit belonging to the primary island (orbit A), another regular orbit from small higher periodic island (orbit B) and one specific realization of the chaotic trajectory filling the whole stochastic layer (orbit C). In Figure 2 three orbits with different degree of chaoticity and with different global parameters are given (orbits D, E, F).

After this long integration time the mLCE of the regular orbits A and B decrease to the value around $\tilde{\lambda}_{\max} \approx 10^{-6} M^{-1}$, which let us conclude that these orbits are not chaotic on time scale shorter than $10^6 M$. From this conclusion it is obvious, that the convergence of this method is very slow.

Even though the formal definition of the maximal Lyapunov exponents (2.1) is based on the limiting process when time goes to infinity, hence this quantity should be constant within one connected stochastic layer (which is densely filled by one chaotic trajectory), in fact we can also observe a local behaviour of the orbits. If the chaotic orbit moves in the vicinity of the regular island, it could be trapped in this area for a long time, imitating the behaviour of the regular island during this period. The time-dependent mLCE mirrors this behaviour yielding lower values for this episodes.

To draw attention to this feature we colour the points in the Poincaré surface of section of the chaotic trajectories according to the time of their recording. Hence, when the colour grade of the resulting layer is uniform (composing from randomly scattered points), the orbit evenly fills the section and spends similar amount of time in every part of the layer. Example of such orbit is given on the last row of Figure C.2 (the orbit F). On the other hand, when the orbit is captured in smaller part of the layer, this region gains a specific colour grade according to the appropriate time interval. This type of behaviour could be seen in all the other chaotic orbits in Figure C1 and C2 and it is accompanied by changes of $\tilde{\lambda}_{\max}$. We split orbit D and plot its shorter snapshots in Figure 4.2. There we can see, that at the beginning (for $\tau < 2 \cdot 10^5 M$) the orbit is confined to much smaller region. According to this $\tilde{\lambda}_{\max}$ decreases to values around $5 \cdot 10^{-5} M^{-1}$. But after this time, the orbit outbursts into bigger layer while the value of mLCE correspondingly increases to $\tilde{\lambda}_{\max} \approx 10^{-4} M^{-1}$ (in the top right plot in Figure C.2).

The course of mLCE(τ) provides essential pieces of information about the underlying dynamics. Due to the slow convergence plenty different indexes resulting from the basic definition of mLCE is introduced in the literature, see Section 2.3. We adopt the FLI and MEGNO for our analysis and give the results in the next Section. We will also estimate mLCE by the methods processing the time series and we will compare the results in Section 4.2.3.

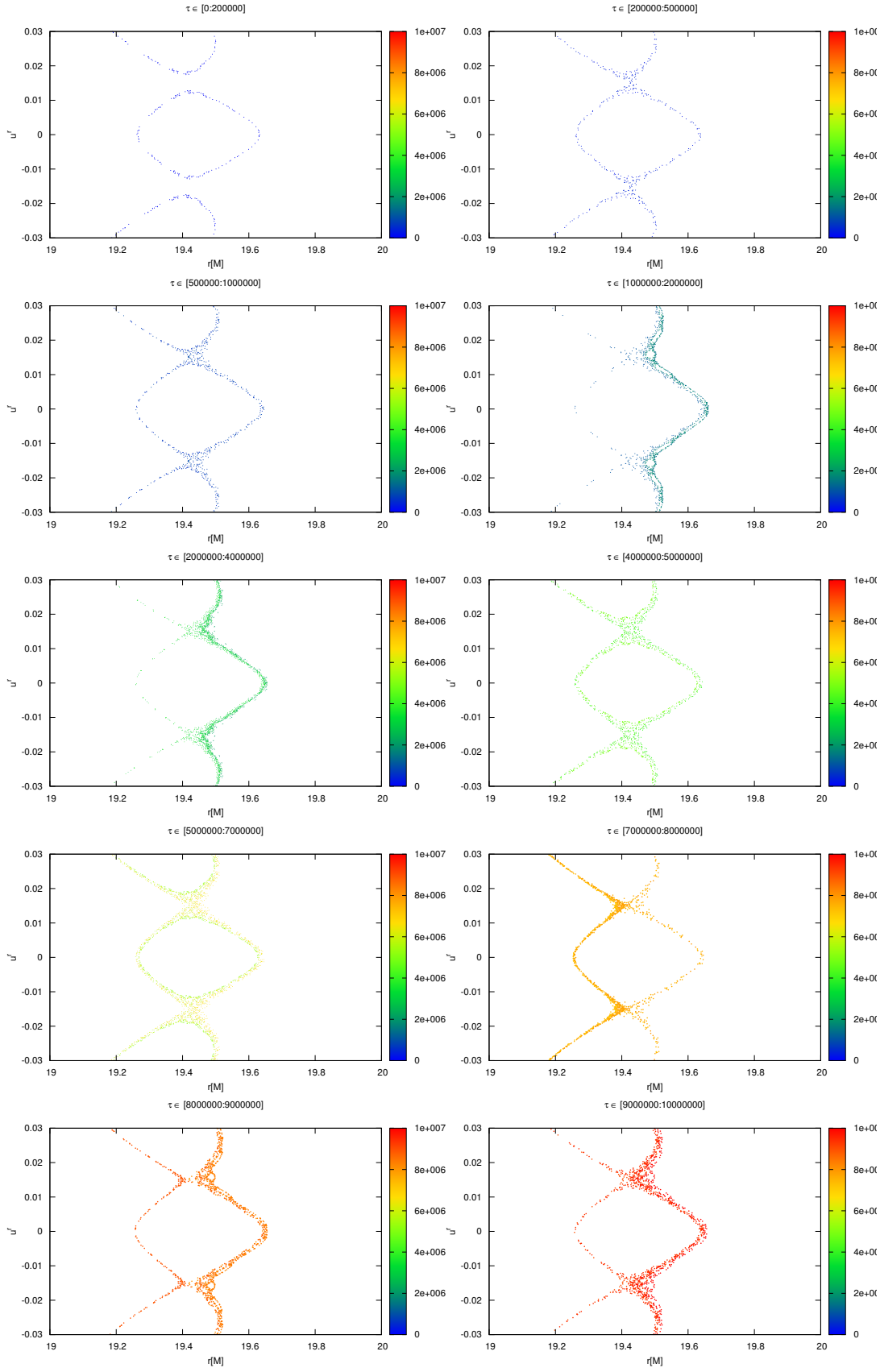


Figure 4.2: Poincaré surfaces of section for motion of test particle with $\mathcal{E} = 0.947$ and $\ell = 4$ around a black hole with first iMM disc with $\mathcal{M} = 0.94M$ and $r_{\rm disc} = 20M$. The orbit with $\tau_{\rm max} = 10^7 M$ is divided into several parts.

4.1.3 FLI and MEGNO

We can overcome the slow convergence of the direct computation of mLCE with different approaches. At first we can realize that for distinguishing between chaotic and regular motion we do not have to compute the actual *value* of mLCE. We can use the fact that the evolution of the deviation vector $\Delta\mathbf{x}$ is different for chaotic and regular motion right from the beginning of the computation. On this observation is based the FLI method described in Section 2.3. With this method we follow the rate of elongation of the deviation vector, which is polynomial for regular motion and exponential for chaotic one.

We denote the logarithm of the ratio between the actual norm of $\Delta\mathbf{x}$ to the initial value as FLI(τ) according to the relation (2.5). For the same six orbits mentioned earlier we plot FLI(τ) in Figures C.4 and C.5. On the first sight we can see the crucial difference between regular and chaotic FLI, approaching values around 4 for the former while exceeding several thousands or more for the latter (even for the weakly chaotic orbit D). Hence we can significantly shorten the integration time and thus compute more orbits with different initial condition to map the whole phase space analogically to Section 4.1.1 within a reasonable CPU time.

At first we map the phase space of orbits A, B, C, which means that we launch few hundreds of trajectories with initial conditions somehow uniformly distributed around the surface of section with $\tau_{\max} = 250\,000M$. We compute the final value FLI($\tau_{\max}$) and according to this value we colour all the points of the particular trajectory in the surface of section. The resulting FLI-map of the phase space is given in the first row in Figure C.6, the values lie in range FLI(τ) $\in (0 \div 400)$ (the orbits with FLI($\tau_{\max}$) > 300 are all plotted with the red colour). This map again reveals the local behaviour of trajectories inside the stochastic layer, namely now the integration time is not long enough for the particle to leave the region around the regular islands, hence the values are significantly lower in the vicinity of the islands than in the rest of the chaotic sea. In fact we can see three different regions with clearly distinct values going from the less chaotic around the islands to the most chaotic at the edge of the lobe. Small regular islands embedded inside the chaotic sea are visible.

On the picture in the second row of Figure C.6, the disadvantage of FLI shows up. Namely it is the time dependence of the final value of FLI. We can not say in advance how big the value for regular motion will be, because this relies on the total integration time and also on the poperties of the system (the velocity of the evolution, the exact position of the orbit in the phase space etc.). Therefore we have to look at some orbits by another method and to find some regular orbit's FLI($\tau_{\max}$) (in our case we can easily use the Poincaré's surface of section, but this could be quite problem for another dynamical systems, e.g. the systems with higher dimension). After that we can choose some threshold to distinguish the regular and chaotic orbits. But the relation between the discovered regular FLI($\tau_{\max}$) and the threshold is also uncertain (we only know that the threshold has to be higher). In the situation, when the phase space contains only sufficiently chaotic orbits, we can find a gap between obtained low and high values of FLI, which clearly leads to picking the threshold inside this gap. But when there are weakly chaotic orbits, the FLI values are distributed along the whole interval between the minimal and maximal obtained FLI and we can not

set up the threshold only on the basis of the obtained spectrum of FLI. This is quite important point for those who want to automatically map lot of settings of dynamical systems with different behaviour. Seeking for the same, we suggest to create the maps according to the value of MEGNO, more precisely the final average value $\bar{Y}(\tau_{\max})$, not the FLI. For the relation between FLI and MEGNO see Section 2.3.

The properties of MEGNO overcome the above mentioned disadvantage of FLI because it converges to 2 for regular orbits regardless of the total integration time, and increase linearly for chaotic orbits with the coefficient equal to the mLCE ($Y(\tau) \approx \lambda_{\max}\tau$). Therefore, we can just set *only one* threshold for every map we compute, in our case we choose $\delta = 4$, and we know that we could make mistakes only for few very slightly chaotic orbits (the orbits which are chaotic on the time scales comparable to the total integration time or longer). Actually, we can say in advance that with this method we are able to recognize the chaotic orbits, whose $\lambda_{\max} \gtrsim 2\delta/\tau_{\max}$, hence when we choose $\tau_{\max} = 250\,000M$ the resolution is around the value $\lambda_{\max}(\tau_{\max}) \gtrsim 3 \cdot 10^{-5}M^{-1}$.

In Figure C.6 the MEGNO-maps (right column) are given for comparison with the FLI-maps (left column). Regarding the chosen threshold we add a constant number (200) to $\bar{Y} > \delta$, which provides us a better colour and visual distinction between the regular and chaotic motion. On the MEGNO-map, the small periodic islands "pop out" from the thin stochastic layers.

One more comparison of FLI- and MEGNO-maps is given in Figure C.7. Here we increase the total time to $\tau_{\max} = 10^6 M$ to give a chance to FLI to obtain better resolution, but even in this case the MEGNO performs considerably better. The reason is again the presence of very weakly chaotic orbits in the phase space. In the second row of this Figure we present a zoom of the complicated region of the phase space, where tiny higher periodic islands and thin stochastic layers appear. Note the very narrow chaotic layer plotted in dark green colour which envelops a separatrix around the periodic orbits which with period 4 winds around another higher periodic orbit and which is revealed by MEGNO, but looks regular at FLI-map (the coordinates of one one island is approx. $r = 18.7M, u^r = 0.05$).

In Figures 4.3 and 4.4 we plot several FLI- and MEGNO-maps for light Bach-Weyl rings, which could be compared to the Figures A.10. For the masses $\mathcal{M} = 0.01M$ and $0.02M$ the phase space looks very complicated, but the values of FLI (MEGNO) reveal, that there are not chaotic trajectories. For higher masses, some chaotic motion appears.

The evolution of phase space with changing energy $\mathcal{E}$ for the Bach-Weyl ring is depicted in Figures 4.5 and 4.6 using the MEGNO maps. For lowest energy the motion is confined to region close to the ring, with the growing energy the accessible lobe grows together with appearance of various period islands. For the energies $0.952 - 0.954$ the primary island splits, leaving the original stable period one orbit unstable. For high energies the particles from chaotic layer escape to the black hole quite quickly but also several big regular islands establish.

The influence of the (4,4)-th disc with the power law density profile with growing mass is presented in Figures 4.7 and 4.8. The mass of the disc is higher to achieve similar behaviour of particle moving around the first iMM disc. Similar plots are also given for the fourth iMM disc in Figures 4.9 and 4.10. With high mass of the disc (around twice the mass of the black hole) the motion is chaotic

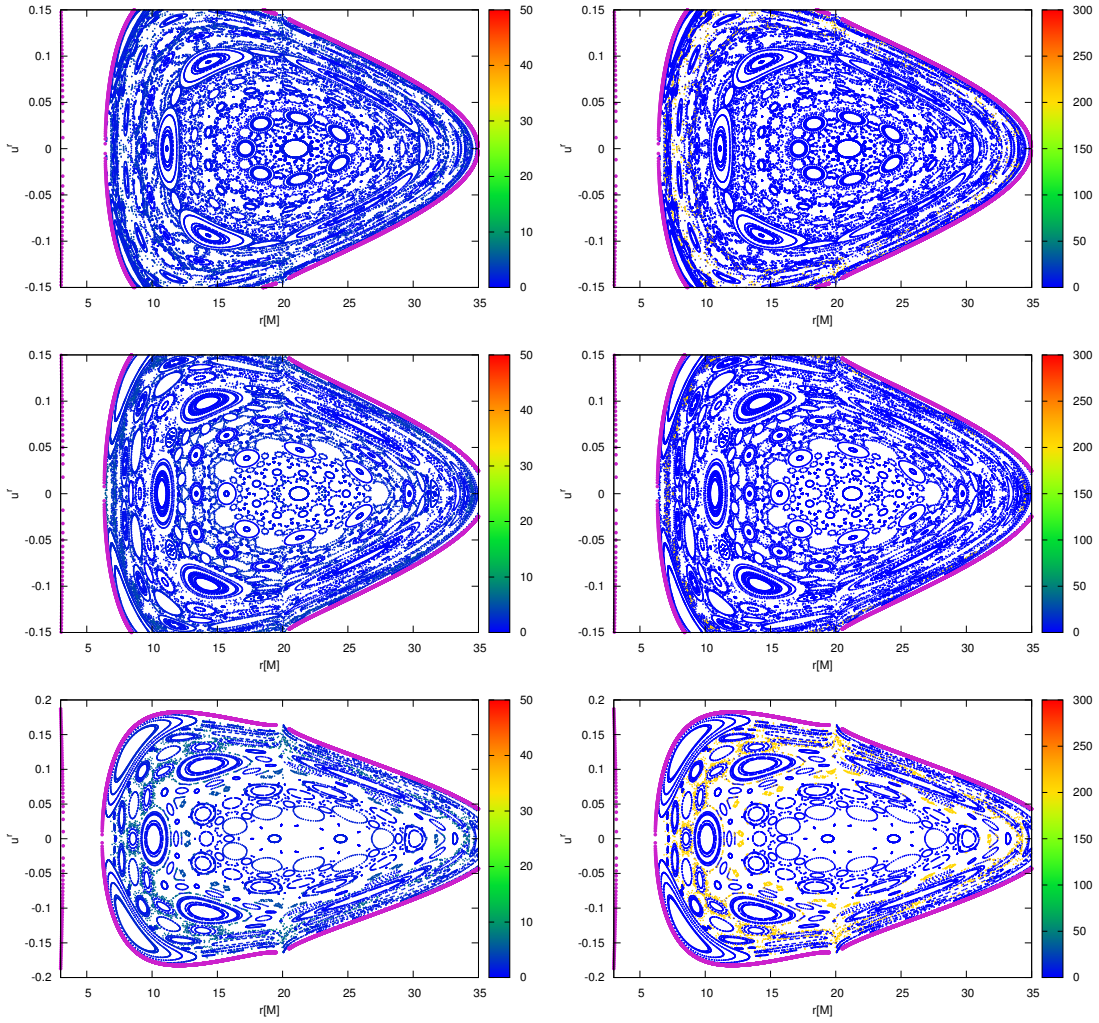


Figure 4.3: FLI-map (left column) and MEGNO-map (right column) for motion of test particle with $\mathcal{E} = 0.947$ and $\ell = 4$ around a Schwarzschild black hole with Bach-Weyl with $r_{\text{ring}} = 20M$ and $\mathcal{M} = 0.01M$ (first row), $\mathcal{M} = 0.02M$ (second row) and $\mathcal{M} = 0.04M$ (third row).

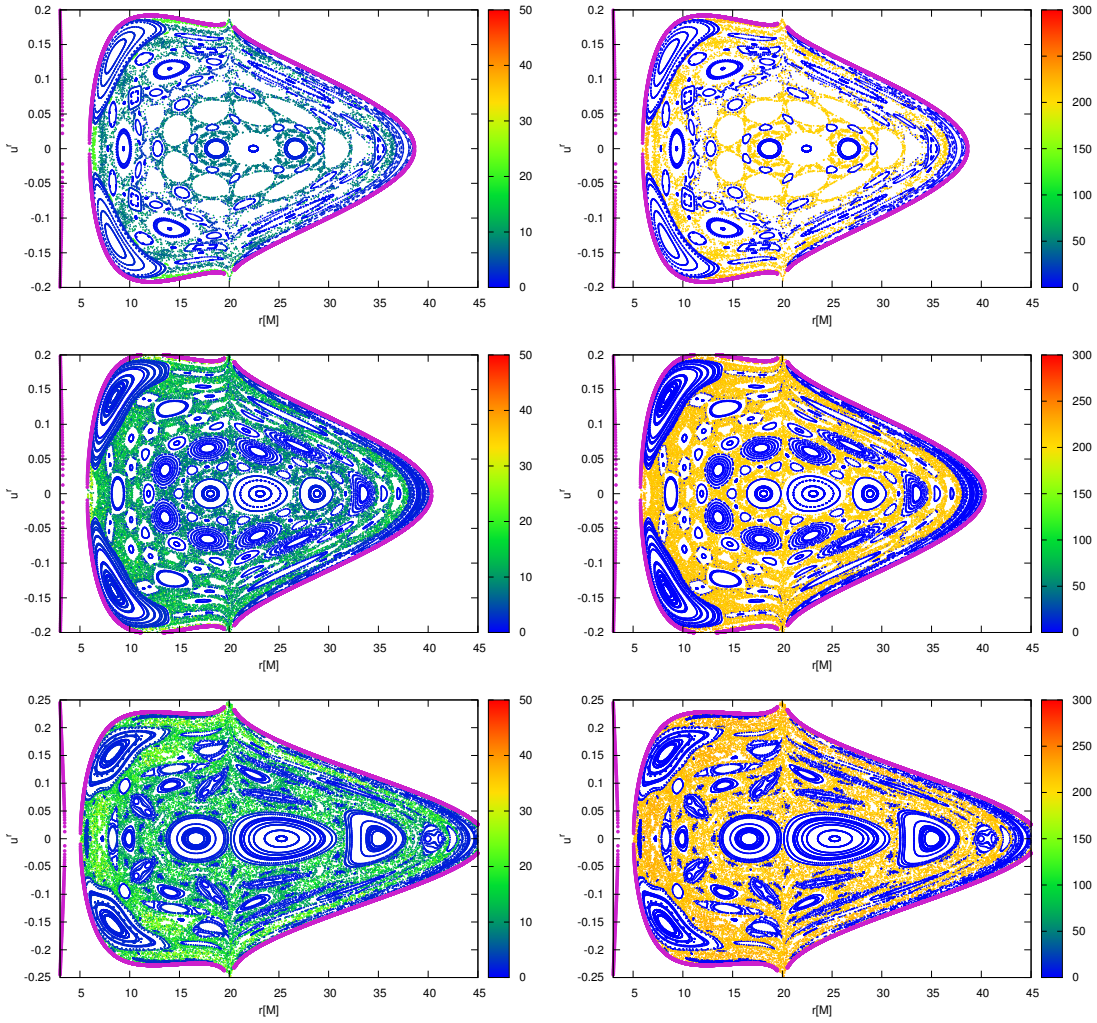


Figure 4.4: FLI-map (left column) and MEGNO-map (right column) for motion of test particle with $\mathcal{E} = 0.947$ and $\ell = 4$ around a Schwarzschild black hole with Bach-Weyl with $r_{\text{ring}} = 20M$ and $\mathcal{M} = 0.07M$(first row), $\mathcal{M} = 0.1M$ (second row) and $\mathcal{M} = 0.2M$ (third row).

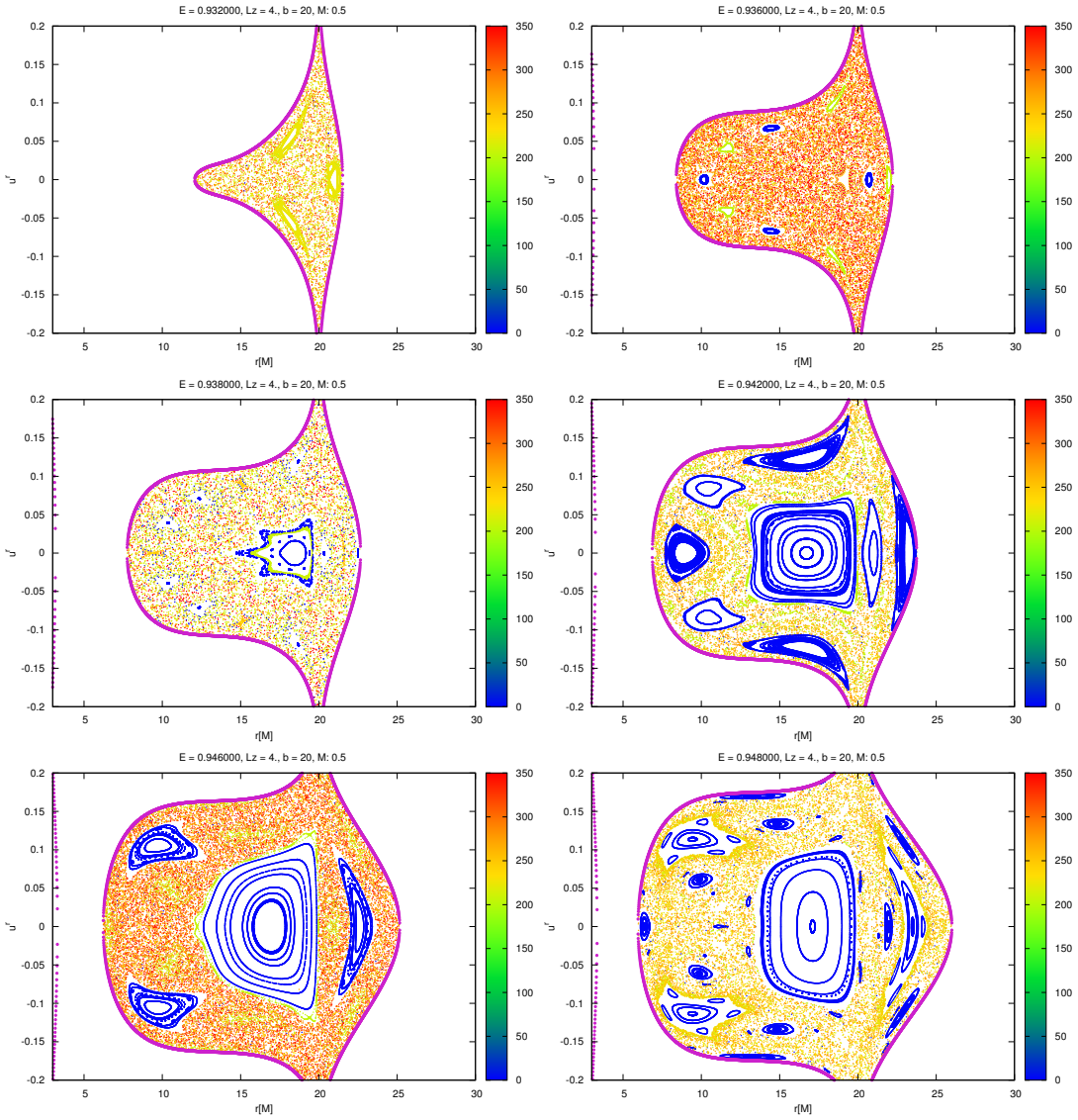


Figure 4.5: MEGNO maps for motion of test particle with $\ell = 4$ and changing energy $\mathcal{E} = 0.932, 0.936, 0.938, 0.942, 0.946, 0.948$ around a black hole with Bach-Weyl ring with $r_{\rm disc} = 20M$ and $\mathcal{M} = 0.5M$.

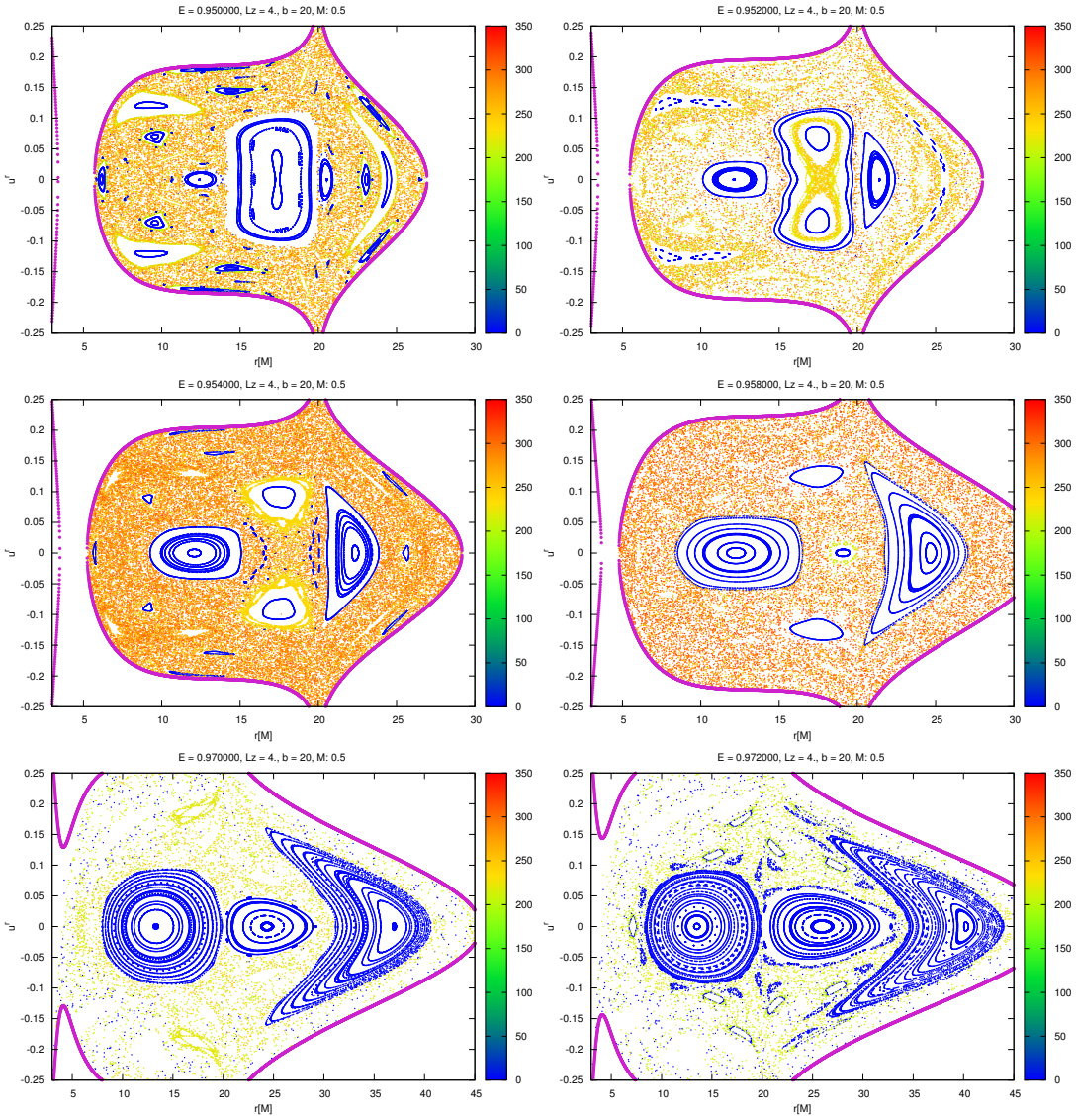


Figure 4.6: MEGNO maps for motion of test particle with $\ell = 4$ and changing energy $\mathcal{E} = 0.95, 0.952, 0.954, 0.958, 0.97, 0.972$ around a black hole with Bach-Weyl ring with $r_{\text{disc}} = 20M$ and $\mathcal{M} = 0.5M$.

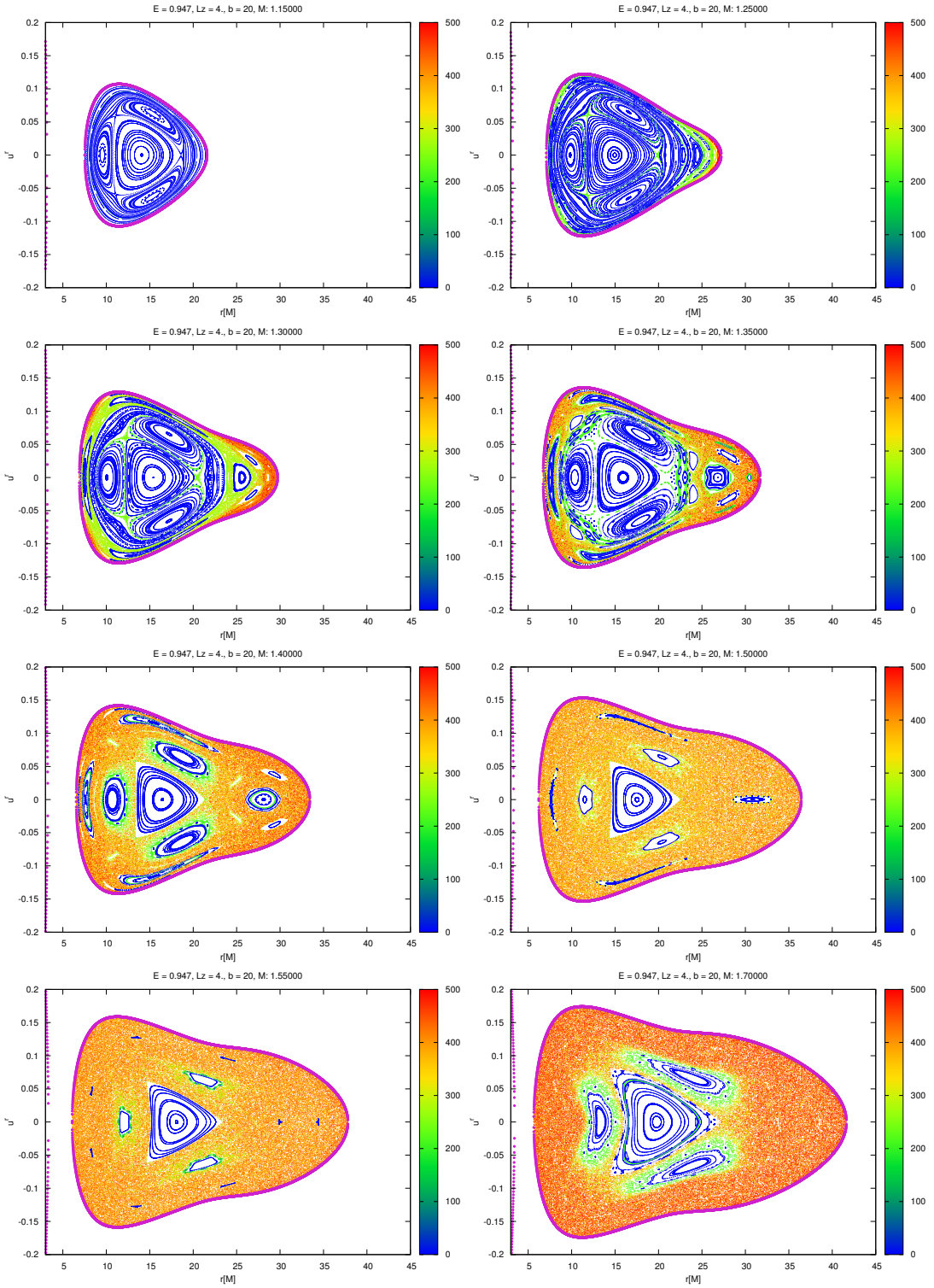


Figure 4.7: MEGNO maps for motion of test particle with $\mathcal{E} = 0.947$ and $\ell = 4$ around a black hole with (4,4)-th power-law disc with $r_{\rm disc} = 20M$ and changing mass $\mathcal{M} = 1.15M, 1.25M, 1.3M, 1.35M, 1.4M, 1.5M, 1.55M, 1.7M$.

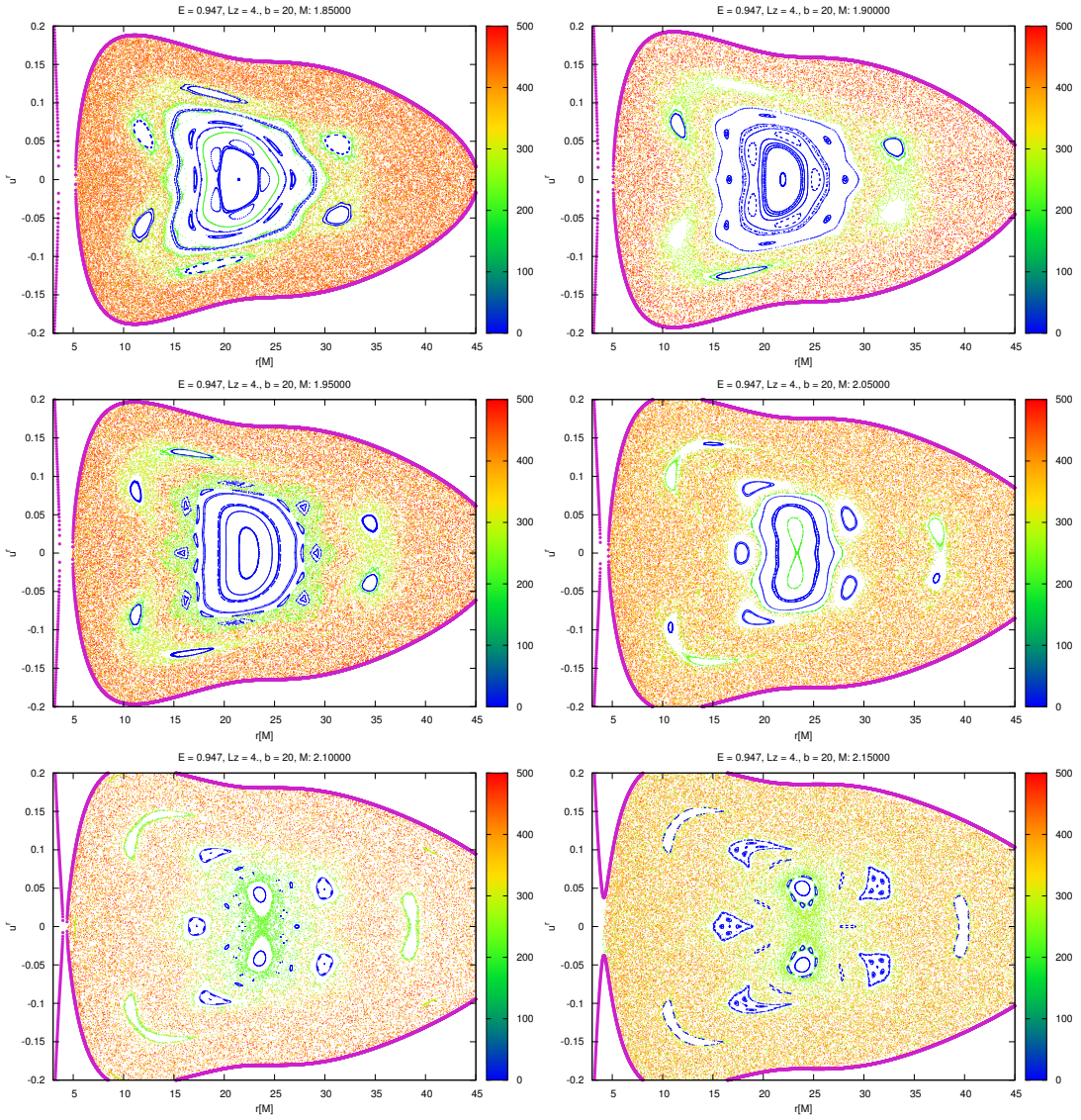


Figure 4.8: MEGNO maps for motion of test particle with $\mathcal{E} = 0.947$ and $\ell = 4$ around a black hole with (4,4)-th power-law disc with $r_{\rm disc} = 20M$ and changing mass $\mathcal{M} = 1.85M, 1.9M, 1.95M, 2.05M, 2.1M, 2.15M$.

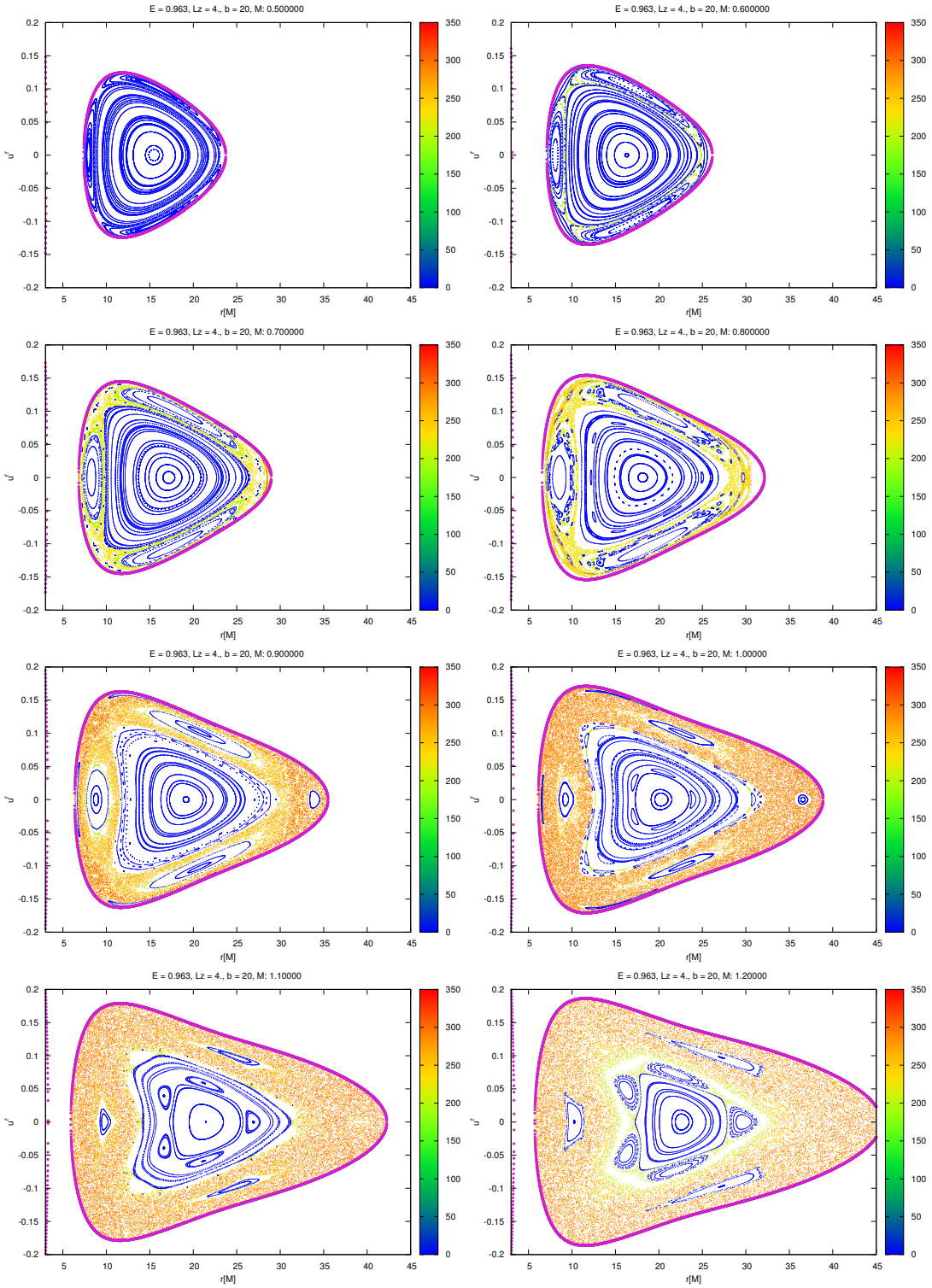


Figure 4.9: MEGNO maps for motion of test particle with $\mathcal{E} = 0.963$ and $\ell = 4$ around a black hole with fourth iMM disc with $r_{\rm disc} = 20M$ and changing mass $\mathcal{M} = 0.5M, 0.6M, 0.7M, 0.8M, 0.9M, 1.0M, 1.1M.1.2M$.

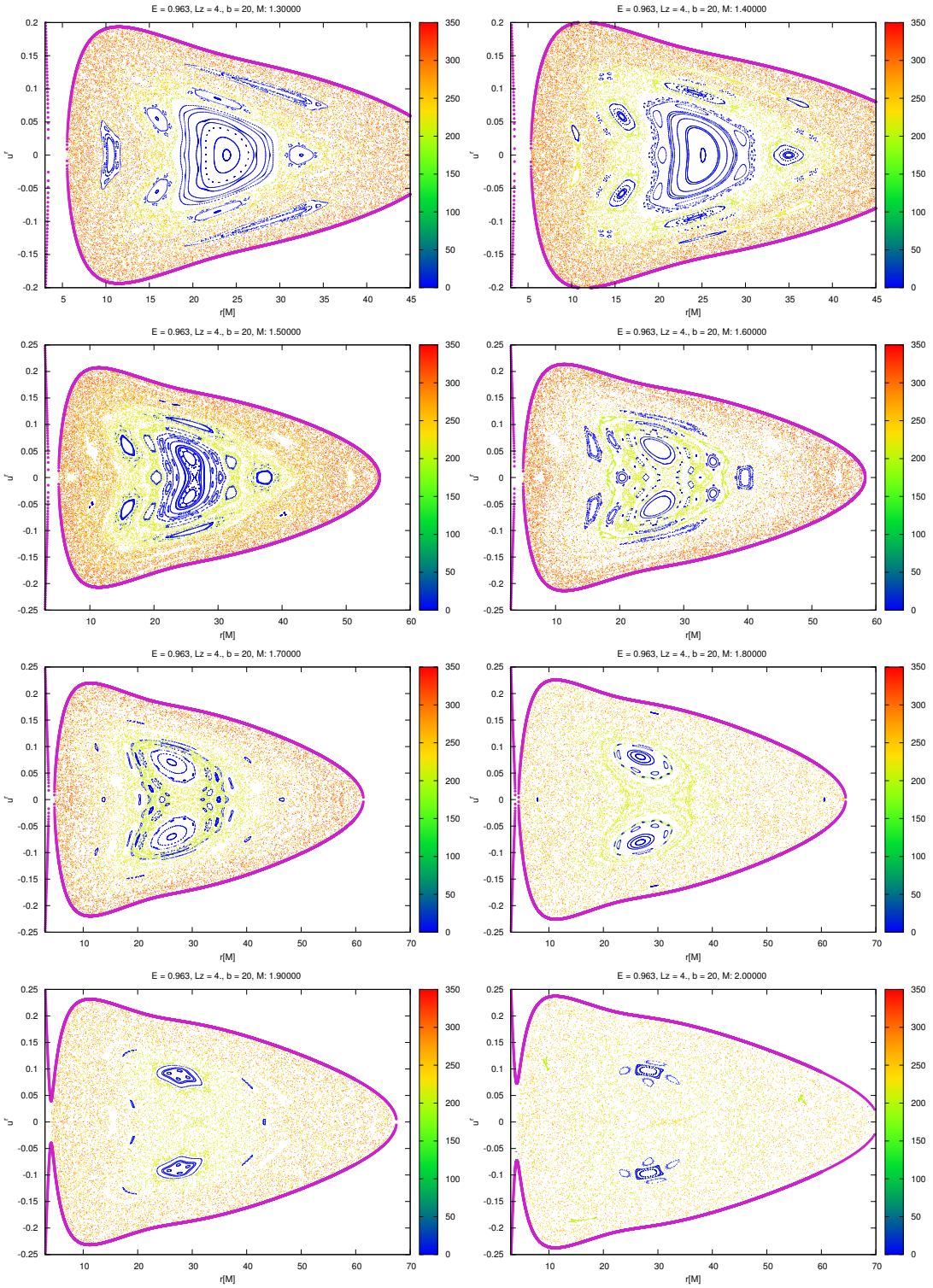


Figure 4.10: MEGNO maps for motion of test particle with $\mathcal{E} = 0.963$ and $\ell = 4$ around a black hole with fourth iMM disc with $r_{\rm disc} = 20M$ and changing mass $\mathcal{M} = 1.3M, 1.4M, 1.5M, 1.6M, 1.7M, 1.8M, 1.9M, 2M$.

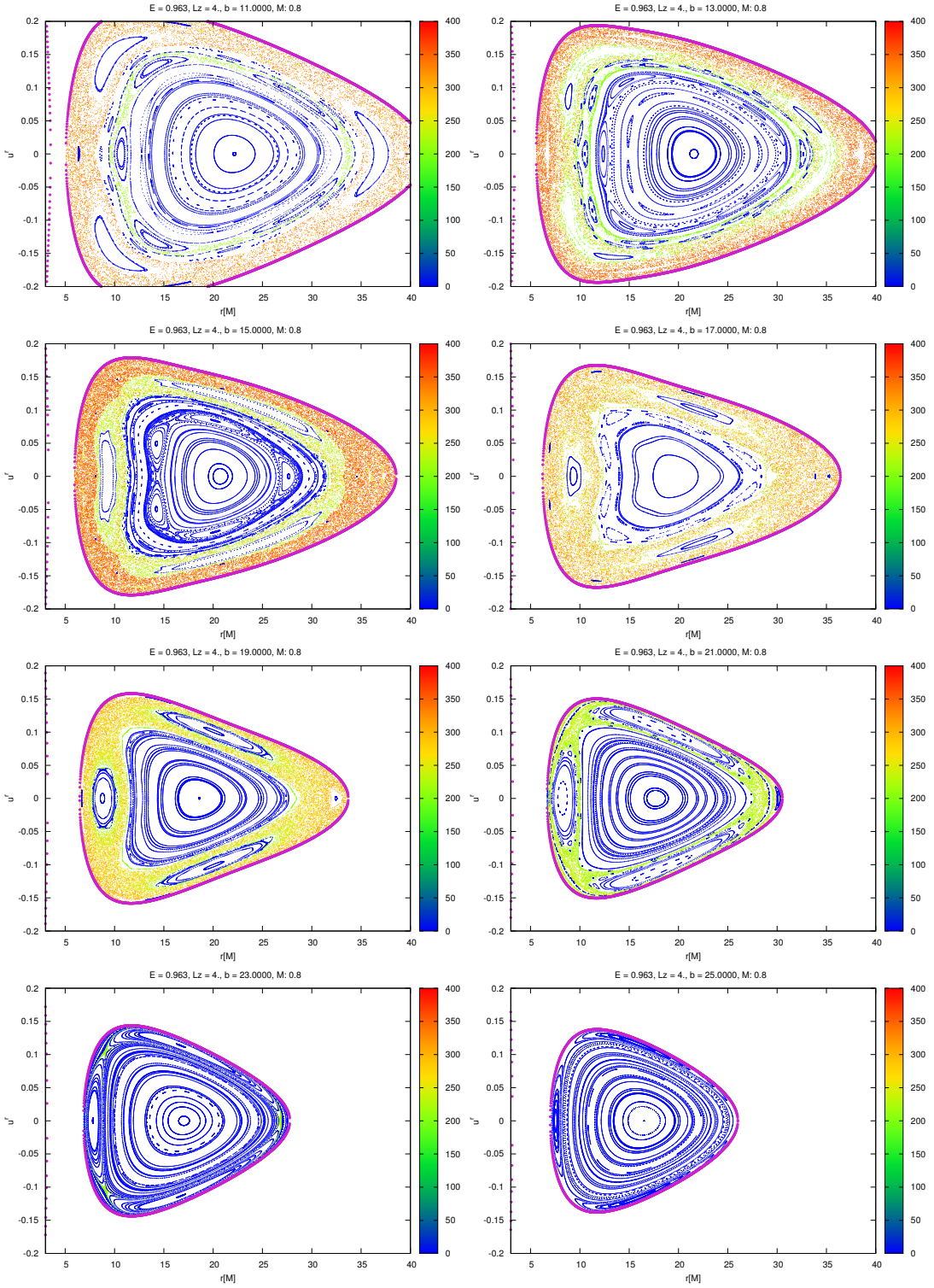


Figure 4.11: MEGNO maps for motion of test particle with $\mathcal{E} = 0.963$ and $\ell = 4$ around a black hole with fourth iMM disc with $\mathcal{M} = 0.8M$ and changing position $r_{\text{ring}} = 11M, 13M, 15M, 17M, 19M, 21M, 23M, 25M$.

in substantial part of phase space. In Figure 4.11 the dependence of the position of the inner rim for the fourth iMM disc is provided. Moving the disc further from the black hole, thus further from the moving particles lowers the influence of the disc on the motion.

On the attached DVD also several animations of the changing phase space are available.

Beside the improved resolution and better attributes for automatic mapping, the MEGNO also gives us a chance to estimate the mLCE with much better convergence than the direct computation presented above. This is based on the linear regression of $2\bar{Y}(\tau)$ because the asymptotic is $Y(\tau) \approx \lambda_{\max}\tau$. For the orbits A – F we plot the linear regression in Figures 4 and 5 in Appendix C together with the $Y(\tau)$ and $\bar{Y}(\tau)$ or $2\bar{Y}(\tau)$ for regular and chaotic orbits, respectively. The values obtained by these two methods are compared in Table 1 in Appendix C. The agreement for the chaotic trajectories is very good (difference are smaller than 5 percent) and for the regular trajectories the $\tilde{\lambda}_{\max}^{\mathrm{MEGNO}}$ are by one or two orders smaller.

The better convergence of computing $\lambda_{\max}^{\mathrm{MEGNO}}$ is due to the different behaviour of $\bar{Y}$ for longer τ. We therefore do not compute the linear regression from the whole curve $\bar{Y}(\tau)$, but we skip some time at the beginning and consider only $2\bar{Y}(\tau)$, $\tau \in (c\tau_{\max}, \tau_{\max}), c \in (0,1)$. In this way we can also improve our previous result, where we stated, that we can not distinguish orbits, which do not approach the threshold δ. In Figure 4.12 we plot two orbits, which both have $2\bar{Y} < 8$. The first one is regular and the second one is the part of orbit D from the Figure C.2 computed only for $\tau_{\max} = 200\,000M$, which we proved to be chaotic earlier. We computed several fits to obtain $\tilde{\lambda}_{\max}^{\mathrm{MEGNO}}(\tau_{\max}, c)$ with $c \in [0.1, 0.9]$. The obtained values are plotted in the third row of the Figure 4.12. Although the two orbits are computed for the same total time, the fitted values $\tilde{\lambda}_{\max}^{\mathrm{MEGNO}}(\tau_{\max}, c)$ for the regular orbits are lower. Moreover they decrease as c increases following the logarithmic decay. This is caused by the fact, that $\bar{Y}(\tau)$ converges to 2. The second orbits yields higher values of $\tilde{\lambda}_{\max}^{\mathrm{MEGNO}}(\tau_{\max}, c)$, which are increasing first. The reason for this behaviour could be seen best in the plots in the second row of Figure 4.12, where the curves $2\bar{Y}(\tau)$ together with the linear fits for $c = 0.1, 0.3, 0.5, 0.7$ and 0.9 are given. For some of the orbits, which were wrongly denoted as regular by the threshold δ, the examination of the curve $\tilde{\lambda}_{\max}^{\mathrm{MEGNO}}(\tau_{\max}, c)$ depending on c could reveal their chaotic nature.

Possibility of chaos near the galactic centers

In this Section we will consider such parameters which could represent the motion of stars in the vicinity of the supermassive black holes. In our geometrized unit system the absolute scale is given by the mass of the black hole. Because the best observational data naturally involve the center of our Galaxy, we will take into account the current estimates of its parameters. However, the situation in other galaxies could be slightly or even significantly different.

In the literature (see Section 4 in Appendix C for extensive list of references) many observational data concerning the center of our galaxy could be found. Recently the estimate of the black hole mass has been updated to $M \approx 4.3{\cdot}10^6 M_\odot$, which establishes our units as $1M \approx 21.5s$, $1pc \approx 5 \cdot 10^6 M$ (see e.g. [22]). The gravitationally most important sources are the central black hole and two different

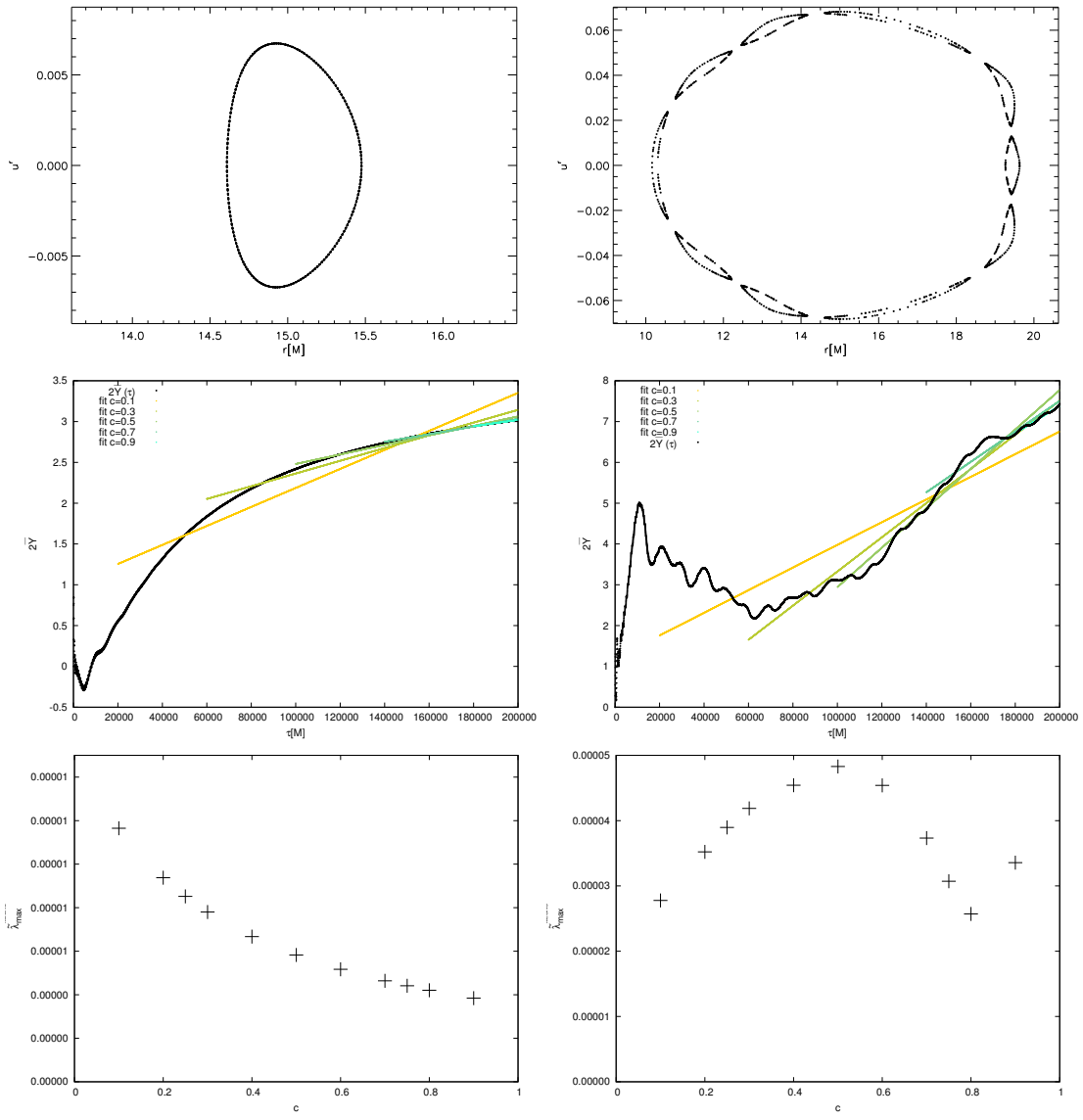


Figure 4.12: Fitting of MEGNO to obtain K_2 for regular and weakly chaotic trajectory with $\mathcal{E} = 0.947$ and $\ell = 4$ around a Schwarzschild black hole with first inverted Morgan-Morgan disc with $\mathcal{M} = 0.94M$ and $r_{\text{disc}} = 20M$, which both do not approach the threshold δ.

molecular tori called circumnuclear rings (CNR). The inner one is placed at the radii $r_{\text{ring}} \in (1.2 \div 3)pc$ and the estimates of its mass range between $10^4 M_\odot$ and $10^6 M_\odot$ (see e.g. [14], [38], [34]). The outer ring is much heavier, $\mathcal{M} \approx 3 \cdot 10^7 M_\odot$, and it has roughly elliptical shape with the half-axes $60pc$ and $100pc$ (see [17]). Also the accretion disc is present very close to the black hole (it extends to some hundreds or thousands of Schwarzschild radii), but its total mass is probably much lower than 1% of the mass of the black hole.

At first we will concentrate on the motion of the S-stars, which are the closest stars to Sgr A* moving in the region $r \approx 5 \cdot 10^3 M \div 10^5 M$. In Figure C.8 we examine the possible influence of the Bach-Weyl ring with the same mass as the black hole placed at different radii in the range $2 \cdot 10^4 \div 2 \cdot 10^5 M$. This set of plots reveals that the dynamic is very sensitive to the position of the ring with respect to the size of the accessible lobe, namely the ring affects mainly those orbits, which get in its vicinity. Thus, changing the position in quite narrow range of radii lead to substantial change of the behaviour of the geodesic flow. Similar behaviour could be seen in Figure C.9, where we shift the mass of the ring from $0.1M$ to $1M$ keeping the rim at $10^5 M$. Again, altering the mass only by a factor 10 leads from completely regular behaviour to mostly chaotic. The detailed discussion is presented in Section C.4.1.

Now, we will simulate the real tori by the one dimensional Bach-Weyl ring placed at median radius ($r_{\text{ring}} \approx 10^7 M \approx 2pc$ for the inner CNR and $r_{\text{ring}} \approx 4 \cdot 10^8 M \approx 80pc$). As we have seen earlier the ring affects mainly the particles which can get close to it. Our calculations confirm this statement also for the real parameters of the tori, therefore the motion of the S-stars is regular with both those tori, because they do not reach the region where the motion would be influenced significantly. But when we focus on particles moving further from the black hole, the chaos for the upper limit on the inner torus mass has been found (see Figure C.10) for particles with quite reasonable velocities, for the probably unrealistic mass $\approx 1M$ (the estimates of the mass of CNR in the literature are quite widely spread) the chaos is substantial.

Hence, we can conclude that the presence of a massive ring in the vicinity of the black hole can significantly affect the geodesic flow in the superposed field. Another question is if the the real observed circumnuclear ring could have the same effect. Here we have to remind that mainly those particles which come close to the ring turn out to be chaotic. In that case the approximation of the torus by a thin ring is not sufficient, the torus should rather have a smooth density profile spread within larger region. It is thus uncertain, if the real massive toroidal structures in the galactic center could induce chaotic motion. On the other hand our results show that this approximation is possibly not adequate in some cases and could bring some artificial effects when used in other types of simulations.

We also tried to compute the motion of the S-stars around the black hole surrounded by an accretion disc simulated by the first inverted Morgan-Morgan disc. Even for the very unrealistic mass $\mathcal{M} = 0.01M$ the motion of the stars above the maximum of the density profile (placed around 100M) does not show any chaotic behaviour. The presence of the accretion disc thus probably does not influence S-stars which move above the radius $r = 3000M$, it could have some impact only on particles on much smaller radii.

4.1.4 Latitudinal action

We can also compute other quantities along the trajectory of the test particle, which can reveal some information about the motion. An example of such quantity is the latitudinal action J_θ, which we introduced in Section 2.4. We can understand this quantity as an approximation of the last constant of motion for the regular orbits. Even though is not the exact form of the fourth integral of motion, it steadily oscillates around a mean value, which is constant along the whole orbit. The amplitude of these oscillations is very small for orbits belonging to islands with low period, especially for the orbits forming the primary island, and it is higher for higher-periodic islands.

Naturally the chaotic orbits do not possess any other integral of motion, hence for them this quantity is not conserved at all. More likely it changes rather wildly without any apparent mean value. In Figure D.1 in the bottom row, one regular and one chaotic trajectory is depicted, together with their power spectra and the latitudinal action. The fiercely changing profile correspond to the chaotic orbit, the regular orbit yields the evenly oscillating profile with small amplitude around the value 0.117.

When the particle undergoes a period of sticky motion (see Section 4.2), thus it imitates the regular behaviour, the latitudinal action also shows a more or less regular oscillations. For chaotic orbits which enclose some regular islands it is typical that they spend some time in their vicinity and then they return to the chaotic sea. This periods of motion could interchange irregularly. Examples of these orbits are given in Figure A.17. The seeming "mean value" during the sticky period is not conserved during the more chaotic phase of motion, actually the J_θ could oscillate around another mean value in another sticky segment of the orbit.

4.2 Time series analysis

So far we have presented the features of our system, which were described by quantifiers arising from the equations of motion, in other words we proceeded the systematic study of a given (which means *known*) dynamical system, which is an approximation of the situation around black holes. Now we want to turn our attention to methods, which are able to reveal important information about the dynamical system only from the available experimental data, i.e. *without* knowing the equations of motion. This is important for studying the motion around real astrophysical black holes, e.g. around the supermassive black holes inside the centers of galaxies, because the physical processes in such regions are too complicated to be precisely described by some exact model.

In practise astronomers measure some quantity, e.g. the apparent position of the star on the sky, repeatedly with some time interval. Hence the experimental data comprise the time series of dynamical variables. To mimic the situation of an experimental physicist but on the other hand to be able to compare the results with those obtained earlier from the equations of motion we generate such time series by our model using the dynamical equations and then we proceed time series analysis on the obtained data. Thanks to this the accuracy and difficulty of different methods could be compared. For this purpose we choose the time

series $z(\tau) = r(\tau)\cos\theta(\tau)$, representing the vertical position off the equatorial plane.

4.2.1 Power spectra

The chaotic behaviour of the particle is reflected by the irregular course of the dynamical variables influenced by multiple frequencies. Hence it is quite natural to compute the spectrum of a time series of such variable and compare the regular and chaotic case.

An example of the 3D portrayal of a regular and chaotic trajectory is given in Figure 13 of Appendix A together with the corresponding Poincaré surfaces of section and the power spectra. This Figure reveals the typical look of the power spectra for both types of motion. In regular regime, the motion is driven by a few characteristic frequencies which are clearly visible in the form of distinct peaks, otherwise the spectrum is flat and smooth. The set of frequencies is characteristic for a whole periodic island, which reflects the similarity of the motion within the same island (see Figure A.14 for comparison of spectra from different islands). The chaotic $z(\tau)$ is much more irregular given rise to a fuzzy spectrum showing no particular distinct peaks but a noisy increase of amplitude from high frequencies down to the few hundredths M^{-1} followed by the white noise in the low frequencies.

According to the shape of spectrum in the low frequencies we can distinguish two types of chaotic motion. The first one is the "heavy" chaotic motion occurring within the big "chaotic sea" which shapes a white noise in the low frequencies. The second one is a so called sticky motion, which is produced by the chaotic orbits lingering for a long time in the vicinity of regular islands. This type of motion was recognized also in other systems (e.g. see paper [26]) and it yields a $1/f$ spectrum in the low frequencies. Examples of such trajectories are given in the last row of Figure A.14 together with their spectra, where the $1/f$ tendency is clearly visible.

We have to accent one remark concerning this feature, namely that is only a local property of the trajectory related to a finite segment of the orbit, where it is trapped near the regular islands. This statement is supported by the plot in Figure A.16, where several orbits with distinct initial conditions within one connected stochastic layer is plotted, each by another color. Near the period two island the orbits are lingering for a long time, which is emphasised by another color shade in this area. The corresponding spectra both exhibiting the $1/f$ course and not are given below. We have to bear in mind, that these trajectories eventually leave the lingering region and spread out into the big chaotic layer which is in fact densely covered by a single chaotic trajectory with $\tau \to \infty$ (and maybe after some time they return back near the regular islands). The counterpart of the sticky motion in the course of latitudinal action in discussed in Section 4.1.4.

4.2.2 Weighted average of directional vectors

As we have seen earlier on the power spectra, the non-existence of the fourth integral of motion (and thus the irregularity of the motion) leave traces on the $z(\tau)$ behaviour. We will now study these traces in more detail. We follow the

work of Kaplan and Glass published in [24], who employ the procedure of time-delay reconstruction of the phase space for detecting the deterministic signals in the measured data.

We construct the directional vectors in phase space boxes in the same way they did (see Section 2.6.3), but instead of examining the dependence of the length of the resulting vector in a particular box on the number of passages through that box we are interested in the over-all tendency of the average norm of the directional vectors weighted against the average length of the random walk step with the increasing time lag $\Delta\tau$. Namely for a given $\Delta\tau$ we compute one value $\bar{\Lambda}(\Delta\tau)$ (WADV) according to the relation (2.26) which reflect the difference between the norm of the resulting vector in each box and the respective length of average step of the random walk in 3D with n_j steps averaged through all the occupied boxes.

For increasing $\Delta\tau$ we connect the actual position of the test particle with two copies of its more distant history. Unlike the regular orbits that proceed in the same way during their whole evolution, hence the return of 10 or 20 cycles does not influence the resulting value, the chaotic motion changes in time significantly according to the exponential divergence of nearby orbits. In other words a segment of trajectory, which is currently very close to another segment (hence they are both in the same box) was in the past at very different position. The two directional vectors arising out from this two segments will most likely have different directions, therefore the resulting norm of its normalized vector addition would be smaller. When summing more directional vectors in the same box, we are connecting different episodes of the orbits history. For small $\Delta\tau$ the deterministic connection between the "not so far past" and now is strong, given by the equations of motion, for high $\Delta\tau$ this "deterministic" connection is lost due to the exponential divergence of nearby orbits.

The obtained results confirm this statement. In particular, for regular orbits $\bar{\Lambda}(\Delta\tau)$ remains very close to one with the exception of multiples of some value $\Delta\tau_{\mathrm{orb}}$, which is related to the orbital period of the motion (namely the half of the period). In Figure 4.13 the course of $\bar{\Lambda}(\Delta\tau)$ for the orbits A, B, C and D is given, whose Poincaré surface of section and other characteristic are plotted in Figures C.1 through C.5. In the left column of Figure 4.13 we plot WADV in a chosen interval of $\Delta\tau \in [25000, 25800]M$ corresponding to approximately 100 cycles around the center. The first two orbits A and B are regular, the former belongs to the primary island and the latter to the higher periodic island. The maximal values of $\bar{\Lambda}(\Delta\tau)$ during one orbital period go very close to unity (they exceed 0.999 for orbit A and 0.99 for orbit B).

In the right column we present $\bar{\Lambda}(\Delta\tau)$ for large range of $\Delta\tau$, where we compute $\bar{\Lambda}(\Delta\tau)$ for twenty close values of $\Delta\tau$ spread within approximately 2 orbital cycles, and then increase $\Delta\tau$ significantly. In this way we reach the delay $\Delta\tau \approx 10^5$M, i. e. around 300 - 500 cycles. Here we have to remark, that we used a segment of the orbit with the length $\tau_{\max} = 10^6 M$ for this analysis, therefore the double shift by $10^5 M$ cuts rather long part of the trajectory away, the reconstructed phase space path is thus approx. by 20% shorter, yielding lower number of passages through the boxes. This does not affect the WADV for the regular orbits, which is still very close to unity, but it has some impact on the chaotic WADV (see e.g. Figure 4.14) in such a way, that the values are slightly higher for the longer $\Delta\tau$

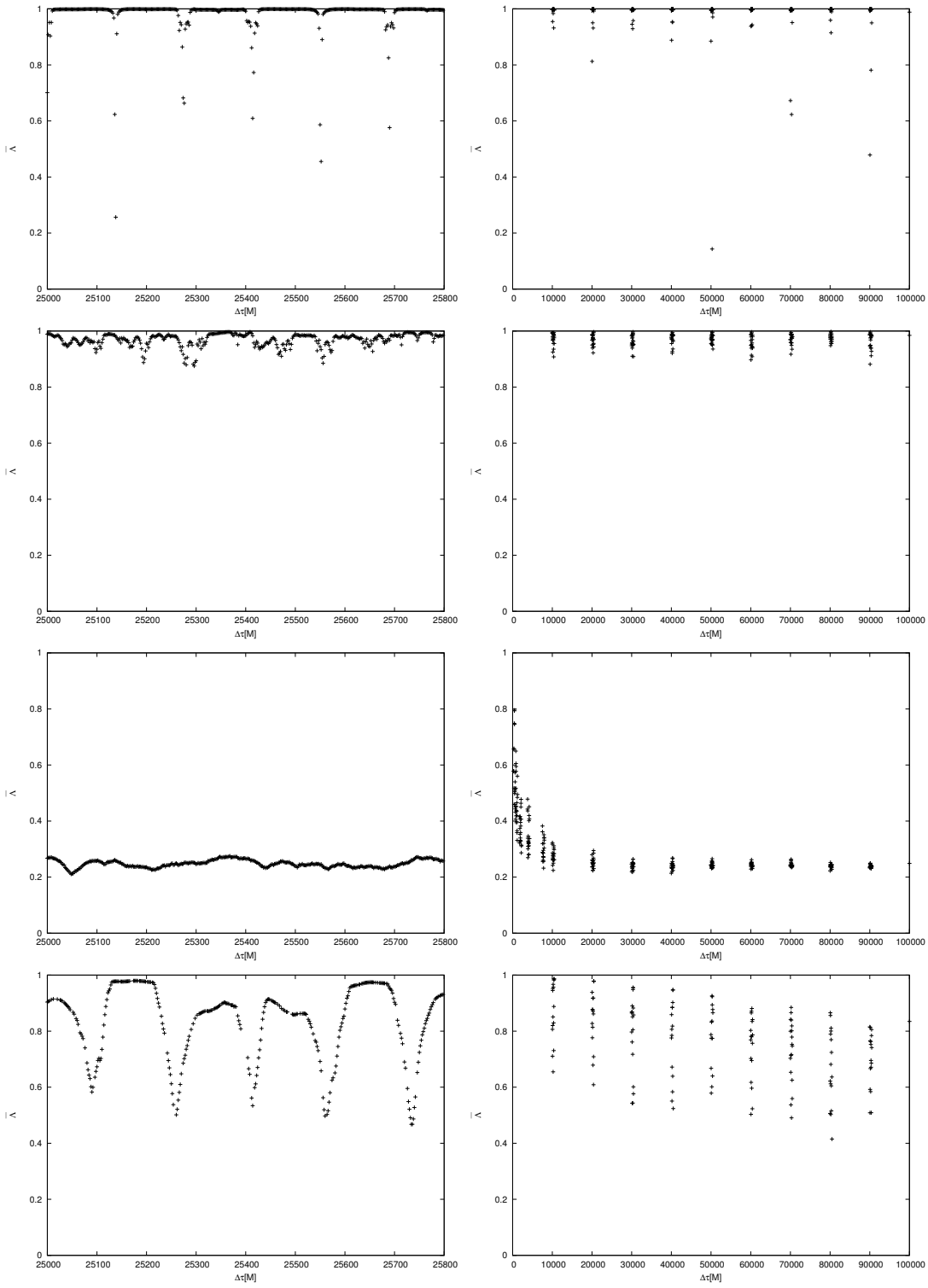


Figure 4.13: The course of $\bar{\Lambda}(\Delta\tau)$ for a chosen interval of the delay $\Delta\tau$ (left column) and their values computed in several windows of length approximately two orbital cycles for significantly increasing delay (right column) for the orbits A, B, C and D from the Figures C.1 and C.2.

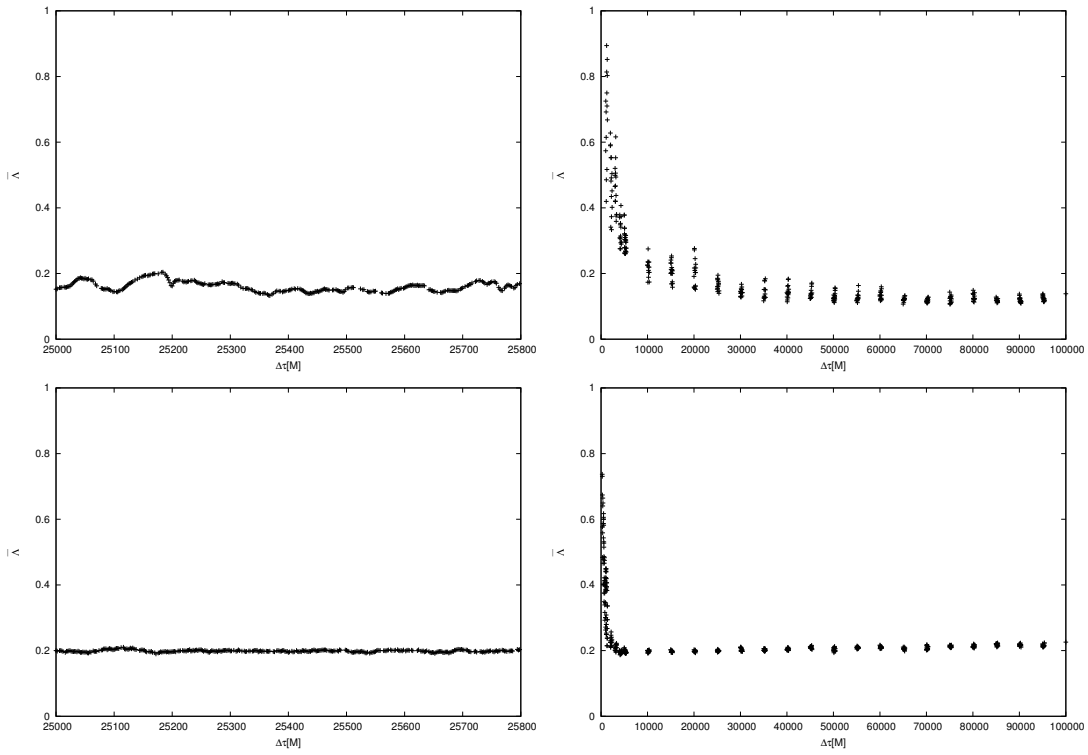


Figure 4.14: The course of $\bar{\Lambda}(\Delta\tau)$ for a chosen interval of the delay $\Delta\tau$ (left column) and their values computed in several windows of length approximately two orbital cycles for significantly increasing delay (right column) for the orbits E and F from the Figures C.2.

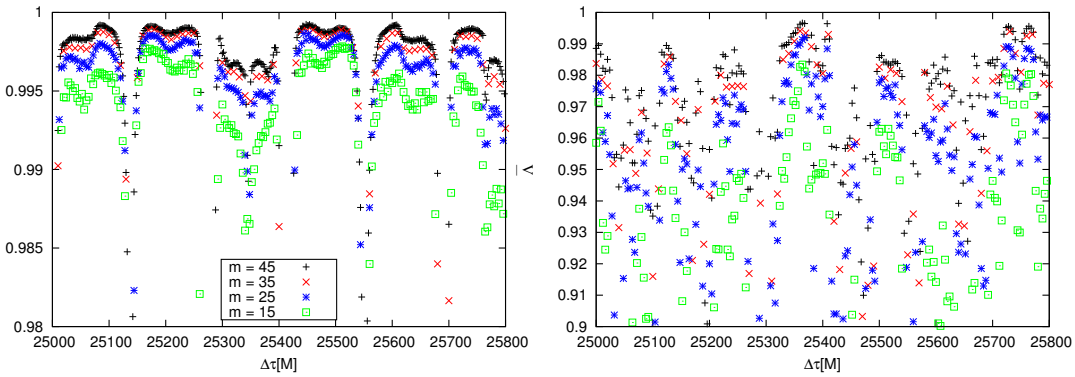


Figure 4.15: Comparison of the resulting $\bar{\Lambda}(\Delta\tau)$ for different resolution of the coarse-graining of the phase space $m = 15, m = 25, m = 35, m = 45$ for two regular orbits (orbits A and B from Figure C.1).

due to lower number of passages through the boxes.

In Figure C.3 $\bar{\Lambda}(\Delta\tau)$ in three different ranges of delay is computed densely for orbits D, E and F, which are sorted according to the ascending degree of chaos, which is also proven by the Lyapunov exponents and other quantifiers. These plots together with Figures 4.13 and 4.14 reveal that $\bar{\Lambda}(\Delta\tau)$ decays from unity to very low values with respect to the value of mLCE. The first sign of the decay is visible around the time given by the reciprocal value of mLCE. The same behaviour could be seen in Figure G.2, where WADV for two distinct ranges of $\Delta\tau$ is plotted for several trajectories differentiated by colours. $\bar{\Lambda}(\Delta\tau)$ of strongly chaotic orbits decays already for low $\Delta\tau$, whereas the weakly chaotic orbits are distinguish from the regular ones in the window with much higher $\Delta\tau$. Hence, from the course of $\bar{\Lambda}(\Delta\tau)$ a rough estimate on mLCE could be obtained.

The accuracy of WADV is limited by the length of the trajectory which is available together with the sampling frequency. The more dense the data are recorded, the smaller boxes we can construct, which of course increases the values of $\bar{\Lambda}(\Delta\tau)$; especially for the regular orbits the values are much closer to one. But even for quite large boxes compared to the whole inhabited phase space region the results are sufficient for the analysis. The comparison of two different division with different number of boxes in one row $m = 20$ and $m = 32$ is given in Figure E.4 for the chaotic orbit, in Figure 4.15 the comparison for $m = 15, m = 25, m = 35, m = 45$ for two regular orbits is plotted. For lower resolution the values are slightly lower, but the behaviour of $\bar{\Lambda}(\Delta\tau)$ is well-kept even for the lowest value $m = 15$.

We also applied this method on the classical dissipative system, comprising a spring and a dashpot with non-standard constitutive relation, the results are given in Section 5.4 for the rigid-elastic spring with linear dashpot and in Section 5.5 for linear spring in the Bingham fluid.

4.2.3 Recurrence analysis

We will now pay attention to the recurrences of the orbit to itself within a threshold ε. The underlying theory is briefly described in Section 2.6.2, a very detailed

comment on this topic is given in [31].

For the purposes of the recurrence analysis N. Marwan provided the software `Commandline recurrence plots`, whose inputs is a file with the sampled orbit (the number of columns corresponds to the dimension) and the output comprise the values of RQA quantifiers introduced in Section 2.6.2, the file containing the recurrence matrix and the file with the histogram of diagonal lines.

In [25] it was shown that the results of recurrence analysis does not depend strongly on the chosen norm used in the phase space for computing the distance between the points. Therefore we describe the trajectory in the cartesian-like coordinates, which are given in terms of the Schwarzschild coordinates as follows

$$x = r\sin\theta\cos\phi, \tag{4.1}$$
$$y = r\sin\theta\sin\phi, \tag{4.2}$$
$$z = r\cos\theta, \tag{4.3}$$

with the corresponding velocities u^x, u^y and u^z, and we use the euclidean norm.

Because the coordinates could have very different values during the motion we renormalise each coordinate time series separately to have zero mean and unit standard deviation. We have computed many RP plots from all six coordinates without using the time-delay embedding but also many others emanating only from the course of $z(\tau)$ with the 3D embedding. The results are comparable for both approaches.

Two examples of recurrence plots are given in Figure B.8. Because only one half of the plot is important (due to its symmetry), we could join them together. Because the time scale is the same for both parts of the orbit (see also Figure B.3), we can compare directly the two patterns. The difference between the slightly and the heavy chaotic segment is clearly visible. On the upper triangle also the switching between the two regions is expressed in the dark and light blocks in accordance with the time series of the equatorial passages (Figure B.3 second row left).

The series of RP's with increasing chaotic behaviour is presented in Figure B.9 and could be compared with the power spectra and WADV plotted in Figure B.5. With the growing chaos (within the big chaotic layer) the diagonal structures in the RP diminish and the diagonal boxes, where the motion proceeds similarly, shrink to much shorter time segments.

The recurrence analysis also provides us the possibility of estimating the lower bound of the sum of the positive Lyapunov exponents from the slope of cumulative histogram of diagonal lines (see Section 2.6.2). The examples of this fitting for one regular and one weakly chaotic orbit from Figure B.6 are given in Figure B.10. The obtained value for the weakly chaotic orbit is about 50-times higher than the regular value.

In the Section 4.1.3 we also presented a way of estimating the $\lambda_{\max}$ from the slope of MEGNO, which is computed by the two-particle method. We compare the results for several chosen trajectories, see the Table C.1, only the total time for the recurrence analysis was shorter ($10^6 M$ versus $10^7 M$ for the other methods). The reason for cutting the orbits is that the computer demandingness of recurrence analysis grows much faster with the number of points due to the computation of the recurrence matrix. At the same time, sufficient number of

points during one orbital cycle is needed for reasonable results. Thus, the maximal length of the analysed segment for practical computations is limited by the available RAM.

For the chaotic orbits C – F the recurrence analysis yields a little bit lower values than other methods as expected. For the regular trajectories A and B K_2 is lower than the values obtained by direct computation (see Section 4.1.2), even though the total time $\tau_{\max}$ is ten times shorter, but the convergence of MEGNO method is much better and yields the lowest estimates.

This results thus justify the ability of recurrence analysis to estimate the mLCE from the measured data.

Among the recurrences quantifiers the inverse of the longest diagonal line DIV has also connection with the mLCE. The appropriate length $L_{\max}$ indicates the maximal time, within which the two different segments of trajectory remain close, it is thus related to the rate of divergence of nearby trajectories. In Appendix F we showed that this quantifier is very sensitive to occurrence of chaos, when we computed several hundreds of orbits with increasing energy keeping all other parameters and initial conditions constant. The course of DIV is depicted in F.2 and it reveals clearly also the weakly chaotic motion. Hence, using this quantity we can also map the phase space. In Figure G.1 one example of such map is given together with the RQA quantifiers computed for orbits launched around the line $u^r = 0$ (red line in the figure). The changing values of all of them indicate the different layers, within which the initial conditions go through, but only the DIV responds also to very thin chaotic layers enclosing e.g. the period five orbit.

From what was said above we can conclude that the quantifier DIV is able to distinguish between different degrees of chaoticity. However, its exact value depends also on the chosen threshold ε, the "density" of the orbit in phase space etc., so the mLCE could not be easily deduced from DIV, but rather from K_2. Since K_2 is more sophisticated and also complicated for evaluation, in Figure G.2 we compare K_2 and DIV for several coloured trajectories. When the parameters of the analysis are reasonably set, the correlation between them is obvious. In the last row of this Figure, the WADV with corresponding colours is plotted, where the rate of its decreasing is in accordance with the values of K_2.

We also confront two phase space maps constructed from the obtained values of DIV and K_2, respectively, see Figure B.12. Even though the ranges are slightly different, the topological structures are revealed by both. Therefore it seems to be plausible to analyse the properties of the phase space by the quantifiers DIV computed from the normalised time series (see Section 3.6) of only one dynamical variable, which could be in principle measured also for the astrophysical systems, e.g. for the motion of stars in the galactic center.

We also studied the dependence of the RQA quantifiers on the chosen threshold ε. Within a reasonable range of ε (corresponding to reasonable values of recurrence points, RR, which means that there is not very few or very many recurrence points in the recurrence matrix), the main properties of the quantifiers are held, although for very high ε some artificial effects of the tangential motion occur, e.g. the increase of the vertical quantifiers, such as LAM or V ENTROPY inside the regular regions. The course of these quantifiers for different values ε are plotted in Figure B.13 with different colours.

The finite value of the threshold ε is reflected also in the dependence of the

obtained K_2 on the threshold. With growing ε more false long lines appears which originate when two shorter lines merge due to the high "neighbour radius". As it is shown in Figure B.14 this does not influence significantly the regular estimate on K_2, but it leads to decreasing K_2 for chaotic orbits.

We also applied this method on the classical dissipative system, comprising a spring and dashpot with non-standard constitutive relation, the results are given in Section 5.4 for the rigid-elastic spring with linear dashpot and in Section 5.5 for linear spring in the Bingham fluid.

5. Class of mechanical oscillators described by a non-standard constitutive relations

To compare our results obtained by the used methods applied on the geodesic flow in general relativistic systems, we examine a class of classical dissipative systems which also exhibit the chaotic behaviour. Because we do not want to just reproduce the known results, we choose the systems of spring and dashpot described by a non-standard constitutive relations, which have not been studied in the literature so far. The work was done in cooperation with prof. K. R. Rajagopal from the Texas A&M University, College Station, Texas. These systems are the non-standard counterparts of the well-known Duffing oscillator and have their meaning as a simple model of viscoelastic fluids. The results summarized in this Chapter are prepared for publication in Non-linear dynamics.

5.1 Introduction

Mechanical oscillators comprising of springs and dashpots are usually described by constitutive relations for the forces in terms of the relevant kinematical variables which are then substituted into the balance of linear momentum for the lumped parameter system, thereby leading to an ordinary differential equation for the displacement. If one considers a simple system as described by Figure 5.1, the balance of linear momentum takes the form

$$m\ddot{x} = F_{\mathtt{app}} - F_s - F_d, \tag{5.1}$$

where $F_{\mathtt{app}}$, F_s and F_d represent the applied force, the force in the spring and the force in the dashpot, respectively, x is the displacement and m is the mass of the body, the dot denotes time derivatives. The constitutive relations for the spring and the dashpot takes the form

$$F_s = f(x), \tag{5.2}$$
$$F_d = g(\dot{x}). \tag{5.3}$$

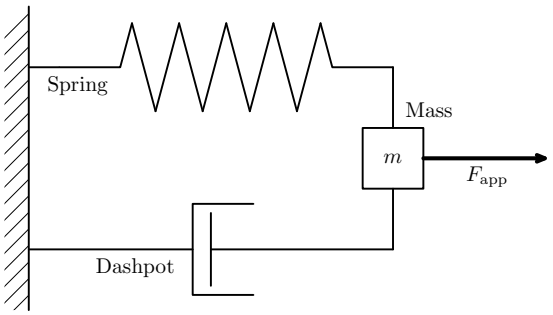


Figure 5.1: Oscillatory system with standard spring and dashpot.

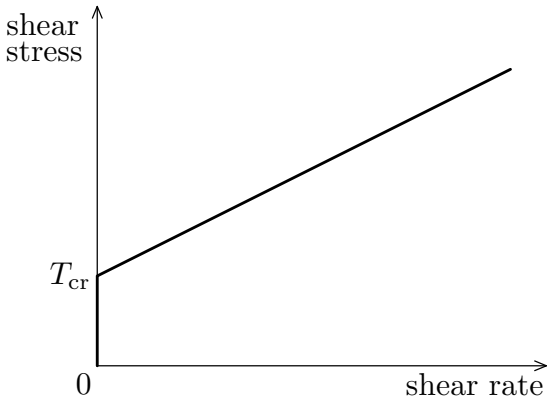


Figure 5.2: Shear stress for the Bingham fluid.

The system is rendered determinate by providing the initial conditions

$$x(0) = x_0 \tag{5.4}$$

and

$$\dot{x}(0) = v_0. \tag{5.5}$$

When f and g are non-linear functions, the differential equation leads to a challenging problem and various non-linear functions have been studied.

Rajagopal and co-workers (see [42], [41]) have recently articulated the rationale for using a different form of constitutive relations for the spring and dashpot wherein the kinematical variable is defined in terms of the force in that element, namely

$$x = h(F_s) \tag{5.6}$$

and

$$\dot{x} = l(F_d). \tag{5.7}$$

Since the functions h and l may not be invertible, the system (5.6) and (5.7) cannot be inverted to yield (5.2) and (5.3). It is possible to have mechanical oscillatory systems which are far more complicated wherein the constituents of the system could be given by implicit equations of the form:

$$f_1(x, F_s) = 0, \tag{5.8}$$

and

$$f_2(\dot{x}, F_d) = 0, \tag{5.9}$$

or even more general implicit relation of the form

$$f_1(x, \dot{x}, F_s, F_d) = 0 \tag{5.10}$$

and

$$f_2(x, \dot{x}, F_s, F_d) = 0. \tag{5.11}$$

Two important examples immediately come to mind wherein the constitutive relationships of the form (5.2) and (5.3) are completely inadequate. The first is a dissipative mechanism which is not a viscous dashpot but due to solid friction. In

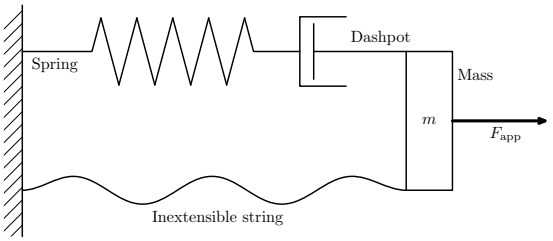


Figure 5.3: System that consists in a spring, dashpot, inextensible string and mass.

this case, an equation of the form (5.3) will fail to capture the physics. Similarly, if the dissipative mechanism is a dashpot wherein the fluid is a Bingham fluid wherein one has to overcome a yield stress before the fluid starts flowing (see Fig. 5.2) we find once again a constitutive equation of the form (5.3) cannot capture the physics. In both these cases, one needs a more general structure for the constitutive relation, namely one needs to use a more general constitutive equation than that of the form (5.3).

Another interesting example wherein a constitutive relation of the form (5.2) and (5.3) fail is the system depicted in Fig. 5.3 that consists in a spring, dashpot, inextensible string and mass. We shall not discuss the above examples in detail as such a discussion can be found in [42] and [41].

It is important to recognize that contrary to statements found in standard books on vibration such as Meirovitch [32], classical solutions do not exist when the dissipative mechanism is Coulomb friction, for which one may find a solution in the sense of Fillipov (see [19]).

Also, unilateral constraints lead to problems that are best studied within the context of constitutive equations which take the form (5.8) and (5.9).

Zaki et al. [56] studied the response of a mass-spring system wherein the mass is hanging from a spring that is comprised of a non-linear elastic solid. The mass can undergo radial motion and can also rotate about the point to which the spring is pinned. They showed that motion of the system goes from a periodic attractor to a chaotic attractor, the route to chaos being a secondary Hopf bifurcation followed by torus-doubling bifurcation which eventually ends in torus breaking.

In this paper, we are interested in studying the response of several mechanical oscillatory systems, damped and undamped, whose components are given by constitutive equations of the form (5.8) and (5.9). We shall compare their response to their classical counterparts. We shall also concern with the possible chaotic motion of these oscillators. For our study we will use classical methods, such as the Poincare's surface of section, bifurcation diagrams and Lyapunov exponents. We will also perform a recurrence analysis on the trajectories that are obtained (for further details see [11] and [31]) and compute the weighted average of directional vectors (WADV – see [24] and [46]), which were used recently also for studying chaos in geodesic motion ([48],[49],[25]).

We will start by studying systems that are undamped.

5.2 A spring with a non-standard cubic constitutive relation

We first study the problem wherein we have a very simple system, what we refer to as the inverse cubic constitutive relation for the spring, that is a spring defined through

$$x = \alpha F_s + \beta F_s^3, \tag{5.12}$$

where α and β are constant and

$$F_d = 0. \tag{5.13}$$

In this case the problem reduces to

$$m(\alpha + 3\beta F_s^2)\ddot{F}_s + 6\beta m F_s \dot{F}_s^2 + F_s = F_{\mathtt{app}}. \tag{5.14}$$

The appropriate initial conditions are

$$F_s(0) = 0, \qquad \dot{F}_s(0) = \frac{1}{\alpha} v_0. \tag{5.15}$$

We shall consider the problem when the applied force is given by

$$F_{\mathtt{app}} = A\cos\omega t + B, \tag{5.16}$$

where A and B are constants.

In Fig. 5.4, the force in the spring F_s is plotted as a function of time and the respective Poincare's surfaces, the recurrence plots and the WADV's for specific values of α and β, and different initial conditions and a specific value of frequency ω and amplitude A. Regular motion is seen in these plots, which means closed curves in the surface of section, long diagonal lines in the recurrence plot and values close to $\Lambda = 1$ even for big time delays Δt for WADV.

For the same parameters the Poincare surface in the phase space is depicted in the first row of plots in Fig. 5.5 for a lot of trajectories with different initial conditions and it indicates regular motion. The zoom of the plot shows the primary island and the embedded islands with higher period. Similarly, Poincare's surfaces for other sets of parameters are given in the second and third row in Fig. 5.5 and they also indicate that the motion is regular, even for the case with negative α. We were unable to find chaotic motion, but since we have only tried specific choices for α, β, A and ω, we cannot conclude that chaotic motion is not possible in such systems.

5.3 A non-standard Duffing oscillator

The non-standard Duffing oscillator that we shall consider is constitutively described by

$$x = \alpha F_s + \beta F_s^3 \tag{5.17}$$

and

$$\dot{x} = \gamma F_d. \tag{5.18}$$

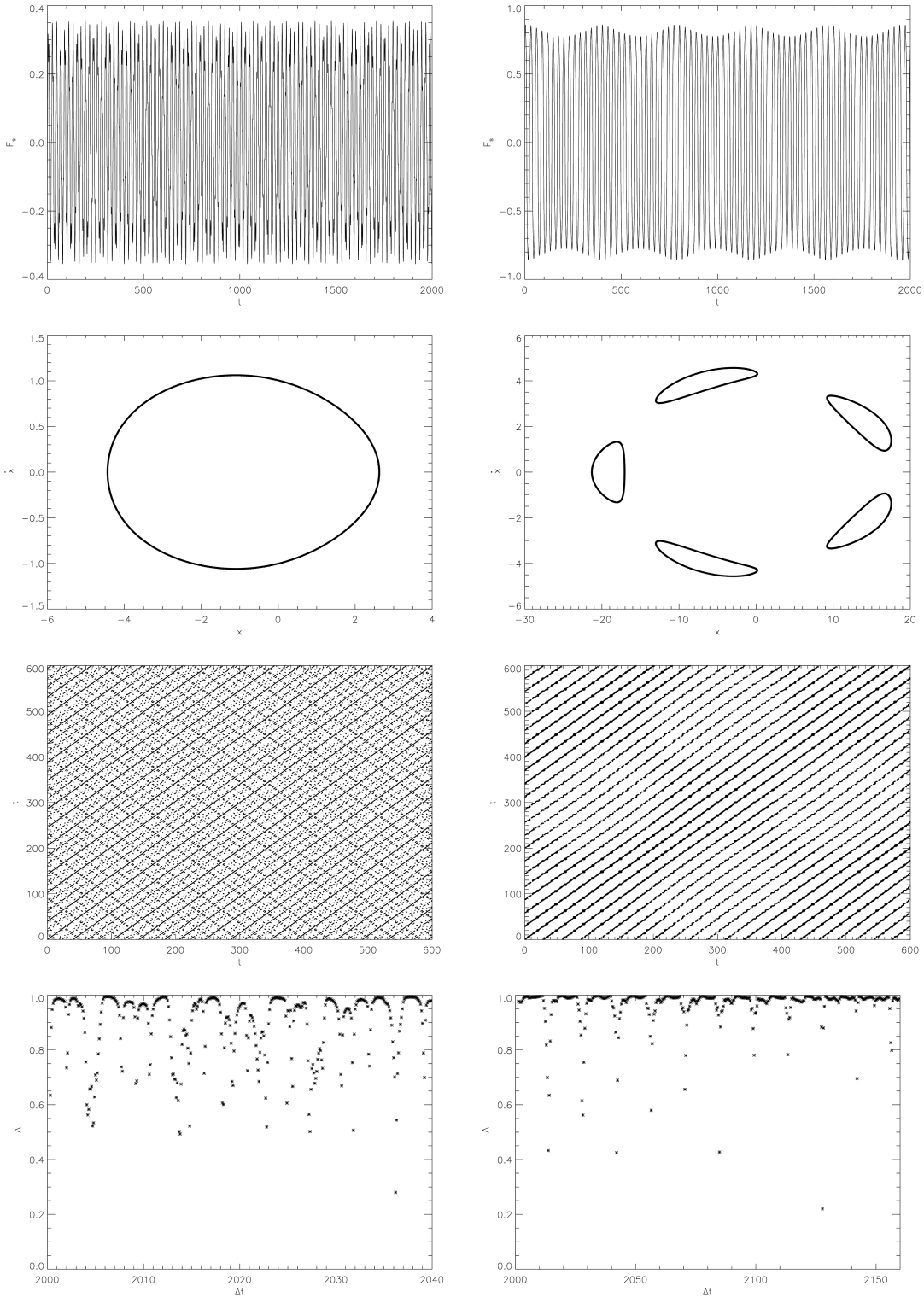


Figure 5.4: Inverse cubic spring with $m = 1$, $\alpha = 10$, $\beta = 20$, $A = 1.1$, $\omega = 1.1$, first column: $F_s(0) = -0.1$, $\dot{F}_S(0) = 0.1$, second column: $F_s(0) = 0.76$, $\dot{F}_S(0) = 0.05$

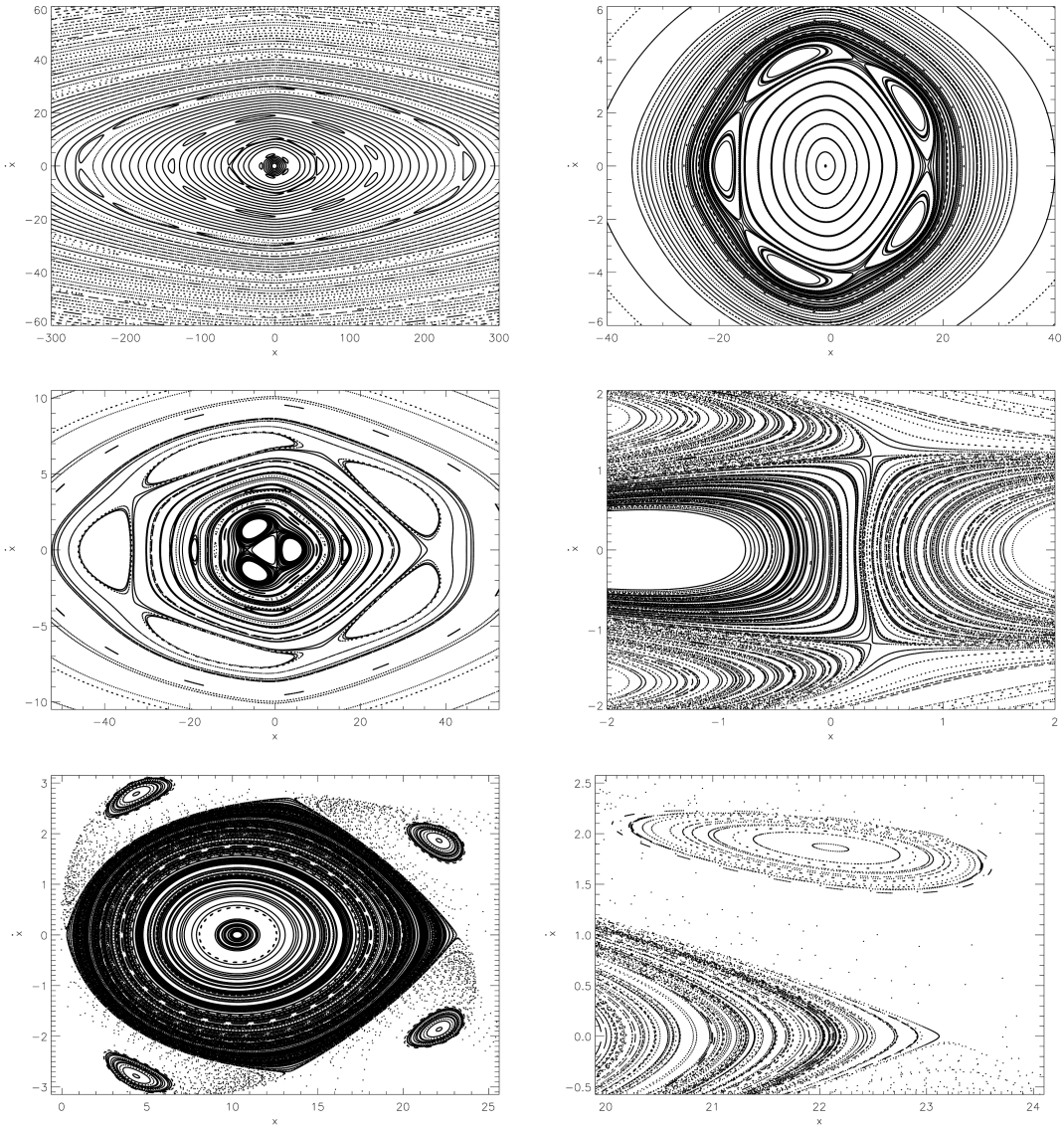


Figure 5.5: Inverse cubic spring – Poincare's surface of section depicting part of the phase space and the zoom of this plot on the right. We can see regular motion, the most important primary regular island and embedded islands with higher period.
first row: $m = 1$, $\alpha = 10$, $\beta = 20$, $A = 1.1$, $\omega = 1.1$,
second row: $m = 1$, $\alpha = 7.3$, $\beta = 33.7$, $A = 1.3$, $\omega = 0.85$,
third row: $m = 1$, $\alpha = -0.6$, $\beta = 1.5$, $A = 0.5$, $\omega = 1.0$

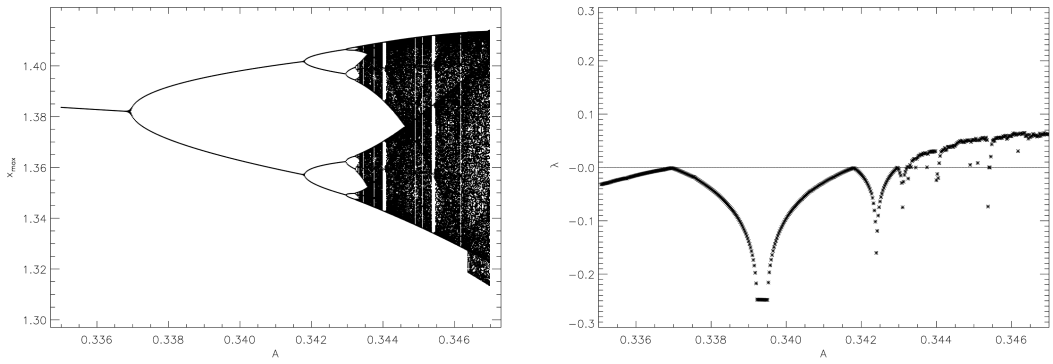


Figure 5.6: Bifurcation diagram for the standard Duffing oscillator with $m = 1$, $\alpha = -1$, $\beta = 1$, $\gamma = 0.5$, $\omega = 0.9$ and Lyapunov exponents obtained by the two-particle method.

The above relations immediately imply that

$$F_d = \frac{\dot{x}}{\gamma} = \frac{1}{\gamma}(\alpha \dot{F}_s + 3\beta F_s^2 \dot{F}_s). \tag{5.19}$$

Thus, it follows from (5.1) and (5.19) that

$$\ddot{F}_s = \frac{F_{\mathtt{app}} - F_s - 6\beta m F_s \dot{F}_s^2}{m(\alpha + 3\beta F_s^2)} - \frac{1}{\gamma m}\dot{F}_s. \tag{5.20}$$

If

$$\alpha + 3\beta F_s^2 = 0, \tag{5.21}$$

then

$$\dot{F}_s = \left(\frac{F_{\mathtt{app}} - F_s}{6\beta m F_s}\right)^{\frac{1}{2}}. \tag{5.22}$$

Once again, let us suppose that $F_{\mathtt{app}}$ is given by (5.16). It turns out that for certain values of α and β, the square root on the right hand side of (5.22) cannot be computed as the term within the parenthesis is negative. This statement holds mainly for the case when α and β have different signs, which is the case of standard Duffing oscillator. Thus, direct comparison of the response characteristics of the standard Duffing oscillator and the non-standard Duffing oscillator which we have introduced is impossible.

The orbits of the dissipating system settle down after some time into the attractor. For regular motion the Poincare's surface of section for the attractor consists only of few distinct points, and the chaotic attractor has non-integer dimension and yields fractal structure in the surface of the section. Contrary to conservative systems, in dissipative systems we can study the bifurcation diagram, where we plot the maxima of $x(t)$ or $F_s(t)$ against a changing parameter of the system. In these diagrams the sudden changes (called bifurcations) of the orbits' nature at a specific value of the parameter can be seen as well as the regular and the chaotic windows. The bifurcation diagram for the standard Duffing oscillator is well known, we give one example in Fig. 5.6. The bifurcation diagrams for the non-standard Duffing oscillator which we obtained show only regular motion (for both α and β positive), example is given in Fig. 5.7.

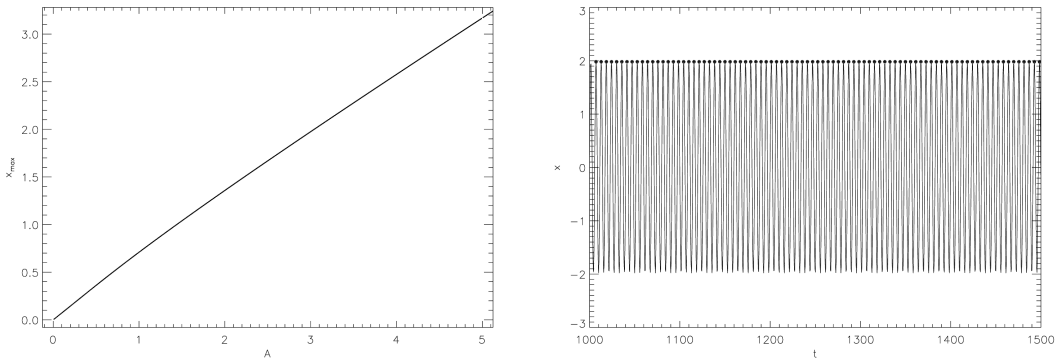


Figure 5.7: Bifurcation diagram for non-standard Duffing oscillator, $m = 1$, $\alpha = 0.7$, $\beta = 1.1$,$\gamma = 0.8$ and $\omega = 1.1$. In the right plot $x(t)$ for the particular trajectory with $A = 3.01$ is given with maxima of $x(t)$ labelled with points.

5.4 Rigid-elastic spring with linear dasphot

We will continue our study of non-standard dissipative systems with the rigid-elastic spring combined with linear dashpot. The deflection of the spring is given by the relation (5.6), where

$$h(u) = \begin{cases} 0 & |u| \leq \delta \\ \beta(u-\delta) & u > \delta \\ \beta(u+\delta) & u < -\delta \end{cases} \tag{5.23}$$

and the velocity is given by the force in the dashpot as

$$\dot{x} = \alpha F_d. \tag{5.24}$$

Equation (5.23) is non-invertible, thus F_s can not be written in terms of x, but we can derive equations which hold for $|F_s| < \delta$ and for $|F_s| > \delta$. First we compute the derivative of the relation (5.23)

$$\frac{\mathrm{d}h(u)}{\mathrm{d}u} = \begin{cases} 0 & |u| < \delta \\ \beta & |u| > \delta \end{cases}, \tag{5.25}$$

which holds everywhere except the points $|u| = \delta$.

Now we proceed separately in both regions:

- $|F_s| < \delta$

  From (5.23) the deflection of the spring is $x = 0$, which leads to $\dot{x} = 0$ and $\ddot{x} = 0$. The spring is at rest, therefore the force in the dashpot is also zero and from the equation of motion (5.1) we get a relation between the force in the spring and the applied force in the simple form

  $$F_s = F(t). \tag{5.26}$$

  Until the force in the spring reaches the threshold value δ again, the system is at rest.

- $|F_s| > \delta$

  We invert the relation (5.24) and get the force in the dashpot in terms of the velocity. Then using (5.25) and $\dot{x} = \frac{\mathrm{d}h}{\mathrm{d}u}\dot{F}_s$ we link force in the dashpot and force in the spring:

$$F_d = \frac{\dot{x}}{\alpha} = \frac{\beta}{\alpha}\dot{F}_s. \tag{5.27}$$

  The acceleration is given by $\ddot{x} = \frac{\mathrm{d}^2h}{\mathrm{d}u^2}\dot{F}_s + \frac{\mathrm{d}h}{\mathrm{d}u}\ddot{F}_s$ and by differentiating (5.25) the term $\frac{\mathrm{d}^2h}{\mathrm{d}u^2}$ drops out. Next we obtain the second derivative of x in terms of F_s, hence we are able to rewrite the equation of motion (5.1) in the form of a differential equation for F_s:

$$\ddot{x} = \beta\ddot{F}_s \tag{5.28}$$

$$\ddot{F}_s = \frac{F(t) - F_s - \frac{\beta}{\alpha}\dot{F}_s}{m\beta} \tag{5.29}$$

We solve this set of equations with Runge-Kutta method of the 6th order with adaptive time step and we obtain $F_s(t)$ and $\dot{F}_s$ from which we are able to compute $x(t)$ and $\dot{x}(t)$.

In Fig. 5.8 bifurcation diagrams against changing amplitude A of the applied force (5.16) are given. In this system, we have chaotic behaviour for various values of the parameters. In the zoom of the bifurcation diagram very similar structures to the bifurcation diagram of the standard Duffing oscillator (Fig. 5.6) can be seen, which is a typical demonstration of period-doubling bifurcation leading to chaotic motion.

For obtaining Lyapunov exponents we adopt the two-particle approach, in which maximal Lyapunov exponent λ is given by

$$\lambda = \lim_{t\to\infty} \frac{1}{t} \ln \frac{\Delta\xi(t)}{\Delta\xi(0)}, \tag{5.30}$$

where $\xi(t)$ is the deviation vector between the the trajectory of the main particle $\mathbf{x}$ and its shadow $\mathbf{x}^s$ in phase space. In our system the question is if we should compute the deviation vector as $[F_s(t) - F_s^s(t), \dot{F}_s(t) - \dot{F}_s^s(t)]$ or $[x(t) - x^s(t), \dot{x}(t) - \dot{x}^s(t)]$. On the first sight we would choose the norm in the physical phase-space $[x(t) - x^s(t), \dot{x}(t) - \dot{x}^s(t)]$. But these physical coordinates $x(t), \dot{x}(t)$ are not coordinates, that fully describe the system, because for all $F_s(t) < \delta$, $x = 0$ and $\dot{x} = 0$, but the trajectory is not given uniquely and could be different with different F_s and $\dot{F}_s$. Also the renormalization in the context of the physical coordinates is not possible, because the relation (5.6) is non-invertible, so we can not set the value of x and $\dot{x}$ and compute the corresponding $F_s, \dot{F}_s$ during the renormalization process. Therefore we have chosen to compute the deviation vector as $[F_s(t) - F_s^s(t), \dot{F}_s(t) - \dot{F}_s^s(t)]$.

In Fig. 5.8 we plot the time-dependent mLE $\lambda(t_{\max})$ which instead of computing the limit in relation (5.30) is the value attained after the time of computation $t_{\max}$. In the regular region, this value is less then zero, because our system is dissipative, in the chaotic domain $\lambda(t_{\max}) > 0$.

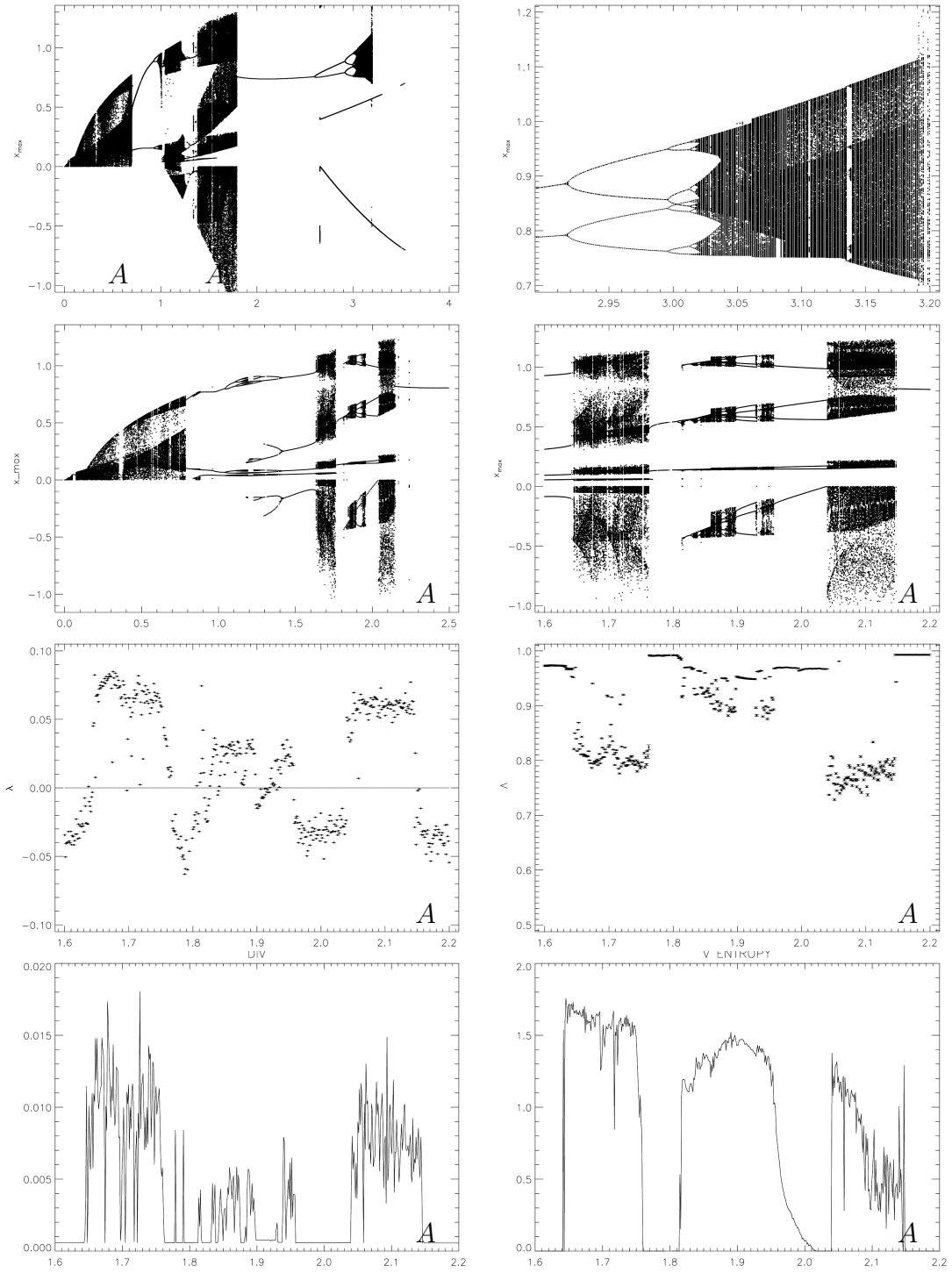


Figure 5.8: Rigid-elastic spring: first row: $m = 1$, $\alpha = 0.8$, $\beta = 1.5$, $\delta = 0.8$, $\omega = 1.0$, bifurcation diagram and its zoom, next rows: $m = 1$, $\alpha = 0.6$, $\beta = 1.5$, $\delta = 0.9$, $\omega = 1.0$, bifurcation diagram and its zoom, Lyapunov exponents and WADV, the reccurence quantifiers DIV and V_ENTROPY for the zoomed window.

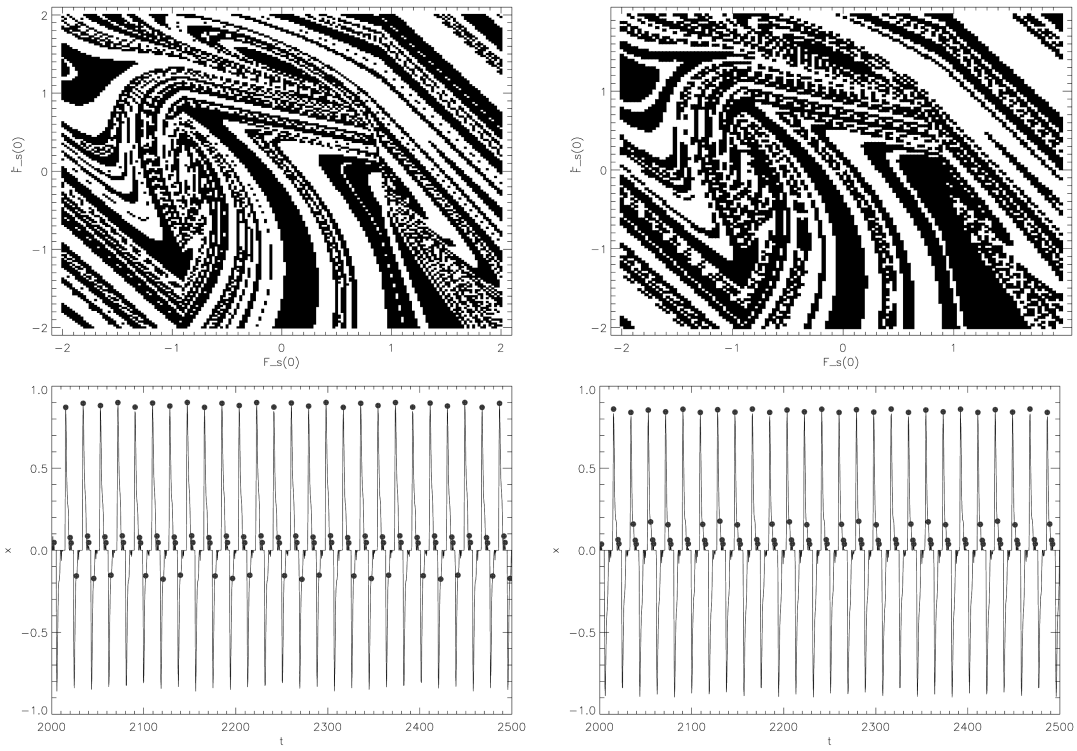


Figure 5.9: Rigid-elastic spring: $m = 1$, $\alpha = 0.6$, $\beta = 1.5$, $\delta = 0.9$, $\omega = 1.0$, map of basins of two different attractors for the amplitude $A = 1.2$ (left) and $A = 1.3$ (right) in the first row, the course of $x(t)$ for the two attractors for $A = 1.2$ in the second row.

Similarly, for the recurrence analysis and the computation of WADV we use the time series $F_s(t)$ instead of $x(t)$. These two methods are based on the recurrence of the system in the phase space and therefore if one uses $x(t)$ the results are marred by the degeneracy of the system at the point $[x(0), \dot{x}(0)]$. On the other hand, on using the coordinates $[F_s, \dot{F}_s]$ both these method work perfectly. The WADV together with the recurrence quantifiers DIV and V ENTROPY are given in the remaining plots in Fig. 5.8.

For a certain range of amplitudes there exists more than one attractor in the phase space, in our case for the same parameters for which the former analysis was done we have two different attractors. In Fig. 5.9 we plot $x(t)$ for those attractors ($A = 1.2$) and we mark the maxima with dots. The set of initial conditions which leads to one specific attractor is called the basin of attraction. We can map the phase space by computing many trajectories with initial condition spread on a grid and label the points according to which basin they belong. Since we have two different attractors, we plot the initial condition with a black dot when it belongs to the basin of the first attractor while we do not plot a dot for the second. Examples of such maps for two different amplitudes are given in Fig. 5.9.

5.5 Bingham fluid

We complete our exploration of non-standard oscillating systems with a dashpot wherein the fluid is a Bingham fluid. This material does not flow unless a certain threshold in the force in reached in the dashpot, and when F_d is above a given treshold δ the viscous and elastic response is linear. Thus, the functions (5.6) and (5.7) have the following form

$$x = \alpha F_s, \tag{5.31}$$

$$\dot{x} = g(F_d) = \begin{cases} 0 & |F_d| \leq \delta \\ \beta(F_d - \delta) & F_d > \delta \\ \beta(F_d + \delta) & F_d < \delta \end{cases}, \tag{5.32}$$

which is an analog of the rigid-elastic spring discussed in the previous section. We will now proceed to obtain the differential equation for our system. At first we differentiate and invert (5.31) to obtain expressions for the time derivative of F_s.

$$\dot{x} = \alpha \dot{F}_s \Rightarrow \dot{F}_s = \frac{\dot{x}}{\alpha}. \tag{5.33}$$

Further we differentiate the equation of motion (5.1)

$$m\ddot{x} = F_{app} - F_s - F_d \tag{5.34}$$

to obtain

$$m\dddot{x} = \dot{F}_{app} - \dot{F}_s - \dot{F}_d. \tag{5.35}$$

We proceed to study the two regions separately.

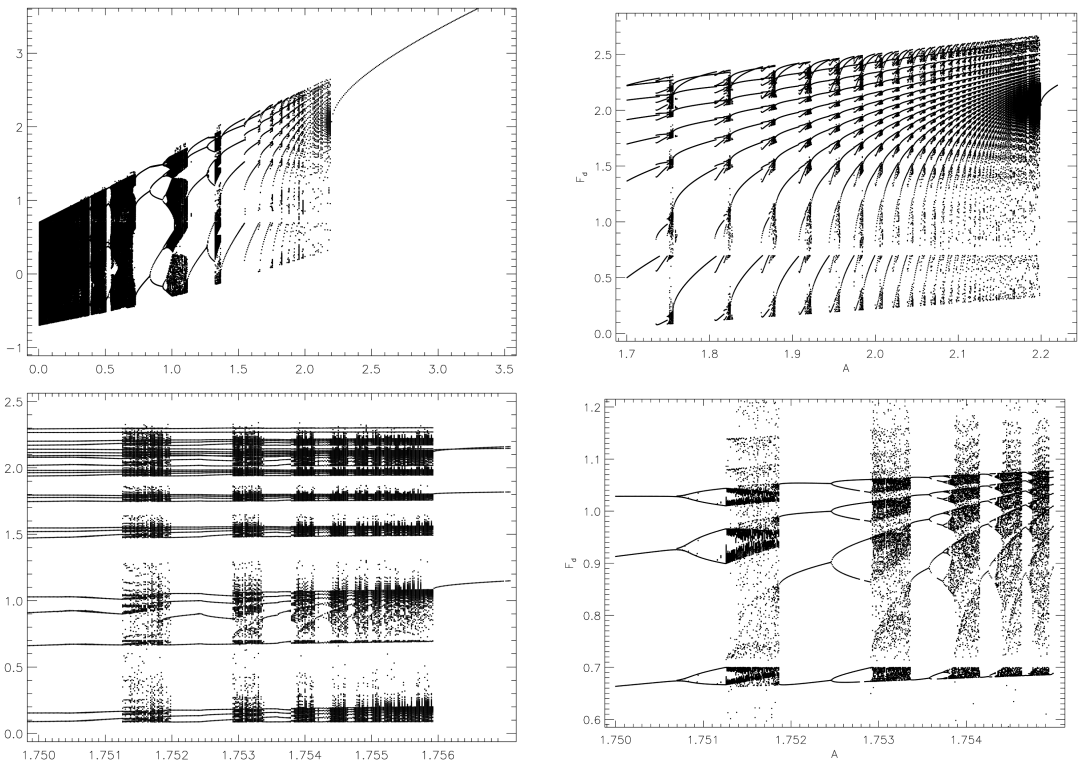


Figure 5.10: Bingham fluid: $m = 1$, $\alpha = 0.6$, $\beta = 1.5$, $\delta = 0.7$, $\omega = 1.0$, Bifurcation diagram of the system with changing the amplitude of the driving force and zoomed slices of it.

- $|F_d| < \delta$:

  For forces below the value of the threshold, the velocity of the fluid is zero $\dot{x} = 0$, therefore the deflection $x = \text{const}$ and also $F_s = \text{const}$. From equation (5.35) we get the relation

$$\dot{F}_{app} \quad = \quad \dot{F}_d. \tag{5.36}$$

- $|F_d| > \delta$:

  Differentiating (5.32) we express the time derivatives of x in terms of F_d.

$$\ddot{x} = \beta \dot{F}_d, \qquad \dddot{x} = \beta \ddot{F}_d. \tag{5.37}$$

  Using (5.33) and (5.37) from (5.35) we get a differential equation for F_d,

$$m\beta \ddot{F}_d \quad = \quad \dot{F}_{app} - \frac{\beta}{\alpha}(F_d - \text{sign}(F_d)\delta) - \dot{F}_d. \tag{5.38}$$

  The deflection of the spring is then given by an integral

$$x(t) \quad = \quad \int_{s=0}^{t} g(F_d(s))\mathrm{d}s + x_0. \tag{5.39}$$

  Thus, we compute a second order differential equation for F_d and we insert initial conditions $F_d(0)$ and $\dot{F}_d(0)$. They are related to the initial conditions $F_s(0)$ and $F_d(0)$ in the following way

$$\dot{F}_d(0) \quad = \quad \frac{F_{app}(0) - F_s(0) - F_d(0)}{m\beta} \qquad F_d(0) > \delta. \tag{5.40}$$

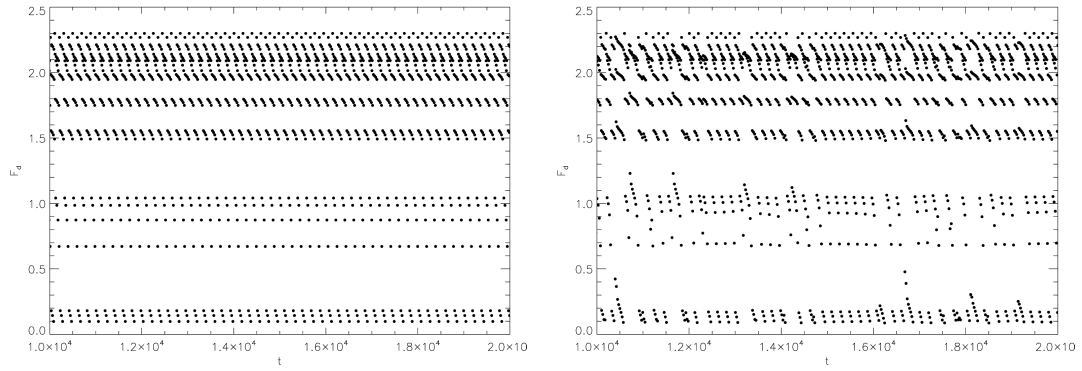


Figure 5.11: Bingham fluid: $m = 1$, $\alpha = 0.6$, $\beta = 1.5$, $\delta = 0.7$, $\omega = 1.0$, maxima of $F_d(t)$ of the trajectories with high period, which exist for the amplitude $A = 1.7527$ (left) in the regular window and $A = 1.7532$ (right) in the chaotic region. These orbits belongs into the bifurcation diagram depicted below.

In Fig. 5.10 the bifurcation diagram (computed from $F_d(t)$) and its successive zooms are plotted. We can see the period-doubling bifurcations leading to chaotic regions, which end in regular windows with higher period. This pattern repeats within shorter and shorter amplitude periods, the regular and chaotic windows are shorter and shorter, therefore they are not visible in the big bifurcation diagram due to the sampling, but they appear after zooming.

In Fig. 5.12 another zoom of the preceding bifurcation diagram is shown which is similar to the bifurcation diagram of the standard Duffing oscillator. In this picture we can clearly see the process of period doubling, the emergence of chaotic motion and also small regular windows embedded inside the chaotic region. At the end of the chaotic region periodic oscillation occurs again with one more maximum. The same pattern repeats itself again and again, which we can observe from the zoom in Fig. 5.12 a typical snapshot appearing at a different scale during the whole bifurcation diagram until the amplitude is high enough and only period-one attractor exists. For this segment we also plot the Lyapunov exponents, WADV and different RQA quantifiers.

In Fig. 5.13 we show four different attractors, which are present for specific values of the parameters together with the map of basins of attraction. On the map, the complicated structure of the boundary between two basins is shown, which is visible also in the zoom of the map.

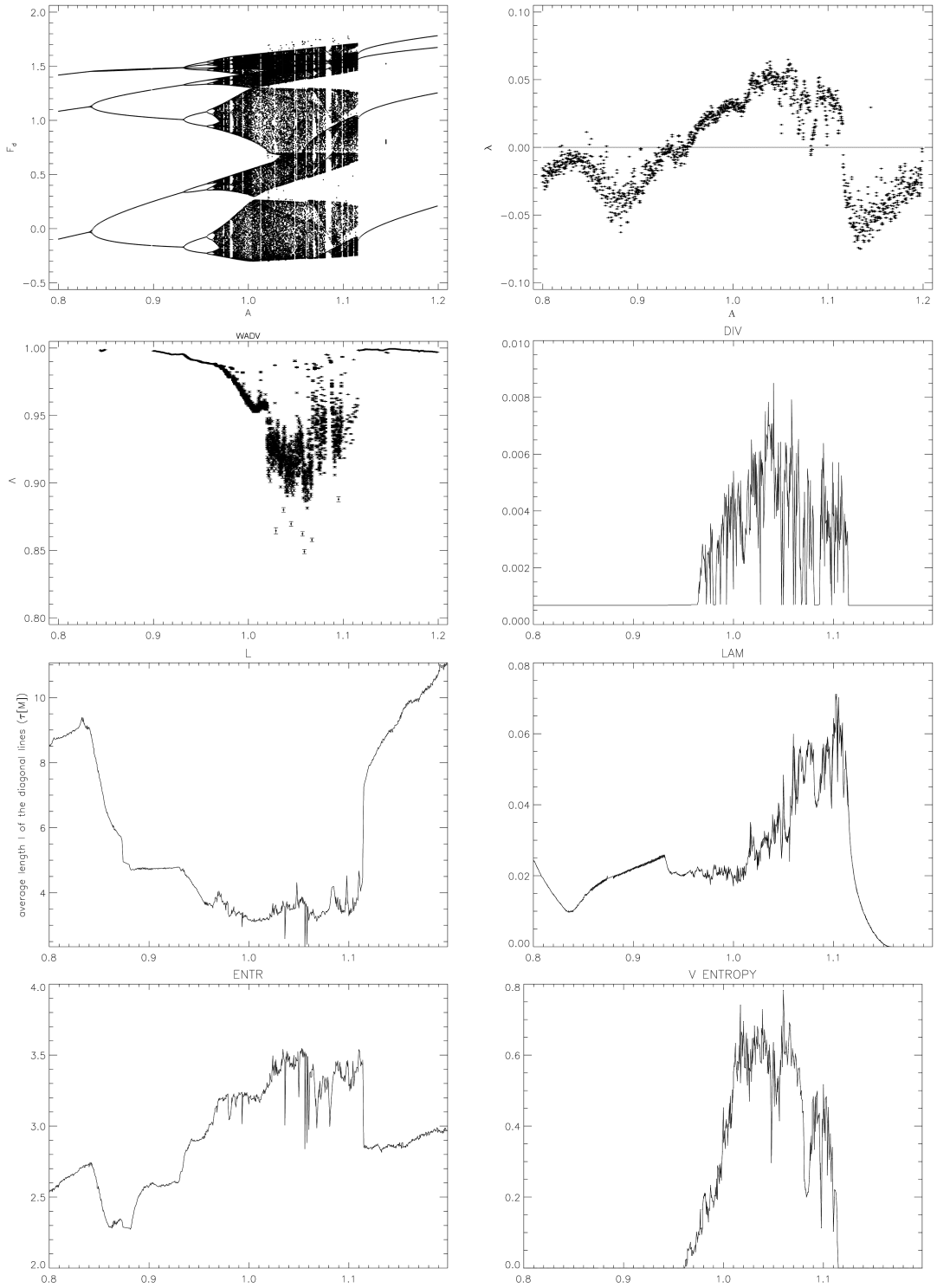


Figure 5.12: Bingham fluid: $m = 1$, $\alpha = 0.6$, $\beta = 1.5$, $\delta = 0.7$, $\omega = 1.0$, another zoom of the same bifurcation diagram as in the previous picture and the corresponding WADV and reccurence quantifiers.

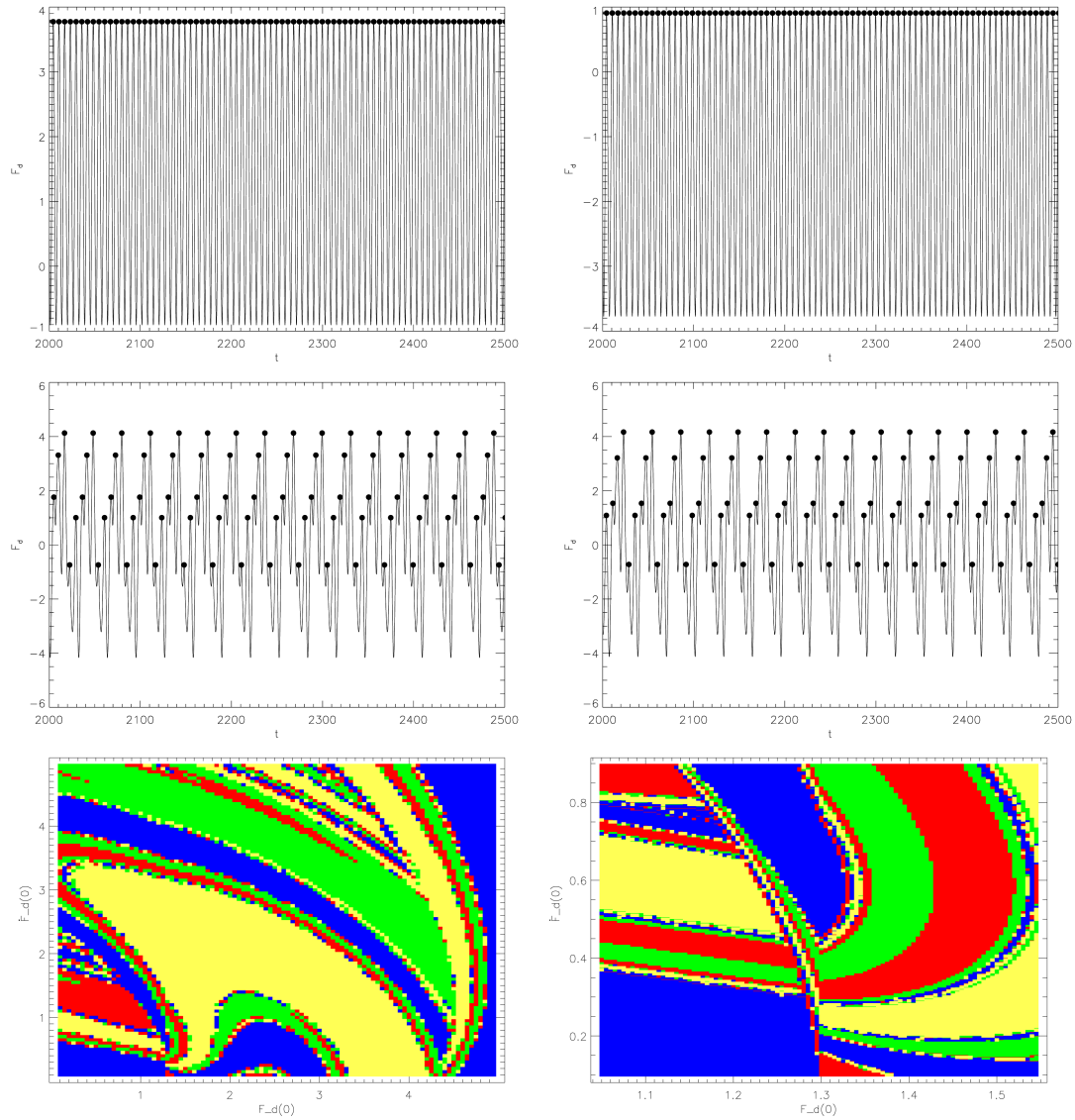


Figure 5.13: Bingham fluid: $m = 1$, $\alpha = 1.1$, $\beta = 1.9$, $\delta = 1.3$, $\omega = 1.0$, $A = 2.37$, four different attractors existing for the same parameters and the map of basins of attraction, where each color correspond to one of the attractors.

Conclusions

We first examined the dynamics of the systems with wide parameter ranges on Poincare's surfaces of section and observed the progression of chaotic layers in phase space. We were able to see typical features of a nearly-integrable Hamiltonian system where chaotic orbits arise near the separatrix between distinct types of motion after the perturbation is strong enough to break the invariant surfaces near the resonances. The islands chains are formed repeatedly on different scales, embedding islands inside islands combined with thin stochastic layers. This complicated phase space picture corresponds to the well known KAM theory. These structures evolve with increasing energy of the test particle, chaotic layers merge to big "chaotic sea", small islands of higher and higher resonances emerge and disappear again. At certain energy our test particle's motion could become highly chaotic in substantial part of the accessible phase space, even destroying completely the primary island of regular motion. For very high energies the motion "calms down" again in most of the area with growing primary island pushing higher resonances towards the margin of the accessible zone. The process of growing mass of the additional source is similar, when the most chaotic motion is achieved for the case of comparable masses of both sources with inner rim lying quite close to the black hole (around $r_{\mathrm{disc/ring}} = 20M$).

After getting acquainted with the global topological features and tendencies of the phase space we focused more on particular trajectories and the traces of chaos hidden in the time series of dynamical quantities (such as position and velocity) which can be in principle observable. The topological properties of orbits are reflected strongly in their time evolution and different time series analysing methods can be used for revealing the nature of the motion. We performed the Fourier transformation on the evolution of the particle's "vertical position" $z(\tau)$ and the obtained spectra distinct clearly between the regular and chaotic orbits presenting only few sharp peaks for the regular motion and noisy spectrum for the chaotic ones. Furthermore the spectra also show the degree of chaoticity of the trajectories when yielding $1/f$ shape of spectrum in low frequencies for the so called "sticky motion" and white-noise type of spectrum for highly chaotic orbits filling the chaotic sea. The sticky motion refers to the weakly chaotic segments of trajectories during which the orbits adhere to regular islands (typically two) and linger within narrow bands in Poincare's surface of section for most of the time, switching abruptly between the regular islands.

Further we showed that the method of computing the average of directional vectors proposed by Kaplan and Glass in 1992 for testing the deterministic character of given signal [24] could also be used for distinguishing between regular and more or less chaotic orbits. Also the recurrence analysis, which has been used in broad branches of science from the physics, mathematics to medicine or financial market, proved to be robust in the field of general relativity regardless of the used norm in the phase space. An effective program package has been written by N. Marwan [30] which could be used also in our situation.

We incorporated several methods for estimating the Lyapunov-like exponents which quantify the rate of two nearby trajectories diverging. This could be done using either the two-particle approach or the geodesic equation approach. Both

these methods bring their own difficulties for the computation. The former approach is questionable in the accurate computing of the phase space distance between the particle and its shadow and the correct renormalisation of the deviation vector while the latter demands solving of complicated variational equations which are quite cumbersome for relativistic systems. We adopted the two-particle approach for computing the Fast Lyapunov Index (FLI) which proved to be powerful indicator of degree of chaoticity, distinguishing between different chaotic layers in the phase space. Because an analytic relation between FLI and MEGNO was proposed recently by [33], we further improved our analysis by computing the MEGNO for our system which is more suitable for automatic surveys of the phase space.

In order to make our models even more astrophysically reliable we adjusted the parameters to correspond to the motion of individual stars near the supermassive black hole settled in the galactic center. Particularly, we imitate the galactic centre situation by considering a massive ring far away from the central black hole and tracking the particle moving inside this ring. In our Galaxy there seems to be two different massive ring-like structures, called the CNR (circumnuclear rings), one is placed at the distance around (1,5 $\div$ 3) pc from the center with the total mass ranging from $10^4 M_\odot$ to $10^6 M_\odot$, the other is farther $(60 \div 100)pc$ and heavier ($\mathcal{M} \approx 3 \cdot 10^7 M_\odot$). Within the validity of the used model we showed that there is probably not induced chaos in the motion of low energetic stars in our Galaxy due to the presence of these structures, but the upper estimate on the inner CNR mass is quite close to the case where chaos is induced in the motion of stars moving close to the ring for some time. It is thus possible that in other galaxies such configuration could exist. In reality the CNR are certainly not described accurately by the thin ring which is significant specifically for the orbits getting close to the ring. Therefore, chaos could be weaker in the case, when we use a more extended model for the tori. Hence we should bear in mind that modelling the toroidal structures in the galactic center by thin rings need not to be accurate in some situations, bringing an artificial effect in the form of the chaotic behaviour of geodesic flow.

We also modelled the gravitational effect of the accretion disc which is supposed to be very close to the black hole stretching only to some hundreds or thousands of Schwarzschild radii with the first inverted Morgan Morgan disc. Since the mass of the accretion disc should be by few orders smaller than the mass of the black hole we examined the case with (probably) highly overshot value $\mathcal{M} = 0.01M$. This case turned out to be regular for the motion in the region inhabited by the S-stars, thus we conclude that for the lower accretion masses the result would be the same.

During our cooperation with K. R. Rajagopal we studied the motion of mechanical oscillators described by non-standard constitutive relations. These counterparts of the Duffing oscillator are classical dissipative systems which exhibit chaotic behaviour. We dealt with some new phenomena related to the chaos in dissipative systems when constructing the bifurcation diagram or the maps of basins of attractors, but we also used the same methods (Poincaré surface of section, recurrence analysis, weighted average of directional vectors or Lyapunov exponents) and we verified the capability of these methods to work in wide range of applications.

Bibliography

[1] V. V. S. Afraimovich and S.-B. Hsu, *Lectures on chaotic dynamical systems.*, vol. 28, AMS Bookstore, 2003.

[2] R. Bach and H. Weyl, *Neue lösungen der einsteinschen gravitationsgleichungen. b. explizite aufstellung statischer axialsymmetrischer felder*, Math. Zeit. **13** (1922), 134.

[3] S. Basilakos and M. Plionis, *Cosmological constraints from x-ray agn clustering and type ia supernova data*, Monthly Notices of the Royal Astronomical Society: Letters **360** (2005), no. 1, L35–L38.

[4] L. Bombelli and E. Calzetta, *Chaos around a black hole*, Classical and Quantum Gravity **9** (1992), no. 12, 2573.

[5] M. Bursa, M. A. Abramowicz, V. Karas, and W. Kluźniak, *The upper kilohertz quasi-periodic oscillation: a gravitationally lensed vertical oscillation*, The Astrophysical Journal Letters **617** (2004), no. 1, L45.

[6] L. Cao, *Practical method for determining the minimum embedding dimension of a scalar time series*, Physica D: Nonlinear Phenomena **110** (1997), no. 1, 43–50.

[7] P. M. Cincotta and C. Simó, *Simple tools to study global dynamics in non-axisymmetric galactic potentials-i*, Astronomy and Astrophysics Supplement Series **147** (2000), no. 2, 205–228.

[8] C. M. Danforth, *http://mpe2013.org/2013/03/17/chaos-in-an-atmosphere-hanging-on-a-wall/*, 2013.

[9] A. P. S. de Moura and P. S. Letelier, *Chaos and fractals in geodesic motions around a nonrotating black hole with halos*, Physical Review E **61** (2000), no. 6, 6506.

[10] U. Dressler and G. Nitsche, *Controlling chaos using time delay coordinates*, Physical Review Letters **68** (1992), no. 1, 1.

[11] J.-P. Eckmann, S. Oliffson Kamphorst, and Ruelle D., *Recurrence plots of dynamical systems*, Europhysics Letters **4** (1987), 973.

[12] A. M. Ghez et al., *Measuring distance and properties of the milky way's central supermassive black hole with stellar orbits*, The Astrophysical Journal **689** (2008), no. 2, 1044.

[13] H. D. I. Abarbanel et al., *Predicting physical variables in time-delay embedding*, Physical Review E **49** (1994), no. 3, 1840.

[14] M. A. Requena-Torres et al., *Great confirms transient nature of the circumnuclear disk*, Astronomy & Astrophysics **542** (2012), L21.

[15] R. Shafee et al., *Estimating the spin of stellar-mass black holes by spectral fitting of the x-ray continuum*, The Astrophysical Journal Letters **636** (2006), no. 2, L113.

[16] S. Gillessen et al., *New observations of the gas cloud g2 in the galactic center*, The Astrophysical Journal **763** (2013), no. 2, 78.

[17] S. Molinari et al., *A 100 pc elliptical and twisted ring of cold and dense molecular clouds revealed by herschel around the galactic center*, The Astrophysical Journal Letters **735** (2011), no. 2, L33.

[18] B. R. Fayad, *Analytic mixing reparametrizations of irrational flows*, Ergodic Theory and Dynamical Systems **22** (2002), 437–468.

[19] A. F. Filippov, *Classical solutions of differential equations with multi-valued right-hand side*, SIAM Journal on Control **5** (1967), no. 4, 609–621.

[20] A. M. Fraser and H. L. Swinney, *Independent coordinates for strange attractors from mutual information*, Physical Review A **33** (1986), no. 2, 1134.

[21] C. Froeschlé, E. Lega, and R. Gonczi, *Fast lyapunov indicators. application to asteroidal motion*, Celestial Mechanics and Dynamical Astronomy **67** (1997), no. 1, 41–62.

[22] R. Genzel, F. Eisenhauer, and S. Gillessen, *The galactic center massive black hole and nuclear star cluster*, Reviews of Modern Physics **82** (2010), no. 4, 3121.

[23] E. Gueron and P. S. Letelier, *Chaos in pseudo-newtonian black holes with halos*, arXiv preprint astro-ph/0101140 (2001).

[24] D. T. Kaplan and L. Glass, *Direct test for determinism in a time series*, Physical Review Letters **68** (1992), no. 4, 427.

[25] O. Kopáček, V. Karas, J. Kovář, and Stuchlík Z., *Transition from regular to chaotic circulation in magnetized coronae near compact objects*, The Astrophysical Journal **722** (2010), no. 2, 1240.

[26] H. Koyama, K. Kiuchi, and T. Konishi, *1/f fluctuations in spinning-particle motions around a schwarzschild black hole*, Physical Review D **76** (2007), no. 6, 064031.

[27] J. P. S. Lemos and P. S. Letelier, *Exact general relativistic thin disks around black holes*, Physical Review D **49** (1994), no. 10, 5135.

[28] A. J. Lichtenberg and M. A. Lieberman, *Regular and stochastic motion*, Research supported by the US Department of Energy, US Navy, and NSF. New York, Springer-Verlag (Applied Mathematical Sciences. Volume 38), 1983, 516 p. **38** (1983).

[29] E. N. Lorenz, *Deterministic nonperiodic flow*, Journal of the Atmospheric Sciences **20** (1963), no. 2, 130–141.

[30] N. Marwan, *http://tocsy.pik-potsdam.de/commandline-rp.php*, 2006.

[31] N. Marwan, M. Carmen Romano, M. Thiel, and J. Kurths, *Recurrence plots for the analysis of complex systems*, Physical Reports **438** (2007), 237.

[32] L. Meirovitch, *Elements of vibration analysis, second edition*, McGraw-Hill, New York, 986.

[33] M. F. Mestre, P. M. Cincotta, and C. M. Giordano, *Analytical relation between two chaos indicators: Fli and megno*, Monthly Notices of the Royal Astronomical Society: Letters **414** (2011), no. 1, L100–L103.

[34] M. Montero-Castano, R. M. Herrnstein, and P. T. P. Ho, *Gas infall toward sgr a* from the clumpy circumnuclear disk*, The Astrophysical Journal **695** (2009), no. 2, 1477.

[35] T. Morgan and L. Morgan, *The gravitational field of a disk*, Physical Review **183** (1969), 1097–1101.

[36] A. E. Motter, *Relativistic chaos is coordinate invariant*, Physical Review Letters **91** (2003), no. 23, 231101.

[37] A. E. Motter and A. Saa, *Relativistic invariance of lyapunov exponents in bounded and unbounded systems*, Physical Review Letters **102** (2009), no. 18, 184101.

[38] T. Oka, M. Nagai, K. Kamegai, and K. Tanaka, *A new look at the galactic circumnuclear disk*, The Astrophysical Journal **732** (2011), no. 2, 120.

[39] E. Ott, *Chaos in dynamical systems*, Cambridge university press, 2002.

[40] J. Poutanen and A. C. Fabian, *Spectral evolution of magnetic flares and time lags in accreting black hole sources*, Monthly Notices of the Royal Astronomical Society **306** (1999), no. 3, L31–L37.

[41] D. Pražák and K. R. Rajagopal, *Mechanical oscillators described by a system of differential-algebraic equations*, Applications of Mathematics **57** (2012), no. 2, 129–142.

[42] K. R. Rajagopal, *A generalized framework for studying the vibrations of lumped parameter systems*, Mechanics Research Communications **37** (2010), no. 5, 463 – 466.

[43] R.Dwayne Ramey and N.L. Balazs, *Hamiltonian chaos in homogeneous adm cosmologies?*, Foundations of Physics **31** (2001), no. 2, 371–398.

[44] O. Semerák, *Gravitating discs around a schwarzschild black hole: Iii*, Classical and Quantum Gravity **20** (2003), no. 9, 1613.

[45] O. Semerák and P. Suková, *Free motion around black holes with discs or rings: between integrability and chaos - I*, Monthly Notices of the Royal Astronomical Society **404** (2010), no. 2, 545.

[46] O. Semerák and P. Suková, *Free motion around black holes with discs or rings: between integrability and chaos–II*, Monthly Notices of the Royal Astronomical Society **425** (2012), no. 4, 2455–2476.

[47] O. Semerák, *Exact power-law discs around static black holes*, Classical and Quantum Gravity **21** (2004), no. 8, 2203.

[48] P. Suková, *Chaotic geodesic motion around a black hole and disc*, Journal of Physics: Conference Series, vol. 314, IOP Publishing, 2011, p. 012087.

[49] P. Suková and O. Semerák, *Recurrence of geodesics in a black-hole-disc field*, AIP Conference Proceedings, vol. 1458, 2012, p. 523.

[50] S. Suzuki and K. Maeda, *Chaos in schwarzschild spacetime: The motion of a spinning particle*, Physical Review D **55** (1997), no. 8, 4848.

[51] M. Takahashi and H. Koyama, *Chaotic motion of charged particles in an electromagnetic field surrounding a rotating black hole*, The Astrophysical Journal **693** (2009), no. 1, 472.

[52] G. Tancredi, A. Sánchez, and Roig F., *A comparison between methods to compute lyapunov exponents*, The Astronomical Journal **121** (2001), no. 2, 1171.

[53] X. Wu and T.-Y. Huang, *Computation of lyapunov exponents in general relativity*, Physics Letters A **313** (2003), no. 1–2, 77 – 81.

[54] X. Wu, T.-Y. Huang, and H. Zhang, *Lyapunov indices with two nearby trajectories in a curved spacetime*, Physical Review D **74** (2006), 083001.

[55] U. Yurtsever, *Geometry of chaos in the two-center problem in general relativity*, Physical Review D **52** (1995), no. 6, 3176.

[56] K. Zaki, S. Noah, K. R. Rajagopal, and A. R. Srinivasa, *Effect of nonlinear stiffness on the motion of a flexible pendulum*, Nonlinear Dynamics **27** (2002), no. 1, 1–18.

List of Figures

1.1 Bifurcation diagram of logistic map 10

2.1 Construction of the Poincaré's surface of section 14
2.2 Illustration of Lypunov exponents 16
2.3 Appearance of the diagonal line in RP 21
2.4 Recurrence plot for a random data series and a regular trajectory 22
2.5 Recurrence plots for two different chaotic trajectories. 24
2.6 Illustration for computation of WADV 27

3.1 Potential of the Schwarzschild black hole 31
3.2 Potential of inverted Morgan-Morgan disc 32
3.3 Potential of disc with the power-law profile 34
3.4 Potential of the Bach-Weyl ring 35

4.1 Poincaré surface of section for Schwarzschild BH 42
4.2 Poincaré surfaces of section for BH + 1. iMM disc 47
4.3 FLI and MEGNO maps for BH + BW ring 50
4.4 FLI and MEGNO maps for BH + BW ring 51
4.5 MEGNO maps for Schwarzschild BH and Bach-Weyl ring 52
4.6 MEGNO maps for Schwarzschild BH and Bach-Weyl ring 53
4.7 MEGNO maps for Schwarzschild BH and PL disc 54
4.8 MEGNO maps for Schwarzschild BH and PL disc 55
4.9 MEGNO maps for Schwarzschild BH and 4. iMM disc 56
4.10 MEGNO maps for Schwarzschild BH and 4. iMM disc 57
4.11 MEGNO maps for Schwarzschild BH and 4. iMM disc 58
4.12 K_2 for regular and weakly chaotic orbit 60
4.13 $\bar{\Lambda}(\Delta\tau)$ for several orbits around the BH + 1. iMM disc 65
4.14 $\bar{\Lambda}(\Delta\tau)$ for several orbits around the BH + 1. iMM disc 66
4.15 Comparison of $\bar{\Lambda}(\Delta\tau)$ for different resolution 67

5.1 Oscillatory system with standard spring and dashpot. 71
5.2 Shear stress for the Bingham fluid. 72
5.3 System that consists in a spring, dashpot, inextensible string and mass. 73
5.4 Two orbits of inverse cubic spring 75
5.5 Poincare's surface of section for the inverse cubic spring 76
5.6 Bifurcation diagram for the standard Duffing oscillator 77
5.7 Bifurcation diagram for the non-standard Duffing oscillator 78
5.8 Various quantifiers for rigid-elastic spring 80
5.9 Map of basins of attractors for rigid-elastic spring 81
5.10 Bifurcation diagram for Bingham fluid 83
5.11 Trajectories of Bingham fluid 84
5.12 Various quantifiers for Bingham fluid 85
5.13 Attractors for Bingham fluid and thieir maps of basins 86

List of Notations

AGN	active galactic nuclei
BH	black hole
CNR	circumnuclear ring
CZV	curve of zero velocity
DET	ratio between all recurrence points and those forming a diagonal line
DIV	inverse of the longest diagonal line
ENTR	Shannon entropy of the diagonal lines
FLI	fast Lyapunov index
$\mathcal{E}$	energy per unit mass
f	frequency
F_s	force in the spring
F_d	force in the dashpot
$g_{\mu\nu}$	metric
GR	general relativity
J_θ	latitudinal action
K_2	Rényi entropy of second order
ℓ	angular momentum per unit mass
$L_{\max}$	longest diagonal line in the recurrence matrix
$l_{\min}$	minimal number of points of the diagonal line
LAM	ratio between all recurrence points and those forming a vertical line
$\mathcal{M}$	mass of the additional source
$M_\odot$	mass of the Sun
MEGNO	mean exponential growth factor of nearby orbits
mLCE	maximal Lyapunov exponent
$\mathcal{P}$	phase space
$\mathbf{R}_{i,j}(\varepsilon)$	recurrence matrix
$P(\varepsilon, l)$	histogram of diagonal lines in recurrence matrix
$\bar{R}^3_{n_j}$	average displacement per step for a random walk with n_j steps in a 3D space for random processes
r_{disc}	inner radius of the disc
r_{ring}	radius of the ring
RP	recurrence plot
RR	recurrence rate
$\mathcal{S}$	surface of section
Sgr A*	Sagittarius A*
T1	recurrence time of the first type
T2	recurrence time of the second type
TT	traping time – average length of the vertical lines
$\mathbf{u}$	four-velocity
V ENTR	Shannon entropy of the vertical lines
$\mathbf{V}_j$	the sum of the directional vectors in the j-th box
WADV	weighted average of directional vectors

$\mathbf{w}$	vector in phase space
$\mathbf{x}$	vector in configuration space
Y	mean exponential growth factor of nearby orbits
$\bar{Y}$	averaged mean exponential growth factor of nearby orbits
$\lambda_{\max}$	maximal Lyapunov exponent
$\lambda(\rho, z)$	metric function
δ	threshold for MEGNO for regular orbits
$\bar{\Lambda}(\Delta\tau)$	weighted average of directional vectors through all boxes
ε	threshold for the recurrence analysis
$\boldsymbol{\delta}(t)$	deviation vector satisfying the variational equation
$\nu(\rho, z)$	metric function
φ_t	map induced by the flow of the dynamical system during time t
ω	angular frequency
τ	proper time

Attachments

A. Free motion around black holes with discs: between integrability and chaos – I

Published in: Semerák, O. and Suková, P.: Free motion around black holes with discs or rings: between integrability and chaos – I, Monthly Notices of the Royal Astronomical Society 404 (2010), 545

http://dx.doi.org/10.1111/j.1365-2966.2009.16003.x

Preprints: arXiv:1211.4106 [gr-qc]

Monthly Notices
of the
ROYAL ASTRONOMICAL SOCIETY

Mon. Not. R. Astron. Soc. **404,** 545–574 (2010) doi:10.1111/j.1365-2966.2009.16003.x

Free motion around black holes with discs or rings: between integrability and chaos – I

O. Semerák★ and P. Suková

Institute of Theoretical Physics, Faculty of Mathematics and Physics, Charles University, Prague, Czech Republic

Accepted 2009 November 5. Received 2009 November 3; in original form 2009 October 5

ABSTRACT

Geodesic dynamics is regular in the fields of isolated stationary black holes. However, due to the presence of unstable periodic orbits, it easily becomes chaotic under various perturbations. Here, we examine what amount of stochasticity is induced in Schwarzschild space–time by the presence of an additional source. Following astrophysical motivation, we specifically consider thin rings or discs lying symmetrically around the hole, and describe the total field in terms of exact static and axially symmetric solutions of Einstein's equations. The growth of chaos in time-like geodesic motion is illustrated on Poincaré sections, on time series of position or velocity and their Fourier spectra, and on time evolution of the orbital 'latitudinal action'. The results are discussed in terms of dependence on the mass and position of the ring/disc and on geodesic parameters (energy and angular momentum). In the Introduction, we also add an overview of the literature.

Key words: black hole physics – gravitation – relativity.

1 INTRODUCTION

It became evident no later than the 19th century that linear dynamical systems do not always represent adequately what happens in nature and society. It was also found that non-linear systems may behave in a complicated, 'chaotic' way, even if governed by fully deterministic rules and effects. Since the non-linearity occurs in cases so simple as a set of three Newtonian gravity centres, linear systems in fact proved to be just marginal tips within a vast non-linear tangle. In the 20th century, mathematical background for the dynamical systems was notably supplied by the ergodic theory and by the study of differential equations (KAM theorem). However, it was only during the past half-century that the 'theory of chaos' was really established, focusing on simple non-linear dynamical systems whose orbits show a highly sensitive dependence on initial conditions. Computers and numerical techniques allowed researchers to follow and visualize the long-term evolution of these systems and chaotic processes were soon detected in almost every discipline – the days of non-linear science have come (Scott 2007).

It is for about 40 years now that chaotic behaviour has been studied in general relativity. The amount of chaos can be expected to be higher in such an inherently non-linear theory, allowing the space–time dynamics itself to turn irregular. The latter has naturally been examined in cosmological solutions, mainly in Bianchi IX (Mixmaster) models. While the secular debate about chaoticity and the very nature of these universes continues (Coley 2002; Fay & Lehner 2004; Benini & Montani 2004; Soares & Stuchi 2005; Heinzle, Röhr & Uggla 2006; Buzzi, Llibre & da Silva 2007; Andriopoulos & Leach 2008; Heinzle & Uggla 2009), one of the later attractors is to assess the effect of the cosmological constant and/versus that of a scalar field within the Friedmann–Lemaître–Robertson–Walker model dynamics (Jorás & Stuchi 2003; Faraoni, Jensen & Theuerkauf 2006; Hrycyna & Szydłowski 2006; Lukes-Gerakopoulos, Basilakos & Contopoulos 2008; Maciejewski et al. 2008). [We only give several more recent references here. Earlier ones can be found in Hobill, Burd & Coley (1994), for example.]

The other type of dynamical system investigated in general relativity is test motion in a *given* space–time. In this field, developed over the last 20 years, several obvious lines of research arise. First, it is interesting to start from some background where the (geodesic, or electrogeodesic) flow is regular and then consider various types of its 'perturbations' in order to study whether and how much stochasticity is induced. In gravitational systems, the most common ingredients are (i) how the background field and interaction are described (in a Newtonian, pseudo-Newtonian, post-Newtonian, post-Minkowskian or exact relativistic manner; and with or without a 'dark energy' contribution), (ii) how the test body is described (mainly whether it is point-like, without structure, or endowed with more multipoles) and (iii) whether and how the gravitational and electromagnetic radiation emissions and corresponding reactions on the body are taken into account. Such a study actually reveals whether the respective approximations (neglects) are admissible in judgements concerning the long-term evolution of a

★E-mail: oldrich.semerak@mff.cuni.cz

© 2010 The Authors. Journal compilation © 2010 RAS

given physical system. The 'disentanglement' of the effects of various approximations may be problematic, however, because the latter may furthermore be interlaced intricately.

To top it all, there is the 'dynamics' of the employed numerical code. With how much (and what kind of) chaos do the program itself and round-off errors confuse the results? How are these 'machine instabilities' enlaced with those coming from true physics? Interestingly, all this need not lead to desperation according to the shadowing theorem (Sauer, Grebogi & Yorke 1997) which states that, for some systems (surely for hyperbolic ones), every numerically produced 'pseudo-trajectory' is *shadowed* by a bunch of 'true trajectories' (all of which start from slightly different initial conditions in general) that remain close to it for a certain ('long') time (see Lai, Grebogi & Kurths 1999, Shi et al. 2001 and Judd 2008 for more recent contributions). Anyway, the above uncertainties remind us that it is important to have more ways of studying the dynamics and more indicators of chaos with precisely known interrelations. They also point out the preference for invariant measures of chaos and the principal role of analytical methods (like the Melnikov method, often used in relativity). Let us mention, apropos this emphasis, an important result of Motter (2003): contrary to the opinion prevailing until then, it was shown that the *sign* of Lyapunov exponents is coordinate independent under the conditions when the exponents can be meaningful indicators of chaos (see also the recent sequel by Motter & Saa 2009).

One of the natural backgrounds for the study of general relativistic test-particle dynamics is that corresponding to gravitational waves, because the latter have no Newtonian analogue. The waves may influence the particles in a chaotic manner, as already shown by Varvoglis & Papadopoulos (1992); they considered charged particles moving in a uniform magnetic field and affected by a linearly polarized weak gravitational wave propagating perpendicular to the magnetic field lines. A similar conclusion was obtained for geodesic motion in *pp*-waves (Podolský & Veselý 1998) and recently extended to the waves described by Kundt metrics (Podolský & Kofroň 2007); chaos was detected there by analysing the dimension of boundaries between the sets of initial conditions (basins) leading to different kinds of final outcomes. (Fractal boundaries evidence chaos.)

However, it is doubly apropos to seek chaos around the third principal 'non-Newtonian' prediction of general relativity (besides dynamical cosmology and gravitational waves) – around black holes. Actually, in ancient Greek *chaos* meant a gaping bottomless void, where everything falls endlessly . . .

2 DYNAMICS OF TEST MOTION IN BLACK HOLE FIELDS

Let us start a summary of previous results concerning black hole fields by a quotation from Cornish & Frankel (1997): '. . . even the most pristine black hole space–time harbours the seeds of chaos in the form of isolated unstable orbits. A small perturbation causes these unstable orbits to break out and infect large regions of phase space. Note that the experience with Newtonian systems is very misleading. For example, the Kepler problem has more integrals of motion than are needed for integrability. Keplerian systems are thus impervious to small perturbations. In contrast, black hole space–times are at the edge of chaos, just waiting for the proverbial butterfly to flap its wings.'[1]

The proverbial flap has been provided by various kinds of perturbations and their effect explored by several methods. The first perturbation we mention is on the side of the test particle; it consists of endowing the particle with spin.

2.1 Endowing the particle with spin

Endowing the particle with spin deflects its motion from a geodesic and thus away from a sufficient number of conserved integrals. Suzuki & Maeda (1997) performed long-term integration of the Mathisson–Papapetrou equations (describing the evolution of spinning test particles in a pole–dipole approximation) in a Schwarzschild field, in order to show, on Poincaré sections, that the spin really leads to chaos. Later Suzuki & Maeda (1999) analysed the imprints of particle dynamics on gravitational waves emitted and learned that in a chaotic mode the emitted power increases, the frequency spectrum is 'blurred' and the waveforms may also be changed. Kao & Cho (2005) confirmed the spin-induced chaos by calculating the Melnikov integral. This integral along the unperturbed homoclinic orbit from Poisson brackets of original and perturbation Hamiltonians reveals a 'transversal distance' in phase space between stable and unstable manifolds emanating from a homoclinic orbit. Infinitely repeating zeros of the integral indicate that the stable and unstable manifolds are entangled, thus evidencing the occurrence of chaos. The same system was also studied by Koyama, Kiuchi & Konishi (2007) who were able to classify its chaotic motions into the '1/frequency' and 'white-noise' types on the basis of the power spectrum of time series of the particle's z-position. The '1/frequency' (respectively, 'white-noise') spectrum was detected for smaller (respectively, larger) values of the particle's spin, when the motion tends to be rather weakly (respectively, strongly) chaotic.

The dynamics of spinning particles was studied in the Kerr field too. Hartl (2003a,b) showed, by computing the Lyapunov exponents, that it *may* become chaotic, but only for the spin values that are too large to be astrophysically realistic or even too large for the pole–dipole test-particle approximation to be valid. Rotation of the hole was noted to rather enhance the instability. Han (2008a) found the effect of the centre's rotation just opposite, by plotting Poincaré sections and mainly by computing a modified Lyapunov exponent – the 'fast Lyapunov indicator'. In the meantime, Kiuchi & Maeda (2004) checked whether chaos reflects on emitted gravitational waves. They concluded that the

[1]The role of unstable circular orbits and their relation to homoclinic (separatrix) and zoom-whirl orbits were recently clarified, in the Kerr field, by Levin & Perez-Giz (2009) and Perez-Giz & Levin (2009). The stability of circular orbits (the null ones, in particular) was also related to quasi-normal modes of black holes in the Schwarzschild(–de Sitter) and higher dimensional (Schwarzschild–Tangherlini and Myers–Perry) space–times (Cardoso et al. 2009).

spectrum of waves from non-chaotic orbits contains only discrete characteristic frequencies, whereas that from chaotic orbits is continuous with finite widths (the waveforms did not seem to be altered significantly).

Now let us turn to much wider range of options of perturbing the background.

2.2 Perturbing the background

Like in the above case of the test body, one can 'endow' the background (in a more or less artificial manner) with some extra multipoles. In the literature, their effects on dynamics were mostly inferred from Poincaré surfaces of section. Vieira & Letelier (1996a) thus showed how geodesics around a Schwarzschild black hole become chaotic under the perturbation by a quadrupole, and mainly octupole moments (in a Newtonian limit, the resulting field is an analogue of the Hénon–Heiles potential). Chaos was also detected (Letelier & Vieira 1997a) around a slowly rotating black hole superposed with a dipolar halo; particles counter-rotating with respect to the black hole turned out to be more unstable than the corotating ones. Relativistic, linearized and Newtonian core-shell fields (Schwarzschild centre plus dipole, quadrupole and octupole) were compared by Vieira & Letelier (1999). The dynamics proved to be sensitive to breaking of the reflection symmetry (disappearance of the equatorial plane) which enhanced/inhibited the chaos in oblate/prolate fields. Anyway, the relativistic dynamics was significantly more chaotic than its Newtonian counterpart. The latter was confirmed by Guéron & Letelier (2001) for a black hole (versus a point centre) superposed with a dipolar field. However, the system became even more chaotic (than the exact case) when the Schwarzschild-like centre was simulated by a pseudo-Newtonian (Paczyński–Wiita) potential; this instability was amplified further by incorporating a special relativistic equation of motion. Wu & Huang (2003) tested, on geodesics around the Schwarzschild hole with a dipolar shell, a new coordinate-free prescription for computation of Lyapunov exponents. A dipolar term was also employed as a perturbation of the Reissner–Nordstrøm space–time (Chen & Wang 2003); the geodesic structure again turned chaotic. In the meantime, Guéron & Letelier (2002) superposed a quadrupole with a static or rotating black hole and observed that prolate deformations lead to chaos, whereas the oblate-system dynamics remained regular; in the case of the rotating black hole, chaos preferentially occurred among counter-rotating orbits. Finally, we mention the usage of the basin-boundary method: de Moura & Letelier (2000a) checked the escape of free test particles from a static black hole superposed with dipole, quadrupole and octupole terms, and found null geodesics to be more regular than the time-like ones. This conclusion was reached by analysing the dimension of the boundaries of initial-condition 'basins' that lead to different escape endpoints (in isolated gravitational systems, there are three possible outcomes usually: fall to the centre, escape to infinity and eternal orbiting).

Rather than 'switch on' the multipoles individually, it is also possible to incorporate them by turning to some more general exact stationary (usually also axisymmetric) fields. Sota, Suzuki & Maeda (1996) devoted their study to several *static* axisymmetric space–times, namely those of the Zipoy–Vorhees class describing the fields of finite axial rods (including e.g. the Schwarzschild and Curzon metrics as special cases), and also to the system of N Curzon-type point singularities distributed along the symmetry axis. They diagnosed geodesic chaos on both Poincaré maps and Lyapunov exponents, but mainly tried to relate the known 'reliable' means of recognizing chaos (detection of the homoclinic tangle, in particular) with methods based on curvature properties of the space–time background. Specifically, they studied tidal-matrix eigenvalues and curvature of the fictitious space obtained by energy-dependent conformal mapping within the Newtonian approach, while studying the Weyl-tensor eigenvalues in the relativistic case. Vieira & Letelier (1996b) replied, however, by demonstrating that the criterion suggested in the previous paper is neither necessary nor sufficient for the occurrence of chaos. They admitted there surely exist links between global dynamics and local (curvature) properties of a certain 'configuration manifold' of the system, but concluded that 'any local analysis, in effective or even physical spaces, is far from being sufficient to predict a global phenomenon like chaotic motion'. (The 'geometric' approaches have nevertheless made considerable progress since, see concluding remarks.) Two other, quite recent, papers also illustrate differences that do not so rarely occur in the field. Dubeibe et al. (2007) analysed the geodesic dynamics of the Tomimatsu–Sato space–time and its deformed generalization provided by a particular vacuum case of the five-parametric solution of Manko et al. (considered e.g. as a possible description of the neutron star field). They affirmed regular dynamics in the Tomimatsu–Sato ($\delta = 2$) solution, while in its generalization they found chaos for the oblate case instead of the prolate one; this is in contrast to the results of Guéron & Letelier (2002). Soon afterwards, Han (2008b) re-examined the case of the Manko et al. space–time and came to the opposite conclusion (prolate field chaotic, whereas oblate field regular).

Among the more general stationary axisymmetric black hole backgrounds, the most important are those that might have some astrophysical relevance. These correspond to 'the most symmetric' type of perturbations – by additional axially and reflectionally symmetric bodies (namely a disc or a 'halo'). Referring to the conditions in galactic centres, Vokrouhlický & Karas (1998) computed Newtonian trajectories around a point centre surrounded by a thin disc and monitored how the long-term evolution of their parameters responds to the disc's gravitational field as well as to successive mechanical interactions switched on to simulate crossings of the disc. Saa & Venegeroles (1999) solved a similar problem, with an infinite homogeneous thin disc[2] around a static black hole (relativistic version) or a point mass (Newtonian version). The relativistic system turned out to be more chaotic than the Newtonian. Saa (2000) then compared the results (namely Poincaré sections) with the (Newtonian) case involving a thick disc (homogeneous in the radial direction). Chaos was rather attenuated by the disc thickness. In contrast, perturbations non-symmetric with respect to the disc plane (dipole) turned out to strongly enhance the chaos. The same Newtonian system was later studied by Kiuchi, Koyama & Maeda (2007) on Lyapunov exponents and on time evolution of orbital parameters

[2]Note that the potentials of such discs rise to infinity in the perpendicular direction.

(and the corresponding radial-motion power spectrum). The authors mainly showed, however, that the degree of chaoticity clearly reflects on gravitational waves generated (according to the quadrupole formula) by the orbiting particles, namely on their forms and energy spectra. We note in passing that Ramos-Caro, López-Suspes & González (2008) analysed Newtonian motion in the fields of several members of the Kalnajs disc family (sole discs, *without* the central body) as a possible approximation of the motion of stars in spiral galaxies. They found chaos in the case of disc-crossing orbits (just induced by discontinuity of the field, no mechanical interaction is involved), but regular motion otherwise. Wu & Zhang (2006) recognized, on Poincaré sections and Lyapunov exponents as well, geodesic chaos in the relativistic field of a Schwarzschild black hole superposed with discs of the 'peculiar' family constructed by Lemos & Letelier (1994) from identical halves of two dipoles. Returning to a direct astrophysical setting: Karas & Šubr (2007) proved the relevance of dynamics in the centre–disc fields for the long-term evolution of stellar clusters in galactic nuclei. The disc was found to bring the main 'instability', whereas the spherical-cluster mean field and perihelion advance (included on a post-Newtonian level) rather regularize the dynamics, the total effect still being the increase of probability of close encounters between stars and the centre (probably a supermassive black hole) by a factor of 10.

Among the astrophysically important 'perturbations', there is also counting in a magnetic field. In one of the early papers, Karas & Vokrouhlický (1992) discussed the dynamics of charged particles in the Ernst space–time (Schwarzschild black hole immersed in a magnetic field) with the help of Poincaré sections and Lyapunov exponents. Quite recently, Takahashi & Koyama (2009) plotted the Poincaré sections through the dynamics of charged particles in the field of a Kerr black hole surrounded by Petterson's test dipole magnetic field. They found that the dragging effects tend to suppress the instability;[3] they explain this 'regularization' by the fact that for fast rotating holes the integral $\frac{1}{l}\oint\sqrt{g_{\theta\theta}u^\theta u^\theta}\,\mathrm{d}\tau$ of the test particle's latitudinal four-velocity over one orbital cycle (of length l) becomes approximately conserved.

Another important perturbation is the one by gravitational waves. In another seminal paper, Bombelli & Calzetta (1992) used the Melnikov method in order to detect the influence of a small periodic perturbation (corresponding to weak gravitational waves) on the geodesic structure of Schwarzschild space–time. Later, Letelier & Vieira (1997b) explored, also by the Melnikov method, the chaos in test motion in the Xanthopoulos solution for a Schwarzschild black hole perturbed by a gravitational wave.[4]

Another type of perturbation has already a long history in Newtonian celestial mechanics: perturbation of the test-particle motion in a given background by an additional distant body – Hill's problem. Moeckel (1992) tackled its relativistic version and showed, by calculating the Melnikov integral, that the third body perturbs the two-body homoclinic orbit into a tangle of intersecting stable and unstable manifolds, thus implying that the system went chaotic. Cornish & Frankel (1997) analysed the geodesic structure of the equatorial plane of the extreme Reissner–Nordstrøm black hole, perturbed by an additional distant body. They detected chaos by examining the basin boundaries and pointed out that it may, for example, lead to the increased production of gravitational waves. Chaos was also ascertained by Şelaru et al. (2005), in a Newtonian setting with the primary mass endowed with a potential simulating the Schwarzschild field. Similarly, Steklain & Letelier (2006) compared the Hill problem including the Paczyński–Wiita pseudo-Newtonian (Schwarzschild-like) potential and compared it with the original Newtonian version. They applied Poincaré maps, Lyapunov exponents and basin boundaries on specific systems of (Sun + Earth + Moon) and (Milky Way + cluster + star) parameters and concluded that the pseudo-Newtonian systems are usually – but not always – more unstable than their Newtonian counterparts. Recently, the authors extended the analysis to one of pseudo-Newtonian systems trying to incorporate dragging effects due to the rotation of the centre (Steklain & Letelier 2009); Poincaré maps, Lyapunov exponents and the fractal escape method revealed that the orbits counter-rotating with respect to the centre are more unstable than the co-rotating ones.

When the 'third body' is heavy and nearby, it can no longer be treated as a perturbation and a two-centre (or multicentre) problem arises. The non-rotating centres can stay in equilibrium if both (respectively all) bear charges equal to their masses and electrostatic repulsion just balances gravitational attraction. In relativity it means black holes of the extreme Reissner–Nordstrøm type; their multiple field is described by the Majumdar–Papapetrou class of exact solutions. Examination of the dynamics of free test particles in the field of two such fixed black holes by Contopoulos actually triggered the research in the whole area; a survey of the early papers was, for example, given by Contopoulos & Papadaki (1993). These showed that unlike the Newtonian dynamics in the two-centre background the relativistic problem is strongly chaotic for both photons and massive particles. This was confirmed by Dettmann, Frankel & Cornish (1994) who also (Dettmann, Frankel & Cornish 1995) discussed the appropriateness of various tests of chaos (Lyapunov exponents, topological methods, Poincaré sections) in general relativity on this problem. Yurtsever (1995) showed that the motion of photons in the double-centre Majumdar–Papapetrou field can be translated as geodesic motion in Riemannian space described by the spatial part of the metric. This space has negative curvature, which is known to be a source of chaos. A similar geometric approach was tested (and compared with information from Lyapunov exponents) on static multi-black hole space–times with cylindrical symmetry by Szydłowski (1997). Chaotic scattering of photons by a double Majumdar–Papapetrou centre was studied by Levin (1999). A thorough discussion of photon escape from the system was provided by Alonso, Ruiz & Sánchez-Hernández (2008). They identified a set of unstable periodic orbits that form a fractal repeller, calculated its main characteristics (Lyapunov exponents, Hausdorff dimension and escape rate, among others) and compared them with the results of numerical simulations. They also considered the limit case when one of the black holes may be considered as a small perturbation of the other (it is light and far away). A very thorough treatment of the subject was also presented by Contopoulos & Harsoula (2005). It was mainly focused on (fractal) structure of the basins of attraction of the individual black holes and of the escape basin, and on its dependence on ratio between masses of

[3] A result that can be understood as related to this one was obtained by Letelier & Vieira (1998): in a Taub–NUT space–time, the chaos induced by dipolar perturbation is attenuated by the NUT parameter (which acts as a 'gravitomagnetic monopole', i.e. as a source of dragging).

[4] The inherent iffiness of the delicate problems of non-linear evolution may be illustrated by putting together two of the questions raised above: (i) how chaos in the motion of particles reflects on gravitational waves emitted by them and (ii) how incident gravitational waves perturb the dynamics of particles.

the holes. Several papers generalized or modified the problem. Howard & Wilkerson (1995) analysed Newtonian dynamics in the field of two centres with a finite dipole and discussed the nature of its chaoticity in detail. Aguirregabiria (1997) showed that in the case of *four* extreme centres, the scattering of charged test particles is chaotic both in the Newtonian and in the relativistic description. Cornish & Gibbons (1997) also took into account a dilaton field and observed the transition between regular and chaotic motion for photons and for extremely charged particles. (They added a useful discussion on fractal, topological and curvature methods.) de Moura & Letelier (2000b) considered a slightly different (and more realistic) system – of two *uncharged* black holes, but far away from each other. The approximated motion of photons in this field shows chaotic features: the boundary between capture, orbital and escape basins is fractal, becoming a self-similar Cantor set in the limit of infinite distance between the centres, with its box-counting dimension falling off logarithmically. Hanan & Radu (2007) recently generalized the problem of multiple extreme black holes to higher dimensional space–times (with special attention to the five-dimensional case) and found qualitative similarity of chaos in test dynamics there.

Finally, let us quote the variant of the orbital dynamics where the own field of the orbiting body is *not* negligible. The problem thus ceases to count among those with *given* background and involves dynamics of the Einstein equations themselves. Compact-binary evolution is a prominent astrophysical example of such a challenge. It in fact embodies, in a true *tangle*, all the knottiness both on the general-relativity side and on the side of non-linear dynamics. The chaotic evolution of compact binaries was discussed, on the second post-Newtonian level including spins, by Levin (2000, 2003) and by Wu & Xie (2008); in the last paper, the 'fast Lyapunov indicator' was computed in order to deduce the roles of system parameters. [A great deal of information is also given in the third PN treatment by Grossman & Levin (2009).] Cornish & Levin (2003) also compared it (in the case with zero spins) with *test*-particle dynamics in a Schwarzschild background. For the chaotic, post-Newtonian system the Lyapunov time was sometimes found to be comparable to the time-scale for dissipation due to gravitational waves, which would indicate possible abating of chaos due to waves (were the Lyapunov time longer, chaos would be damped). However, the conclusiveness of any post-Newtonian approximation in the issue of chaos (of course) remains a question (Levin 2006).

In this paper, we study the dynamics of time-like geodesics in exact space–times describing the fields of static and axially symmetric black holes surrounded by thin discs or rings. We try to show, on Poincaré sections, on time series of position or velocity and their Fourier spectra and on behaviour of the 'latitudinal action', how the original, completely integrable Schwarzschild geodesic dynamics grows chaotic when the external source is being 'turned on', and we check how the evolution of phase-space properties depends on the values of geodesic constants.

3 STATIC BLACK HOLE WITH A RING OR DISC

We are interested in the time-like geodesic dynamics in the field of a black hole surrounded by a ring or a thin disc. Let us restrict to the static and axially symmetric case and to discs without charges and currents and without radial pressure. For such sources, the space–time metric can be put into the Weyl form[5]

$$\mathrm{d}s^2 = -\mathrm{e}^{2\nu}\mathrm{d}t^2 + \rho^2\mathrm{e}^{-2\nu}\mathrm{d}\phi^2 + \mathrm{e}^{2\lambda-2\nu}(\mathrm{d}\rho^2 + \mathrm{d}z^2) \tag{1}$$

in (Weyl) cylindrical-type coordinates (t, ρ, z, ϕ), with the two unknown functions ν, λ only depending on ρ and z. The 'gravitational potential' ν satisfies the Laplace equation, so it superposes linearly, while λ is found by quadrature:

$$\lambda = \int_{\mathrm{axis}}^{\rho,z} \rho\left\{\left[(\nu_{,\rho})^2 - (\nu_{,z})^2\right]\mathrm{d}\rho + 2\nu_{,\rho}\nu_{,z}\mathrm{d}z\right\}, \tag{2}$$

computed along any line within the vacuum region. (The requirement that the space is locally Euclidean on the axis implies $\lambda = 0$ on its part lying outside the horizon.)

3.1 Schwarzschild black hole

The Schwarzschild field (of mass M) is described by

$$\nu = \frac{1}{2}\ln\frac{d_1 + d_2 - 2M}{d_1 + d_2 + 2M} = \frac{1}{2}\ln\left(1 - \frac{2M}{r}\right), \tag{3}$$

$$\lambda = \frac{1}{2}\ln\frac{(d_1 + d_2)^2 - 4M^2}{4\Sigma} = \frac{1}{2}\ln\frac{r(r-2M)}{\Sigma}, \tag{4}$$

where

$$d_{1,2} \equiv \sqrt{\rho^2 + (z \mp M)^2} = r - M \mp M\cos\theta,$$

$$\Sigma \equiv d_1 d_2 = [(\rho^2 + z^2 + M^2)^2 - 4z^2M^2]^{1/2} = (r-M)^2 - M^2\cos^2\theta.$$

The second expressions are in Schwarzschild coordinates (r, θ) which are related to the Weyl coordinates by

$$\rho = \sqrt{r(r-2M)}\,\sin\theta, \quad z = (r-M)\,\cos\theta,$$

[5]Geometrized units are used in which $c = G = 1$. The cosmological constant is set to zero. Index-posed commas mean partial differentiation.

© 2010 The Authors. Journal compilation © 2010 RAS, MNRAS **404,** 545–574

or, in the opposite direction

$$r - M = \frac{1}{2}(d_2 + d_1), \quad M\cos\theta = \frac{1}{2}(d_2 - d_1).$$

Superpositions of the Schwarzschild black hole with an additional static and axially symmetric source are often being represented in Schwarzschild coordinates. Outside of the thin source with no radial pressure, the complete metric reads

$$\mathrm{d}s^2 = -\left(1 - \frac{2M}{r}\right)\mathrm{e}^{2\hat{\nu}}\mathrm{d}t^2 + \frac{\mathrm{e}^{2\hat{\lambda}-2\hat{\nu}}}{1-\frac{2M}{r}}\,\mathrm{d}r^2 + r^2\mathrm{e}^{-2\hat{\nu}}(\mathrm{e}^{2\hat{\lambda}}\mathrm{d}\theta^2 + \sin^2\theta\,\mathrm{d}\phi^2), \tag{5}$$

where $\hat{\nu}(r,\theta)$ is the potential of the external source and $\hat{\lambda}(r,\theta) \equiv \lambda - \lambda_{\mathrm{Schw}}$ [λ_{Schw} is given by (4)]. In this paper, the Bach–Weyl ring and several thin discs described by exact solutions of Einstein equations will be chosen as sources surrounding the Schwarzschild black hole in a reflectionally symmetric manner (they will lie in the 'equatorial plane' of the hole).

3.2 Bach–Weyl ring

The thin-ring solution of Bach & Weyl (1922) is given by complete first-kind Legendre elliptic integral $K(k) \equiv \int_0^{\pi/2} \frac{\mathrm{d}\phi}{\sqrt{1-k^2\sin^2\phi}}$:

$$\nu_{\mathrm{BW}} = -\frac{2\mathcal{M}K(k)}{\pi l_2}, \tag{6}$$

$$\lambda_{\mathrm{BW}} = \frac{\mathcal{M}^2k^4}{4\pi^2b^2\rho}\,[(\rho+b)(-K^2 + 4k'^2K\dot{K} + 4k^2k'^2\dot{K}^2) - 4\rho k^2k'^2(k'^2+2)\,\dot{K}^2], \tag{7}$$

where $\mathcal{M}$ is the ring's mass and b its Weyl radius, $\dot{K} \equiv \frac{\mathrm{d}K}{\mathrm{d}(k^2)}$, $k'^2 = \frac{(l_1)^2}{(l_2)^2}$, $k^2 = 1 - k'^2 = \frac{4\rho b}{(l_2)^2}$ and $l_{1,2} \equiv \sqrt{(\rho \mp b)^2 + z^2}$.

3.3 Inverted counter-rotating Morgan–Morgan discs

A physically reasonable family of annular thin-disc solutions was obtained by Lemos & Letelier (1994) by inversion (with respect to the rim) of the finite Morgan–Morgan discs interpreted in terms of two non-interacting streams of dust counter-orbiting on circular geodesics (Semerák 2003). The Newtonian densities of inverted discs are ($m = 1, 2, \ldots$)

$$w^{(m)}(\rho) = \frac{2^{2m}(m!)^2\mathcal{M}b}{(2m)!\,\pi^2\rho^3}\left(1 - \frac{b^2}{\rho^2}\right)^{m-1/2}, \tag{8}$$

where $\mathcal{M}$ is mass and b is the Weyl inner radius. The corresponding potential is quite lucid in oblate spheroidal coordinates (x, y) which are related to the Weyl coordinates by

$$\rho^2 = b^2(x^2+1)(1-y^2), \quad z = bxy: \tag{9}$$

$$v^{(m)}(x,y) = -\frac{2^{2m+1}(m!)^2\mathcal{M}}{\pi b}\,\frac{\sum_{n=0}^{m} C_{2n}^{(m)}\,\mathrm{i}Q_{2n}\!\left(\frac{\mathrm{i}|y|}{\sqrt{x^2+1-y^2}}\right)P_{2n}\!\left(\frac{x}{\sqrt{x^2+1-y^2}}\right)}{\sqrt{x^2+1-y^2}}, \tag{10}$$

where (for $n \le m$)

$$C_{2n}^{(m)} \equiv \frac{(-1)^n(4n+1)(2n)!(m+n)!}{(n!)^2(m-n)!(2m+2n+1)!}$$

and P_{2n}, Q_{2n} denote Legendre polynomials and Legendre functions of the second kind. Note that in computations it is convenient to express the latter as

$$Q_{2n}(\mathrm{i}X) = -\mathrm{i}\,P_{2n}(\mathrm{i}X)\,\mathrm{arccot}X - \sum_{j=1}^{2n}\frac{1}{j}\,P_{j-1}(\mathrm{i}X)P_{2n-j}(\mathrm{i}X).$$

3.4 Annular discs with power-law density profile

Another family of annular thin discs is the one with a power-law radial profile of density (Semerák 2004),

$$w^{(m,n)}(\rho) = \frac{\left(1+\frac{1}{n}\right)_m}{m!}\,\frac{\mathcal{M}b}{2\pi\rho^3}\left(1 - \frac{b^n}{\rho^n}\right)^m, \tag{11}$$

where m and n are natural numbers and $(a)_m \equiv \Gamma(a+m)/\Gamma(a)$ is the Pochhammer symbol. The corresponding fields behave somewhat more regularly at the inner rim than those of the inverted Morgan–Morgan discs. For even n,[6] the potential can be expanded as

$$v^{(m,n)}(\rho,z) = -\frac{\left(1+\frac{1}{n}\right)_m}{n}\,\frac{\mathcal{M}}{b}\sum_{j=0}^{\infty}\frac{P_{2j}(0)P_{2j}\!\left(\frac{z}{\sqrt{\rho^2+z^2}}\right)(\rho^2+z^2)^j}{\left(\frac{2+2j}{n}\right)_{m+1}b^{2j}} \tag{12}$$

in the 'inner region' ($\sqrt{\rho^2+z^2} < b$), while as

[6]When n is odd, the potentials comprise logarithmic terms. We will not consider such a case here.

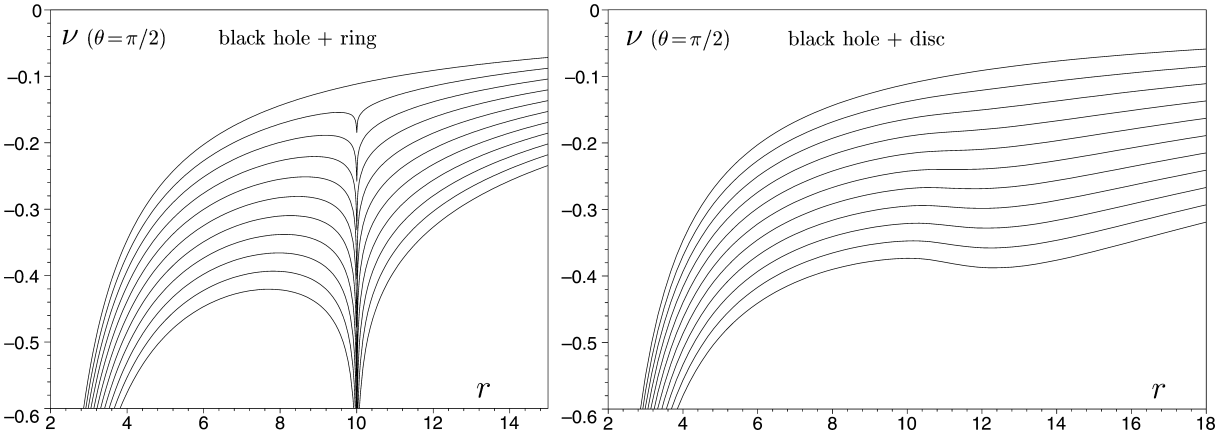


Figure 1. Radial dependence of the equatorial potential of a Schwarzschild black hole surrounded by a Bach–Weyl ring (6) on Schwarzschild radius $r = 10M$ (left-hand panel), or by a power-law disc (12,13) (of $m = 4$, $n = 10$) with Schwarzschild inner radius $r = 10M$ (right-hand panel). The relative masses of the ring are $\mathcal{M}/M = 0, 0.2, 0.4, \ldots, 2.0$ (the singular 'valley' of course becomes more profound along this sequence), while the relative masses of the disc are $\mathcal{M}/M = 0, 0.5, 1.0, \ldots, 5.0$. It is seen that the disc is only scarcely able to develop its own potential minimum near the black hole, even though it is fairly concentrated (towards the rim) and its mass is chosen to be extremely large. Radius is in the units of M; potential is dimensionless.

$$\nu^{(m,n)}(\rho,z) = -\frac{\left(1+\frac{1}{n}\right)_m \mathcal{M}}{\sqrt{\rho^2+z^2}} \left[\sum_{j=0}^{\infty} \frac{P_{2j}(0) P_{2j}\left(\frac{z}{\sqrt{\rho^2+z^2}}\right) b^{2j}}{n\left(\frac{1-2j}{n}\right)_{m+1} (\rho^2+z^2)^j} + \sum_{k=0}^{m} \frac{(-1)^k Q_{kn+1}(0) P_{kn+1}\left(\frac{|z|}{\sqrt{\rho^2+z^2}}\right) b^{kn+1}}{k!(m-k)!\,(\rho^2+z^2)^{\frac{kn+1}{2}}} \right] \tag{13}$$

in the 'outer region' ($\sqrt{\rho^2+z^2} > b$).

3.5 Complete fields

The complete fields are given by sum of the potentials, $\nu = \nu_{\rm Schw} + \hat{\nu}$. The Schwarzschild singularity is the strongest possible source of gravitation, so it is not surprising that the additional sources can hardly affect its field considerably without being unrealistically heavy (and compact). Fig. 1 illustrates this on the Bach–Weyl ring (one-dimensional source) and on one of the (rather concentrated) power-law discs (two-dimensional source). Extended (three-dimensional) sources would have even weaker immediate influence on the black hole field.

4 TIME-LIKE GEODESICS IN WEYL FIELDS

Massive free test particles move along time-like geodesics. In Weyl fields, these read, in the Weyl coordinates,

$$\frac{\mathrm{d}u^t}{\mathrm{d}\tau} = \frac{\mathrm{d}}{\mathrm{d}\tau}\left(\frac{\mathcal{E}}{-g_{tt}}\right) = -\frac{2\mathcal{E}}{\mathrm{e}^{2\nu}}\left(\nu_{,\rho}u^\rho + \nu_{,z}u^z\right), \tag{14}$$

$$\frac{\mathrm{d}u^\phi}{\mathrm{d}\tau} = \frac{\mathrm{d}}{\mathrm{d}\tau}\left(\frac{\ell}{g_{\phi\phi}}\right) = \frac{2\mathrm{e}^{2\nu}\ell}{\rho^3}\left[\rho\left(\nu_{,\rho}u^\rho + \nu_{,z}u^z\right) - u^\rho\right], \tag{15}$$

$$\frac{\mathrm{d}u^\rho}{\mathrm{d}\tau} = -\frac{\mathcal{E}^2\nu_{,\rho}}{\mathrm{e}^{2\lambda}} + \frac{\ell^2\mathrm{e}^{4\nu}}{\rho^3\mathrm{e}^{2\lambda}}(1-\rho\nu_{,\rho}) + (\nu_{,\rho}-\lambda_{,\rho})[(u^\rho)^2-(u^z)^2] + 2(\nu_{,z}-\lambda_{,z})u^\rho u^z, \tag{16}$$

$$\frac{\mathrm{d}u^z}{\mathrm{d}\tau} = -\frac{\mathcal{E}^2\nu_{,z}}{\mathrm{e}^{2\lambda}} - \frac{\ell^2\mathrm{e}^{4\nu}\nu_{,z}}{\rho^2\mathrm{e}^{2\lambda}} - (\nu_{,z}-\lambda_{,z})[(u^\rho)^2-(u^z)^2] + 2(\nu_{,\rho}-\lambda_{,\rho})u^\rho u^z, \tag{17}$$

where $g_{\mu\nu}$ is the metric tensor, $u^\mu \equiv \frac{\mathrm{d}x^\mu}{\mathrm{d}\tau}$ is the test-particle four-velocity, τ is its proper time and

$$\mathcal{E} \equiv E/m \equiv -u_t = \mathrm{e}^{2\nu}u^t, \quad \ell \equiv L/m \equiv u_\phi = \rho^2\mathrm{e}^{-2\nu}u^\phi$$

are constants of the motion (energy and azimuthal angular momentum per unit mass with respect to an observer staying at rest at spatial infinity). In the vacuum regions (which means everywhere when there are no extended sources), the derivatives of λ can be expressed as

$$\lambda_{,\rho} = \rho(\nu_{,\rho})^2 - \rho(\nu_{,z})^2, \quad \lambda_{,z} = 2\rho\nu_{,\rho}\nu_{,z}$$

from the Einstein field equations. (However, λ itself must in general be found numerically at each point by integrating this gradient.) Both the metric functions are continuous everywhere outside the horizon, they only have a finite jump in normal derivatives on the disc which is given by the 'Newtonian density' of the disc $w(\rho)$ (the one standing in the Poisson equation),

$$\nu_{,z}(\rho, z\to 0^+) = -\nu_{,z}(\rho, z\to 0^-) = 2\pi w(\rho).$$

© 2010 The Authors. Journal compilation © 2010 RAS, MNRAS **404,** 545–574

Note that the equations for u^t and u^ϕ do not contain λ, yet the $(t,\,\phi)$-motion is not fully determined by ν, being coupled to the meridional components u^ρ, u^z which depend on λ explicitly.

The additional-source effect on geodesic motion can be tentatively estimated on effective potential for radial and/or latitudinal motion. From the four-velocity normalization and using the metric (5), one has

$$\mathrm{e}^{2\hat{\lambda}}\left[(u^r)^2 + r(r-2M)(u^\theta)^2\right] = \mathcal{E}^2 - (\mathcal{V}_{\rm eff})^2, \qquad \text{where} \quad (\mathcal{V}_{\rm eff})^2 \equiv \left(1-\frac{2M}{r}\right)\left(1+\frac{\ell^2\mathrm{e}^{2\hat{\nu}}}{r^2\sin^2\theta}\right)\mathrm{e}^{2\hat{\nu}}\,. \tag{18}$$

Above the black hole horizon, the left-hand side is non-negative, so the particle energy $\mathcal{E}$ has to be at least equal to $\mathcal{V}_{\rm eff}$ at a given place.

It is favourable that the effective potential only depends on $\hat{\nu}$ (not on λ). In the equatorial plane ($z=0$), for example, the external gravitational potential reads

$$\hat{\nu}(\rho) \equiv \nu_{\rm BW}(\rho) = -\frac{2\mathcal{M}K\left(\frac{2\sqrt{\rho b}}{\rho+b}\right)}{\pi(\rho+b)} \tag{19}$$

for the Bach–Weyl ring (6), while (Semerák 2003)

$$\hat{\nu}(\rho) \equiv \nu^{(m)}(x=0) = -2^{2m}(m!)^2\frac{2\mathcal{M}}{\pi\rho}\sum_{n=0}^{m}\frac{[(2n)!]^2(m+n)!(4n+1)}{2^{2n}(n!)^4(m-n)!(2m+2n+1)!}\,\mathrm{i}Q_{2n}\left(\mathrm{i}\sqrt{\frac{b^2}{\rho^2}-1}\right) \quad \text{below the rim } (\rho<b), \tag{20}$$

$$\hat{\nu}(\rho) \equiv \nu^{(m)}(y=0) = -2^{2m}(m!)^2\frac{\mathcal{M}}{\rho}\sum_{n=0}^{m}\frac{[(2n)!]^2(m+n)!(4n+1)}{2^{2n}(n!)^4(m-n)!(2m+2n+1)!}\,P_{2n}\left(\sqrt{1-\frac{b^2}{\rho^2}}\right) \quad \text{above the rim } (\rho>b) \tag{21}$$

for the inverted mth Morgan–Morgan disc (10) and (Semerák 2004)

$$\hat{\nu}(\rho) \equiv \nu^{(m,n)}(\rho<b) = -\frac{\left(1+\frac{1}{n}\right)_m}{n}\frac{\mathcal{M}}{b}\sum_{j=0}^{\infty}\frac{[P_{2j}(0)]^2}{\left(\frac{2+2j}{n}\right)_{m+1}}\frac{\rho^{2j}}{b^{2j}} \qquad \text{below the disc rim,} \tag{22}$$

$$\hat{\nu}(\rho) \equiv \nu^{(m,n)}(\rho>b) = -\frac{\left(1+\frac{1}{n}\right)_m}{n}\frac{\mathcal{M}}{\rho}\sum_{j=0}^{\infty}\frac{[P_{2j}(0)]^2}{\left(\frac{1-2j}{n}\right)_{m+1}}\frac{b^{2j}}{\rho^{2j}} \qquad \text{above the disc rim} \tag{23}$$

for the '$(n,\,m)$th' power-law-density disc (n is even) (12, 13). Illustrations of the equatorial effective potential for the fields including Bach–Weyl rings and power-law discs are given in Fig. 2. It is seen that if the external source is sufficiently heavy and compact, there may exist more than one family of unstable and/or stable circular orbits – the orbits going around the black hole alone (staying below the ring/disc) and those skirting both sources. However, the equatorial motion being integrable, its potential provides little clue as to the chaoticity of general geodesics.

The behaviour of the effective potential in the perpendicular, meridional plane can be sketched by drawing there its contour lines, $(\mathcal{V}_{\rm eff})^2(r,\theta;\ell) = \text{constant}$. In Fig. 3, this is done for the angular momenta $\ell = 4M$ and 0.

The potentials simplify most notably on the axis. That of the Bach–Weyl ring reduces just to

$$\hat{\nu}(z) = -\frac{\mathcal{M}}{\sqrt{z^2+b^2}}\,, \tag{24}$$

while the inverted mth Morgan–Morgan disc yields (Semerák 2003)

$$\hat{\nu}(z) = -\frac{2^{2m+1}(m!)^2}{\pi}\frac{\mathcal{M}}{|z|}\sum_{n=0}^{m}C_{2n}^{(m)}\mathrm{i}Q_{2n}\left(\frac{\mathrm{i}b}{|z|}\right) \tag{25}$$

and the $(n,\,m)$th power-law-density disc yields (Semerák 2004)

$$\hat{\nu}(z) = -\frac{\left(1+\frac{1}{n}\right)_m}{m!}\frac{\mathcal{M}}{\sqrt{z^2+b^2}}\sum_{k=0}^{m}\frac{(-1)^k}{kn+2}\binom{m}{k}{}_2F_1\left(\frac{1}{2}\,,1;\,2+\frac{kn}{2};\,\frac{1}{1+b^2/z^2}\right), \tag{26}$$

where ${}_2F_1$ is the Gauss hypergeometric function. The pure axial effective potential (involving $\ell=0$ necessarily) is not very interesting; however, it always grows monotonically to zero when receding from the black hole.

Let us remark that the requirement of stationarity (or even staticity) of self-gravitating sources typically leads to the occurrence of supporting stresses within them. As opposed to Newton's theory, these stresses contribute to gravity in general relativity, which may result in peculiar structure of space–time near the sources. This is most notable in the vicinity of most singular sources. Indeed, the direction-dependent effect of ring sources (even including apparent repulsive features) was noted on geodesics by Semerák, Žáček & Zellerin (1999) and further explored by D'Afonseca et al. (2005).

4.1 Astrophysical motions in black hole and ring/disc fields

Long-term ring/disc structures probably exist around black holes in X-ray binaries and in galactic nuclei. These accretion configurations are usually modelled within the *test* approximation, i.e. their own gravitational effect is neglected. In a 'relativistic' region close to the compact centre, this is almost always apropos as far as *intensity* is concerned, but the additional matter may alter higher derivatives of the field

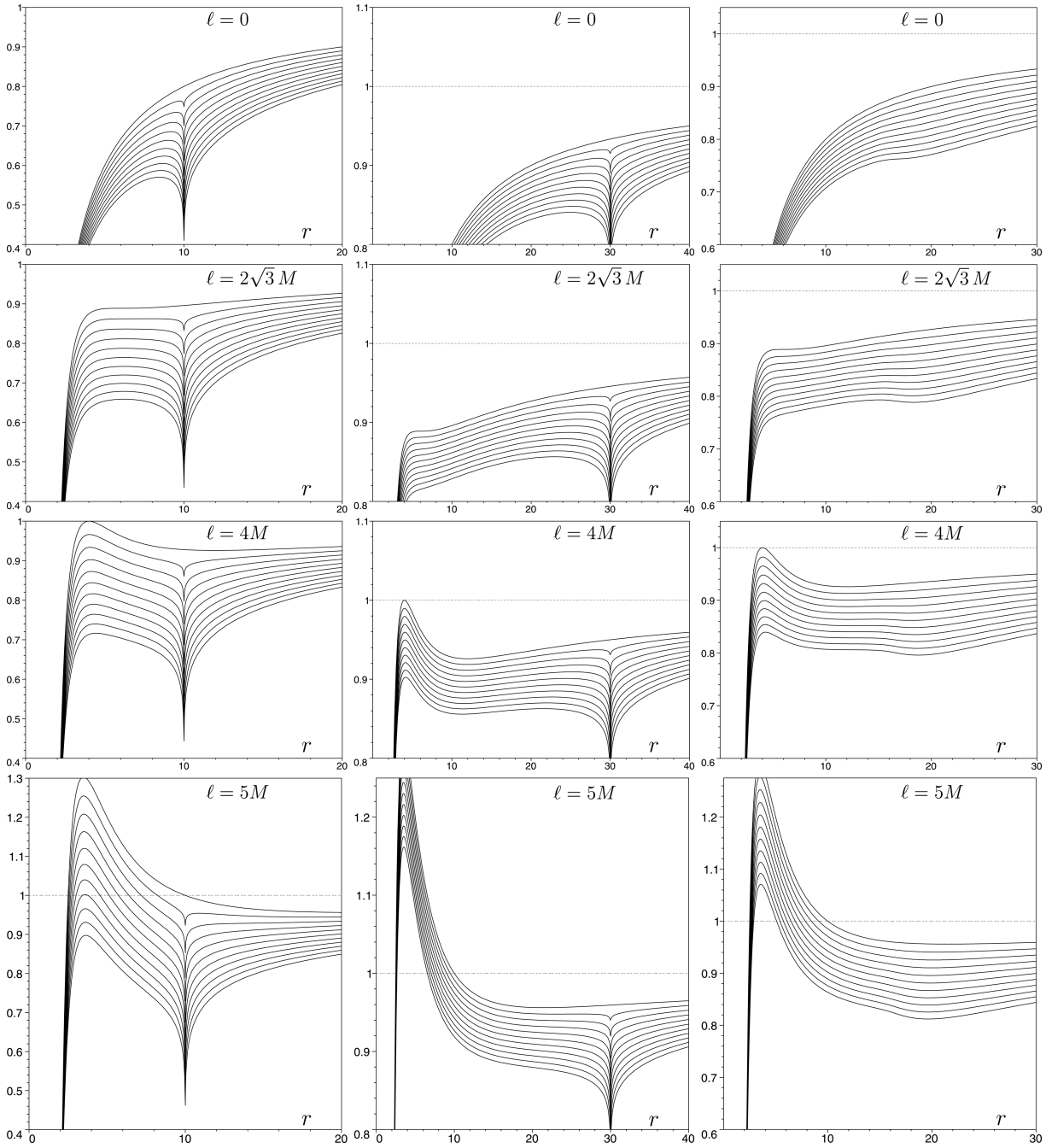


Figure 2. Radial shape of the effective potential squared (18) in the equatorial plane of a Schwarzschild black hole surrounded by a Bach–Weyl ring on Schwarzschild radius $r = 10M$ (left-hand column) and $r = 30M$ (middle column) and by a power-law disc (of $m = 4$, $n = 10$) with Schwarzschild inner radius $r = 15M$ (right-hand column). Relative masses of the ring are $\mathcal{M}/M = 0, 0.1, 0.2, \ldots, 1.0$, while relative masses of the disc are $\mathcal{M}/M = 0, 0.2, 0.4, \ldots, 2.0$ (the curves shift downwards with increasing mass of the additional source; the topmost curves correspond to a pure Schwarzschild black hole). From top to bottom row, the specific angular momentum ℓ is set to $0, 2\sqrt{3}M, 4M$ and $5M$, where M is the black hole mass. Radius is in the units of M; the effective potential is dimensionless (per particle's rest mass). Note that display proportions are only kept fixed within the columns. Basic observations: (i) depending on parameters of the external source, several different configurations of circular orbits are possible; both types of these (unstable and stable) may lie either above or below the source; (ii) the ring being a much 'stronger' (singular) source than the disc, it *always* induces an unstable circular orbit below; (iii) there may exist *two* different unstable circular orbits (and a stable one in between) between the horizon and the ring/disc; a marginal case also exists when the stable and the 'outer' unstable of these orbits coalesce into a marginally stable one.

which – vice versa – determine stability of its configuration. Actually, the most important parameters of the accretion disc like its position and extension may thus be very sensitive to the precise shape of the field which it itself generates. (This issue nicely illustrates the frequently stressed feedback between matter and its field.)

In stellar binaries, however, the accretion structures are supposed to be rather light and the whole accretion system is quite strongly (and non-stationarily) perturbed by the binary companion. Hence, the study of self-gravitating rings or discs – and of the respective perturbed

© 2010 The Authors. Journal compilation © 2010 RAS, MNRAS **404,** 545–574

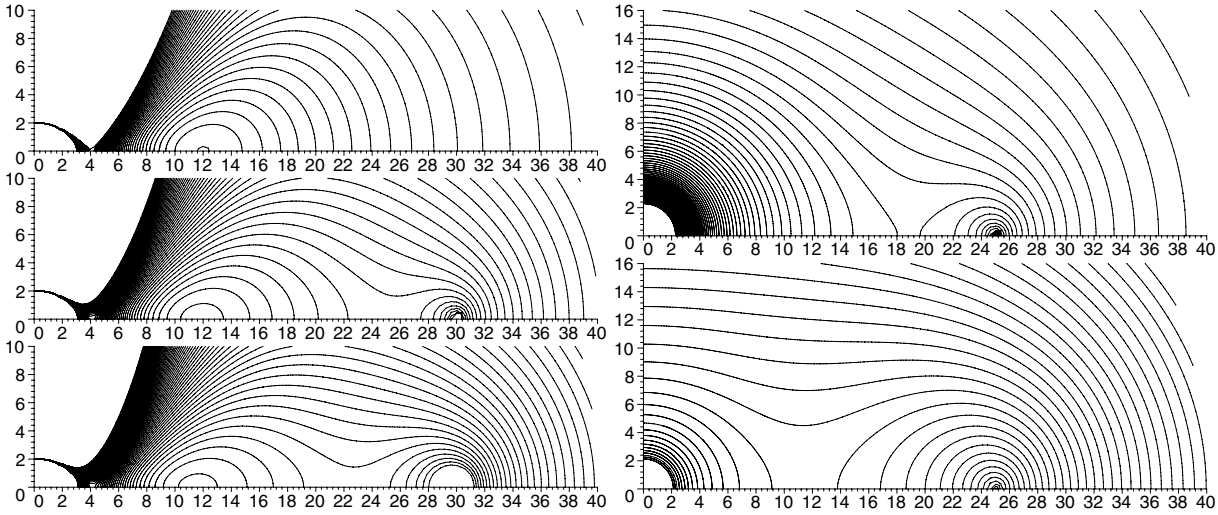


Figure 3. Contour lines of the effective potential squared (18) in the meridional plane ($r\sin\theta$, $r\cos\theta$) of a Schwarzschild black hole surrounded by a Bach–Weyl ring. In the left-hand column, the ring is on Schwarzschild radius $r = 30M$ and has mass $\mathcal{M} = 0, 0.4M, 0.8M$ (from top to bottom); the angular momentum is $\ell = 4M$. In the right-hand column, the ring is on Schwarzschild radius $r = 25M$ and has mass $\mathcal{M} = 2M, 20M$; the angular momentum is $\ell = 0$. (We have chosen such unrealistic values of the ring mass in order to show that even the singular ring has to be *extremely heavy* in order to attract locally as strongly as the hole.) The coordinates are in the units of the black hole mass M.

dynamics – seems to have more relevance for the galactic nuclei. There the black holes are surrounded, in addition to inner accretion discs, by a central star cluster and massive cold tori on a larger radius. The behaviour of central stars, for example, in our Galaxy is not yet fully understood and it is natural to ask about the influence of the other elements on their dynamics. In the first approximation, the torus can be described by a potential of a thin ring, the inner disc by that of an infinitely thin disc and, possibly, the cluster by an additional spherical term. In this paper, we will thus be interested in motions of free test particles (stars) below and above the radius of the ring/disc and monitor, in particular, whether their orbital parameters cannot change significantly over the long time-spans. When the 'star' passes through the equatorial plane above the disc's inner radius, it would be also affected by the disc *mechanically*, but we do not try to model this interaction here (only the *gravitational* effect is taken into account). This complements the approach of Vokrouhlický & Karas (1998) who considered the Newtonian description, while *taking* the mechanical interaction into account.

Let us stress, however, that we try to get a first idea about the system here, not to model any actual astrophysical situation. Namely, in scanning through the phase space, the ranges of parameters are not necessarily limited to 'realistic' values.

5 POINCARÉ SECTIONS

It can be expected that the originally regular, Schwarzschild geodesic dynamics will gradually grow chaotic when increasing the external-source (ring or disc) mass. We will begin the study of the system by plotting the Poincaré sections. Actually, the $(t, \phi; u^t, u^\phi)$ phase subspace being completely regular due to the conservation of u_t and u_ϕ, the motion is only 'non-trivial' in the $(\rho, z; u^\rho, u^z)$ subspace. Because of the four-velocity normalization

$$-1 = g^{\alpha\beta}u_\alpha u_\beta = -\mathrm{e}^{-2\nu}\mathcal{E}^2 + \mathrm{e}^{2\nu}\frac{\ell^2}{\rho^2} + \mathrm{e}^{2\lambda-2\nu}[(u^\rho)^2 + (u^z)^2],$$

it is confined to a three-dimensional hypersurface there. This corresponds to a system with two-dimensional Hamiltonian. In such a case, the phase-space layers with regular and stochastic motion are neighbours of each other (along KAM surfaces) and Poincaré sections are an appropriate and well-tried method of how to study their arrangement. (In higher dimensional systems, the stochastic layers form a dense web that approaches arbitrarily close to any regular orbit.)

In a stationary, axially symmetric and reflectionally symmetric field, it is natural to choose the equatorial plane ($z = 0$) as a section on which the passages of orbits will be recorded (namely the radius and the radial component of four-velocity are usually registered). Orbits with $\ell = 0$ may also be registered on the symmetry axis. Each individual Poincaré section will show passages of a set of particles with given energy and azimuthal angular momentum (given $\mathcal{E}$ and ℓ).[7]

[7]When deciding the way of choosing the initial conditions, the question always arises of what trajectories 'go together'. This surely depends on the problem solved, but one usually has two major possibilities of how to define the given set of trajectories – by fixing either their 'local', or 'global' parameters. When studying space–time motion, the 'local' choice (launching the particles with given velocity in various directions, as measured by a local physical observer) usually feels more physical, because it more closely resembles the actual astrophysical processes and does not rely on quantities referring to conditions that might nowhere occur along the trajectories (e.g. like referring to 'infinity'). However, the problem of regular/chaotic dynamics is tightly connected with the existence and values of integrals of motion, so we will adhere to these 'global' quantities in assigning the initial conditions. Fixing such 'global' parameters also more probably confines the orbits to similar regions in phase space, which makes the comparison of their long-term evolution easier.

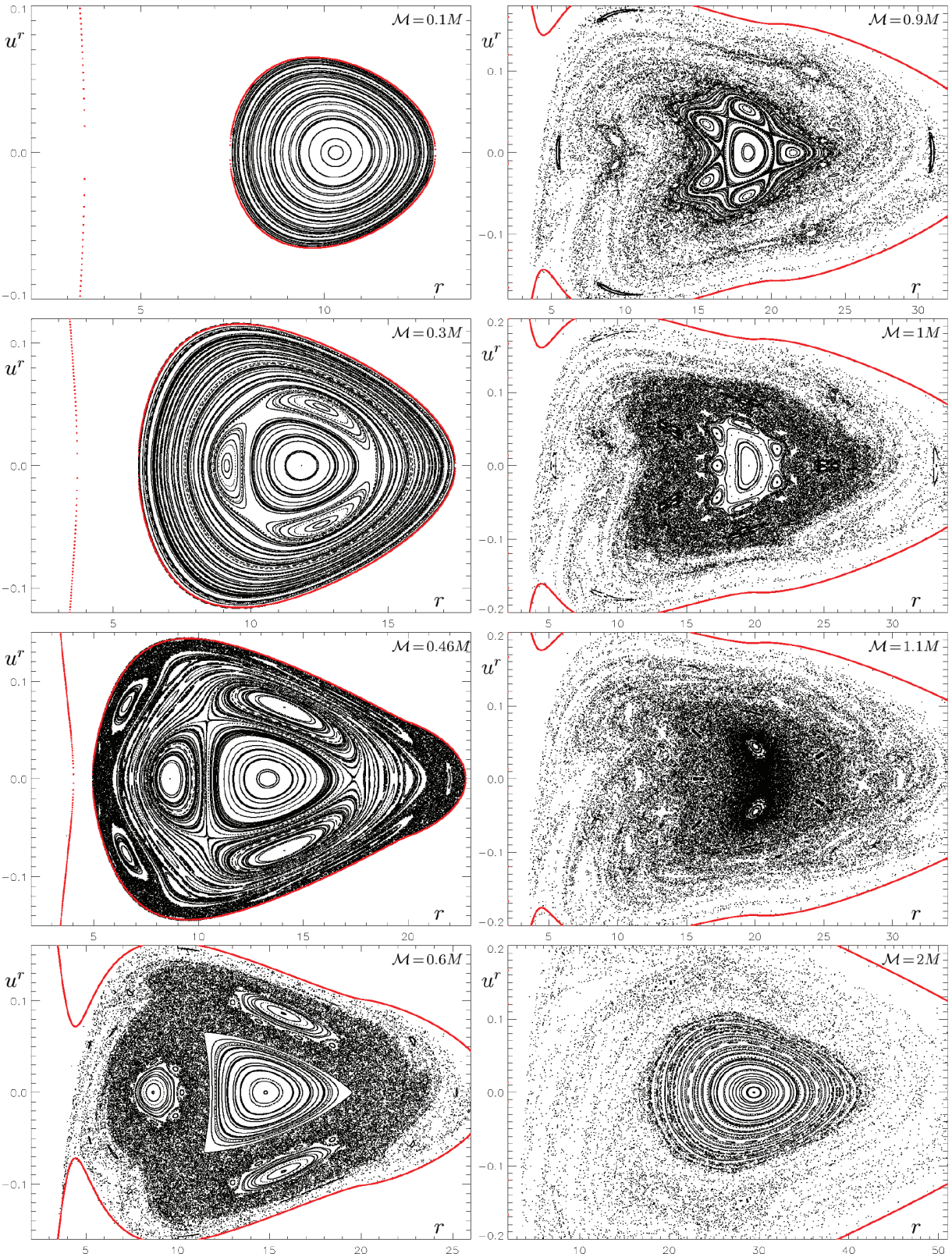


Figure 4. Geodesic dynamics in the field of a Schwarzschild black hole surrounded by the inverted first Morgan–Morgan disc (with radius $r_{\rm disc} = 20M$): dependence on relative disc mass $\mathcal{M}/M$ (its value is indicated in the plots). Passages of orbits with $\ell = 3.75M$, $\mathcal{E} = 0.955$ through the equatorial plane are drawn. The boundary of the accessible region of phase space is indicated in red (this applies to all figures).

© 2010 The Authors. Journal compilation © 2010 RAS, MNRAS **404,** 545–574

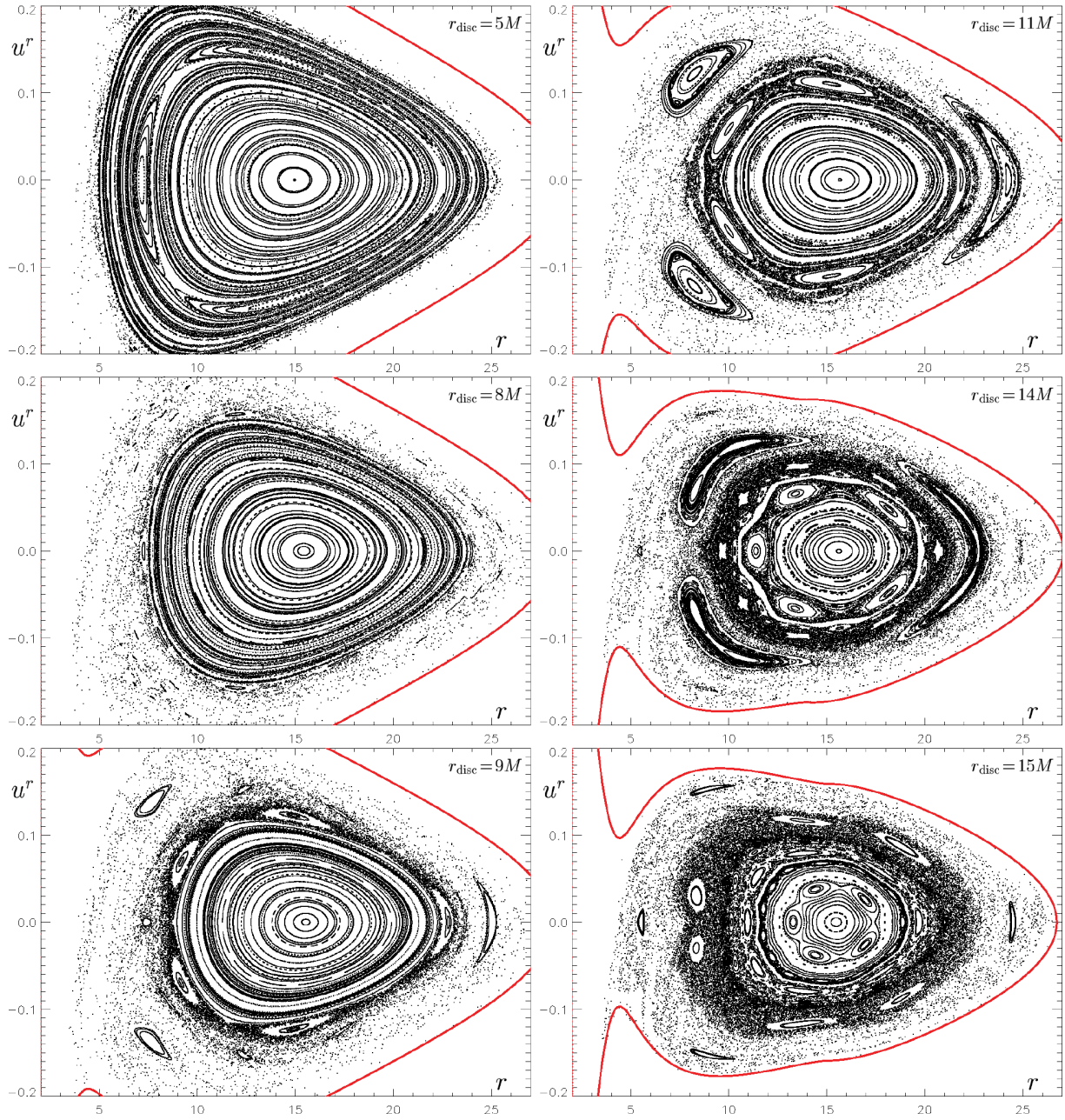


Figure 5. Geodesic dynamics in the field of a Schwarzschild black hole surrounded by the inverted first Morgan–Morgan disc (with mass $\mathcal{M} = 0.5M$): dependence on disc inner radius $r_{\rm disc}$ (its value is indicated in the plots). Passages of orbits with $\ell = 3.75M$, $\mathcal{E} = 0.955$ through the equatorial plane are drawn. The figure continues on the next page.

The existence and nature of the constants of motion imply that certain subsets of geodesics will remain regular, whether the additional source is present or not. Specifically, $\mathcal{E}$ is purely connected with u^t and ℓ with u^ϕ, plus there is the four-velocity normalization, so the regularity applies to the geodesics lying fully within the three-dimensional world sheets spanned by t, ϕ and one of the meridional coordinates. For our systems, this factually means the geodesics bound to the equatorial plane ($z = 0$, $u^z = 0$): due to the reflectional symmetry, $u^z = 0$ is their fourth integral of motion.

We will study, on Poincaré sections, the change of time-like geodesic structure in dependence (i) on relative mass and position of the external ring/disc and (ii) on constants of the geodesic motion (namely energy; the dependence on angular momentum is less intriguing). The geodesics are computed using the (adjusted) program written by M. Žáček for our earlier paper (Semerák et al. 1999) where the motion of free test particles was followed in similar fields to those we deal with here. In all figures, a set of several hundreds of particles is launched from a certain region of relevant radii in the equatorial plane, with given $\mathcal{E}$ and ℓ (which determine u^t and u^ϕ, respectively), with several different values of u^r within the local light cone and u^θ components fixed accordingly from the four-velocity normalization. In most plots, the particles are followed for about $150\,000M$–$250\,000M$ of proper time; this usually corresponds to some 200–1000 orbital periods, i.e. to 400–2000 recorded points (since our section $z = 0$ is the plane of symmetry, we can register passages in both directions).

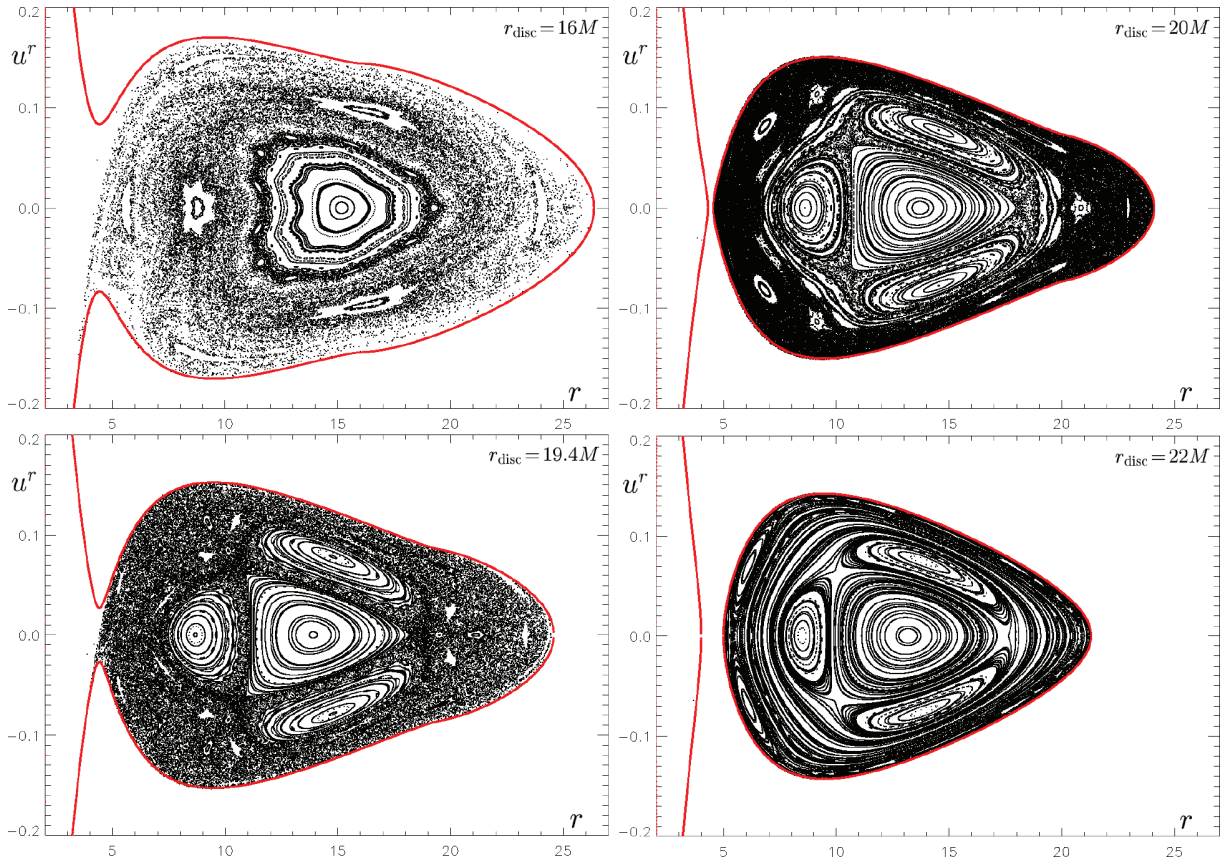


Figure 5 – *continued*

Let us note that there is no point in specifying the initial conditions and evolution of individual orbits precisely, because the figures cannot be compared 'invariantly' anyway: they correspond to different space–time backgrounds (this applies to sequences showing dependence on $\mathcal{M}$ and on $r_{\rm in}$) or at least to different regions of permitted $u^r(r)$ (as in sequences showing dependence on $\mathcal{E}$). This also implies that the plots naturally do not represent the same number of particles or the same average 'density' of crossings. In particular, those with the permitted (r, u^r)-region opened towards the horizon tend to be more 'diluted' due to the escape of particles into a black hole.

The geodesic dynamics of perturbed systems is usually rather complicated and one has to look through many Poincaré sections in order to catch its evolution with the parameters. Even a single section is often quite rich and requires enough space in order to be represented properly. We hope the following groupings of plots are a reasonable compromise between providing accurate information and keeping the paper tolerably long.

Figs 4–6 concern the space–time of a Schwarzschild black hole surrounded by the inverted first Morgan–Morgan disc; they illustrate the dependence of geodesic dynamics on relative mass of the disc $\mathcal{M}/M$, on its inner radius $r_{\rm disc}$ and on energy of the geodesics $\mathcal{E}$, respectively. For comparison with different discs, Figs 7 and 8 show the dependence on $\mathcal{M}/M$ and $r_{\rm disc}$ for the Schwarzschild black hole surrounded by the inverted fourth Morgan–Morgan disc, and Fig. 9 shows the dependence on $\mathcal{M}/M$ for the hole with the ($n = 4$, $m = 4$) power-law-density disc. Finally, Figs 10–12 provide the same kind of information for fields involving the most concentrated, singular external source – the Bach–Weyl ring. In all the figures, the Schwarzschild radius r is given along the horizontal axis in units of the black hole mass M. The boundary of the accessible region of phase space is indicated in red.

The presented sequences of plots can be best annotated by a quotation from the introduction of the book by Lichtenberg & Lieberman (1992). When describing the phase-space portrait of nearly integrable systems and KAM theory, the authors write: 'The invariant surfaces break their topology near resonances to form island chains. Within these islands, the topology is again broken to form yet other chains of still finer islands. On ever finer scale, one sees islands within islands. But this structure is only part of the picture, for densely interwoven within these invariant structures are thin phase space layers in which the motion is stochastic.' (It should be remarked, however, that the KAM theory usually assumes a continuous force field, which is not satisfied along orbits crossing the disc.)

We do not present any systematic comparison of different additional sources or a thorough account of dependences on parameters here; the selected figures should just illustrate overall tendencies. Although they clearly contain a number of interesting details, it would be too lengthy to take note of them individually. Therefore, let us only mention rather generic observations.

(i) Dependence on angular momentum. Larger angular momentum means larger part of (some given) energy allotted to azimuthal motion. This component of motion is 'held' by the conserved value of ℓ, however, so larger angular momentum favours regularity. Larger ℓ also

© 2010 The Authors. Journal compilation © 2010 RAS, MNRAS **404,** 545–574

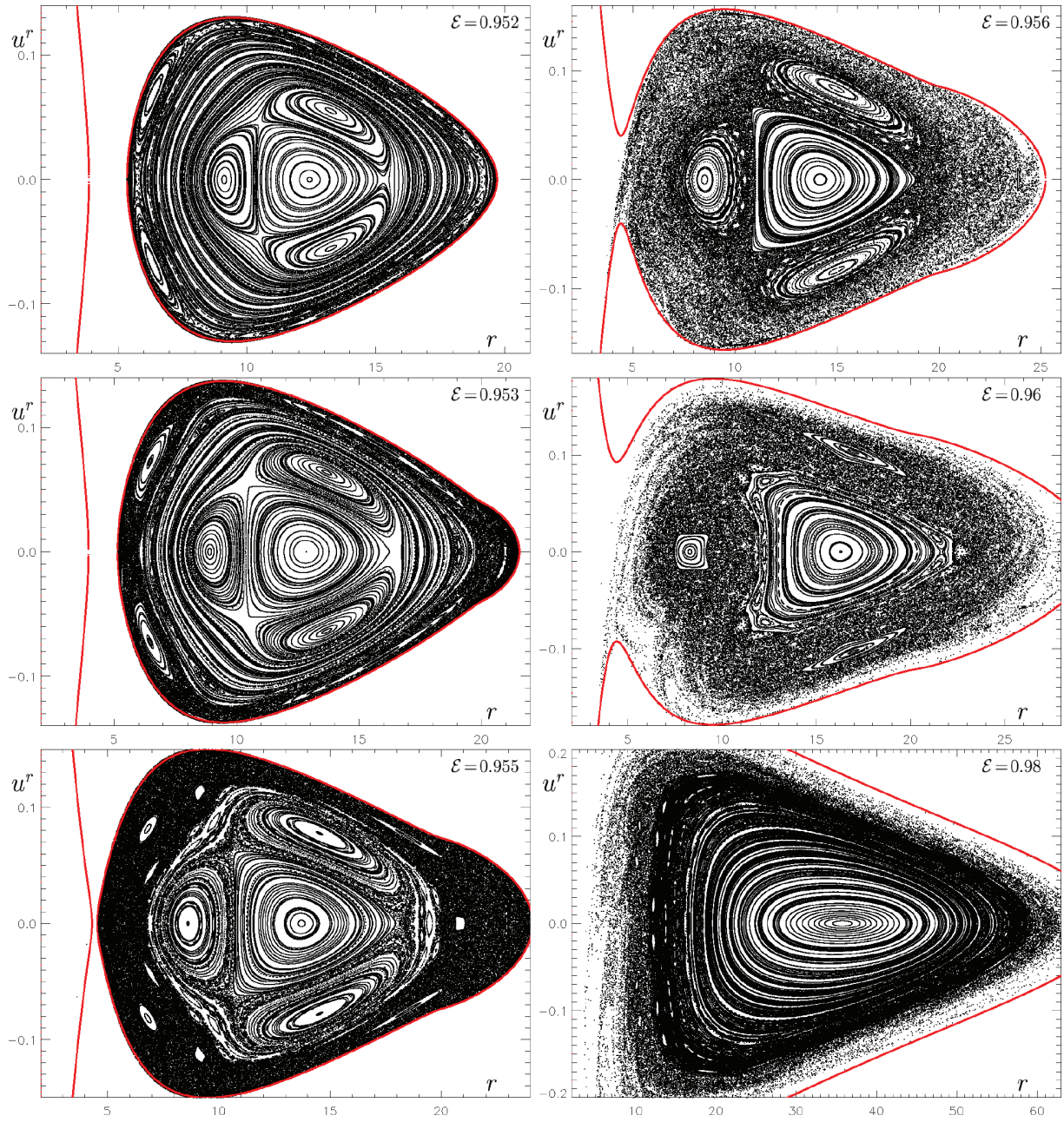


Figure 6. Geodesic dynamics in the field of a Schwarzschild black hole surrounded by the inverted first Morgan–Morgan disc (with $\mathcal{M} = 0.5M$, $r_{\rm disc} = 20M$): dependence on orbital energy at infinity $\mathcal{E}$ (its value is indicated in the plots). Passages of orbits with $\ell = 3.75M$ through the equatorial plane are drawn.

means higher centrifugal barrier around the black hole; for a certain value of ℓ, the barrier even prevents the particles from falling into a hole. This is advantageous for the present study since the particles then do not 'drop out' of the phase space and can be followed for a sufficient number of orbital periods. (The dependence on ℓ is otherwise not so interesting and we do not focus on it. When exploring the dependence on other parameters, we mostly choose $\ell = 3.75M$.)

(ii) Dependence on energy. The picture begins with one regular island around an orbit with periodicity $k = 1$. With increasing energy, the primary island enlarges and shifts to higher radii, smaller islands of higher periodic orbits arise within it and stochastic layers gradually develop from separatrices around them (mainly from the latter's vertices, i.e. hyperbolic points of the KAM theory, and near the boundary of the accessible region first). Stochastic layers tend to coalesce and form a 'chaotic sea' while smaller islands of higher and higher resonances emerge (and often disappear again). At certain phase, the picture is rather complicated, containing both the residues of regular islands of various sizes, narrow stochastic layers of 'almost regular' trajectories (which remain very close to some regular orbit for a long time, while only slightly changing their action) and also a large 'chaotic sea' of orbits with strongly variable action (usually spread from the boundaries of the phase-space region accessible to the particles with given constants of motion). For large energies, the higher resonance islands continue to shrink towards the margin of the accessible zone, but the primary island begins to grow back and finally occupies almost all phase space

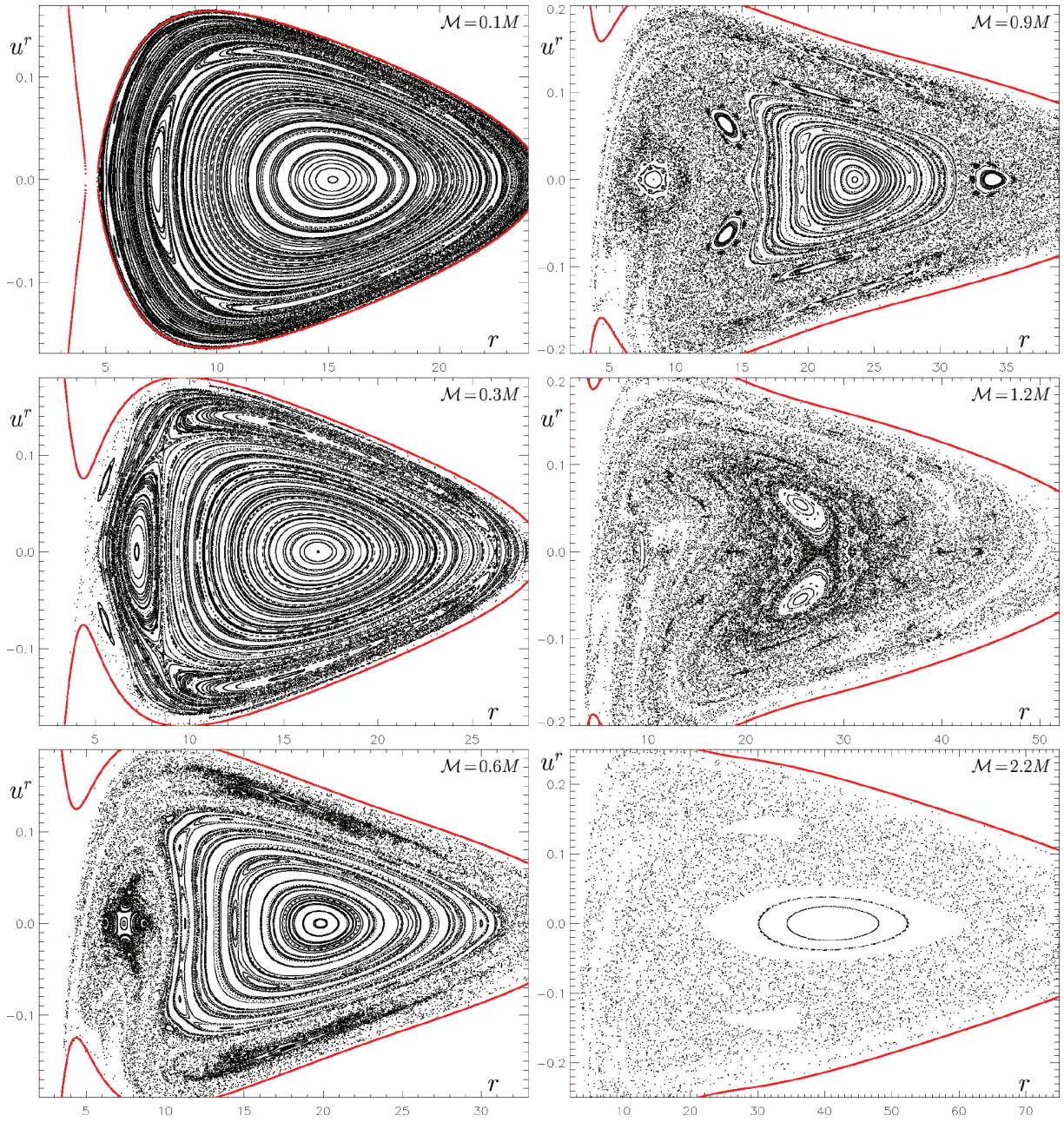


Figure 7. Geodesic dynamics in the field of a Schwarzschild black hole surrounded by the inverted forth Morgan–Morgan disc (with $r_{\rm disc} = 20M$): dependence on relative disc mass $\mathcal{M}/M$ (its value is indicated in the plots). Passages of orbits with $\ell = 3.75M$, $\mathcal{E} = 0.968$ through the equatorial plane are drawn.

again. This is also connected with the evolution of the accessible region (its boundaries are indicated in red in the figures). For small energies, it typically consists of two parts, one just above the horizon and the second below (and/or around) the external source. With increasing energy, the two lobes get closer and finally join, permitting the particles to fall below the horizon. This effectively drains the chaotic particles (the most eccentric ones) from the system.

(iii) Dependence on mass of the additional source (strength of the perturbation). The behaviour is similar to the dependence on energy: with increasing relative mass, higher and higher resonances gradually appear, release into a developing chaotic sea and shrink towards the boundary of the accessible zone. The degree of chaoticity is highest when the masses of both sources are comparable. (Even the $k = 1$ orbit may become unstable and its island may break up, giving way to chaos in the central region.) When the total gravity of the external source prevails, however, the system rather inclines back to regularity – the central 'circular' orbit again turns stable and its island gradually spreads out.

(iv) Dependence on position of the additional source. The position of the ring/disc may affect the total potential even more than the external-source mass and this also reflects on geodesics. When the source is very close to the hole, it does not 'develop' its own potential minimum with 'its own' periodic orbits (unless it is extremely massive), so the dynamics remains almost regular (the particles only feel

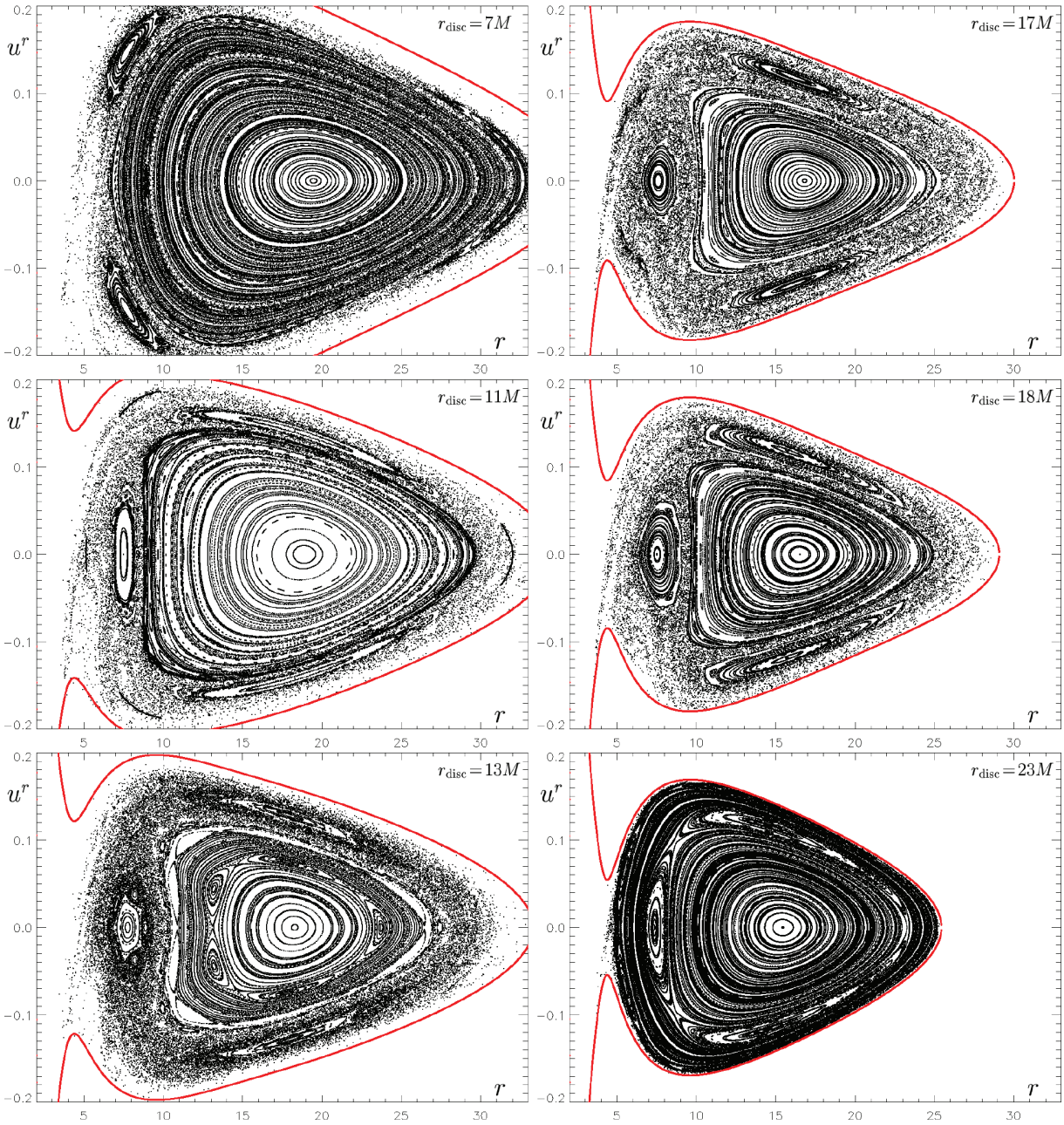


Figure 8. Geodesic dynamics in the field of a Schwarzschild black hole surrounded by the inverted forth Morgan–Morgan disc (with $\mathcal{M} = 0.5M$): dependence on disc inner radius $r_{\rm disc}$ (its value is indicated in the plots). Passages of orbits with $\ell = 3.75M$, $\mathcal{E} = 0.964$ through the equatorial plane are drawn.

the centre to be heavier). Shifting the source farther from the hole, the potential valleys with periodic orbits originate. Their islands and separatrices evolve in a complicated manner, making way to stochastic layers and arising again elsewhere. However, when the ring/disc is above some radius, the chaotic orbits begin to gather into narrow belts again, invariant curves finally emerge and form a primary and the higher islands, gradually spreading towards the margins of the accessible region.

Several more general points are as follows.

(i) A more compact source perturbs the dynamics more. The Poincaré section series thus reveals slower evolution with parameters for sources that are more 'diffuse'. Of the discs considered here, the inverted first Morgan–Morgan disc is more compact than the fourth, the power-law disc ($n = 4, m = 4$) being quite similar to the latter. The Bach–Weyl ring is of course the most compact perturbation and deserves a separate comment. The ring being singular, it *always* has a certain potential valley of its own where particles may evolve without passing over to the black hole sphere of influence. In this region surrounding the ring, the phase-space structures behave similarly as we described above, in particular the geodesic motion may become chaotic there to a large measure. At the same time, a completely regular closed region may exist around a potential minimum between the hole and the ring – see e.g. Fig. 11. (In our figure series, the accessible lobes are mostly joined,

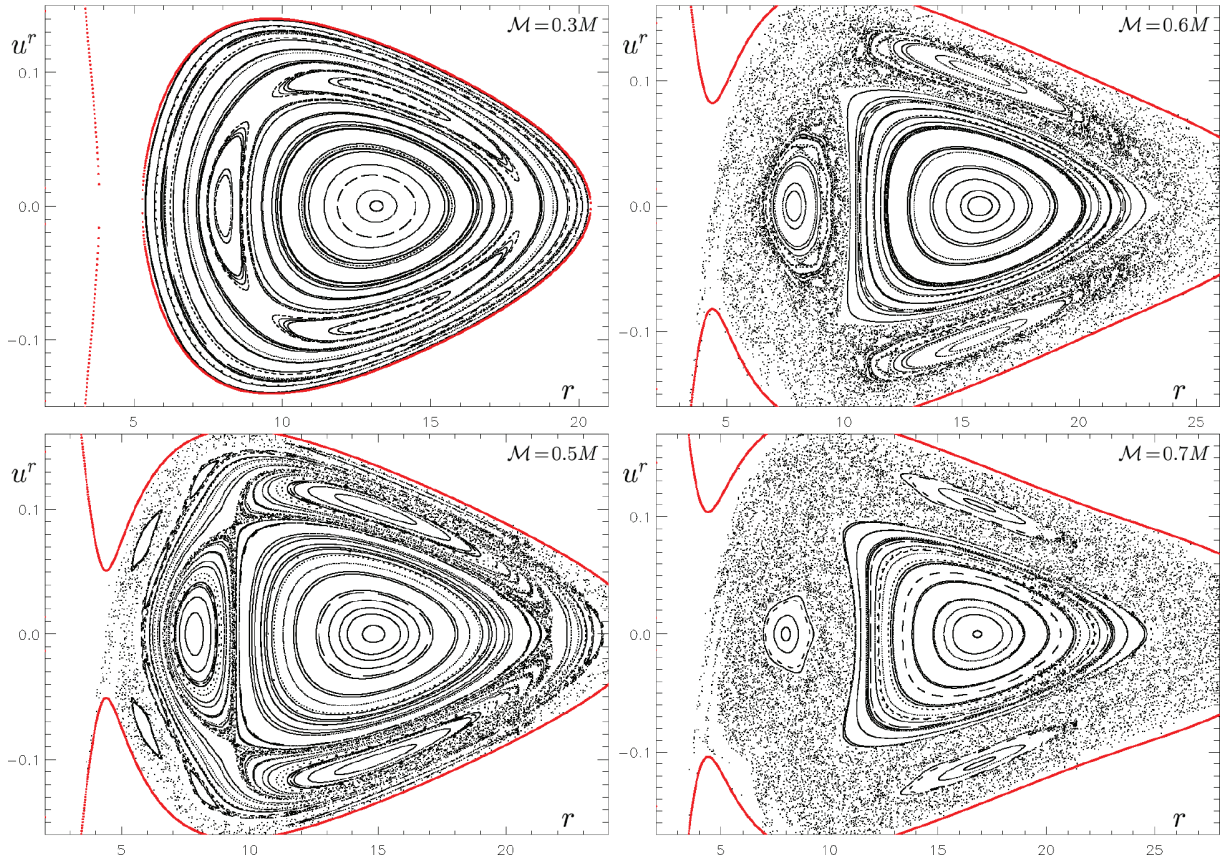


Figure 9. Geodesic dynamics in the field of a Schwarzschild black hole surrounded by the $(n = 4, m = 4)$ power-law-density disc (with $r_{\rm disc} = 20M$): dependence on relative disc mass $\mathcal{M}/M$ (its value is indicated in the plots). Passages of orbits with $\ell = 3.75M$, $\mathcal{E} = 0.96$ through the equatorial plane are drawn.

however.) The figures show that the hole–ring phase portrait is extremely rich and very strongly dependent on the parameters. Although the overall tendencies are similar to those observed with discs, there are much more and distinct higher resonances, already occurring at lower values of the parameters. For instance, the ring of mass $\mathcal{M} = 0.001M$ already induces a considerable perturbation of the phase pattern in almost the whole volume of the accessible zone (cf. Fig. 10). However, no chaotic sea is formed until values around $\mathcal{M} = 0.1M$; the numerous regular islands and chaotic layers remain densely interwoven.

(ii) The dynamics does not respond to the change of perturbation parameters in a 'monotonic' (and by no means 'linear') way. Within some intervals of the parameter space just minor quantitative changes occur, whereas elsewhere the picture 'quickly' alters considerably (regularity islands suddenly disappear, sometimes arising in a totally different arrangement in a moment, indicating change in orbital periodicity. (A similar remark may even apply to one single trajectory in one single background – see Section 6).

(iii) When increasing a given parameter, one often notes *several* periods of prevailing regularity and several rather stochastic ones; however, the dynamics typically inclines to regularity for *both very small and very large* values of the parameters. [This behaviour has also been observed in other systems – cf. Stránský, Kurian & Cejnar (2006), for example.]

(iv) For our gravitational systems, the geodesic dynamics rather tends to 'break up' from the boundaries of the accessible phase-space region, while a certain regular region mostly (though not always) survives in the interior.

(v) The Poincaré sections are generally not symmetrical with respect to $u^r = 0$. This specifically applies to those cases where the accessible region of phase space is open towards the black hole. Namely the asymmetry is due to the particles that fall into the hole (note, in those cases, the excess of dots with $u^r < 0$ at low radii); these are not necessarily balanced by counterparts that would be launched outwards from near the horizon.

(vi) We also drew several axial sections $\theta = 0$ for orbits with zero angular momentum, but these are not presented here.

5.1 A comment on numerics

We solve the geodesic-equation system (14)–(17) by the Runge–Kutta (actually the Hut'a) sixth-order method with variable proper-time step, on the cluster Tiger operated at the Astronomical Institute of our university. The numerical and computational demands strongly depend on specific space–time background. The case with the Bach–Weyl ring and with the first inverted Morgan–Morgan disc can be integrated quite fast and with high precision – constants of the motion and four-velocity normalization are conserved there with relative error 10^{-14} or less.

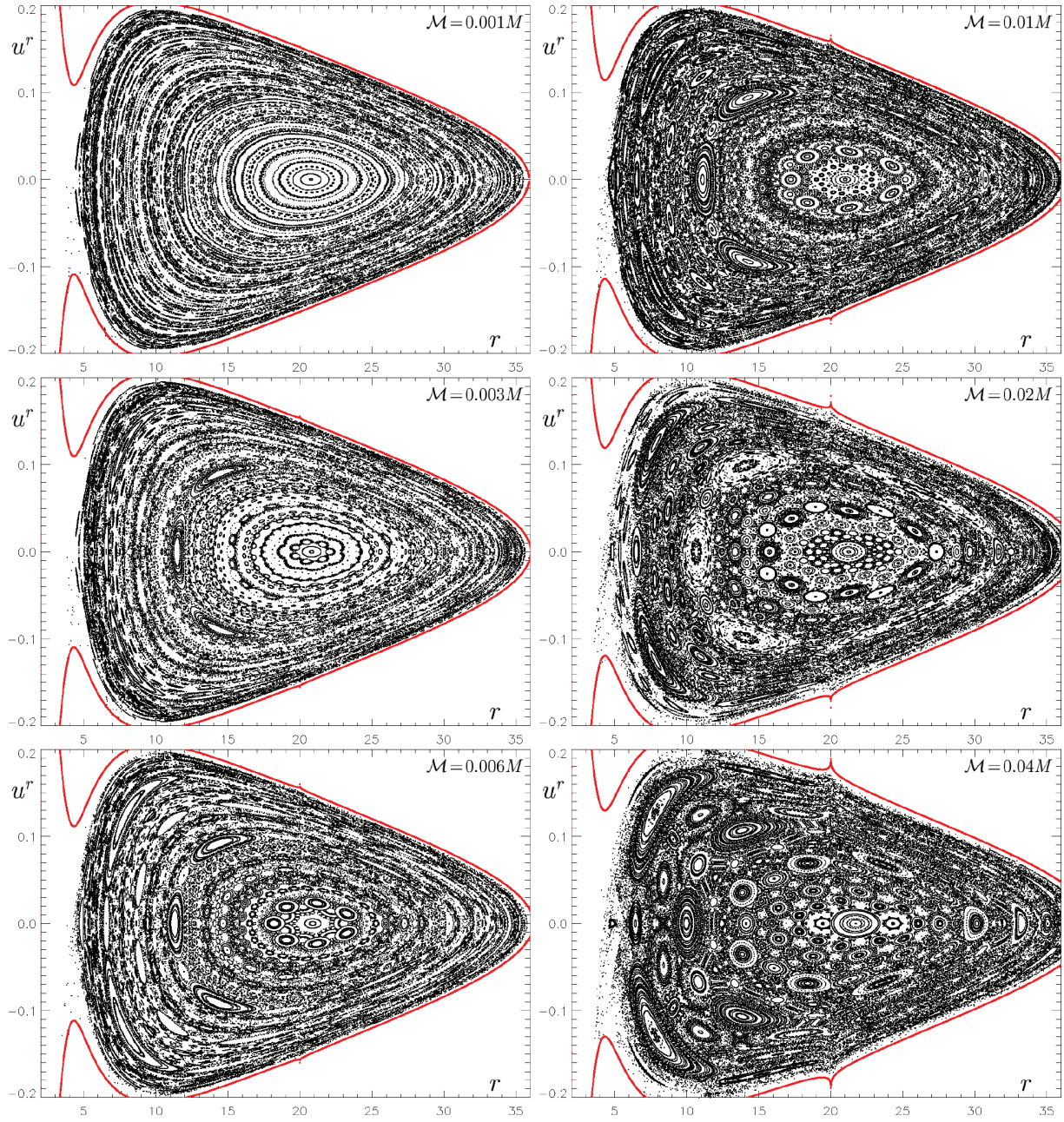


Figure 10. Geodesic dynamics in the field of a Schwarzschild black hole surrounded by the Bach–Weyl ring (with radius $r_{\rm ring} = 20M$): dependence on relative ring mass $\mathcal{M}/M$ (its value is indicated in the plots). Passages of orbits with $\ell = 3.75M$, $\mathcal{E} = 0.977$ through the equatorial plane are drawn. The figure continues on the next page.

For the fourth inverted Morgan–Morgan disc, the error is about an order larger. For the power-law-density disc, the computation takes about 30 times longer than with the previous sources and the error is larger, about 10^{-10} (which is not always sufficient as seen in Fig. 9: contours within the regular regions often get blurred there at places where the phase space is more 'dense'). This is because its potential is given by an infinite sum of Legendre polynomials, namely (12) or (13): the latter converge rather slowly and have to be cut somewhere. In the code, we add up all terms that are greater then 10^{-13} in both the sums. Here, we mean the sums themselves, without the coefficients in front. (For the particular disc we consider, i.e. $n = 4$, $m = 4$, the front coefficient $\frac{(1+\frac{1}{n})_m}{n}\frac{\mathcal{M}}{b}$ is approximately $9.7\mathcal{M}/b$ which is typically of the order of 0.01–1.) For comparison, at the location of the worst behaviour, $\sqrt{\rho^2+z^2} \simeq b$, the magnitude of the leading ($j = 0$) term of the sums is about 0.034. Trying to estimate the tendency of farther terms, one finds that on the axis ($\rho = 0$) at $|z| = b$, the jth term of the sum (12) reads $[(\frac{2+2j}{n})_{m+1}]^{-1}\frac{(-1)^j(2j)!}{2^{2j}(j!)^2}$; for $n = 4$, $m = 4$, this falls off as $\sim j^{-11/2}$ at large values of j. (We note in passing that 388 terms have to be summed there according to our 10^{-13} criterion; close to the disc, even more of them may be necessary. On the other hand, in regions farther from the $\sqrt{\rho^2+z^2} \simeq b$ interface, several tens of terms usually suffice.)

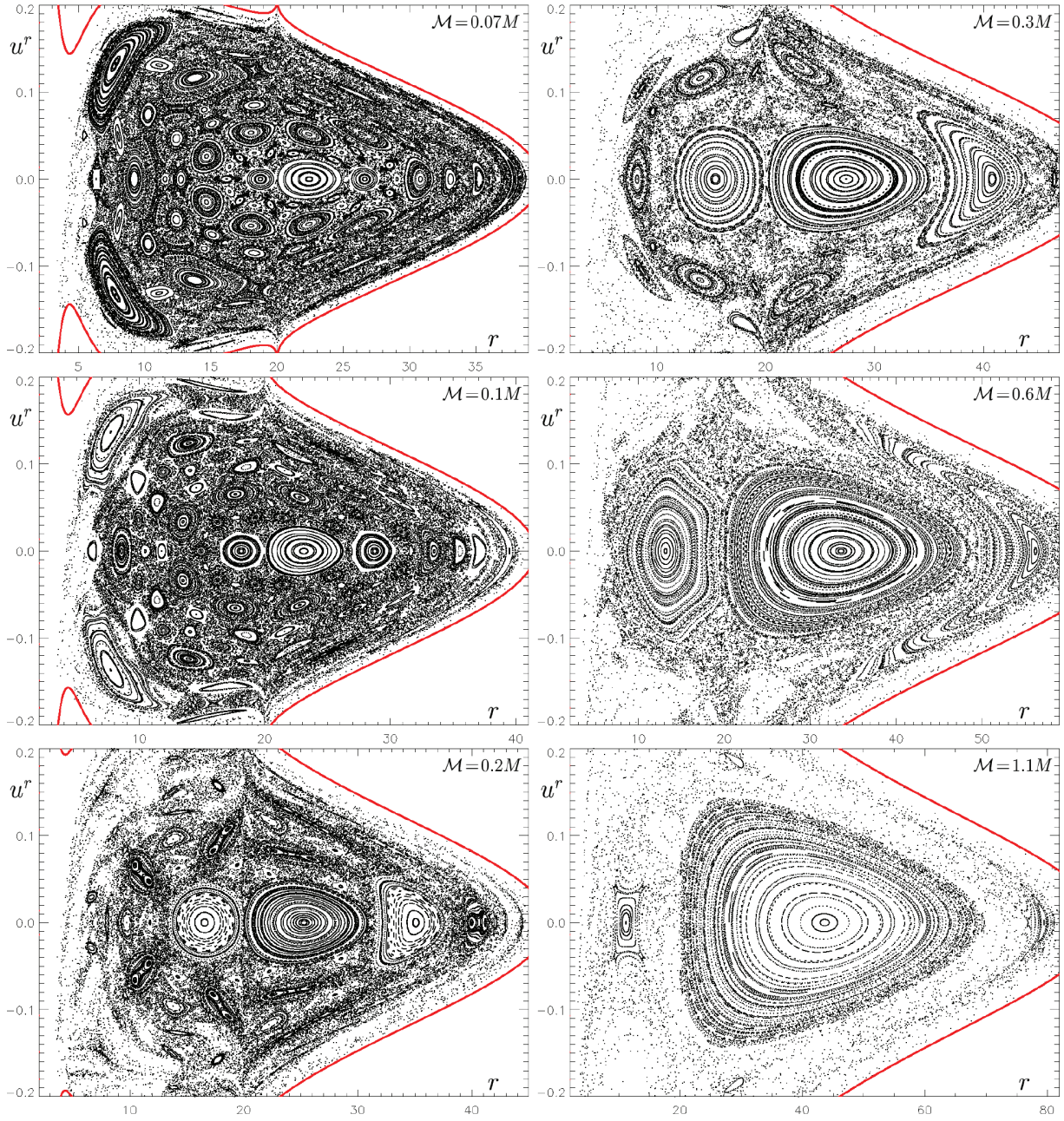


Figure 10 – *continued*

Finally, let us add that the numerical integration is not accurate close to the horizon (regardless the type of the external source): note that some of the particles plunging into the hole got *beyond* the boundary of the accessible zone.

6 TIME SERIES AND THEIR FOURIER SPECTRA

'Chaoticity' of the system may surface in many respects. Its various characteristics tend to evolve in a more 'random' way when they are not bound by a sufficient number of isolating integrals. One simple test is thus to plot the time series of selected quantities and their Fourier spectra. For 'chaotic' systems, one expects the series to exhibit more randomness and the spectra to contain more 'lower harmonics' (possibly even blurred clusters of frequencies). We have picked the radial velocity and vertical position, and also the particle's 'latitudinal action', obtained by averaging the latitudinal four-velocity over an orbital period. (For these purposes, we followed the geodesics for a longer span, up to a coordinate time of about $10^6 M$ which typically corresponds to several thousand orbital periods.)

The easiest time series are those of phase variables. We have plotted the vertical position z and the radial velocity u^r plus their Fourier spectra for several orbits encountered in the previous (*Poincaré*) section. (We show only the z behaviour here, but the u^r series behave similarly.) In Fig. 13, we pick two orbits around a black hole with the inverted first Morgan–Morgan disc and plot their spatial traces,

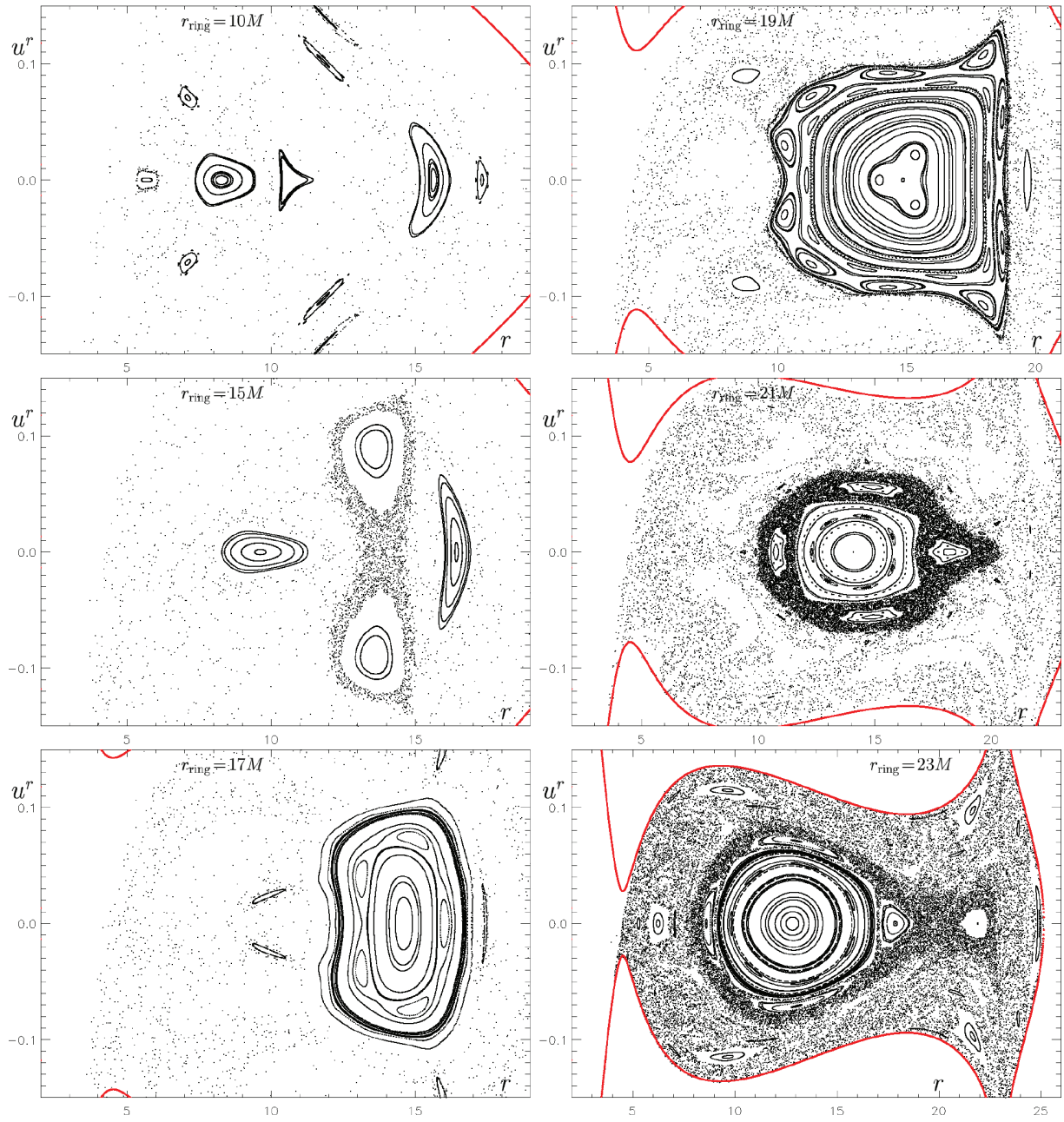


Figure 11. Geodesic dynamics in the field of a Schwarzschild black hole surrounded by the Bach–Weyl ring (with mass $\mathcal{M} = 0.5M$): dependence on ring radius $r_{\rm ring}$ (its value is indicated in the plots). Passages of orbits with $\ell = 3.75M$, $\mathcal{E} = 0.94$ through the equatorial plane are drawn. The figure continues on the next page.

Poincaré sections, time series of their z position and the latter's Fourier spectra. For the regular orbit (which produces smooth curves on Poincaré surfaces), the time series follows regular oscillations, its Fourier spectrum only contains several distinctive peaks and goes over to nearly constant function at low frequencies. A chaotic orbit (which produces densely dotted, 'stochastic' layers on Poincaré surfaces), on the other hand, corresponds to a complicated, inharmonic time series and fuzzy Fourier spectrum spanning 'all' frequencies including the low ones. The irregularity of evolution can be seen at various scales, it need not be only 'local' – from time to time, the orbital parameters may 'suddenly' change substantially and then calm down again for a longer period. This type of behaviour is very important for the evolution of astrophysical systems (it is known from backtracking of the Solar system history, for example).

Koyama et al. (2007) found, in studying the dynamics of spin particles in the Schwarzschild field, that two cases can be further distinguished within irregular orbits according to the low-frequency shape of their time-series spectra. The 'highly chaotic' orbits (filling a large area – the 'chaotic sea' – in Poincaré sections) show 'white noise' there, i.e. noise with a relatively low and approximately constant mean value. On the other hand, the 'less chaotic' orbits (filling just narrow chaotic layers, namely confined to the vicinity of regular

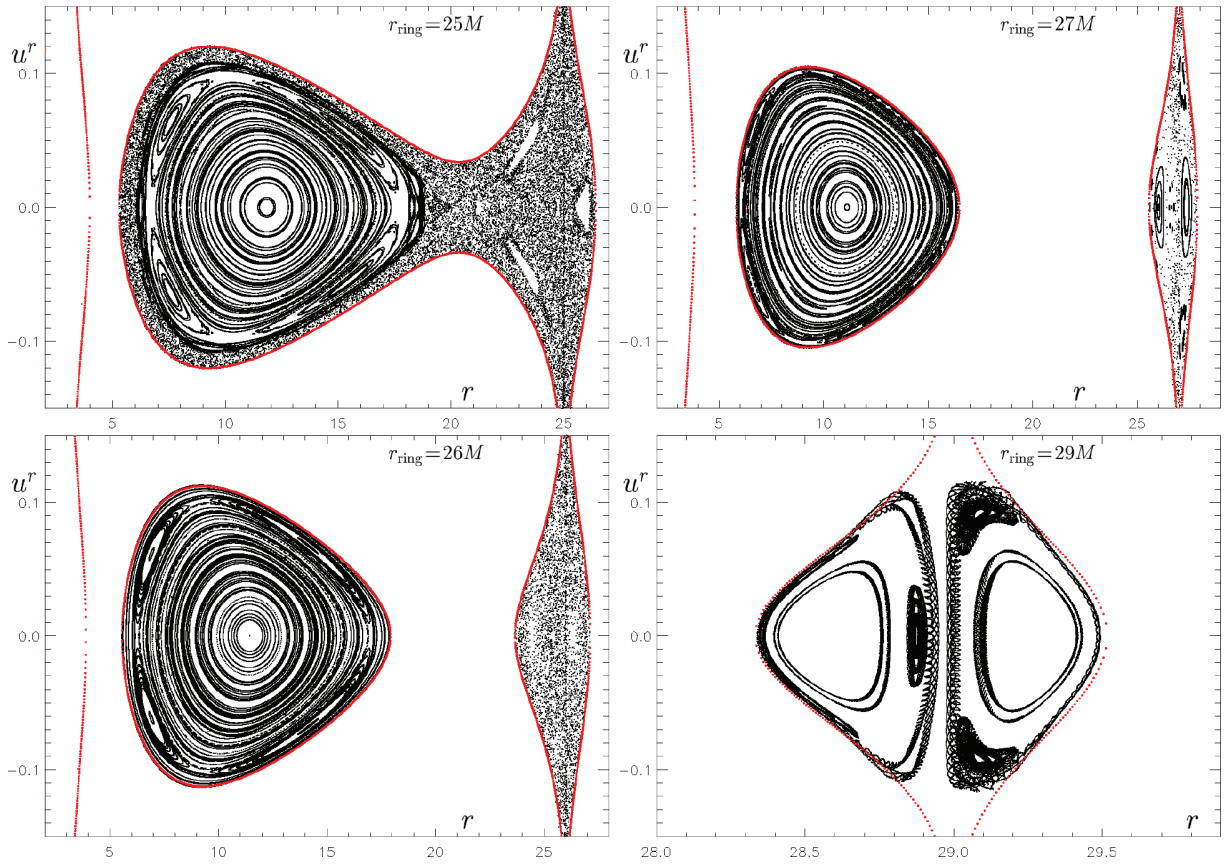


Figure 11 – *continued*

islands – this case is being called 'sticky motion') show the $1/f$ dependence at low frequencies (the spectrum begins at higher amplitudes and goes down with frequency). We have checked whether similar behaviours can be found in our systems too.

In Fig. 14, we compare several rather low-energy ($\mathcal{E} = 0.953$) orbits from the 'moderately chaotic' phase space of a black hole surrounded by the inverted first Morgan–Morgan disc ($\mathcal{M} = 0.5M$, $r_{\rm disc} = 20M$). First, we took 'most regular' orbits that live deep in the primary island, almost unaffected by perturbation (pink, light blue and violet). Their spectrum is very smooth, containing just a few peaks at nearly the same frequencies. The second triple (orange, blue and green) comes from the regular island of periodicity $k = 3$. The spectra are again smooth with distinct peaks at similar frequencies, now containing more of them (these orbits only exist due to the perturbation and are more complicated then those belonging to the primary island). 'Even less regular' are the trajectories living on the outskirts of the primary island, encircling also the higher periodic (e.g. the $k = 3$) orbits and neighbouring the chaotic layer. (These trajectories break up into the chaotic sea when energy is increased.) Their spectra already contain many more harmonics (near the separatrices, the resonances are very close to each other), but the low-frequency part is still smooth and constant. Finally, we took three orbits from the stochastic layer which, however, keep close to the $k = 2$ islands and so might be only 'weakly chaotic' (black, red and green on the second Poincaré section on the right; mainly the black trajectory is seen to linger in the vicinity of the regular islands for a long time). The spectra of all these orbits are clearly chaotic and show the $1/f$ dependence at low frequencies.

The figures confirm that the results of Koyama et al. (2007) apply to our systems as well. We wanted to see in further detail the difference between the 'almost-regular' black trajectory, sticking to the $k = 2$ island for a considerable amount of time, and the truly regular trajectory belonging to that island. In Fig. 15, one can see a clear difference between time series of z obtained for these seemingly very similar orbits. However, in proper times between $\tau = 6.7 \times 10^5 M$ and $\tau = 9.4 \times 10^5 M$ the chaotic orbit really behaves very much like a regular one. This is also confirmed by the spatial picture of the orbits in the figure: in the above stage, the chaotic orbit is almost indistinguishable from the regular one, although it clearly looks chaotic at other times.

Koyama et al. (2007) suggested that the degree of orbital chaoticity depends on the strength of the perturbation (magnitude of the particles' spin in their case) rather than on energy. In order to check this on our system, we compared a few more orbits computed in the field with a much heavier disc ($\mathcal{M} = 1.3M$) and with constants of motion for which the phase space is strongly chaotic. In Fig. 16, eight orbits filling the chaotic sea are compared with four orbits spending most of the time in the vicinity of regular islands. Power spectra of the z-position time series are different and indicate that the first set belongs to the white-noise type, whereas the second set belongs to the $1/f$ type. Hence, even in a more strongly perturbed and thus rather chaotic system there exist trajectories that 'mimic' the behaviour of regular ones for a

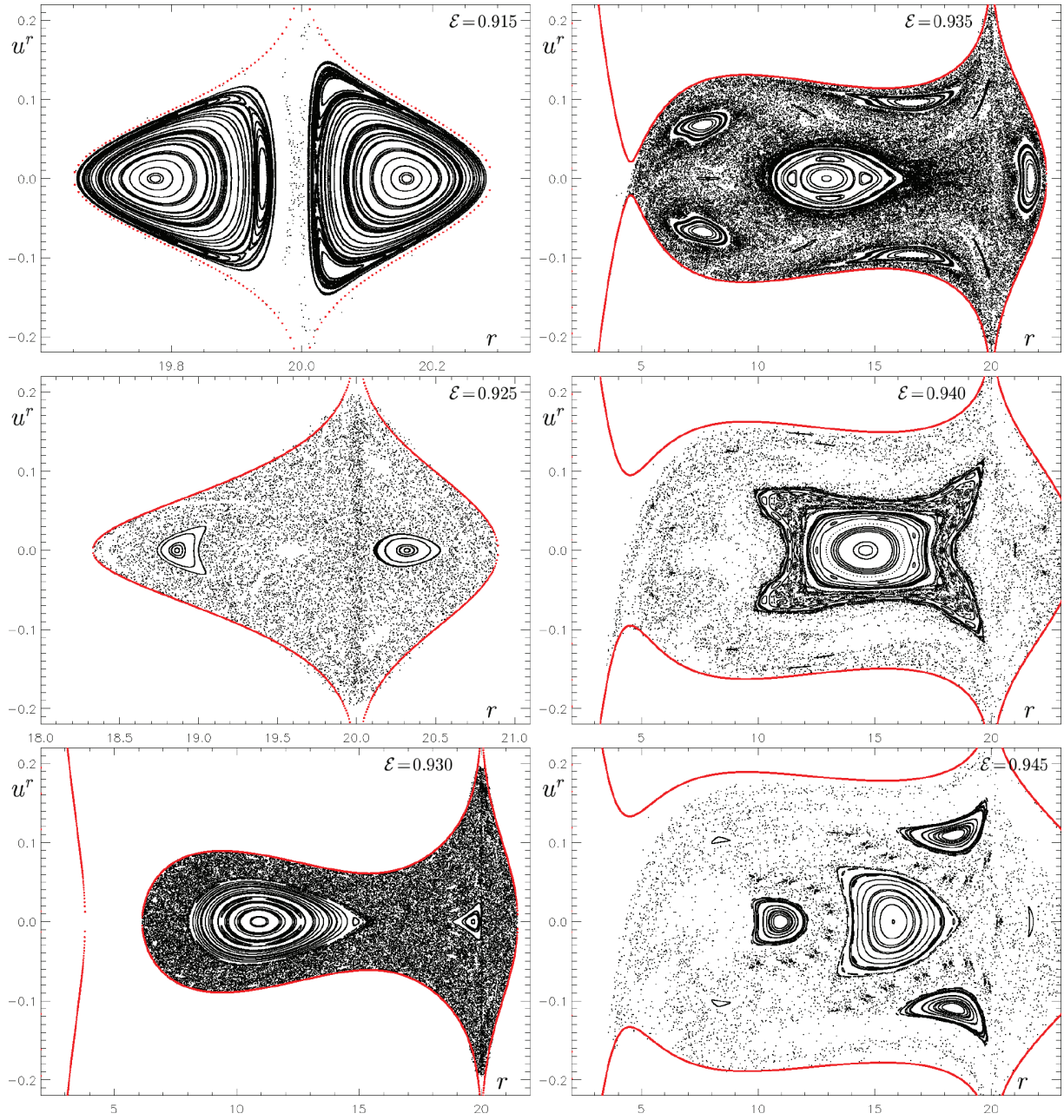


Figure 12. Geodesic dynamics in the field of a Schwarzschild black hole surrounded by the Bach–Weyl ring (with $\mathcal{M} = 0.5M$, $r_{\rm ring} = 20M$): dependence on orbital energy at infinity $\mathcal{E}$ (its value is indicated in the plots). Passages of orbits with $\ell = 3.75M$ through the equatorial plane are drawn. The figure continues on the next page.

certain amount of time (the action changes only slightly there), and this reflects in the $1/f$ shape of their low-frequency power spectra, even if they may inhabit larger portions of phase space at other times. The power-spectrum behaviour is thus a property of the phase-space layer to which the given orbit belongs, rather than of the space–time – or the dynamical system – as such.

Let us add that we obtained similar results for the other discs (other than the inverted first Morgan–Morgan) too.

7 'LATITUDINAL ACTION' INTEGRAL

There are various other variables whose time series should reflect the nature of the system dynamics. For example, one could register the time intervals between the particle's returns to a given r or a given θ, the times between reaching turning points, etc. In a paper on charged particle motion in an electromagnetic field surrounding a rotating black hole, Takahashi & Koyama (2009) considered the 'latitudinal action'

$$J_\theta \equiv \frac{1}{l}\oint \sqrt{g_{\theta\theta}u^\theta u^\theta}\,{\rm d}\tau, \tag{27}$$

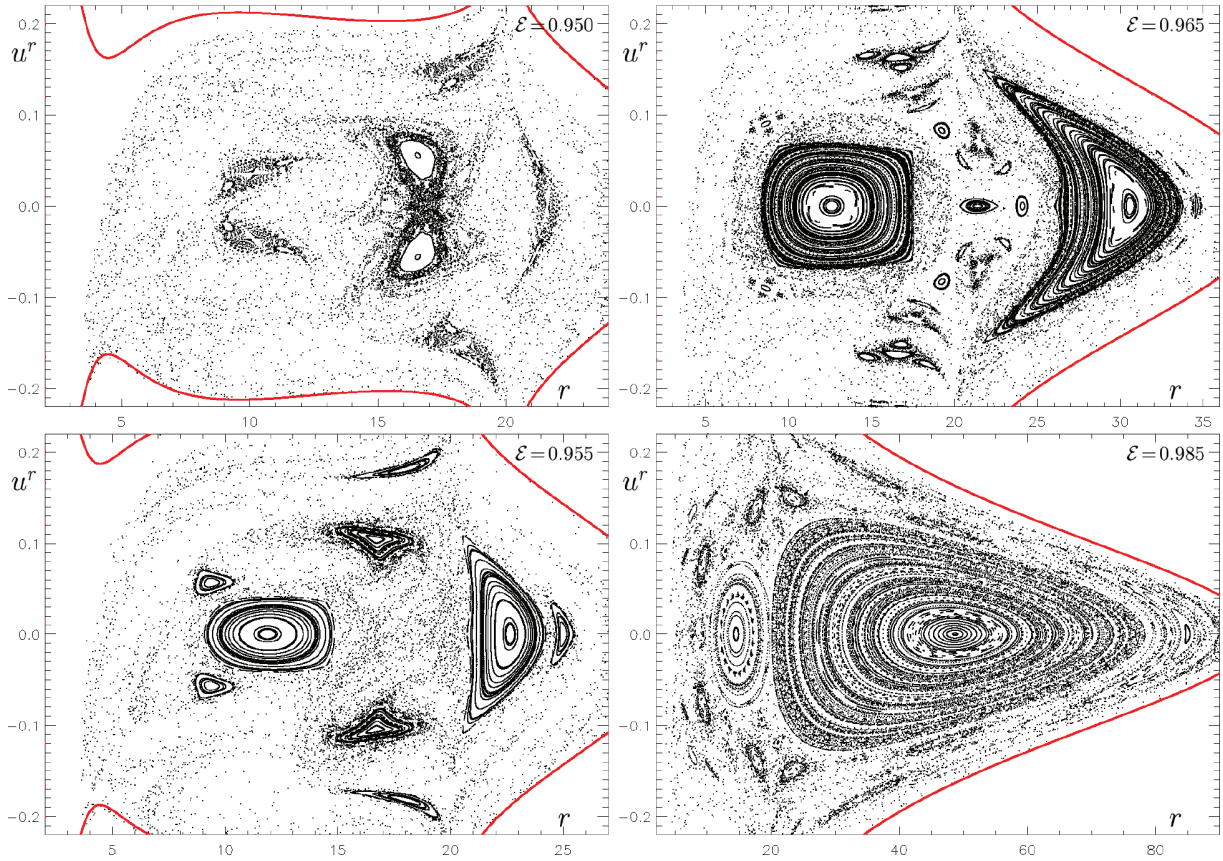


Figure 12 – *continued*

given by averaging the test-particle latitudinal four-velocity over one orbital cycle (of length l). They compared its time evolution with Poincaré maps and evolution of θ and really observed clear correlation. We were curious whether a similar observation can be made in our disc/ring-perturbed systems too.

For regular orbits, we obtained regular oscillations of the action around a certain constant mean value. The amplitude of these oscillations is very small for orbits close to the primary resonance ('circular' periodic orbit) and larger for orbits belonging to higher periodicity islands. For chaotic orbits, the action integral does not evolve in a harmonic way and is not tied to any obvious mean value. In Fig. 17, the behaviour of action is drawn for the four 'weakly chaotic' orbits from Fig. 16 (spectra of their z-position are given at bottom right of that figure). All these trajectories are 'stuck on' regular islands in certain stages of their evolution – and it is seen now that in those stages their action really behaves almost like along regular orbits (almost regular moderate oscillations around almost constant mean value).

Let us conclude with a trajectory that also adheres to a regular island for a certain time, but its power spectrum still does *not* show the $1/f$ shape at low frequencies. In Fig. 16, it is the dark blue geodesic occurring in the vicinity of the $k = 3$ islands. In Fig. 18, we plot the time series of its latitudinal action and spectrum of its z-position evolution. Clearly, the action behaves quite regularly for a considerable time (mainly in periods from 0 to $150M$ and from $400M$ to $1600M$), yet the z-motion spectrum is still of clear 'white-noise' type, not showing any signs of the $1/f$ dependence. Perhaps the latter would only appear if the spectrum were calculated solely for the 'almost regular' phase of the orbit.

8 CONCLUDING REMARKS

We have tried to get a basic idea about how the dynamics of free massive test particles in a Schwarzschild black hole field is perturbed by gravity of a static, axially symmetric and reflectionally symmetric ring or disc. Poincaré sections have proved that it becomes chaotic and the degree of stochasticity grows with compactness and relative mass of the external source and with energy of the particles. However, for large values of these parameters, the dynamics rather returns towards the regular regime. The shape of stochastic regions depends very much on the radius of the additional source. This is clearly the consequence of how the parameters affect the shape of the effective potential, in particular of whether

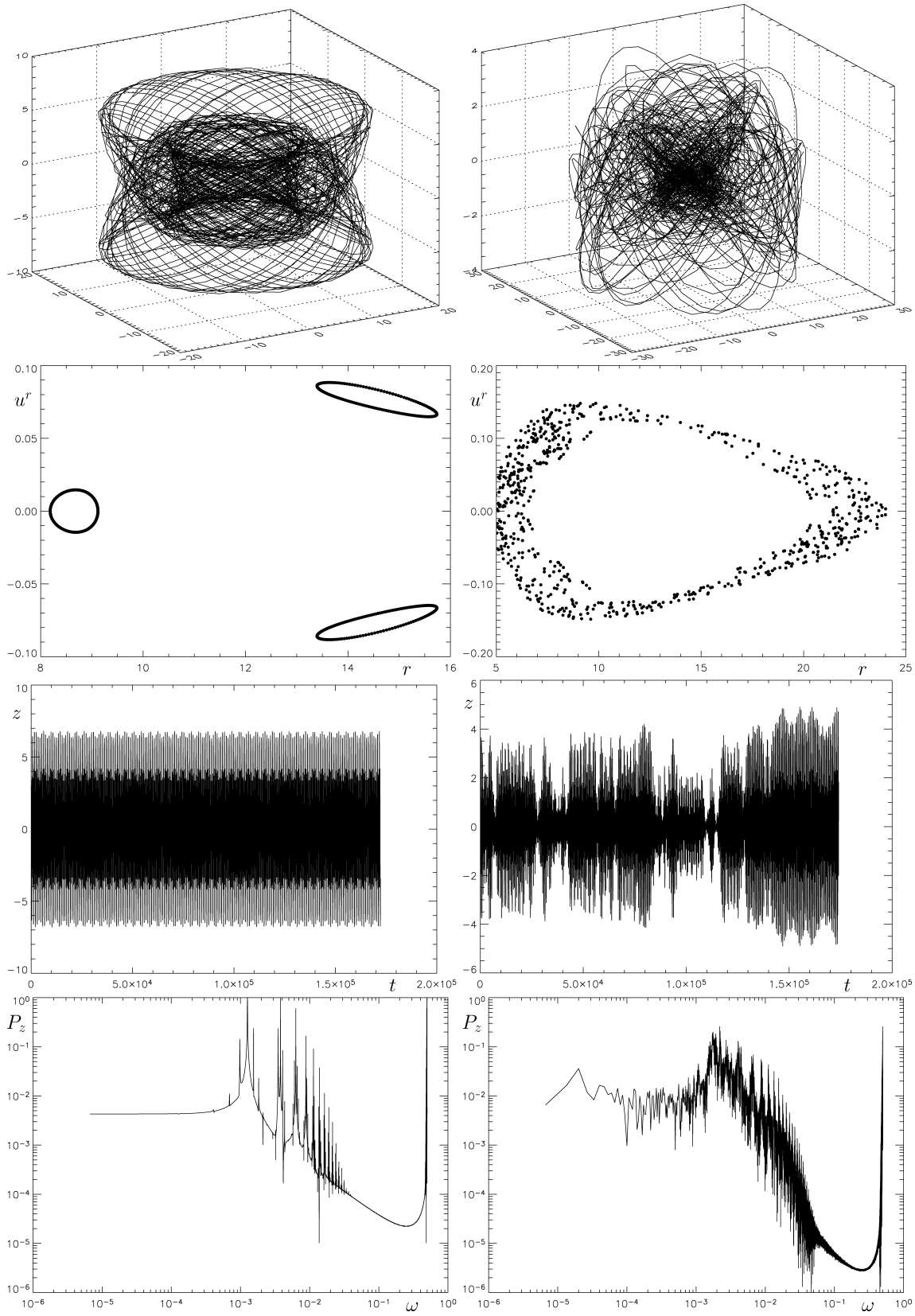


Figure 13. Comparison of a selected regular (left) and chaotic (right) orbit, both with constants $\mathcal{E} = 0.955$, $\ell = 3.75M$ and obtained in the field of a Schwarzschild black hole surrounded by the inverted first Morgan–Morgan disc with $\mathcal{M} = 0.5M$, $r_{\rm disc} = 20M$. From top to bottom, the rows contain spatial tracks of the orbits, their Poincaré sections $z = 0$ (r, u^r), time series of the z position and corresponding Fourier spectra. Coordinates are in the units of M, frequencies in the units of $1/M$.

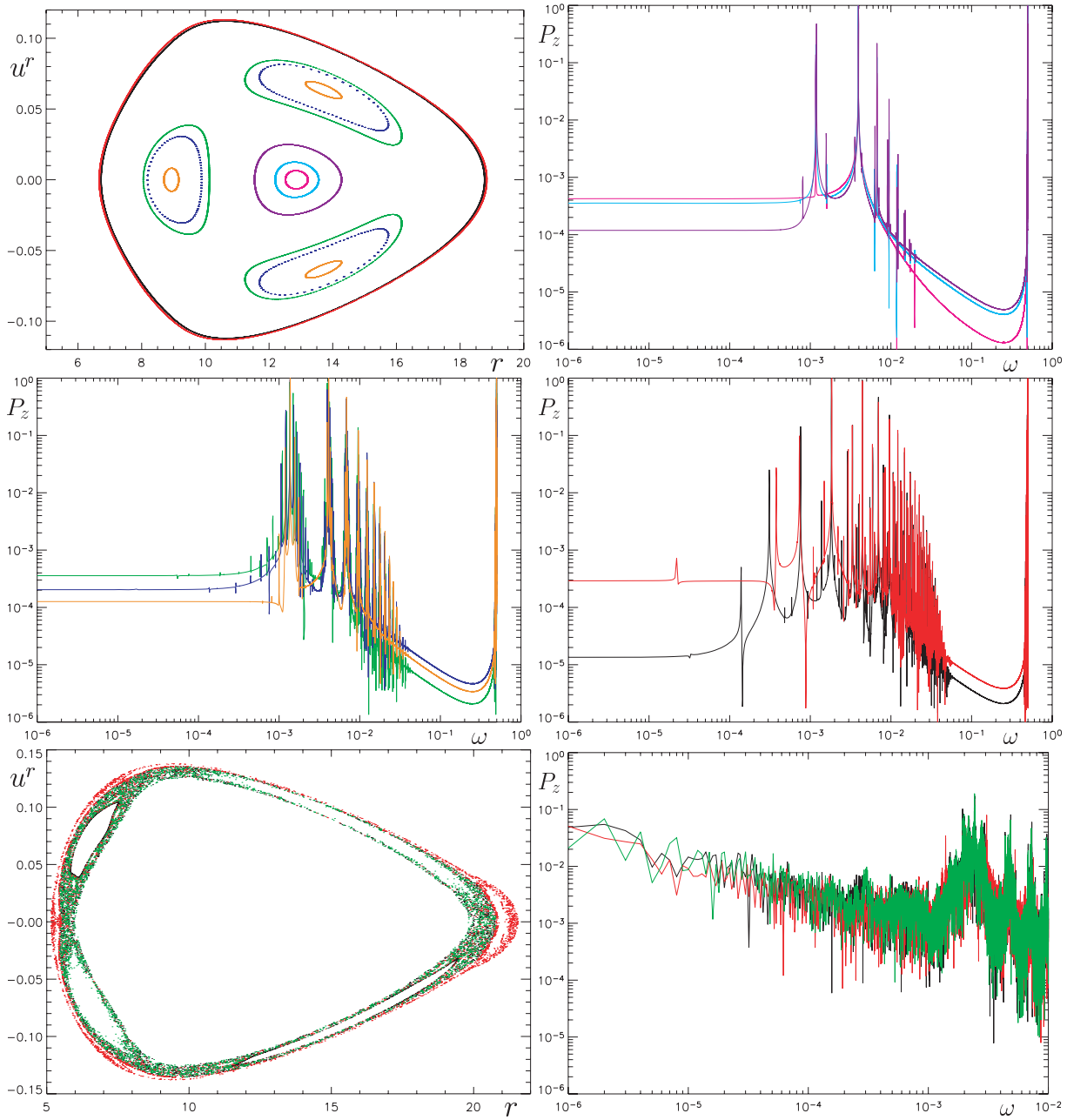


Figure 14. Comparison of selected orbits with constants $\mathcal{E} = 0.953$, $\ell = 3.75M$, obtained in the field of a Schwarzschild black hole surrounded by the inverted first Morgan–Morgan disc with $\mathcal{M} = 0.5M$, $r_{\rm disc} = 20M$. In the top-left panel, three types of regular orbits are chosen in respective Poincaré section. The spectra of their z-position time series are given in the top-right panel (three primary-island orbits), middle left panel (three orbits from islands of periodicity $k = 3$) and middle right panel (two orbits skirting the whole island and neighbouring the chaotic layer). In the bottom row, three 'weakly chaotic' orbits are chosen in the same Poincaré section and their spectra shown on the right. The individual orbits are given in different colours. Radius is in the units of M, frequency in the units of $1/M$.

and where there are regions that allow 'permanent' orbital motion. Our system shows typical features of a nearly integrable Hamiltonian system; the behaviour revealed on Poincaré sections is a good illustration of the KAM theory. (Strictly speaking, the latter should only be applied to orbits which do not cross the disc, however.)

The appearance of selected orbits in Poincaré sections was compared with their spatial picture, with the time series representing evolution of their vertical (z) position, with the latter's Fourier spectra and with the evolution of the 'latitudinal action' assigned to their individual loops (fixed by θ-periodicity). Chaotic orbits are clearly distinguishable from regular in all these respects. Within the chaotic trajectories, one can further recognize those that adhere to regular orbits, lingering within narrow bands in Poincaré diagrams for most of the time, and those that fill a large area ('chaotic sea') there in a rather uniform way. The degree of chaoticity is reflected in time series and their Fourier spectra: the 'weakly chaotic' orbits produce nearly regular and moderate oscillations around a nearly constant mean value, which typically gives rise to

© 2010 The Authors. Journal compilation © 2010 RAS, MNRAS **404,** 545–574

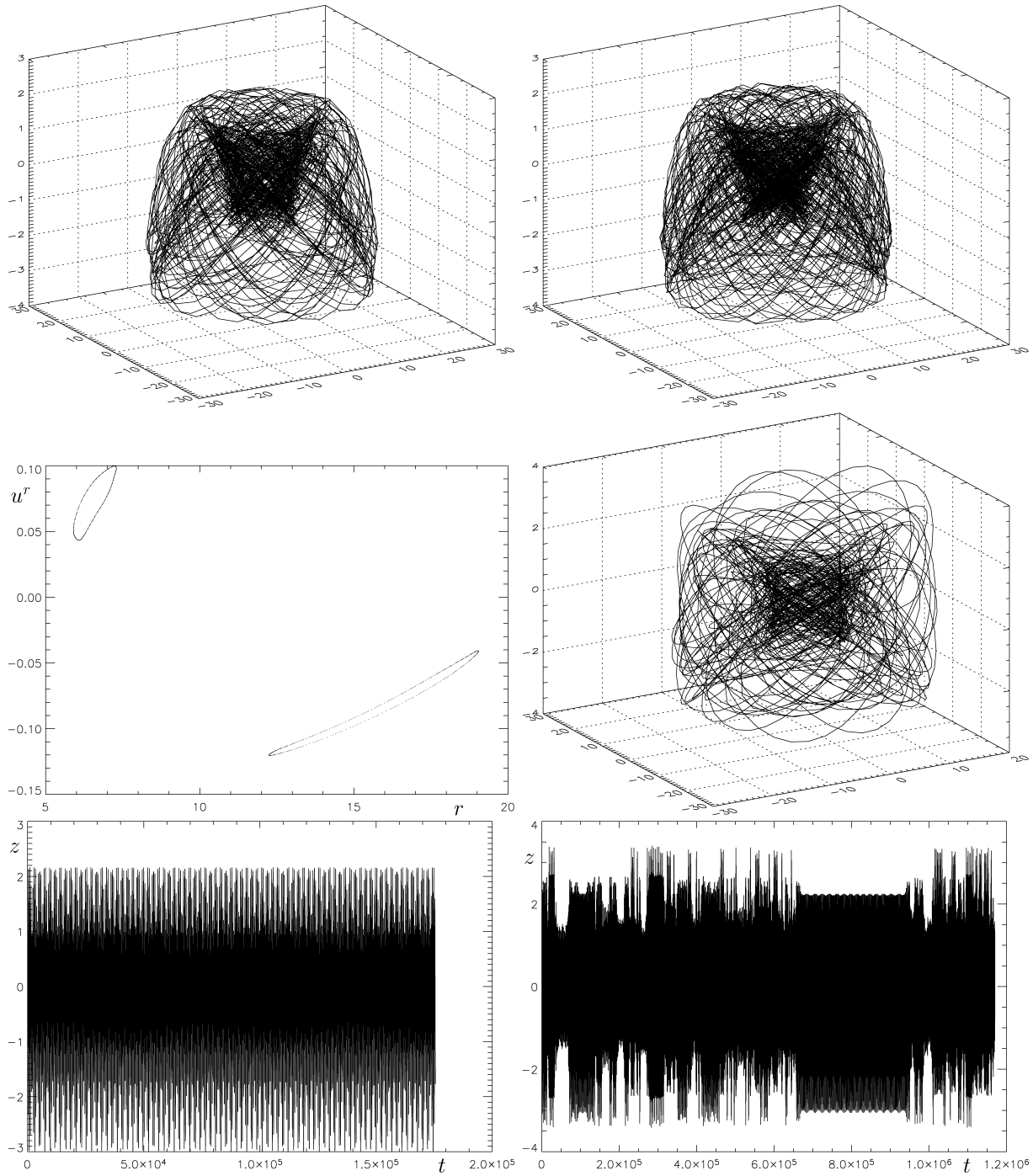


Figure 15. Further comparison of the orbit sticking to the $k = 2$ islands in Fig. 14 (the black one in the bottom row) and a selected regular orbit belonging to these islands. On the left-hand side, the spatial track (top panel), the Poincaré section (middle panel) and the time series of z (bottom panel) are drawn for the regular orbit. On the right-hand side, the spatial tracks for the weakly chaotic orbit are drawn, at 'almost regular' times $7 \times 10^5 M < \tau < 9 \times 10^5 M$ (top panel) and at more chaotic times $\tau < 100\,000M$ (middle panel); the time series of z is given in the bottom panel.

the '1/frequency' shape of the spectrum at low frequencies, whereas 'strongly chaotic' orbits produce strongly irregular times series without any distinct mean value, which corresponds to the 'white-noise' shape at the low end of the spectrum (relatively flat curve at rather low values). The most interesting are chaotic orbits in strongly perturbed systems which undergo both the 'sticky motion' near regular islands and 'unrestrained' phases of drifting around the chaotic sea. The power spectra of their evolution usually 'take note' of the almost regular phase and fall under the $1/f$ type, but we also came across a trajectory whose spectrum showed a clear white noise, although it behaved in a quite orderly way for a considerable time.

The study of any specific dynamical system may develop in several obvious ways. First, there should be a running check of genericity/stability of the dynamical regime found. This involves going through the initial conditions in an exhaustive manner, changing the

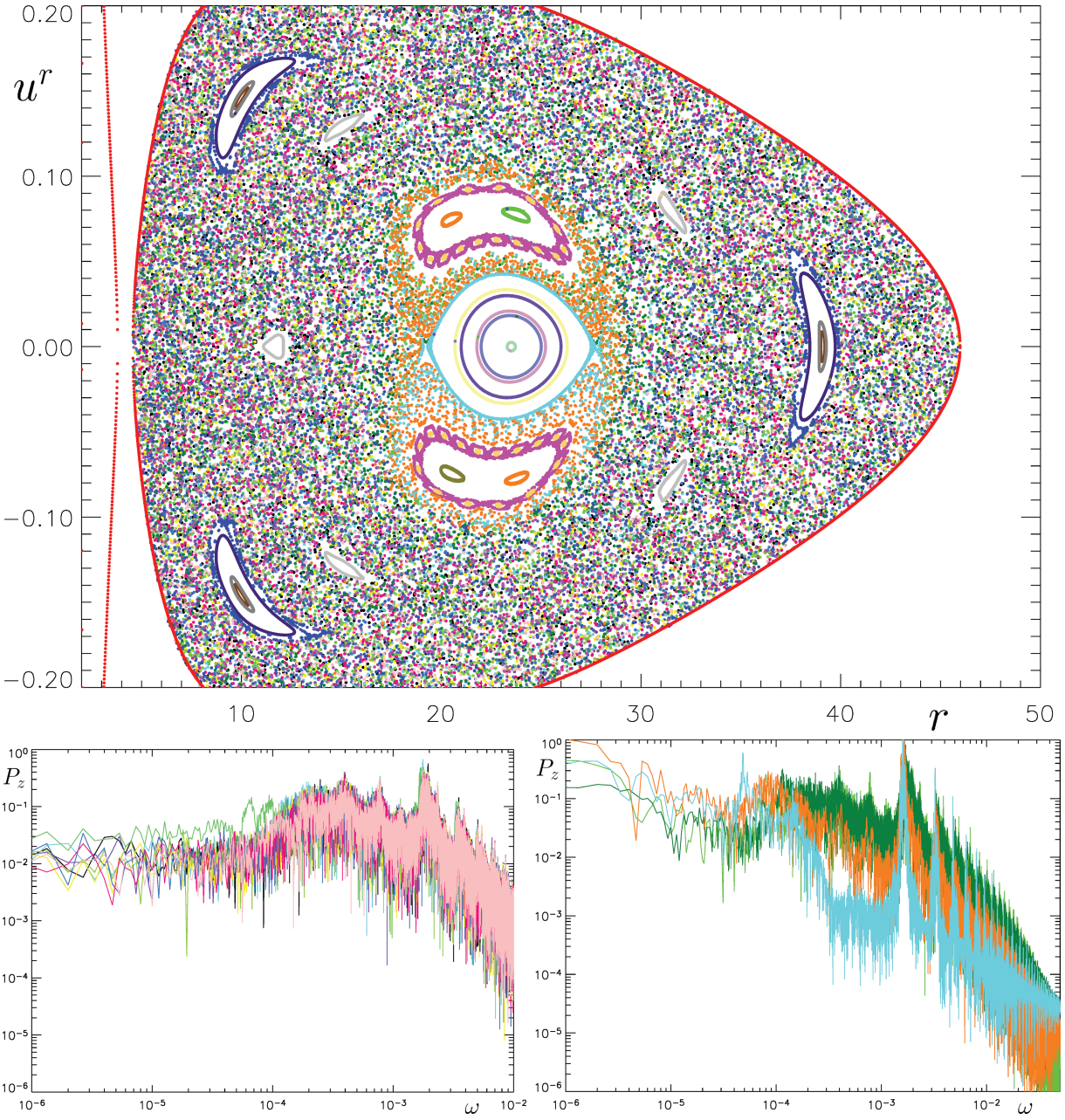


Figure 16. Two types of chaotic orbits (with constants $\mathcal{E} = 0.956$, $\ell = 4M$) found in the field of a black hole surrounded by the inverted first Morgan–Morgan disc with $\mathcal{M} = 1.3M$, $r_{\rm disc} = 20M$. Eight orbits filling the 'chaotic sea' on the Poincaré section (top panel) have their z-position power spectra in the bottom-left panel, while four orbits dwelling mostly in the vicinity of regular islands in the centre have their spectra in the bottom-right panel.

parameters of the system, trying different numerical schemes... Secondly, one may elaborate the model of the explored system in order to make it as realistic as possible, try to estimate and examine the consequences and mutual couplings of different 'perturbations'/neglects as well as their astrophysical importance. Finally, it is very appropriate to study the dynamics of the specific system by more methods and observe the relations between different aspects of its chaoticity. This is our next plan.

Concerning the last point(s), let us note that there especially arises the question about the role of features which are specific for the theory that underlies the phase space. In general relativity, such a special feature is the space–time curvature. It is clear that chaos is *not* solely caused by space–time curvature. [See the quotation from Vieira & Letelier (1996b) in Section 2.2. As a matter of fact, some systems are chaotic both in Newton's theory and in special and general relativity.] However, the example of Einstein's theory of gravitation itself suggests that it might be possible to interpret the dynamics of some systems as geodesic flows in suitably defined manifolds. This would certainly depend on the type of interaction, but also on some integral properties of the specific trajectory (like constants of the motion). This direction has been notably pursued by Szydłowski and coworkers, see e.g. Szydłowski (1998,1999) and references therein, while the dynamics of specific systems was interpreted 'geometrically' in some of the papers already cited in Section 2.2 (Yurtsever 1995; Sota et al. 1996) [cf. section 2.3 of Cornish & Gibbons (1997)]. More recent contributions to this line of research include mainly Casetti, Pettini & Cohen (2000), Ramasubramanian &

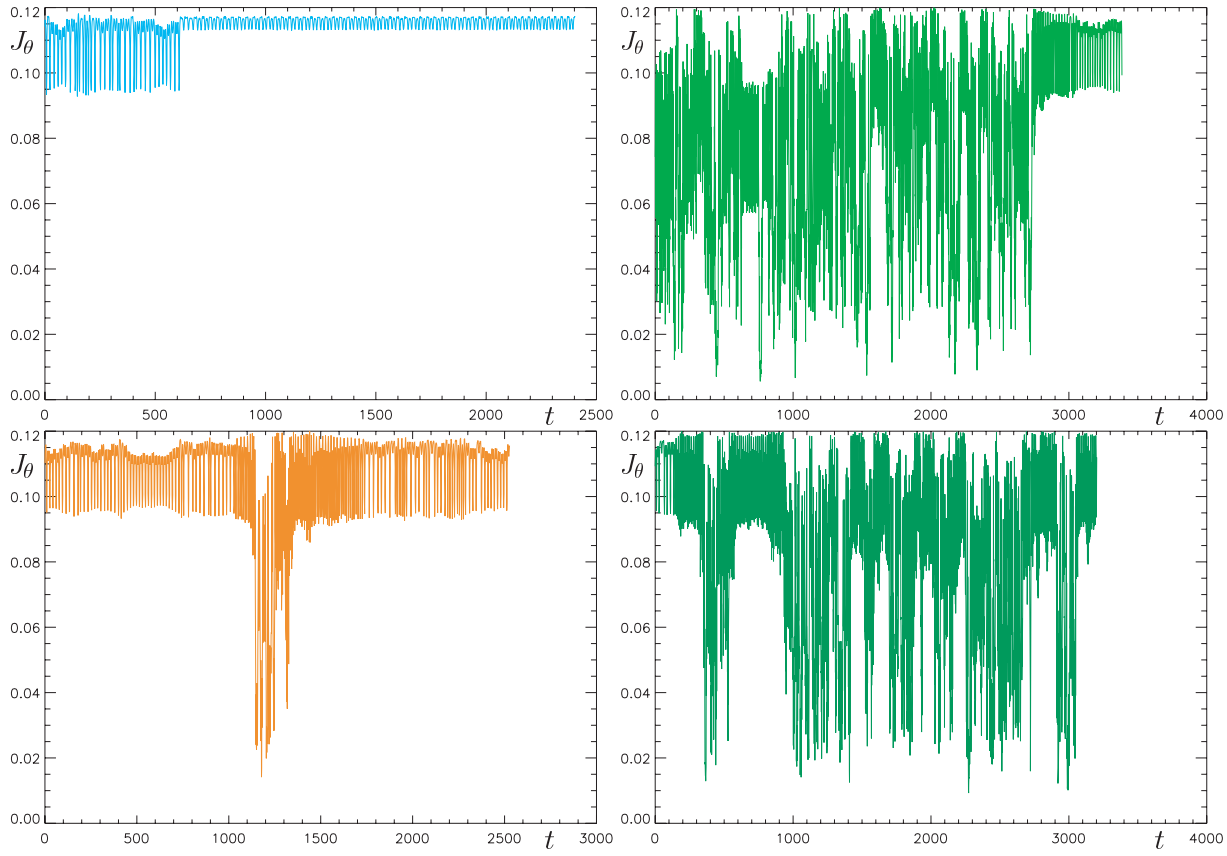


Figure 17. Time series of the latitudinal action (27) as registered for the four weakly chaotic trajectories from Fig. 16. (Fourier spectra of their z-position time series are given in the bottom-right panel of that figure.) The colours are kept the same as there. To be specific, we plot the action integral as divided by the length of the given orbital loop in terms of proper-time lapse.

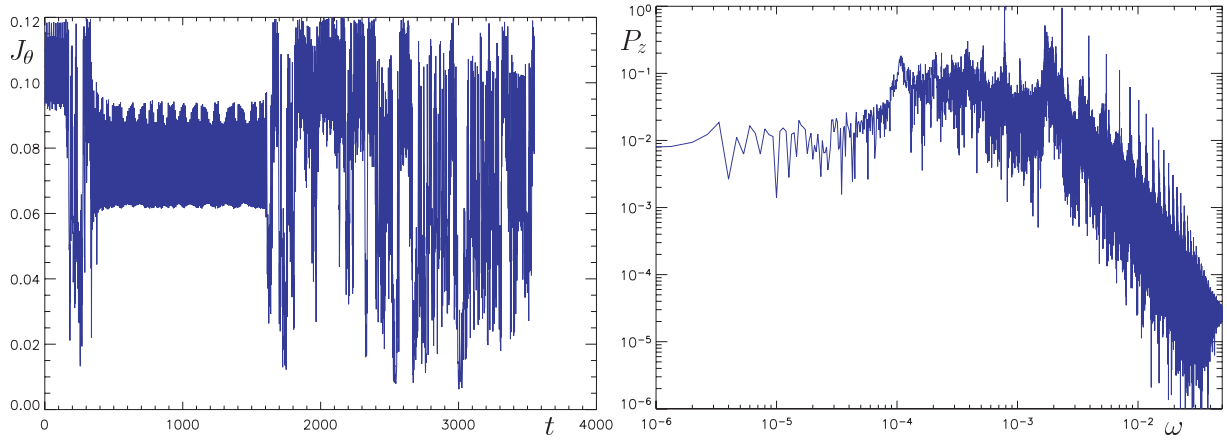


Figure 18. Time series of the latitudinal action (left-hand panel) and z-position power spectrum (right-hand panel) for the 'dark blue' orbit from Fig. 16. The orbit spends quite a long time very near the regular islands of periodicity $k = 3$ (they are not far from the boundary of the accessible region), but its power spectrum still does not show any signs of the 1/frequency behaviour at low frequencies.

Sriram (2001), Clementi & Pettini (2002), Kawabe (2005), Horwitz et al. (2007), Cafaro (2008), Zion & Horwitz (2008) and Cerruti-Sola et al. (2008) (further references are given therein).

ACKNOWLEDGMENTS

We are grateful to M. Žáček who kindly provided us with his numerical code, and to L. Šubr and D. Heyrovský for hints and discussions. OS thanks Professor F. de Felice for hospitality at the Department of Physics, University of Padova. This work was supported by the grants GACR-202/09/0772 (OS) and GAUK-86508 (PS) and by the Czech Ministry of Education under the projects MSM0021610860 and LC06014.

REFERENCES

Aguirregabiria J. M., 1997, Phys. Lett. A, 224, 234
Alonso D., Ruiz A., Sánchez-Hernández M., 2008, Phys. Rev. D, 78, 104024
Andriopoulos K., Leach P. G. L., 2008, J. Phys. A, 41, 155201
Bach R., Weyl H., 1922, Math. Zeit., 13, 134
Benini R., Montani G., 2004, Phys. Rev. D, 70, 103527
Bombelli L., Calzetta E., 1992, Class. Quantum Gravity, 9, 2573
Buzzi C. A., Llibre J., da Silva P. R., 2007, J. Phys. A, 40, 7187
Cafaro C., 2008, Int. J. Theor. Phys., 47, 2924
Cardoso V., Miranda A. S., Berti E., Witek H., Zanchin V. T., 2009, Phys. Rev. D, 79, 064016
Casetti L., Pettini M., Cohen E. G. D., 2000, Phys. Rep., 337, 237
Cerruti-Sola M., Ciraolo G., Franzosi R., Pettini M., 2008, Phys. Rev. E, 78, 046205
Chen J., Wang Y., 2003, Class. Quantum Gravity, 20, 3897
Clementi C., Pettini M., 2002, Celest. Mech. Dyn. Astron., 84, 263
Coley A. A., 2002, Class. Quantum Gravity, 19, L45
Contopoulos G., Harsoula M., 2005, Celest. Mech. Dyn. Astron., 92, 189
Contopoulos G., Papadaki H., 1993, Celest. Mech. Dyn. Astron., 55, 47
Cornish N. J., Frankel N. E., 1997, Phys. Rev. D, 56, 1903
Cornish N. J., Gibbons G. W., 1997, Class. Quantum Gravity, 14, 1865
Cornish N. J., Levin J., 2003, Class. Quantum Gravity, 20, 1649
D'Afonseca L. A., Letelier P. S., Oliveira S. R., 2005, Class. Quantum Gravity, 22, 3803
de Moura A. P. S., Letelier P. S., 2000a, Phys. Rev. E, 61, 6506
de Moura A. P. S., Letelier P. S., 2000b, Phys. Rev. E, 62, 4784
Dettmann C. P., Frankel N. E., Cornish N. J., 1994, Phys. Rev. D, 50, R618
Dettmann C. P., Frankel N. E., Cornish N. J., 1995, Fractals, 3, 161
Dubeibe F. L., Pachón L. A., Sanabria-Gómez J. D., 2007, Phys. Rev. E, 75, 023008
Faraoni V., Jensen M. N., Theuerkauf S. A., 2006, Class. Quantum Gravity, 23, 4215
Fay S., Lehner T., 2004, Gen. Relativ. Gravitation, 36, 2635
Grossman R., Levin J., 2009, Phys. Rev. D, 79, 043017
Guéron E., Letelier P. S., 2001, A&A, 368, 716
Guéron E., Letelier P. S., 2002, Phys. Rev. E, 66, 046611
Han W., 2008a, Gen. Relativ. Gravitation, 40, 1831
Han W., 2008b, Phys. Rev. D, 77, 123007
Hanan W., Radu E., 2007, Mod. Phys. Lett. A, 22, 399
Hartl M. D., 2003a, Phys. Rev. D, 67, 024005
Hartl M. D., 2003b, Phys. Rev. D, 67, 104023
Heinzle J. M., Röhr N., Uggla C., 2006, Phys. Rev. D, 74, 061502
Heinzle J. M., Uggla C., 2009, Class. Quantum Gravity, 26, 075016
Hobill D., Burd A., Coley A., eds, 1994, NATO ASI Ser. 332, Deterministic Chaos in General Relativity. Plenum Press, New York
Horwitz L., Zion Y. B., Lewkowicz M., Schiffer M., Levitan J., 2007, Phys. Rev. Lett., 98, 234301
Howard J. E., Wilkerson T. D., 1995, Phys. Rev. A, 52, 4471
Hrycyna O., Szydłowski M., 2006, Chaos Solitons Fractals, 28, 1252
Jorás S. E., Stuchi T. J., 2003, Phys. Rev. D, 68, 123525
Judd K., 2008, J. Nonlinear Sci., 18, 57
Kao J.-K., Cho H. T., 2005, Phys. Lett. A, 336, 159
Karas V., Šubr L., 2007, A&A, 470, 11
Karas V., Vokrouhlický D., 1992, Gen. Relativ. Gravitation, 24, 729
Kawabe T., 2005, Phys. Rev. E, 71, 017201
Kiuchi K., Maeda K., 2004, Phys. Rev. D, 70, 064036
Kiuchi K., Koyama H., Maeda K., 2007, Phys. Rev. D, 76, 024018
Koyama H., Kiuchi K., Konishi T., 2007, Phys. Rev. D, 76, 064031
Lai Y.-C., Grebogi C., Kurths J., 1999, Phys. Rev. E, 59, 2907
Lemos J. P. S., Letelier P. S., 1994, Phys. Rev. D, 49, 5135
Letelier P. S., Vieira W. M., 1997a, Phys. Rev. D, 56, 8095
Letelier P. S., Vieira W. M., 1997b, Class. Quantum Gravity, 14, 1249
Letelier P. S., Vieira W. M., 1998, Phys. Lett. A, 244, 324
Levin J., 1999, Phys. Rev. D, 60, 064015
Levin J., 2000, Phys. Rev. Lett., 84, 3515
Levin J., 2003, Phys. Rev. D, 67, 044013
Levin J., 2006, Phys. Rev. D, 74, 124027
Levin J., Perez-Giz G., 2009, Phys. Rev. D, 79, 124013
Lichtenberg A. J., Lieberman M. A., 1992, Regular and Chaotic Dynamics, 2nd edn. Springer, Berlin
Lukes-Gerakopoulos G., Basilakos S., Contopoulos G., 2008, Phys. Rev. D, 77, 043521
Maciejewski A. J., Przybylska M., Stachowiak T., Szydłowski M., 2008, J. Phys. A, 41, 465101
Moeckel R., 1992, Commun. Math. Phys., 150, 415
Motter A. E., 2003, Phys. Rev. Lett., 91, 231101
Motter A. E., Saa A., 2009, Phys. Rev. Lett., 102, 184101

© 2010 The Authors. Journal compilation © 2010 RAS, MNRAS **404,** 545–574

Perez-Giz G., Levin J., 2009, Phys. Rev. D, 79, 124014
Podolský J., Kofroň D., 2007, Class. Quantum Gravity, 24, 3413
Podolský J., Veselý K., 1998, Class. Quantum Gravity, 15, 3505
Ramasubramanian K., Sriram M. S., 2001, Phys. Rev. E, 64, 046207
Ramos-Caro J., López-Suspes F., González G. A., 2008, MNRAS, 386, 440
Saa A., 2000, Phys. Lett. A, 269, 204
Saa A., Venegeroles R., 1999, Phys. Lett. A, 259, 201
Sauer T., Grebogi C., Yorke J. A., 1997, Phys. Rev. Lett., 79, 59
Scott A. C., 2007, The Nonlinear Universe: Chaos, Emergence, Life. Springer, Berlin
Şelaru D., Mioc V., Cucu-Dumitrescu C., Ghenescu M., 2005, Astron. Nachr., 326, 356
Semerák O., 2003, Class. Quantum Gravity, 20, 1613
Semerák O., 2004, Class. Quantum Gravity, 21, 2203
Semerák O., Žáček M., Zellerin T., 1999, MNRAS, 308, 705
Shi P., He D., Kang W., Fu W., Hu G., 2001, Phys. Rev. E, 63, 046310
Soares I. D., Stuchi T. J., 2005, Phys. Rev. D, 72, 083516 (Erratum: 2006, 73, 069901)
Sota Y., Suzuki S., Maeda K., 1996, Class. Quantum Gravity, 13, 1241
Steklain A. F., Letelier P. S., 2006, Phys. Lett. A, 352, 398
Steklain A. F., Letelier P. S., 2009, Phys. Lett. A, 373, 188
Stránský P., Kurian M., Cejnar P., 2006, Phys. Rev. C, 74, 014306
Suzuki S., Maeda K., 1997, Phys. Rev. D, 55, 4848
Suzuki S., Maeda K., 1999, Phys. Rev. D, 61, 024005
Szydłowski M., 1997, Int. J. Mod. Phys. D, 6, 741
Szydłowski M., 1998, Gen. Relativ. Gravitation, 30, 887
Szydłowski M., 1999, J. Math. Phys., 40, 3519
Takahashi M., Koyama H., 2009, ApJ, 693, 472
Varvoglis H., Papadopoulos D., 1992, A&A, 261, 664
Vieira W. M., Letelier P. S., 1996a, Phys. Rev. Lett., 76, 1409
Vieira W. M., Letelier P. S., 1996b, Class. Quantum Gravity, 13, 3115
Vieira W. M., Letelier P. S., 1999, ApJ, 513, 383
Vokrouhlický D., Karas V., 1998, MNRAS, 298, 53
Wu X., Huang T.-Y., 2003, Phys. Lett. A, 313, 77
Wu X., Xie Y., 2008, Phys. Rev. D, 77, 103012
Wu X., Zhang H., 2006, ApJ, 652, 1466
Yurtsever U., 1995, Phys. Rev. D, 52, 3176
Zion Y. B., Horwitz L., 2008, Phys. Rev. E, 78, 036209

This paper has been typeset from a TEX/LATEX file prepared by the author.

B. Free motion around black holes with discs: between integrability and chaos – II

Published in: Semerák, O. and Suková, P.: Free motion around black holes with discs or rings: between integrability and chaos – II, Monthly Notices of the Royal Astronomical Society 425 (2012), 2455

http://dx.doi.org/10.1111/j.1365-2966.2012.21630.x

Preprints: arXiv:1211.4107 [gr-qc]

Monthly Notices of the ROYAL ASTRONOMICAL SOCIETY

Mon. Not. R. Astron. Soc. **425,** 2455–2476 (2012) doi:10.1111/j.1365-2966.2012.21630.x

Free motion around black holes with discs or rings: between integrability and chaos – II

O. Semerák and P. Suková★

Institute of Theoretical Physics, Faculty of Mathematics and Physics, Charles University in Prague, V Holešovičkách 2, 180 00 Praha 8, Czech Republic

Accepted 2012 June 29. Received 2012 May 10

ABSTRACT

We continue the study of time-like geodesic dynamics in exact static, axially and reflection symmetric space–times describing the fields of a Schwarzschild black hole surrounded by thin discs or rings. In the previous paper, the rise (and decline) of geodesic chaos with ring/disc mass and position and with test particle energy was revealed on Poincaré sections, on time series of position or velocity and their power spectra, and on time evolution of the orbital 'latitudinal action'. In agreement with the KAM theory of nearly integrable dynamical systems and with the results observed in similar gravitational systems in the literature, we found orbits of very different degrees of chaoticity in the phase space of perturbed fields. Here we compare selected orbits in more detail and try to classify them according to the characteristics of the corresponding phase-variable time series, mainly according to the shape of the time-series power spectra, and also applying two recurrence methods: the method of 'average directional vectors', which traces the directions in which the trajectory (recurrently) passes through a chosen phase-space cell, and the 'recurrence-matrix' method, which consists of statistics over the recurrences themselves. All the methods proved simple and powerful, while it is interesting to observe how they differ in sensitivity to certain types of behaviour.

Key words: black hole physics – chaos – gravitation.

1 INTRODUCTION

The black holes discussed in most university courses are isolated, stationary and living in asymptotically flat space–times, that is to say they belong to the Kerr(–Newman) family. The metric which describes this family is not entirely simple, but it has a number of 'nice' properties. Among others, its multipole structure – namely that required for the black hole uniqueness theorems to work – is just the one that permits the solution of (electro)geodesic equations in terms of separated first integrals (e.g. Will 2009). This full integrability is mostly lost if any of the assumptions (isolation, stationarity, asymptotic flatness) is released. More precisely, the integrability holds in the whole family of Kerr–Newman–NUT–(anti-)de Sitter space–times (Carter 1968); it is connected with the existence of an irreducible second-order Killing tensor (Walker & Penrose 1970) and has been shown to follow from the existence of a principal (conformal) Killing–Yano tensor there (e.g. Frolov & Kubizňák 2008). All these space–times are of Petrov type D and represent subclass of the Plebański–Demiański solutions with non-accelerated sources. Besides mass, electric charge and rotational angular momentum, they also include cosmological constant, magnetic charge and NUT parameter (of which the last two do not seem to be physically relevant, however).

Although the Kerr(–Newman) metric is being referred to when speaking about black holes in galactic nuclei and X-ray binaries, the above assumptions can only be valid approximately in such astrophysical circumstances; strictly speaking, they are all violated. Indeed, the observability of the supposed black holes alone implies that they have to be interacting with matter, thus non-isolated and non-stationary. Black holes certainly dominate the gravitational potential and intensity in their wide surroundings, but higher derivatives of the field (curvature) may be affected by nearby matter significantly. And these higher derivatives govern stability of motion. Hence, due to its own gravity, the matter may in fact settle down, around a central black hole, to a configuration different from that assumed by a *test* (non-gravitating) matter.

In a non-linear theory like general relativity, it is not simple to specify what violation of the given (Kerr) metric is already large enough to invalidate various related conclusions and to bring physical differences with observable consequences. If the ambient matter is dilute and its self-gravitation effects are correspondingly weak, or when the source is more concentrated but only the field farther from it is relevant, the problem is usually being addressed by perturbation techniques. However, perturbation solutions are given in terms of series that practically must be truncated somewhere, so they cannot represent fully the self-gravitation effects (and in linear order

★E-mail: lvicekps@seznam.cz

© 2012 The Authors
Monthly Notices of the Royal Astronomical Society © 2012 RAS

they do not encompass them at all). The perturbative description is mainly questionable in the case of two- or one-dimensional additional sources (like discs or rings), because even if the total mass of such sources is very small, they, however, constitute a singularity and thus cannot be considered weak in their vicinity.

It is sure in any case that almost any deviation from the Kerr(–Newman) metric implied by the presence of additional matter leads to the loss of complete (electro)geodesic integrability. This is even true when the additional source keeps the symmetries of the 'original', pure black hole space–time, i.e. when their resulting 'superposition' is stationary, axially and reflection symmetric and orthogonally transitive (this last property is ensured if and only if the source elements do not perform any other motion than steady orbiting along the direction of axial symmetry). The loss of integrability in turn means that motion in the field of such a system is chaotic in general. The robustness of this conclusion makes the subtle phenomenon of chaos one of the aspects of astrophysical black hole systems that should be taken into account and that can have observable consequences (see e.g. Lukes-Gerakopoulos, Apostolatos & Contopoulos 2010).

Needless to say, in astrophysical systems with accreting black holes the matter elements have many other (and more serious) reasons to behave in a chaotic way. These extend from microscale processes over (magneto)hydrodynamics of accretion to interaction with (chaotic) radiation. However, as opposed to the case of discrete sources moving in the field of accreting stellar mass black hole (e.g. in an X-ray binary), these 'physical' reasons for chaos should be less important in the case of whole stars orbiting a supermassive black hole in a galactic nucleus. Under the presence of a heavy accretion disc (and/or massive gas torus farther away), the motion of such 'test particles' may exhibit chaotic features on a sufficient timescale, due to the 'gravitational' reasons alone. Admittedly, there are whole star clusters rather than single stars around the nuclear black holes, so each individual star would also 'feel' perturbations from all the other stars. Such a many-body problem is very difficult to tackle in general relativity and even in Newtonian theory it is being treated numerically. A possible simplification is to approximate the influence of the whole cluster on one particular star by means of an additional spherical or other simple-shape potential (see e.g. Karas & Šubr 2007; Löckmann, Baumgardt & Kroupa 2009; Madigan, Levin & Hopman 2009).

In spite of the 'shadowing theorem' (Palmer 2000), it often seems hopeless to model the behaviour of a realistic non-linear dynamical system in detail, because sensitive dependence on initial conditions – one of the characteristic signs of chaos – involves sensitive dependence of conclusions on our ability to describe and treat the system *exactly* (see e.g. Judd & Stemler 2009). Unfortunately, the non-linearity of general relativity as the theory of the underlying configuration space adds another piece of 'sensitivity' to the problem, and furthermore it strongly limits our compass to treat the problem exactly. In particular, the non-linearity severely limits the possibility of describing exactly the gravitational field (i.e. the configuration space) of multicomponent systems, even if they are not extended. At present, the exact analytic treatment of black holes with additional sources is only practically possible in static and axially symmetric case (thus even rotation is excluded in general) with zero cosmological constant. Outside of the sources, the complete space–time can then be described by the (Weyl) metric containing just two unknown functions, one of which has the meaning of Newtonian gravitational potential. In a vacuum, the Einstein equations yield Laplace equation for this potential (like in the Newtonian description), so its 'total' form is obtained simply by adding the contributions from individual sources. The 'non-Newtonian' part of the problem lies in finding the second unknown metric function by a line integral; it is rather an exception than a rule that this can be accomplished explicitly.

We will, however, not repeat this standard introduction to the static and axially symmetric problem; it was summarized, e.g., in the first paper (Semerák & Suková 2010, hereafter Paper I). There, we placed uncharged annular thin discs without radial pressure (and without heat transfer) or their limit – (one-dimensional) rings – symmetrically about the (originally Schwarzschild) black hole in order to approximate the configuration of matter assumed in black hole accretion systems. Considering, in particular, several discs of the inverted Morgan–Morgan counter-rotating family (Lemos & Letelier 1994; Semerák 2003) and the Bach–Weyl ring (Bach & Weyl 1922; D'Afonseca, Letelier & Oliveira 2005) as the additional sources, we studied how the dynamics of time-like geodesics in the field of such a system depends on parameters, mainly on relative mass and position of the external disc/ring and on the energy of test particles. The system showed typical features of a weakly non-integrable dynamical system. We observed, on Poincaré sections and on time series of phase variables and their power spectra, how it gradually turns chaotic when relative mass of the disc/ring or energy of the orbits is increased; we also noted, quite generically, that for very high values of these parameters the system rather recurred to more regular behaviour.

It is a conventional experience how the originally fully regular phase space grains into chains of resonance islands, circumscribed by separatrices from which a net of chaotic filaments originates that gradually spreads and fuses into a 'chaotic sea'. However, besides the overall development of the phase space, it is also interesting to study individual trajectories and try to distinguish different types among them. Actually, it is known (KAM theorem) that in 'weakly perturbed' systems, the phase space contains regions of very different degrees of chaoticity for almost any 'strength' of the perturbation agent. Moreover, even a given *single* orbit may show different degrees of chaoticity/regularity within its different stages. This is especially valid for the orbits prone to 'sticky motion', i.e. those which spend a long time very close to regular islands while only occasionally diverging into a chaotic sea. We already singled out several such orbits in Paper I and illustrated that they can be distinguished from 'strongly chaotic' orbits, drowned in the chaotic sea, according to the power spectra of phase-variable time series [that of 'vertical' position, $z = z(t)$, for example]. In general relativity, this simple method was notably employed by Koyama, Kiuchi & Konishi (2007), who demonstrated (on the problem of spinning particles in a Schwarzschild background) that the power spectra of 'strongly chaotic' orbits have 'white-noise' low-frequency part (relatively flat curve at rather low values), whereas the spectra of 'weakly chaotic' orbits incline to the '1/frequency' shape at low frequencies (and rise to higher values there). This is natural since stronger chaos means more irregular time series with less distinct periods, in particular without marked recurrences even on longer time-scales.

In the present paper, we analyse in more detail several individual orbits selected out of those which – at least for a certain time – adhere to regular regions ('sticky motion'). We show on Poincaré diagrams and on power spectra of the corresponding (z-position) time series that different parts of these orbits present different degree of chaoticity. In stages when the orbits tend to fill uniformly a large area (chaotic sea), the spectrum approaches white noise at low frequencies, whereas almost regular parts of the same orbits indeed generate '1/frequency' shape there. However, even 'highly

regular' parts of such world lines can be clearly distinguished from strictly regular orbits. On the other hand, it is known that even strongly chaotic *deterministic* behaviour is clearly distinguishable from a random one. It is our object here to check the above for selected orbits of our dynamical system. We compare how the character of geodesic dynamics is revealed by z-position power spectra (Section 2), by the 'average directional vector' method based on statistics over the directions in which the trajectory (recurrently) passes through specified phase-space cells (Section 3; see Suková 2011, for preliminary results) and by 'recurrence plots' which visualize the pattern of recurrences to such cells (Section 4). Several useful quantifiers of chaos following from the recurrence plots will also be computed and plotted.

2 POWER SPECTRA OF GEODESICS AND OF THEIR PARTS

Poincaré surfaces of section give a picture of how much regular/chaotic the system with given parameters is. It is a property of 'nearly integrable systems' that some quite irregular trajectories already appear after a tiny perturbation, and vice versa; even a strongly perturbed phase space still harbours some quite regular ones. It can also be recognized on Poincaré diagrams that (in rather strongly perturbed cases) certain orbits behave quite differently within different periods, namely they alternately stick to islands of regular motion and drift around the 'chaotic sea'. Hence, the 'degree of chaoticity' can be ascribed to the system (phase space) on the whole, but also to its individual orbits, while in a sense it is a property of a given part of a given orbit. It should be stressed, however, that such a tracking of regular/chaotic features down to a particular segment of particular orbits has to be taken with much caution, since it is in fact inconsistent with the essence of deterministic chaos as a *global* phenomenon. This is especially clear on systems like billiards, where interaction only occurs at discrete events: one cannot say that their trajectories are almost all regular, with chaos solely occurring at particular points. In systems where the interaction is long range and acts continuously (and, ideally, even smoothly), like the gravitational one in our case, such attempts to 'localize' the character of dynamics are more propitious, but still they do not seem to yield necessary or sufficient criteria (cf. Vieira & Letelier 1996). The global nature of chaos goes together well with the similar attribute of Fourier transform, which probably helps power spectra to be an efficient tool of study of dynamical systems.

We select two geodesic orbits in the field of a black hole (of mass M) surrounded by the inverted first Morgan–Morgan disc with mass $\mathcal{M} = 1.3M$ and inner radius $r_{\rm disc} = 20M$. Such a disc is clearly very massive in comparison with what is considered astrophysically realistic; it causes quite a strong perturbation of the original black hole field and the geodesic dynamics is rather chaotic in general (see Paper I). The selected two orbits have specific energy and angular momentum at infinity $\mathcal{E} \equiv u_t = 0.956$ and $\ell \equiv u_\phi = 4M$, respectively,[1] and initial conditions very close to those of the orbit drawn in light blue in fig. 16 of Paper I; the power spectrum of its z-position is clearly seen in the bottom right-hand panel there, among several other 'weakly chaotic' orbits showing the '1/frequency' spectral shape. Note that the power spectrum is obtained using the discrete Fourier transform:

$$P_\omega(z) = \frac{1}{N}\left|\sum_{n=0}^{N-1} z(\tau_n)\mathrm{e}^{-(2\pi/N)\mathrm{i}\omega\tau_n}\right|, \qquad (1)$$

where N is the total number of samples. The spectrum thus illustrates which frequencies dominate the particle motion perpendicular to the plane where the disc or the ring is placed. Both selected orbits were followed for a long time (of about 10^7M of proper time, which means for some 10^4–10^5 orbital periods) and then divided in parts in order to check how these sections appear in Poincaré diagram and in the power spectrum plot. Rather than showing the figures obtained for all the parts, let us just give several examples. In general, one can repeat the conclusion of Koyama et al. (2007), also supported in our previous paper: the orbits which appear 'strongly chaotic' in Poincaré diagram (filling rather uniformly thick layers there) produce irregular time series whose power spectra have white-noise character at low frequencies (rather flat at low level, without distinct peaks), whereas the orbits which appear 'weakly chaotic' in Poincaré diagram (remaining close to regular islands for considerable periods) produce almost regular time series in the periods of 'sticky motion' (while irregular elsewhere), which brings more power into low frequencies, and the spectrum assumes $1/f$ shape there.

In Fig. 1, the two selected orbits are represented as a whole, first on Poincaré sections showing passages through the equatorial plane in (r, u^r) axes, then on the $u^r(t)$ behaviour and finally on the power spectra of $z(t)$ evolution. The Poincaré sections show that the first (left) trajectory spends some time in the vicinity of the split primary island, but generally it is rather chaotic. The second (right) trajectory fills the chaotic sea less densely and apparently prefers to stay in the layers adjacent to the central regular regions. The time series $z(t)$ and $u^r(t)$ of the second trajectory really contain longer periods of almost regular oscillations, and also the power spectra of $z(t)$ confirm this difference in the above-described sense: the second (right) spectrum is a bit less 'concave' than the first (left) one and it tends more to the power-law, $1/f$ shape, mainly at low frequencies (where it also ends at somewhat higher values). However, both trajectories contain rather chaotic as well as rather regular phases; we give two examples for each of the orbits in Figs 2 and 3. The sections shown on the left are confined to the vicinity of regular islands for considerable intervals, whereas those on the right are quite chaotic as is clear from the respective Poincaré diagrams, $u^r(t)$ courses and power spectra of $z(t)$ evolutions.

Several more specific features can be recognized in the figures. Comparing the weakly chaotic parts of the orbits, one observes that their rather '$1/f$-shaped' power spectra can differ in slope and in noise degree, mainly in the high-frequency part. (Sure: it is important, among others, what is the periodicity of the island that the orbit adheres to.) Some of these spectra can really be almost fitted by a straight line; nevertheless, they typically have distinct peak in the middle part and a 'valley' to the left of this maximum. On the other hand, strongly chaotic parts of the orbits provide 'cat-back', concave spectral shape which cannot be approximated by a straight line; the spectra contain less distinct features, in particular less distinct maximum and valley on its left. However, it would be misleading to generalize *any* tendency seen on certain particular series of spectra, because mainly the quasi-regular phases of motion can involve different amplitudes and periodicities and thus bring different spectral features; this is already clear from the time series themselves. In spite of it, we try to put together a series of orbital sections with different content of chaos/regularity and illustrate how it proves in power spectra (Fig. 4).

[1] We use geometrized units in which $c = G = 1$. The particle's proper time is denoted by τ and its four-velocity by u^μ. The Schwarzschild-type coordinates (t, r, θ, ϕ) are employed, with vertical position $z = r\cos\theta$. In particular, the time t is tied to the time-like Killing symmetry of space–time.

© 2012 The Authors, MNRAS **425,** 2455–2476
Monthly Notices of the Royal Astronomical Society © 2012 RAS

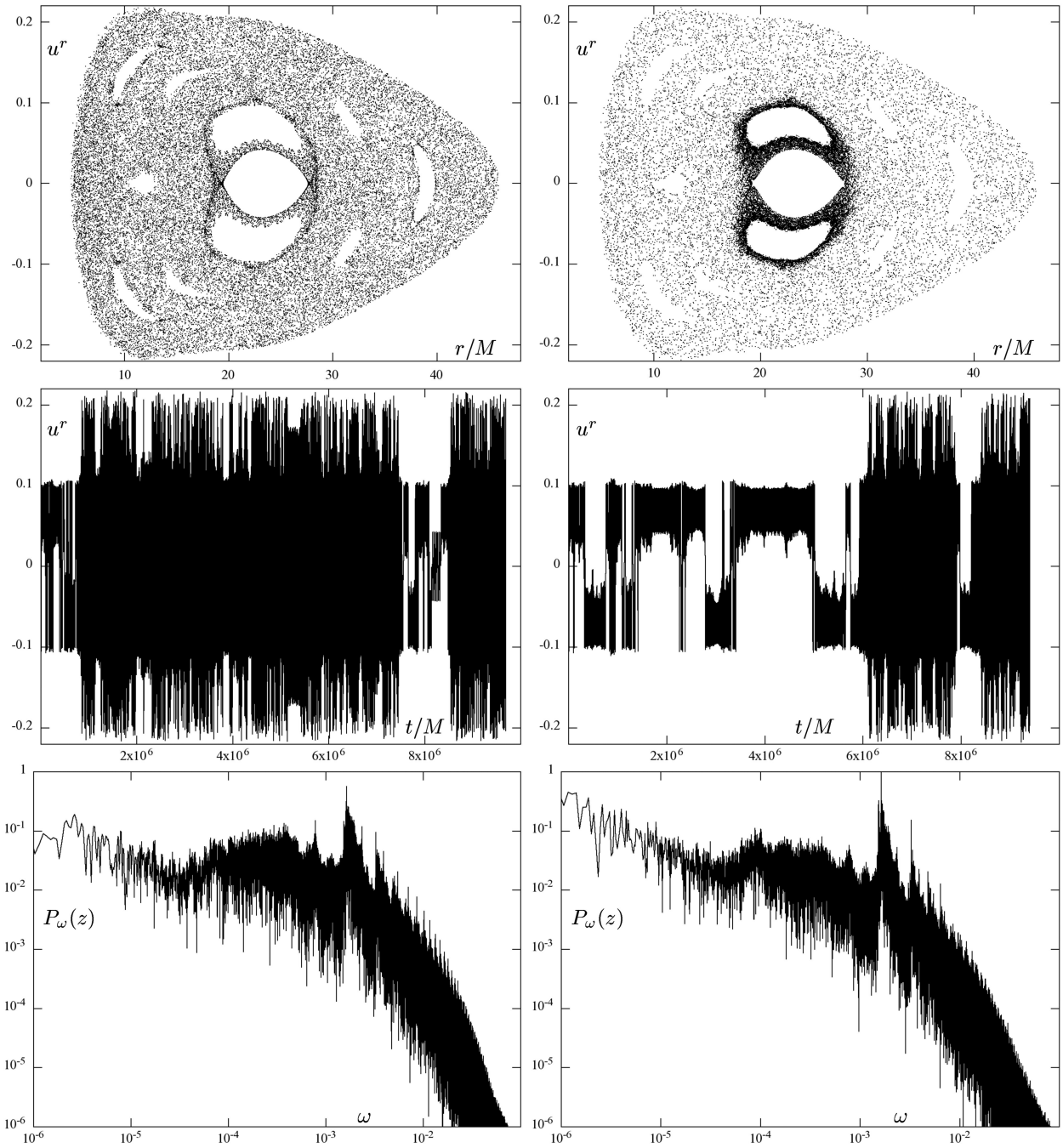


Figure 1. Two geodesic orbits in the field of a black hole (of mass M) surrounded by the inverted first Morgan–Morgan disc with mass $\mathcal{M} = 1.3M$ and inner radius $r_{\rm disc} = 20M$. Both geodesics have specific energy and specific angular momentum at infinity $\mathcal{E} = 0.956$ and $\ell = 4M$. The orbit on the left is clearly more chaotic, the one on the right spends more time in the vicinity of central regular islands in the Poincaré diagram (showing passages across the equatorial plane, top row). The time series of u^r (given by values recorded at passages through the equatorial plane) are plotted in the middle row and the power spectra of the $z(t)$ evolution are plotted in the bottom row.

3 KAPLAN–GLASS METHOD OF DIAGNOSING THE DEGREE OF CHAOS

There exists a large number of methods to recognize the degree of chaoticity – or even stochasticity – present in the time evolution of a given system. We will not give any comparative analysis, and not even a listing of them, but will just illustrate that processing of time series in some other way can yield information which is interesting to compare with what is revealed by power spectra. As an example of a simple but useful method, we will consider the one suggested by Kaplan & Glass (1992). It was designed to distinguish between deterministic and random systems, but we will see that it is quite sensitive and also able to recognize how much chaotic the (deterministic) system is.

The method of Kaplan and Glass is based on monitoring the evolution of tangent to the trajectory in small subsets of phase space. However, it is not the 'original' phase space of the system (this may be unknown), but a d-dimensional embedding 'reconstructed' from

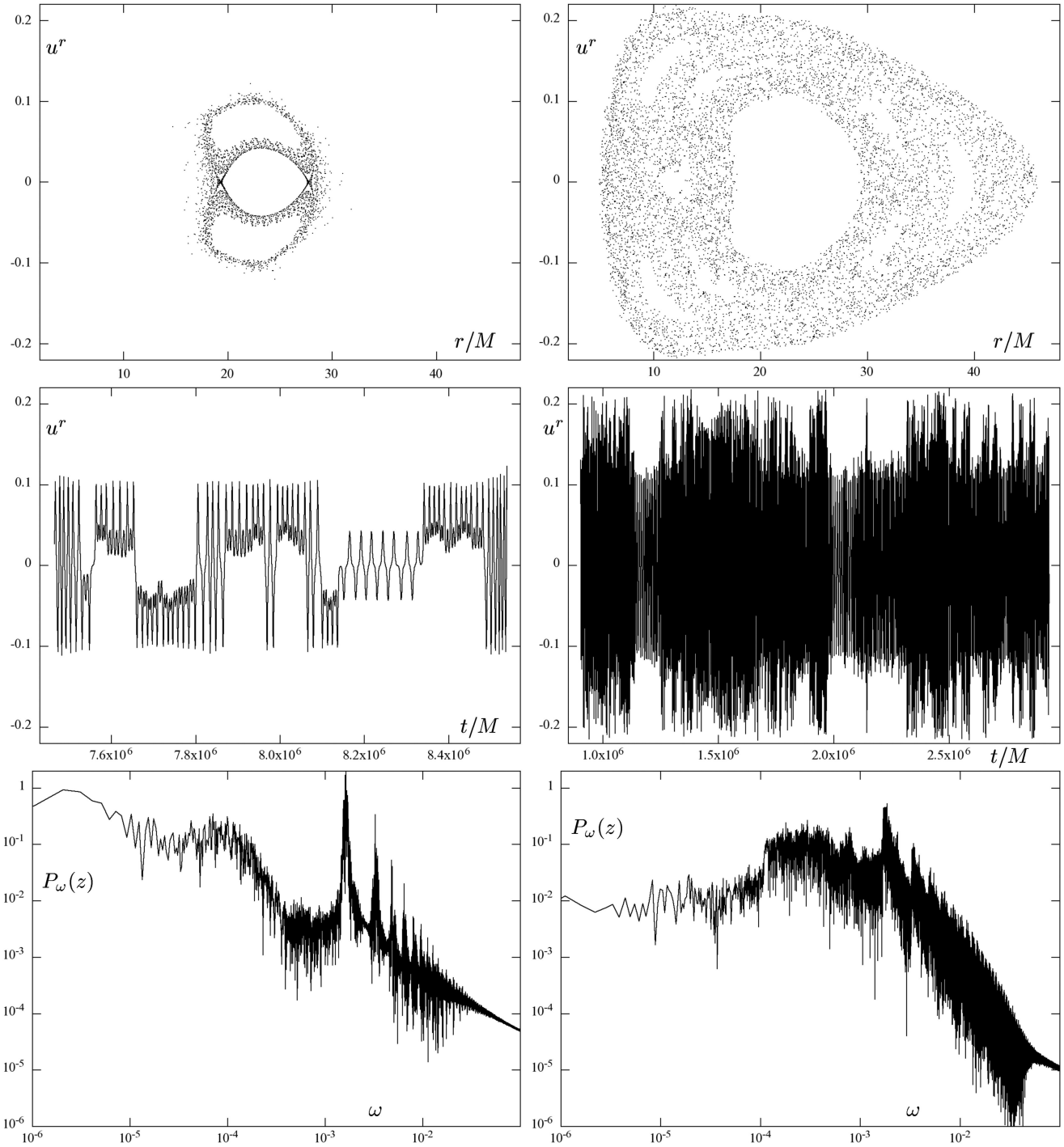


Figure 2. Example of a rather regular (left-hand column) and rather chaotic (right-hand column) phases of the orbit shown in the left-hand column of Fig. 1. Equatorial Poincaré section (top), $u^r(t)$ time series recorded at passages through the equatorial plane (middle) and power spectrum of the $z(t)$ evolution (bottom) are shown.

a given data series $x(\tau)$ by taking the delayed replicas $x(\tau)$, $x(\tau - \Delta\tau)$, $x(\tau - 2\Delta\tau), \ldots, x(\tau - d\Delta\tau)$ as its axes ($\Delta\tau$ is some real-time shift); the reconstruction is justified by the delay embedding theorem of Takens (1981). Such a space is then coarse grained into a grid of m^d cubes and average directions of passages through each of these cubes are added up. Namely, first the average direction of each (kth) pass of a trajectory through the given (jth) box is recorded as a unit form $\boldsymbol{v}_{kj}$ of the vector connecting the point where the trajectory entered the box with the point where it left it. Then the vectors obtained from a large number (n_j) of transits through the jth box are summed (vector addition) and the length of the resulting vector V_j is normalized by n_j:

$$V_j \equiv |\boldsymbol{V}_j| = \frac{1}{n_j} \sum_{k=1}^{n_j} \boldsymbol{v}_{kj} \ .$$

© 2012 The Authors, MNRAS **425,** 2455–2476
Monthly Notices of the Royal Astronomical Society © 2012 RAS

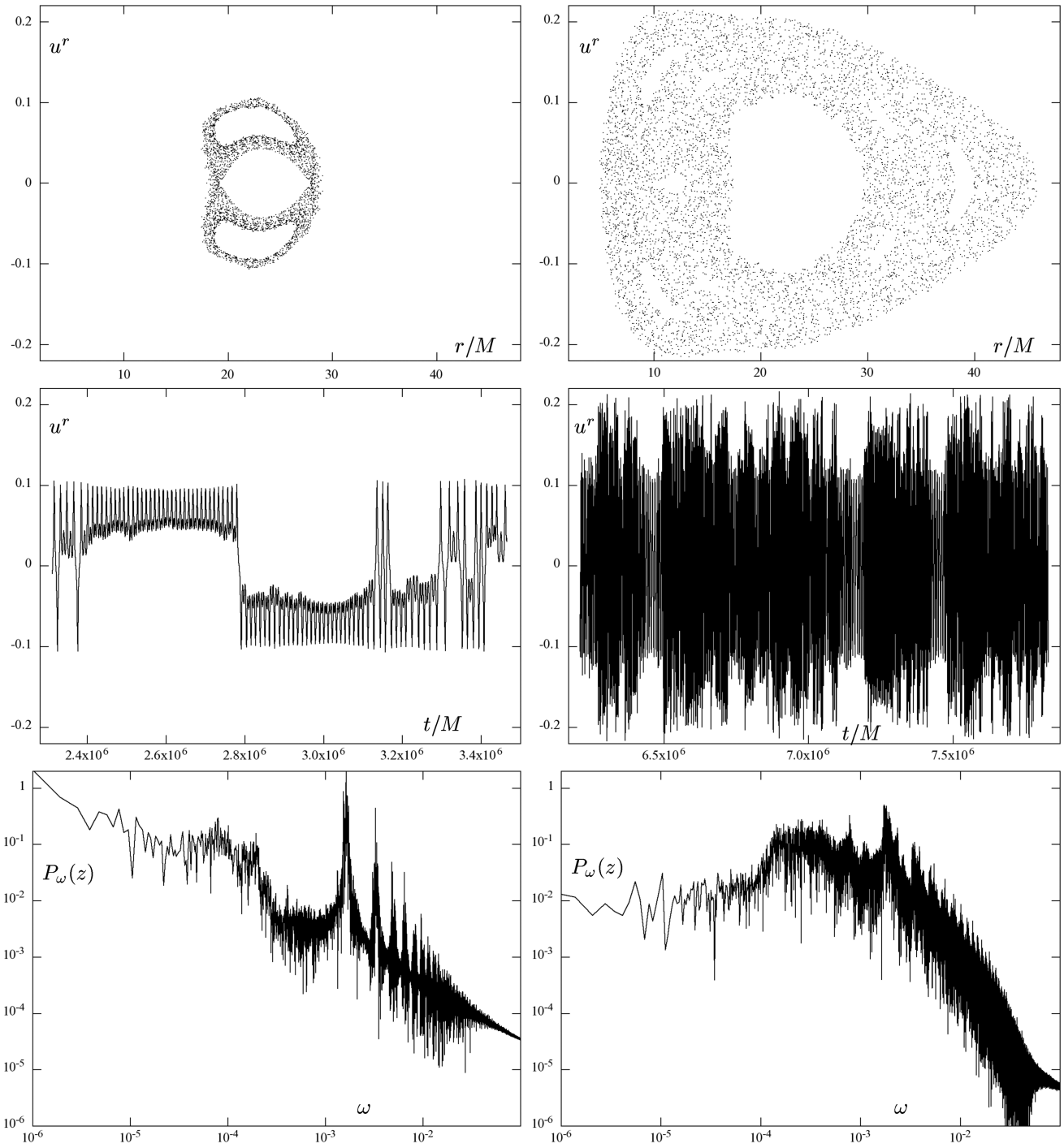


Figure 3. Example of a rather regular (left-hand column) and rather chaotic (right-hand column) phases of the orbit shown in the right-hand column of Fig. 1. Equatorial Poincaré section (top), $u^r(t)$ time series recorded at passages through the equatorial plane (middle) and power spectrum of the $z(t)$ evolution (bottom) are shown.

Finally, the resulting norm V_j is averaged over all boxes which were crossed n times, and the dependence of this average ($\equiv \bar{L}^d_n$) on n is checked. For random data, $\bar{L}^d_n$ decreases with n roughly as $n^{-1/2}$; in particular, the average displacement per step for random walk in d dimensions is (for large n) given by

$$\bar{R}^d_n = \frac{\Gamma\left(\frac{d+1}{2}\right)}{\Gamma\left(\frac{d}{2}\right)} \sqrt{\frac{2}{nd}}\,, \tag{2}$$

where $\Gamma(.)$ denotes the gamma function. (Note that $\bar{R}^{d\to\infty}_n = n^{-1/2}$.) For a deterministic system, the average $\bar{L}^d_n$ decreases more slowly or even remains close to a maximal value of 1; this is due to the fact that in every small neighbourhood the tangent vectors from all transits are almost parallel, so the norm of their vector sum is almost maximal. (It depends on box size, however: theoretically, in the limit of infinitesimally fine grain, which is only conceivable for infinitely long data series, $\bar{L}^d_n = 1$ for the deterministic dynamics.)

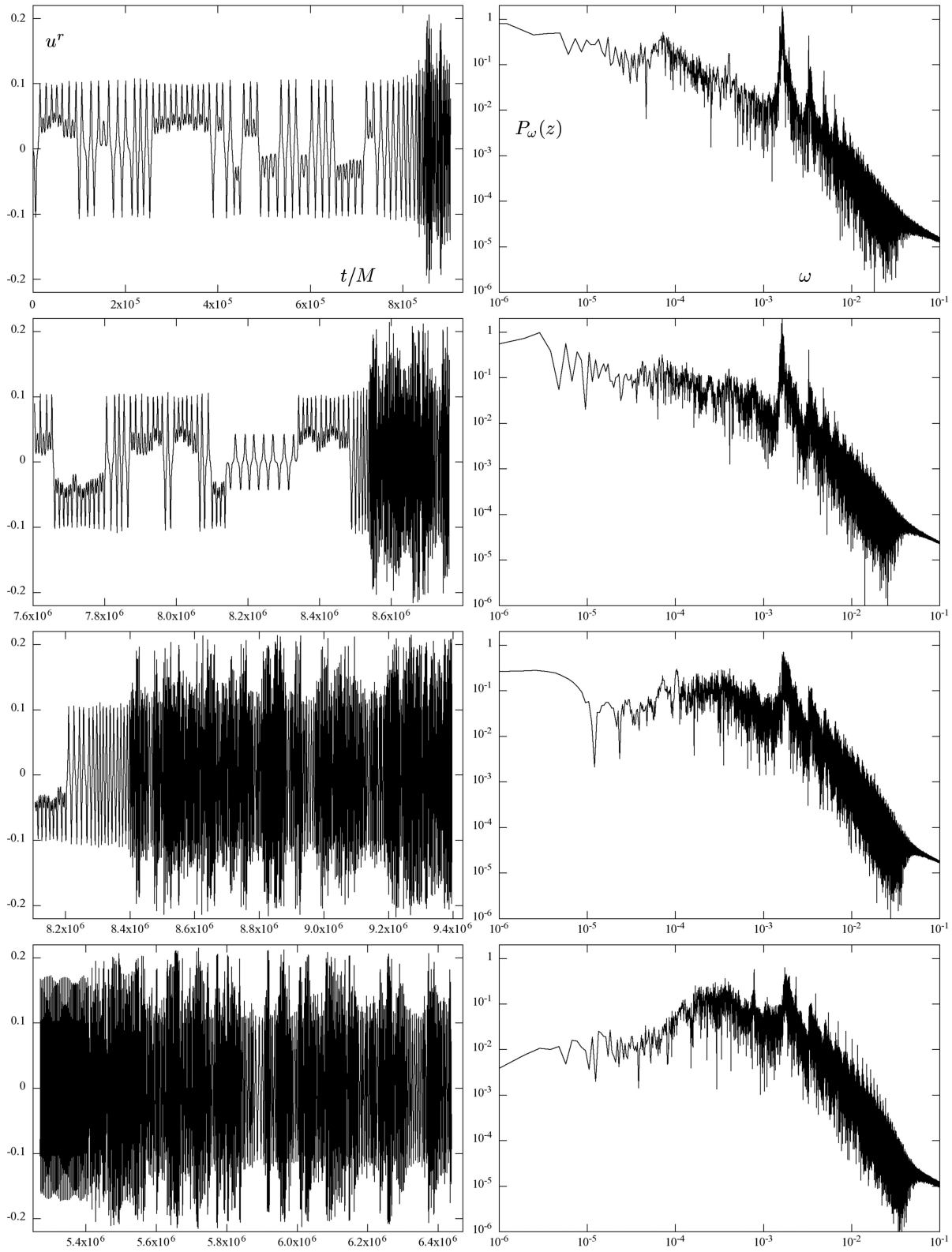


Figure 4. The $u^r(t)$ behaviour (left-hand column) and power spectra of $z(t)$ evolution (right-hand column) of four different sections of orbits shown in Fig. 1; taken from top to bottom, the first, the second and the fourth sections are parts of the first orbit (shown in the left part of Fig. 1), while the third section belongs to the second orbit (right part of Fig. 1). The degree of chaoticity clearly grows from top to bottom.

© 2012 The Authors, MNRAS **425,** 2455–2476
Monthly Notices of the Royal Astronomical Society © 2012 RAS

Besides the size of the lattice boxes, the result clearly depends on the dimension d and the time lag $\Delta\tau$. In particular, the choice of $\Delta\tau$ may be a subtle issue, as discussed in the original paper (Kaplan & Glass 1992). In order to analyse the dependence of $\bar{L}^d_n$ on $\Delta\tau$, one can compare the value of V_j with $\bar{R}^d_{n_j}$ for each box and average this over all occupied boxes:

$$\bar{\Lambda}(\Delta\tau) \equiv \left\langle \frac{(V_j)^2 - \left(\bar{R}^d_{n_j}\right)^2}{1 - \left(\bar{R}^d_{n_j}\right)^2} \right\rangle . \tag{3}$$

In a theoretical limit, $\bar{\Lambda} = 0$ for a random walk, whereas $\bar{\Lambda} = 1$ for a deterministic system. In practice, with finite series and finite 'pixel' size, $\bar{\Lambda}$ falls off roughly as autocorrelation function for randomized signal, while it happens more slowly for a deterministic signal.

For our system of geodesic dynamics in the static and axially symmetric field of a black hole surrounded by a disc or a ring, we choose $d = 3$ and construct the 'phase space' out of the time series of the test particle vertical position $z = r\cos\theta$ (r and θ are Schwarzschild radius and latitude), i.e. the space is spanned by the axes $z(\tau)$, $z(\tau - \Delta\tau)$ and $z(\tau - 2\Delta\tau)$. We choose its 'elementary grain' size of the order of M (thus volume $\simeq M^3$) and focus on the behaviour of $\bar{\Lambda}$ with increasing $\Delta\tau$. Computation of this dependence for a large number of orbits (or their parts) confirmed that the method of Kaplan and Glass is able to reveal the degree of their chaoticity. For rather regular ('sticky') evolutions, $\bar{\Lambda}$ really remains very close to 1 except when $\Delta\tau$ is just multiple of some important orbital period. On the other hand, for strongly chaotic (parts of the) orbits, $\bar{\Lambda}$ has a peak almost approaching 1 for a certain value of $\Delta\tau$ (which is smaller than a period and is related to the first zero of the autocorrelation function) and then it decreases quite rapidly (with some oscillation), because around such orbits the geodesic flow is sensitive to initial conditions and the deterministic connection between the position $x(\tau)$ and $x(\tau - \Delta\tau)$ fades away quickly with the growing time lag. The rate of decrease of $\bar{\Lambda}(\Delta\tau)$ is a simpler (more easily comparable) indicator of the degree of chaoticity of the orbit than the power spectrum. Namely, it is just the *value* of $\bar{\Lambda}(\Delta\tau)$ that is important, whereas the spectrum mainly bears its information in the overall shape and the 'degree of noisiness', of which especially the latter may be difficult to judge and compare. At the same time, the Kaplan–Glass $\bar{\Lambda}(\Delta\tau)$ indicator seems to be quite reliable, and also 'fine' in the sense that it can distinguish between evolutions which appear very similar (or just not easily comparable) on spectra.

Let us illustrate this on several parts of our two orbits discussed in the previous section. Fig. 5 shows spectra of six different orbital sections, of which the first and the fifth are parts of the second orbit and the rest are parts of the first orbit. The sections are placed (top left, top right, middle left, etc.) in the order of increasing chaos. Fig. 5(b) shows the $\bar{\Lambda}(\Delta\tau)$ functions for the same six orbital sections. It is seen how the $\bar{\Lambda}(\Delta\tau)$ behaviour safely distinguishes between the first four examples which are all 'rather regular' and have just slightly different character of spectra. [However, after the clue is provided by $\bar{\Lambda}(\Delta\tau)$, one admits that the spectra also reveal the same tendency.] On the other hand, $\bar{\Lambda}(\Delta\tau)$ appears not to be so sensitive in more chaotic regions: starting from a certain amount of chaoticity, it does not decrease any more and gives similar behaviour for orbital phases which still quite differ in spectra, mainly in the low-frequency tail. [For instance, the last two examples of Fig. 4 yield the same course of $\bar{\Lambda}(\Delta\tau)$.]

We add two more illustrations, one (Fig. 6) showing two orbits in the field of a black hole with the inverted Morgan–Morgan disc of parameters different from above (mass $\mathcal{M} = 0.5M$ and inner radius $r_{\rm disc} = 14M$) and the other (Fig. 7) showing two orbits in the field of a black hole surrounded by a thin, Bach–Weyl ring (of mass $\mathcal{M} = 0.5M$ and radius $r_{\rm ring} = 20M$). The orbits in Fig. 6 are only slightly different, one belonging to five-periodic regular islands and the other sticking closely to the first; we can see how they differ in power spectra and in the $\bar{\Lambda}(\Delta\tau)$ dependence. The orbits presented in Fig. 7 differ much more, one lying very close to the central circular orbit of the primary regular island, while the other filling the chaotic sea around and in the vicinity of the ring.

4 RECURRENCE ANALYSIS OF THE ORBITS

Let us stress again that the above method is just an example of a simple but apparently quite reliable way of judging and classifying the regularity/chaoticity/stochasticity of a given time series. Another example of a simple and powerful method is the recurrence analysis which is based on checking the recurrence of orbits of a dynamical system to a chosen (small) cell of phase space (see Marwan et al. 2007, for a thorough survey). The pattern of recurrences encodes quite credibly the character of the dynamics, clearly distinguishing between regular, chaotic and random evolutions. Within general relativity, the method has recently been employed, e.g., by Kopáček et al. (2010) in their study of orbital dynamics of a charged test particles around a rotating black hole immersed in a magnetic field.

A very useful tool for visualization of the recurrences is *recurrence plot*, introduced by Eckmann, Oliffson Kamphorst & Ruelle (1987). Suppose one knows the phase-space trajectory with constant step of time (we use proper time in our case of geodesic motion in a given space–time).[2] Denoting by $\boldsymbol{X}_i = \boldsymbol{X}(\tau_i)$ the N successive points of the phase trajectory, one defines the so-called recurrence matrix by

$$R_{i,j}(\epsilon) = \Theta\left(\epsilon - \|\boldsymbol{X}_i - \boldsymbol{X}_j\|\right), \qquad i, j = 1, \ldots, N , \tag{4}$$

where ϵ is the radius of a chosen neighbourhood (it is called threshold), $\|\cdot\|$ denotes the chosen norm (in accord with a common experience, the picture of long-term dynamics only slightly depends on which norm is chosen) and Θ is the Heaviside step function. The matrix thus contains only units and zeros and can be easily visualized by representing 1's by black dots (while 0's by blank spaces) at the respective coordinates i, j. For regular systems, the black points tend to arrange in distinct structures, in particular in long parallel diagonal lines (their distance scales with period) and checkerboard structures, whereas for random behaviours the black points are scattered without order. Chaotic systems yield the most 'artistic' plots: they contain blocks of almost-diagonal patterns as well as irregular ones, apparently placed one over another within horizontal and vertical structures. The main diagonal $R_{i,i}$ is trivial ('line of identity') and present in every system (for it is often omitted) and the matrix is symmetric with respect to it. The almost-regular blocks correspond to time intervals when the trajectory sticks to some unstable periodic orbit; the more unstable this orbit is, the earlier the trajectory deviates from it and so the smaller is the block. Horizontal/vertical lines indicate periods when the system is trapped in some region of phase space without much change.

[2] The knowledge of just one phase variable (e.g. position) is in fact enough, since the phase space can be reconstructed from a sequence of its time-delayed series as in the directional vectors method discussed in the previous section.

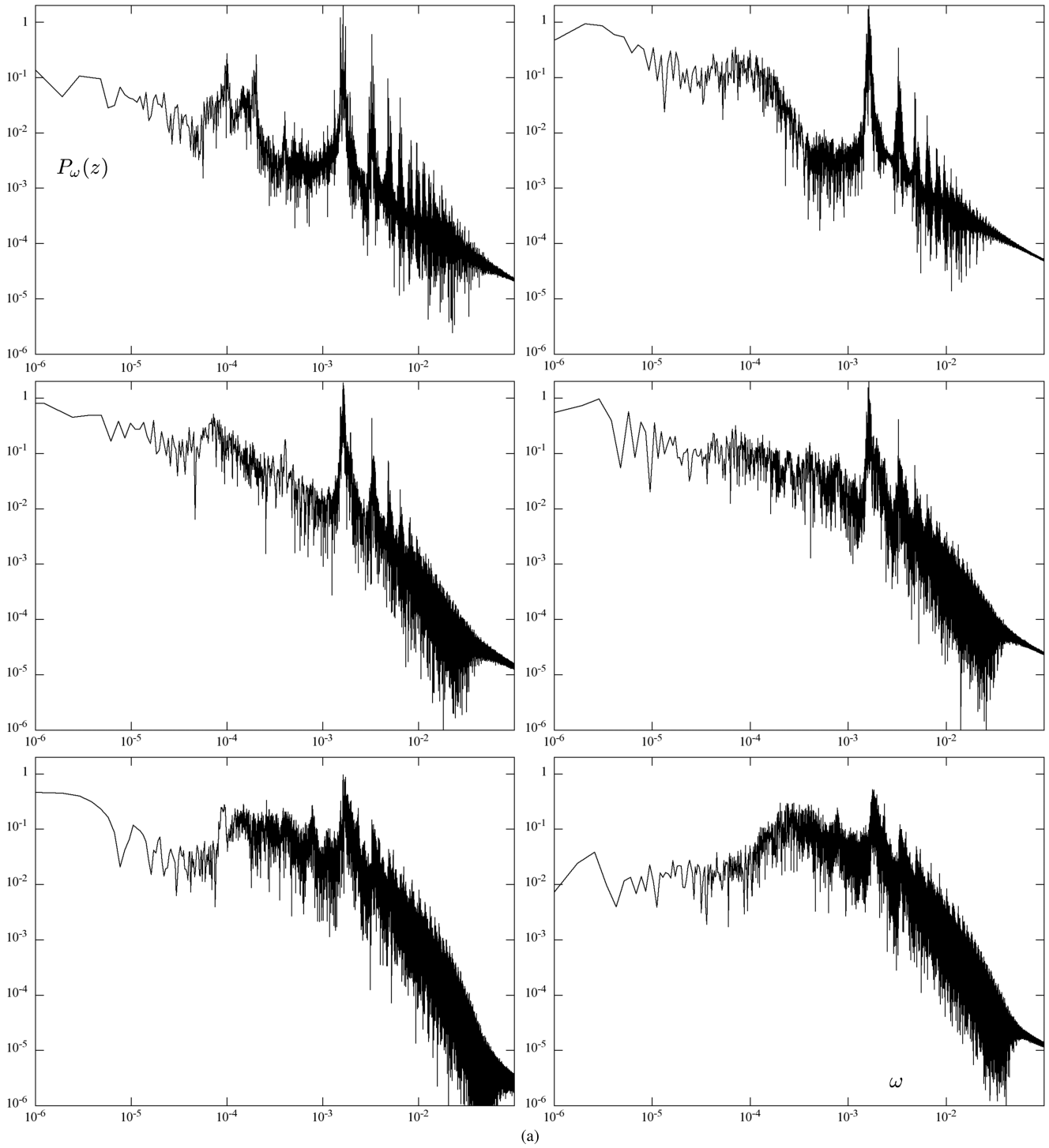


Figure 5. (a) Power spectra of six different parts of the two orbits studied in the last section. In the order from top left to bottom right, their degree of chaoticity increases (but here on spectra it is barely obvious for the first three or four of them). (b) The Kaplan–Glass function $\bar{\Lambda}(\Delta\tau)$ calculated for the same six orbital phases whose power spectra are shown in Fig. 5(a). The behaviour of $\bar{\Lambda}(\Delta\tau)$ clearly distinguishes between these examples, in particular between the first four of them which appear quite similar according to spectra. On the other hand, the last two – quite chaotic – cases are similar here, although their power spectra show somewhat different degree of chaoticity.

Judging the prominence of diagonal or other patterns within the recurrence plot by pure observation is, of course, subjective, so several quantifiers of the recurrence-matrix properties have been proposed. The simplest of them is the recurrence rate, given by ratio of the recurrence points (black ones) within all points of the matrix:

$$RR(\epsilon) = \frac{1}{N^2} \sum_{i,j=1}^{N} R_{i,j}(\epsilon)\,.$$

© 2012 The Authors, MNRAS **425,** 2455–2476
Monthly Notices of the Royal Astronomical Society © 2012 RAS

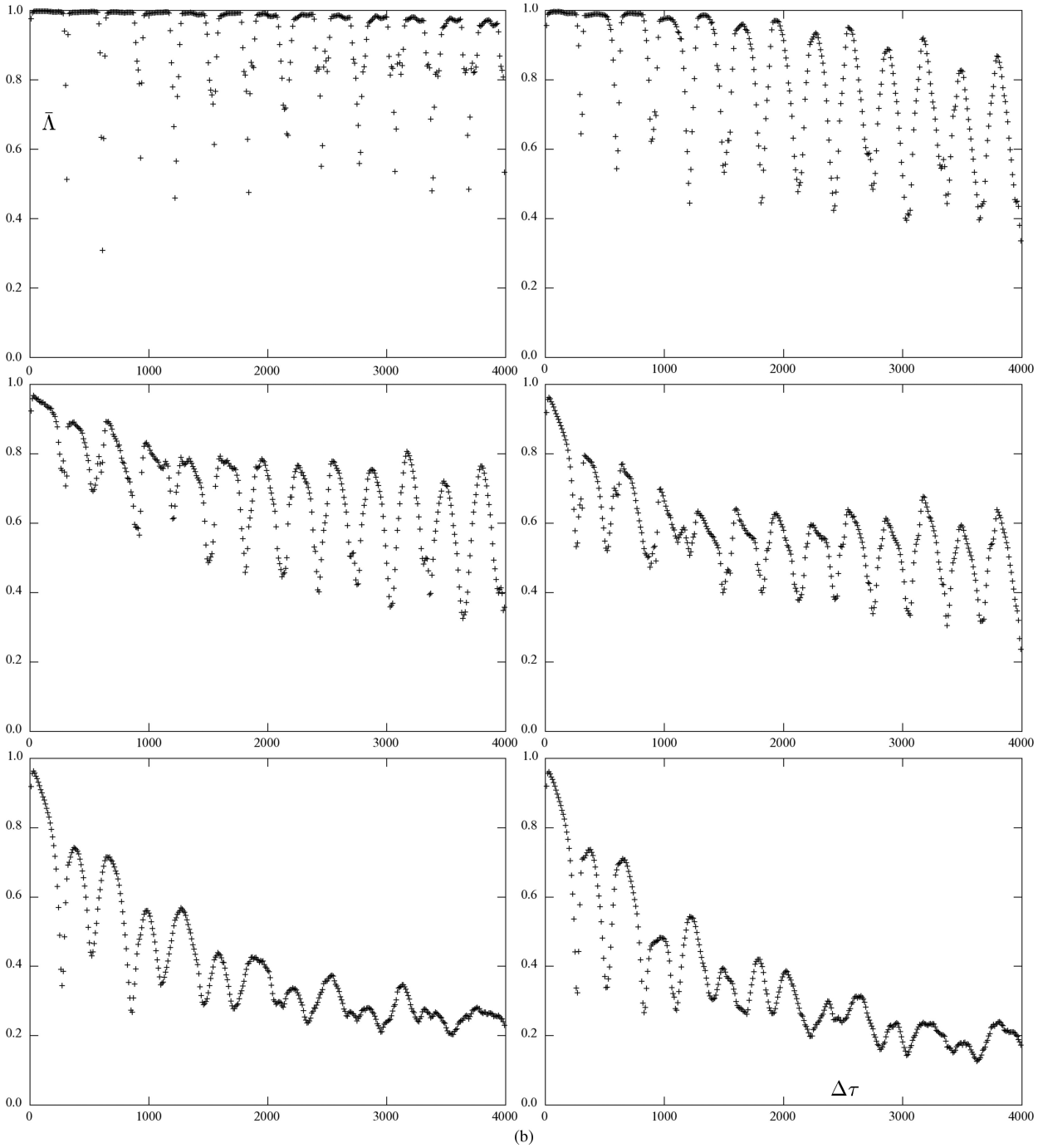


Figure 5 – *continued*

Another most important quantifier is the histogram of diagonal lines of a certain prescribed length l:

$$P(\epsilon, l) = \sum_{i,j=1}^{N} [1 - R_{i-1,j-1}(\epsilon)][1 - R_{i+l,j+l}(\epsilon)] \times \prod_{k=0}^{l-1} R_{i+k,j+k}(\epsilon)\,.$$

Several further quantities can in turn be computed from this histogram. The one called *DET* is given by ratio of the points which form a diagonal line longer than a certain $l_{\min}$ within all the recurrence points:

$$DET(\epsilon) = \frac{\sum_{l=l_{\min}}^{N} l\,P(\epsilon, l)}{\sum_{l=1}^{N} l\,P(\epsilon, l)}\,,$$

while the average length of diagonal lines is

$$L(\epsilon) = \frac{\sum_{l=l_{\min}}^{N} l\,P(\epsilon, l)}{\sum_{l=l_{\min}}^{N} P(\epsilon, l)}\,.$$

The length of the longest diagonal $L_{\max}(\epsilon) = \max_{i=1,\ldots,N}\{l_i\}$ and its inverse $DIV(\epsilon) = 1/L_{\max}(\epsilon)$ are also of interest, since they are

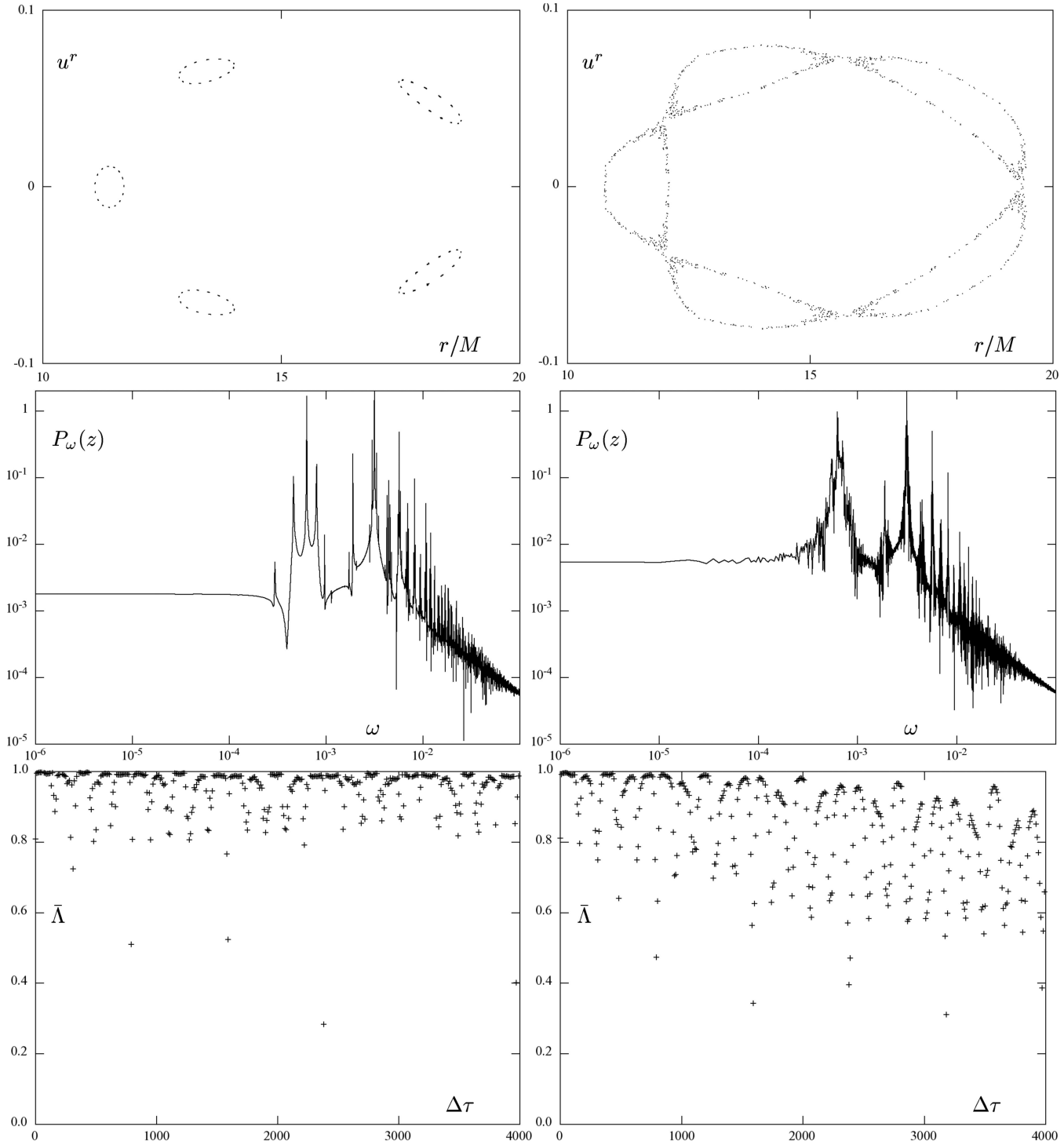


Figure 6. Two geodesic orbits in the field of a black hole (of mass M) surrounded by the inverted first Morgan–Morgan disc with mass $\mathcal{M} = 0.5M$ and inner radius $r_{\rm disc} = 14M$. Both geodesics have specific energy and specific angular momentum at infinity $\mathcal{E} = 0.955$ and $\ell = 3.75M$. The first (left-hand column) belongs to five-periodic regular islands and the other (right-hand column) sticks to these islands rather closely on Poincaré diagrams (top row). The slight difference between the orbits also shows on power spectra of their $z(t)$ evolution (middle row) and on the behaviour of their tangent's autocorrelation represented by the $\bar{\Lambda}(\Delta\tau)$ dependence (bottom row).

most directly related to the rate of divergence of nearby orbits and serve as a rough estimate of the largest Lyapunov exponent.

It is possible to make this estimate more precise, because the cumulative histogram of diagonals yields the second-order Rényi's entropy K_2 (also called correlation entropy), which stands for a lower estimate of the sum of positive Lyapunov exponents. Let the phase space be divided in boxes with size ϵ, numbered in some order by $i_1, \ldots, i_l$. Denote by $p_{i_1,\ldots,i_l}(\epsilon)$ the probability that the point $\boldsymbol{X}(\Delta\tau)$ is in the i_1th box, the following point $\boldsymbol{X}(2\Delta\tau)$ is in the i_2th box and so on, up to the point $\boldsymbol{X}(l\Delta\tau)$. The second-order

© 2012 The Authors, MNRAS **425,** 2455–2476
Monthly Notices of the Royal Astronomical Society © 2012 RAS

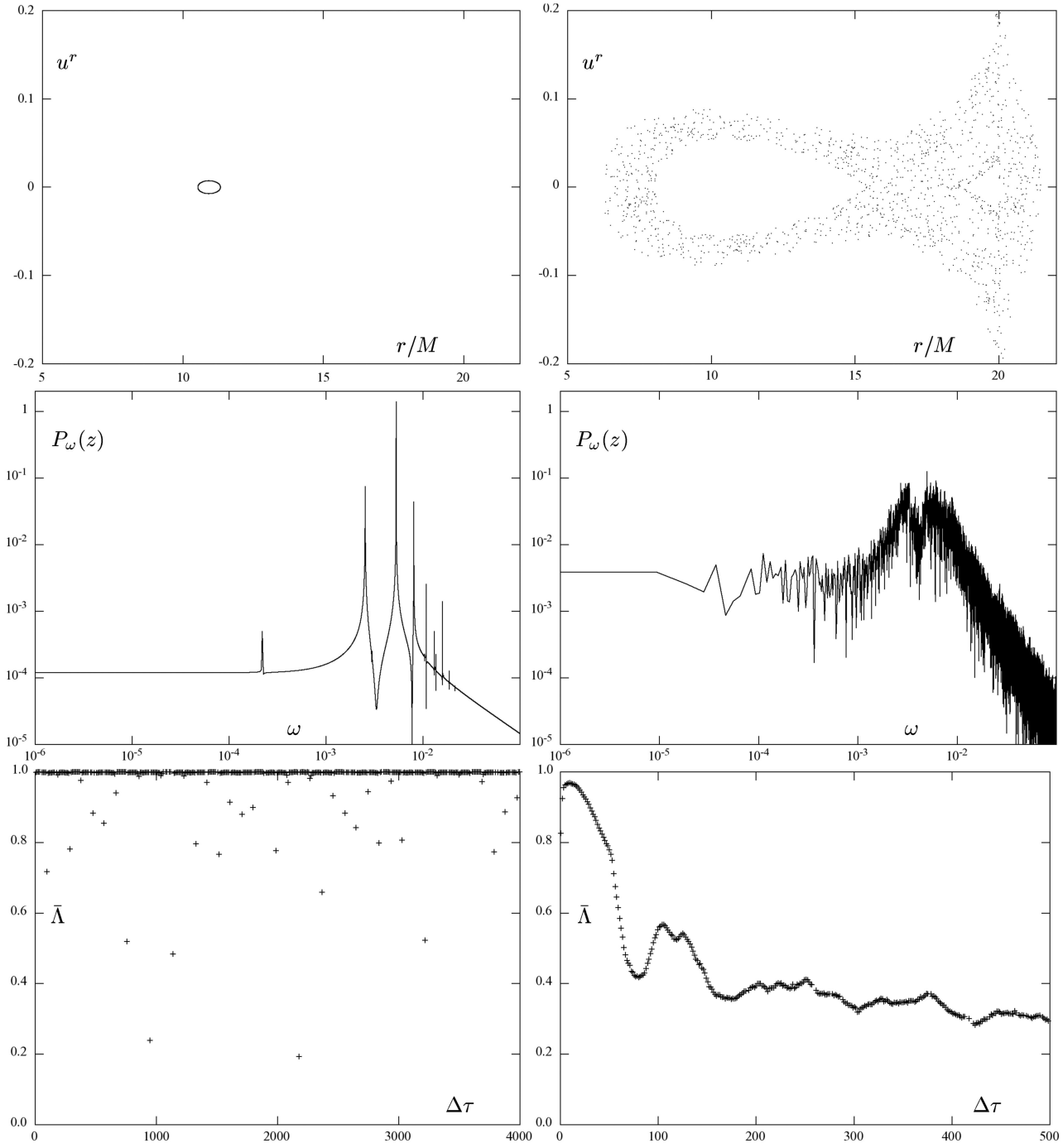


Figure 7. Two geodesic orbits in the field of a black hole (of mass M) surrounded by the Bach–Weyl thin ring with mass $\mathcal{M} = 0.5M$ and radius $r_{\rm ring} = 20M$. Both geodesics have specific energy and specific angular momentum at infinity $\mathcal{E} = 0.93$ and $\ell = 3.75M$. The first (left-hand column) lies deep in the primary regular island, while the other (right-hand column) fills the chaotic sea around and in the vicinity of the ring (see Poincaré diagrams in top row). The big difference between the orbits also shows on power spectra of their $z(t)$ evolution (middle row) and on the behaviour of the Kaplan–Glass averaged autocorrelation parameter $\bar{\Lambda}(\Delta\tau)$ (bottom row).

Rényi's entropy K_2 is given by

$$K_2(\epsilon, l) = -\lim_{\Delta\tau\to 0}\lim_{\epsilon\to 0}\lim_{l\to\infty}\frac{1}{l\Delta\tau}\ln\sum_{i_1}^{i_l} p^2_{i_1,\ldots,i_l}(\epsilon)\,. \tag{5}$$

Realizing that the occurrence of (non-trivial) diagonal of length l means that l successive points of the trajectory $\boldsymbol{X}(\tau), \boldsymbol{X}(\tau+\Delta\tau), \ldots, \boldsymbol{X}(\tau+(l-1)\Delta\tau)$ lie in the ϵ-neighbourhoods of certain other l successive points $\boldsymbol{X}(\tau_0), \boldsymbol{X}(\tau_0+\Delta\tau), \ldots, \boldsymbol{X}(\tau_0+(l-1)\Delta\tau)$, Marwan et al. (2007) showed that (under the assumption of ergodicity) the sum can be approximated by

$$\sum_{i_1}^{i_l} p^2_{i_1,\ldots,i_l}(\epsilon) \approx \frac{1}{N}\sum_{t=1}^{N} p_t(\epsilon, l)\,, \tag{6}$$

where $p_t(\epsilon, l)$ is the probability of finding the line of length l in the boxes centred at points $\boldsymbol{X}(\tau)$, $\boldsymbol{X}(\tau + \Delta\tau), \ldots, \boldsymbol{X}(\tau + (l-1)\Delta\tau)$. Hence, K_2 can be estimated from the relation

$$K_2(\epsilon, l) \approx \hat{K}_2(\epsilon, l) = -\frac{1}{l\Delta\tau} \ln p_c(\epsilon, l)\,, \tag{7}$$

where $p_c(\epsilon, l)$ is the probability of finding a diagonal line whose length is *at least* l. This means that $\hat{K}_2$ is determined by a slope of the cumulative histogram plotted (in logarithmic scale) against the diagonal length l. At the same time, the correlation entropy K_2 was shown to yield a lower estimate of the sum of positive Lyapunov exponents; hence the estimate $\hat{K}_2$ is a good indicator of chaotic behaviour.

Similarly as with diagonal lines, one can plot the histogram of vertical (or horizontal) lines (against their length v):

$$P(\epsilon, v) = \sum_{i,j=1}^{N} (1 - R_{i,j}(\epsilon))(1 - R_{i,j+v}(\epsilon)) \prod_{k=0}^{v-1} R_{i,j+k}(\epsilon)\,,$$

and also the respective measure of vertical structures (parallel of *DET*, called laminarity):

$$LAM(\epsilon) = \frac{\sum_{v=v_{\min}}^{N} vP(v)}{\sum_{v=1}^{N} vP(v)}\,.$$

The average length of vertical lines,

$$TT(\epsilon) = \frac{\sum_{v=l_{\min}}^{N} vP(v)}{\sum_{v=v_{\min}}^{N} P(v)}\,,$$

is called trapping time, because it indicates for how long the system is 'trapped' (without evolution in phase space). Finally, from the probabilities that some chosen diagonal or vertical line has length l, $p(l) = P(l)/N_l$ and $p(v) = P(v)/N_v$, where N_l and N_v are total numbers of diagonal and vertical lines, one can compute the so-called Shannon entropies:

$$L\,ENTROPY = -\sum_{l=l_{\min}}^{N} p(l) \ln p(l)\,,$$

$$V\,ENTROPY = -\sum_{v=v_{\min}}^{N} p(v) \ln p(v)\,.$$

Also relevant as indicator is the size of the 'white gaps' between vertical (or horizontal) lines, because it is related to the recurrence times. For example, let us choose a point $\boldsymbol{X}_i$ on some trajectory and record the sequence of points which fall in its ϵ-neighbourhood, $\{\boldsymbol{X}_{j_1}, \boldsymbol{X}_{j_2}, \ldots\}$ (this set corresponds to black dots in a certain column/row of the recurrence matrix). Compute the recurrence times given by differences between serial numbers of the consecutive recurrence points $\boldsymbol{X}_{j_{k+1}}, \boldsymbol{X}_{j_k}$ multiplied by the respective proper time steps, $T_k(\epsilon) = (j_{k+1} - j_k)\Delta\tau$. The mean of T_k is called the recurrence time of the first type, $T1$. However, the recorded set usually also contains successive points between which the orbit does not leave the given ϵ-neighbourhood, so $T_k(\epsilon) = 1$. These points (called sojourn points) do *not* represent true recurrences, so they should be discarded from statistics. After removing all the sojourn points, the above recurrence set contains just beginnings of the vertical black lines. An average of their distances (average length of white vertical gaps) is called the second-type recurrence time, $T2$. The recurrence times typically behave inversely to *RR*.

For the recurrence analysis to yield plausible results, it is crucial to set the parameters ϵ, $\Delta\tau$, $l_{\min}$ and $v_{\min}$ properly. The dependence of the results on these parameters is itself interesting to explore. In particular, the recurrence matrix and all the quantities computed from it depend critically on the 'target' size ϵ. For example, when ϵ is chosen too large, the time step $\Delta\tau$ rather small and/or $l_{\min}$ (or $v_{\min}$) too small, there are plenty of sojourn points in the recurrence matrix. On the other hand, if ϵ is too small, the matrix may come out too sparse. The $l_{\min}$ limits the occurrence of short diagonal lines which are often formed, when ϵ is large enough, due to the fact that the ϵ-neighbourhoods of the nth and $(n+1)$th recurrence loops have finitely long non-empty intersection, even though the loops may be quite diverging from each other. Finally, there is a subtle issue of misleading long secondary diagonals, which was pointed out by Marwan et al. (2007); let us briefly discuss it here: an abundant occurrence of sojourn vertical sequences involving the main diagonal leads to the occurrence of another long diagonal in the main-diagonal vicinity, which deforms the recurrence quantifiers if they are taken into account. Namely, the usage of $v_{\min}$ only excludes the short sojourn verticals from the statistics, but does not influence the statistics of diagonals; and the usage of $l_{\min}$ only excludes *short* diagonals, not the long ones. Therefore, in order to get rid of the latter, a certain lower bound for the length of vertical lines (called Theiler's parameter, w) is sometimes required *in recording the recurrence matrix* (in addition to the careful choice of ϵ), i.e. only the points are considered whose serial indices i and j satisfy $|j - i| \geq w$. We used the Theiler's parameter only in computing Figs 10 and 14 (right-hand column).

Several examples of recurrence plots obtained for our black hole–disc system are attached. For computation of the recurrence matrix, we used the Euclidean norm (both position and velocity are processed as vectors in Euclidean space) and 'Cartesian' spatial mesh corresponding to spherical Schwarzschild coordinates; each of the three coordinates has been normalized to zero mean value and unit standard deviation. First, we drew the recurrence plots for orbits (or their parts) studied in previous sections in order to compare the information they reveal with that provided by Poincaré maps, time series and their spectra, and by the average directional vector method. Fig. 8 shows recurrence plots of the two orbital sections (one rather regular and one rather chaotic) compared in Fig. 3. The almost regular section occupies the upper left half and the rather chaotic section occupies the lower right half; the contrast in their 'entropy' is obvious. Fig. 9 brings recurrence plots of the six orbital sections whose $z = z(t)$ power spectra and Kaplan–Glass averaged autocorrelation parameter $\bar{\Lambda}(\Delta\tau)$ were presented in Figs 5(a) and (b), respectively. The plots are again ordered in the direction of increasing chaoticity. The first of them really looks like one of the dark boxes of the subsequent plots (these boxes correspond to 'sticky-motion' periods when the orbit is tied to a regular region); the second plot shows a clear checkerboard pattern (the orbital section is rather regular) which then gradually gives way to horizontal/vertical pattern at times when the orbit's behaviour changes to chaotic.[3] Fig. 10 brings recurrence plots and diagonal-line length histograms for the two rather regular orbits whose Poincaré diagrams, $z(t)$ power spectra and tangent's autocorrelation parameter were shown in Fig. 6. The recurrence analysis well distinguishes between the orbits, in particular the histogram slope (indicated in red in the plots) which yields Rényi's entropy is steeper for the less regular orbit.

[3] Note that the middle-row plots of this figure are counterparts of the $z(t)$ time series and spectra shown in the first two rows of Fig. 4. One can check by comparison that the transition to chaos in the $z(t)$ evolution really occurs at times when the recurrence matrix changes from checkerboard to horizontal/vertical regime ('carpet edge' in the recurrence plots).

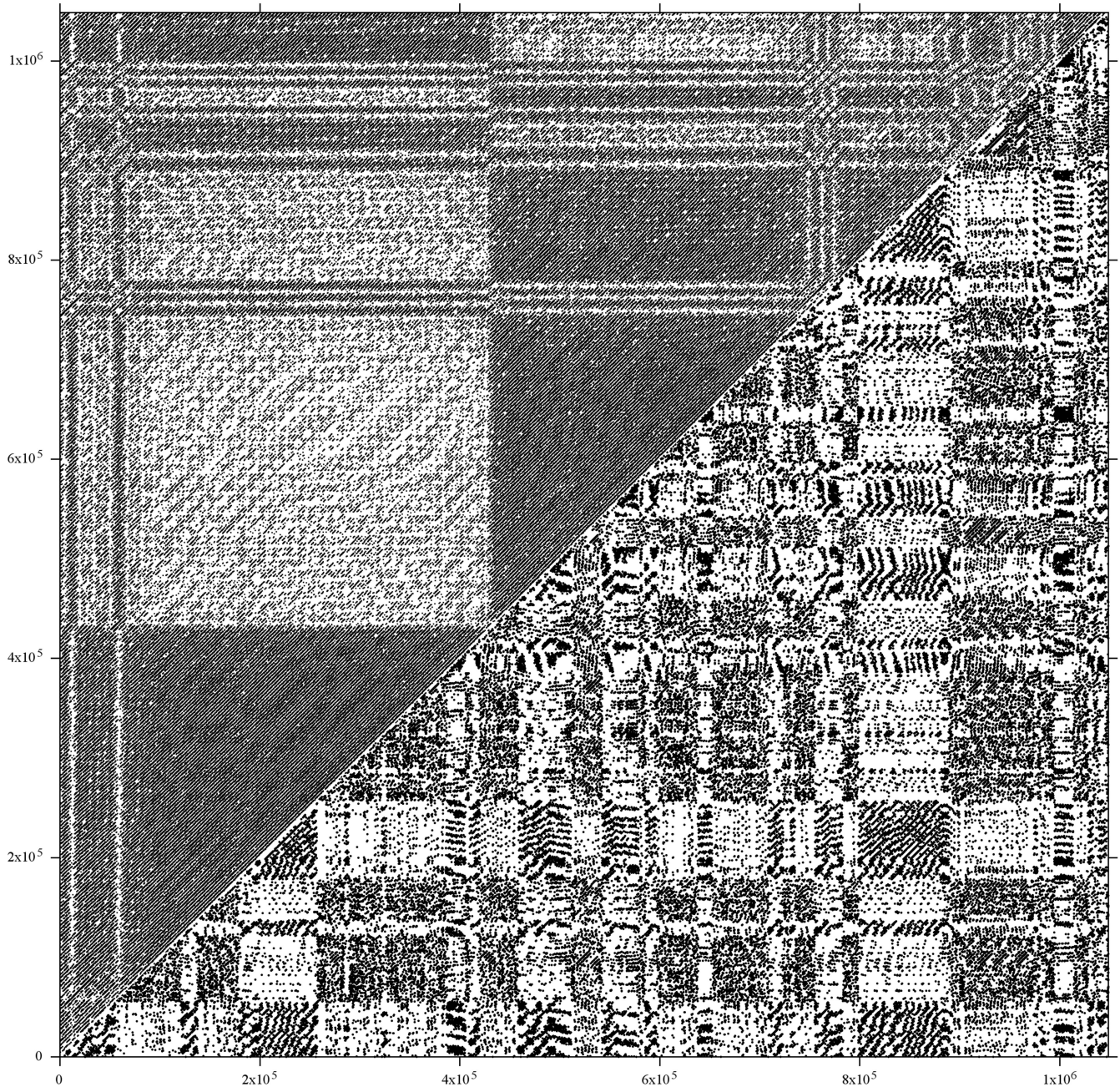


Figure 8. Recurrence plots for the two orbital sections whose Poincaré maps, $z(t)$ evolutions and their power spectra were shown in Fig. 3. We take advantage of the recurrence-matrix symmetry and give just halves of the recurrence plots in one square: the almost regular section (the left-hand column of Fig. 3) is above the main diagonal (upper left triangle), while the rather chaotic section (the right-hand column of Fig. 3) is below the main diagonal (lower right triangle). The axis values indicate proper time in units of M.

Figs 11 and 12 show six (the latter only four) of the recurrence-analysis quantifiers (*RR*, *DET*, *DIV*, *LAM*, *V ENTROPY* and *T*2), computed for large collections of orbits ejected from certain radial ranges within the equatorial plane of the black hole–disc systems. The quantifiers evidently distinguish between regular and chaotic orbits, but their sensitivity to different phase-space features is somewhat different. In Fig. 11, the difference between regular and chaotic region is more distinct, because the orbits in the left part belong to a large regular island, which then quite immediately passes into a chaotic sea (right part of the plots). On the other hand, Fig. 12 scans a more complex phase-space region where several regular islands and chaotic layers are crossed. For a better picture of which region have been considered, the respective Poincaré diagram is also shown in Fig. 12. In the chaotic regime, the recurrence rate and the fraction of diagonal lines are seen to be lower, whereas the vertical measures *T*2 and *V ENTROPY* grow significantly. This means that the system takes more time to get back to the chosen ϵ-neighbourhood and that the vertical-line length oscillates more than in the regular regime; namely, in the regular regime, either there are no vertical lines at all or they are of approximately the same length (note, for example, that if $v_{\min}$ is chosen too small, one gets a lot of 'sojourn' vertical lines of the same length). The *DIV* parameter of course increases

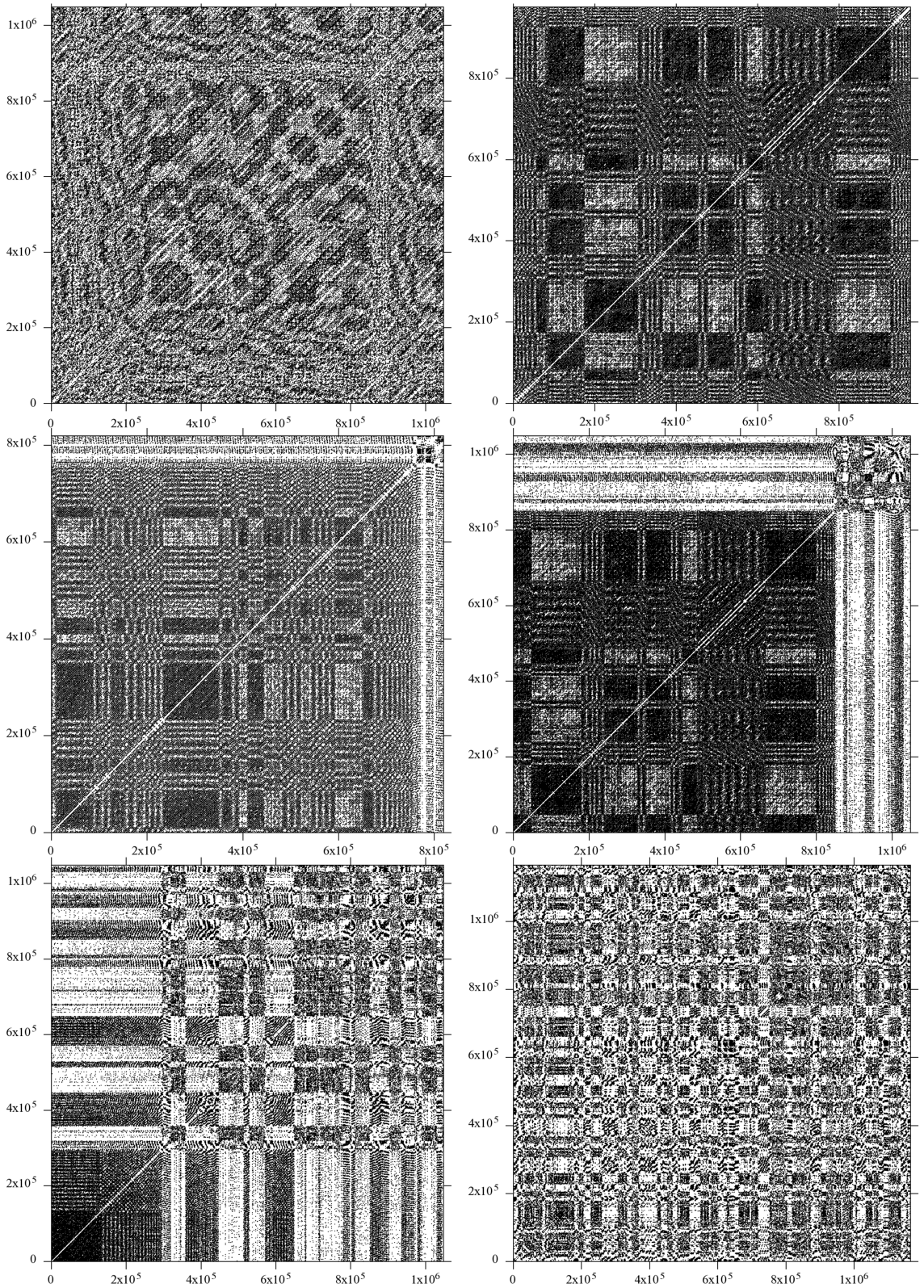


Figure 9. Recurrence plots for the orbital sections whose $z(t)$ power spectra and Kaplan–Glass parameter $\bar{\Lambda}(\Delta\tau)$ were shown in Figs 5(a) and (b). The $z(t)$ evolutions and power spectra corresponding to the middle-row plots are given in the first two rows of Fig. 4. Proper time goes along the axes in units of M.

© 2012 The Authors, MNRAS **425,** 2455–2476
Monthly Notices of the Royal Astronomical Society © 2012 RAS

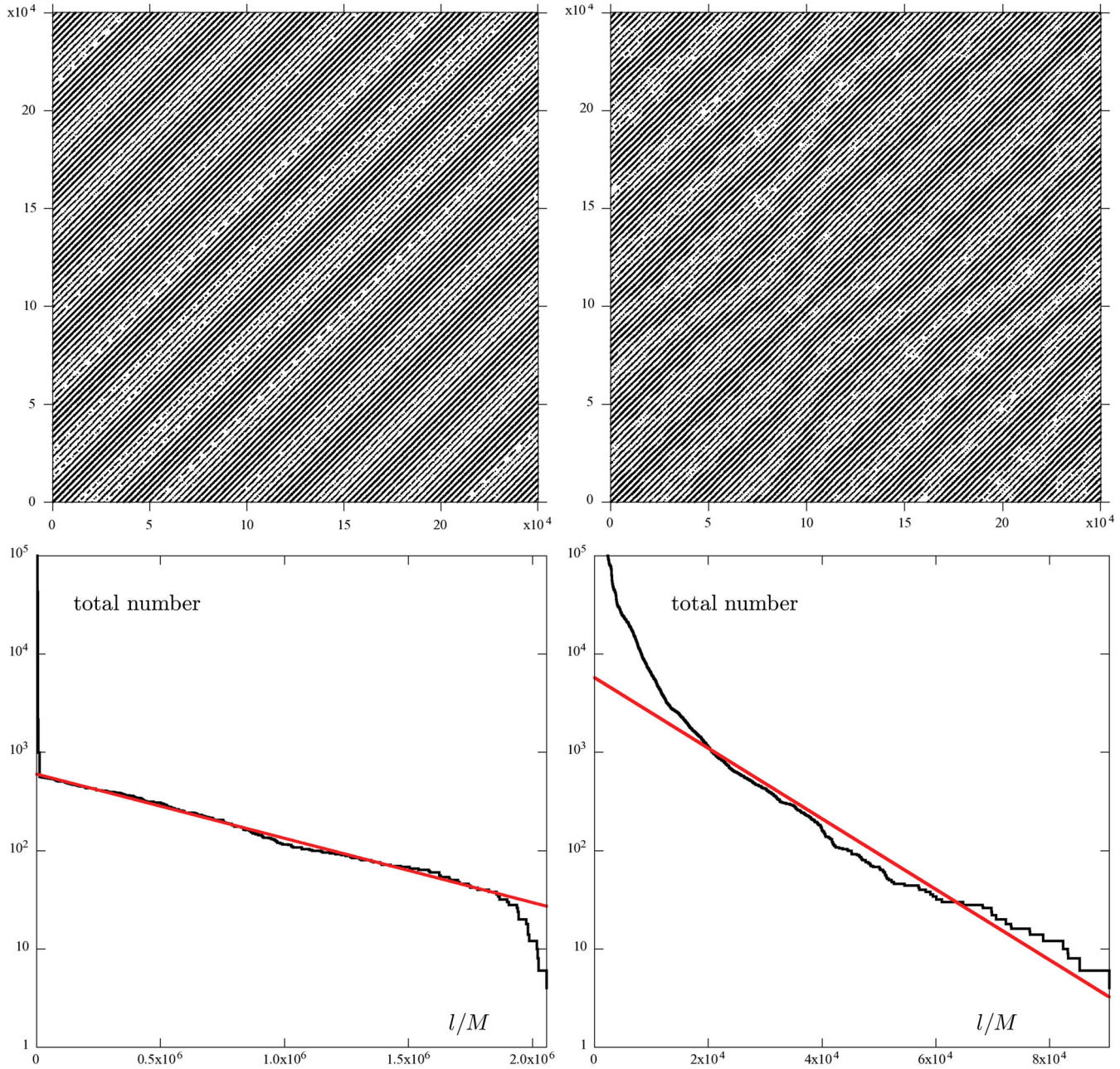


Figure 10. Recurrence plots and histograms of diagonal-line lengths for the two orbits whose Poincaré diagrams, $z(t)$ power spectra and tangent's autocorrelation parameter were shown in Fig. 6. Both orbits are rather regular: left orbit belongs to five-periodic regular islands and the right one sticks to them. Both have been followed up to $2.1 \times 10^6\,M$ of proper time, with $15M$ step; we set $\epsilon = 1.1$ and employed the Theiler's parameter $w = 4$. The recurrence analysis clearly distinguishes between the orbits, in particular, the Rényi's entropy K_2, read off from the slope of the cumulative histogram plotted (in logarithmic scale) against the diagonal length l (bottom plots), comes out about -1.5×10^{-6} for the regular orbit, while it is about -8.27×10^{-5} for the 'sticky' orbit (note that the x-axis ranges are different, so the difference in slopes is much bigger than it appears at first sight). Obviously, the slope has to be determined from the middle part of the histogram, where the latter really reflects recurrence properties and where it can be approximated by a straight line.

in the chaotic region as well as the 'laminarity'. All the quantifiers get considerably more noisy in the chaotic regions.

In order to illustrate how Poincaré diagrams can be supplemented by information provided by recurrence analysis, the passage points are coloured according to the values of selected recurrence quantifiers which apply to the respective orbits (so the colours are of course mixed in chaotic regions); namely, the top left diagram is coloured according to the value of *DIV* and the top right diagram according to the slope of the diagonal-line histogram. We have chosen exactly these two quantifiers, because *DIV* is one of the simplest, whereas the diagonal-histogram slope is more 'sophisticated', tightly connected with Lyapunov exponents. However, it is seen that the two colourings provide almost the same information (only the colour scales are somewhat different, naturally). Therefore, the *DIV* quantifier seems to be more suitable for a quick distinction between regularity and chaos, mainly if large sets of trajectories are to be processed routinely. The cumulative-histogram slope *is* theoretically more sophisticated, but also harder to get (it

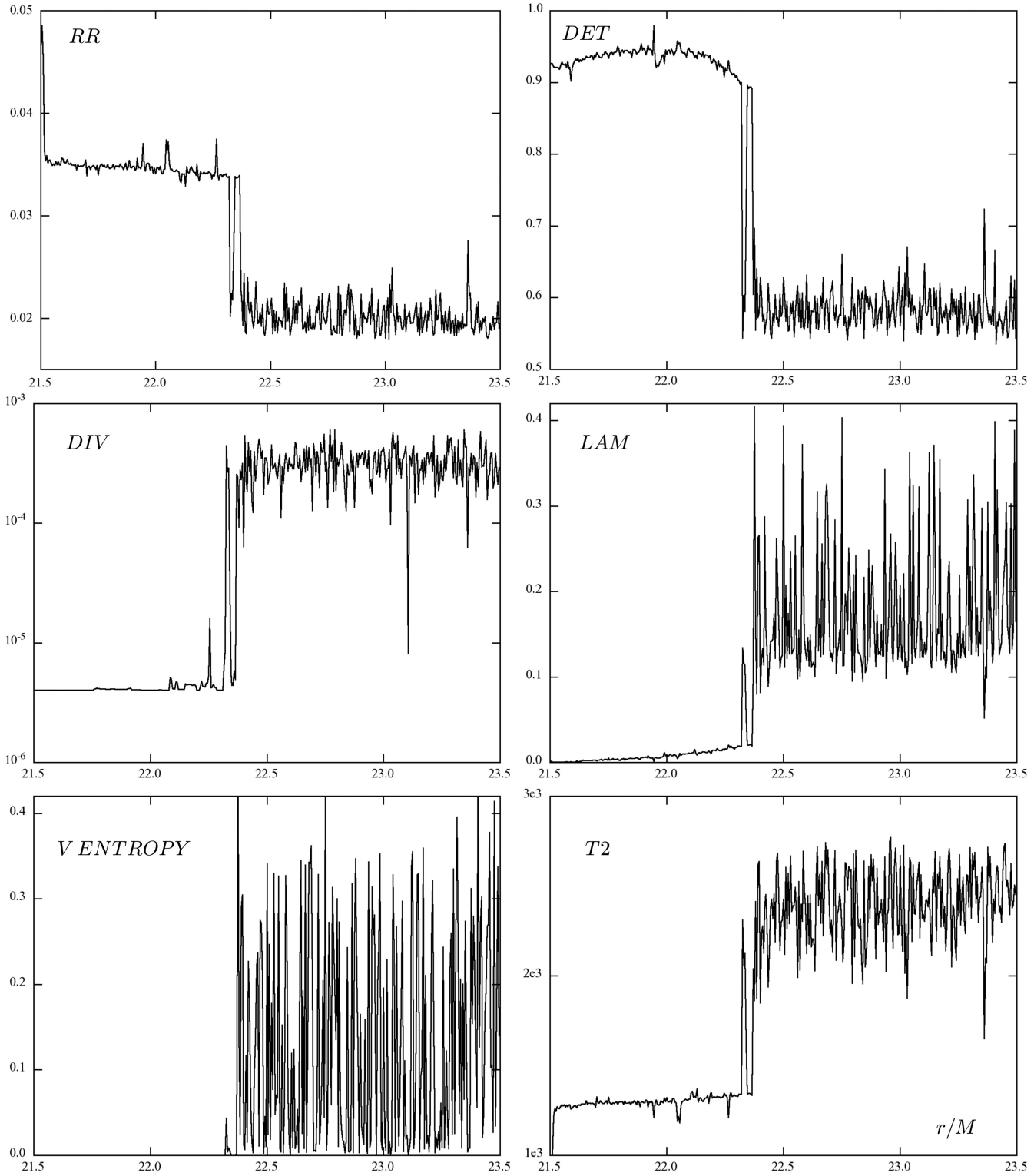


Figure 11. Six of the recurrence-analysis quantifiers, computed for 400 geodesics ejected tangentially (with $u^r = 0$) from radii between $r = 21.5M$ and $23.5M$ (with step $0.005M$) from the equatorial plane of the system of a black hole (of mass M) and the inverted first Morgan–Morgan disc with mass $1.3M$ and inner Schwarzschild radius $20M$. All the orbits have specific energy $\mathcal{E} = 0.934$ and specific angular momentum $\ell = 4M$. The orbits have been followed for about $250000M$ of proper time (thus the minimal achievable *DIV* is 4×10^{-6}) with 'sampling period' $\Delta\tau = 45M$, the minimal length of diagonal/vertical lines has been set at $90M$ and the recurrence threshold at $\epsilon = 1.1$. The left part of the plots scans trajectories belonging to a large secondary regular island, while the right part goes through the chaotic sea. All the quantifiers clearly distinguish between the two regimes.

© 2012 The Authors, MNRAS **425,** 2455–2476
Monthly Notices of the Royal Astronomical Society © 2012 RAS

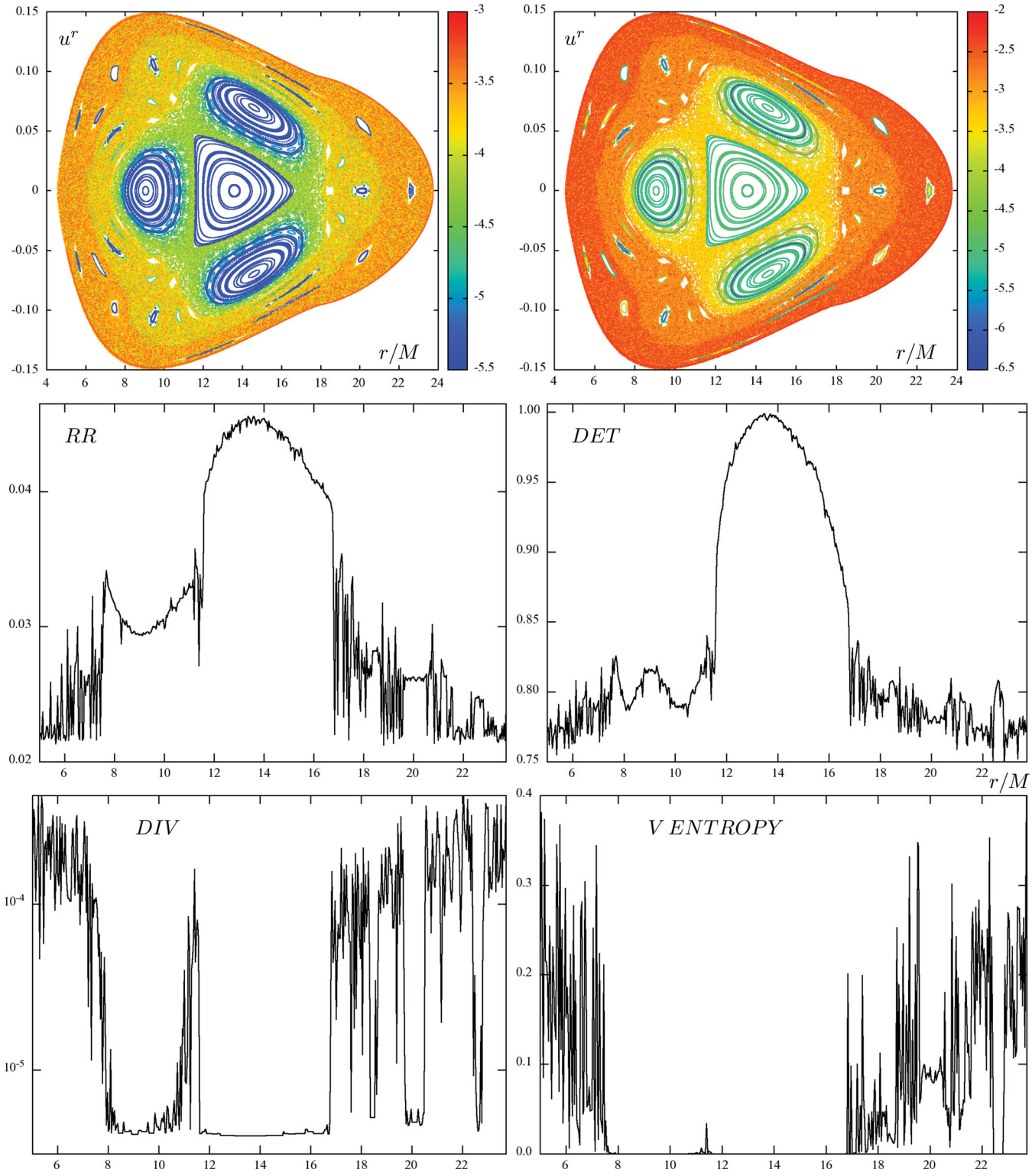


Figure 12. The quantifiers *RR*, *DET*, *DIV* and *V ENTROPY* computed, like in Fig. 11, for 470 geodesics ejected tangentially (with $u^r = 0$) from radii between $r = 5M$ and $24M$ (by $0.04M$) from the equatorial plane of the system of a black hole (M) and the inverted first Morgan–Morgan disc with mass $\mathcal{M} = 0.5M$ and inner radius $r_{\rm disc} = 18M$. All the orbits have specific energy $\mathcal{E} = 0.9532$ and specific angular momentum $\ell = 3.75M$. The orbits have again been followed for about $250\,000M$ of proper time with 'sampling period' $\Delta\tau = 45M$, the minimal length of diagonal/vertical lines has been set at $90M$ and the recurrence threshold at $\epsilon = 1.25$. Poincaré diagram of the system is shown at the top, with orbits coloured according to the value of their *DIV* (top left) and according to the slope of the diagonal-line histogram (top right); the scale is logarithmic. A system with a more complicated phase portrait has been chosen here in order to compare the results with the simple case of Fig. 11 and in order to check how sensitive the quantifiers are to more tiny phase-space features.

is 'higher level') and, mainly, its 'automatic' computer evaluation is much more tricky, because it has to be determined from a proper part of the histogram. Namely, only a certain middle part of the histogram is relevant, since its short-length end typically 'diverges' due to increasing number of sojourn points, while the long-length end typically falls off quickly due to the finite length of the trajectory. (The histogram has to be computed in the limit $l \to \infty$, so the short-length end has actually no sense; the long-length end is of course determined by the fact that practically the trajectories cannot be infinitely long.)

Finally, the dependence of several quantifiers on the choice of ϵ is illustrated in Fig. 13. There, the behaviour of *DIV*, *LAM*, *V ENTROPY* and *T*2 over geodesics starting from a wide range of radii is plotted for 11 different values of ϵ. In all the plots, one can clearly recognize a large primary regular island and two smaller ones. The quantifiers generally show monotonous dependence on ϵ – *LAM* and *V ENTROPY* increase, whereas *DIV* and *T*2 decrease with ϵ, as expected. Fig. 13 may also serve as a further support for the *DIV* quantifier (see Fig. 12 as well). As also confirmed by other similar figures not shown here, the large regular islands can be recognized easily by any of the quantifiers, because the latter fluctuate there much less and around markedly different values than in the chaotic regions. However, only the *DIV* parameter appears to be fairly indicative of small islands as well. Namely, in regular regions (both large and small) it is typically two orders of magnitude lower than in chaotic regions ($DIV \sim 3 \times 10^{-6}$ within regular regions, about an order higher in thin chaotic layers and about 3×10^{-4} in large chaotic regions; this chaotic-sea value corresponds to a divergence time of several thousands M, which represents some 10 cycles about the black hole). For longer trajectories (than those we have treated here) the difference in *DIV* between regular and chaotic regions tends to be even bigger. The other quantifiers only respond to small islands by reducing their oscillation, but not by a noticeable change of the mean value. Loosely speaking, their sensitivity profile is shifted towards larger regular regions (see the *RR* quantifier in Fig. 12, for example). The last Fig. 14 illustrates the difference between regular and chaotic geodesic on a markedly different value of K_2 entropy inferred from the cumulative length histogram of diagonal lines, and also on different dependence on ϵ of this histogram.

5 CONCLUDING REMARKS

In Paper I, we performed an overall check of the time-like geodesic dynamics in the field of a Schwarzschild black hole surrounded by an axially symmetric static thin disc or ring, and of the dependence of its chaoticity on parameters characterizing the additional source and the test particles. In the present paper, we have focused on individual orbits and their different parts and showed how the degree of their irregularity, already visible on Poincaré diagrams, can be judged in more detail by studying the time series obtained for phase variables. We have mainly considered the times series $z(t)$ of the position perpendicular to the disc/ring plane, computed their power spectra and compared the information thus gained with the one provided by the method of Kaplan and Glass which tracks autocorrelation between different parts of the series in dependence on time shift, and also with outcomes of the recurrence-matrix analysis of Eckmann et al. All these methods proved simple and powerful, while they differ in sensitivity to specific types of behaviour.

Let us also include a brief mention of several others' results which appeared in the field recently. Brink (2008) contributed to the topic of complete geodesic integrability, mentioned in Section 1, by studying geodesics in stationary axisymmetric vacuum space–times and the correlation of its fabric with the existence of the 'fourth integral' (cf. also Markakis 2012, for a Newtonian treatment of the integrability problem). Verhaaren & Hirschmann (2010) returned to the study of dynamics of test particles with spin in a Schwarzschild space–time and argued, on Poincaré diagrams and Lyapunov exponents, that smaller values of spin than previously thought can already make the particle motion chaotic. Kovács, Bene & Tél (2011) performed the first post-Newtonian analysis of the Sitnikov system (motion of a test body in the field of an equal-mass binary, along a line perpendicular to the orbital plane and going through the barycentre) and demonstrated, by numerical study of the system in dependence on gravitational radius of the 'primaries', that the relativistic effect of pericentre advance does not destroy its chaotic aspects. Ramos-Caro, Pedraza & Letelier (2011) studied the motion of test particles in the field of a centre with quadrupole deformation surrounded by finite thin discs obtained by superpositions of members of a counter-rotating Morgan–Morgan family. They found that there is a close connection between linear stability/instability of equatorial circular orbits and regularity/chaoticity of general three-dimensional orbits passing through their radii.[4] The same group (Letelier, Ramos-Caro & López-Suspes 2011) also revisited geodesic dynamics in the system composed of a monopole or an isotropic harmonic oscillator and oblate quadrupole, and found several new features not noticed before. Wang & Wu (2011) employed a pseudo-Newtonian potential in order to superpose a rotating black hole with a quadrupole halo. They analysed emission of gravitational waves from particles orbiting in such a field and demonstrated that the radiated amplitude and power are closely related to the degree of chaoticity of the orbit. Galaviz (2011) considered the evolution of a compact binary perturbed by a third body. Within a post-Newtonian version of the Hamiltonian ADM formulation, and using basin-boundary analysis and Lyapunov exponents, he examined the relative importance of different PN orders in inducing chaos in the system. Very recently, Contopoulos, Harsoula & Lukes-Gerakopoulos (2012) have analysed the classical system of two coupled oscillators and free motion in the general relativistic Manko–Novikov space–time (which describes a rotating axisymmetric compact body); they mainly focused on periodic orbits of the systems and on dependence of their properties on orbital energy. Finally, Igata, Ishihara & Takamori (2011) observed on Poincaré maps that the time-like geodesics bound in the field of the Emparan–Reall five-dimensional black ring show chaotic features.

To conclude, it should be admitted that once the evolution of a given dynamical system is mastered with sufficient numerical accuracy, it is rather easy to produce various decorative figures. However, it is also true that these can indeed yield a good picture of how much irregular the system is and how the irregularity depends on system parameters. This in turn indicates how much the 'perturbations' acting on real systems degrade the corresponding simplified exact models and helps to evaluate the validity of various approximations. Turning to our particular problem of orbiting in a static compact-centre space–time, it would be suitable to employ such methods in order to estimate and compare the significance of various 'perturbations' present in real astrophysical situations.

[4] We would like to remember Professor Patricio Letelier who was a leading expert in the fields of general relativity and chaotic dynamics. He left us just at the time when the paper Ramos-Caro et al. (2011) appeared in MNRAS.

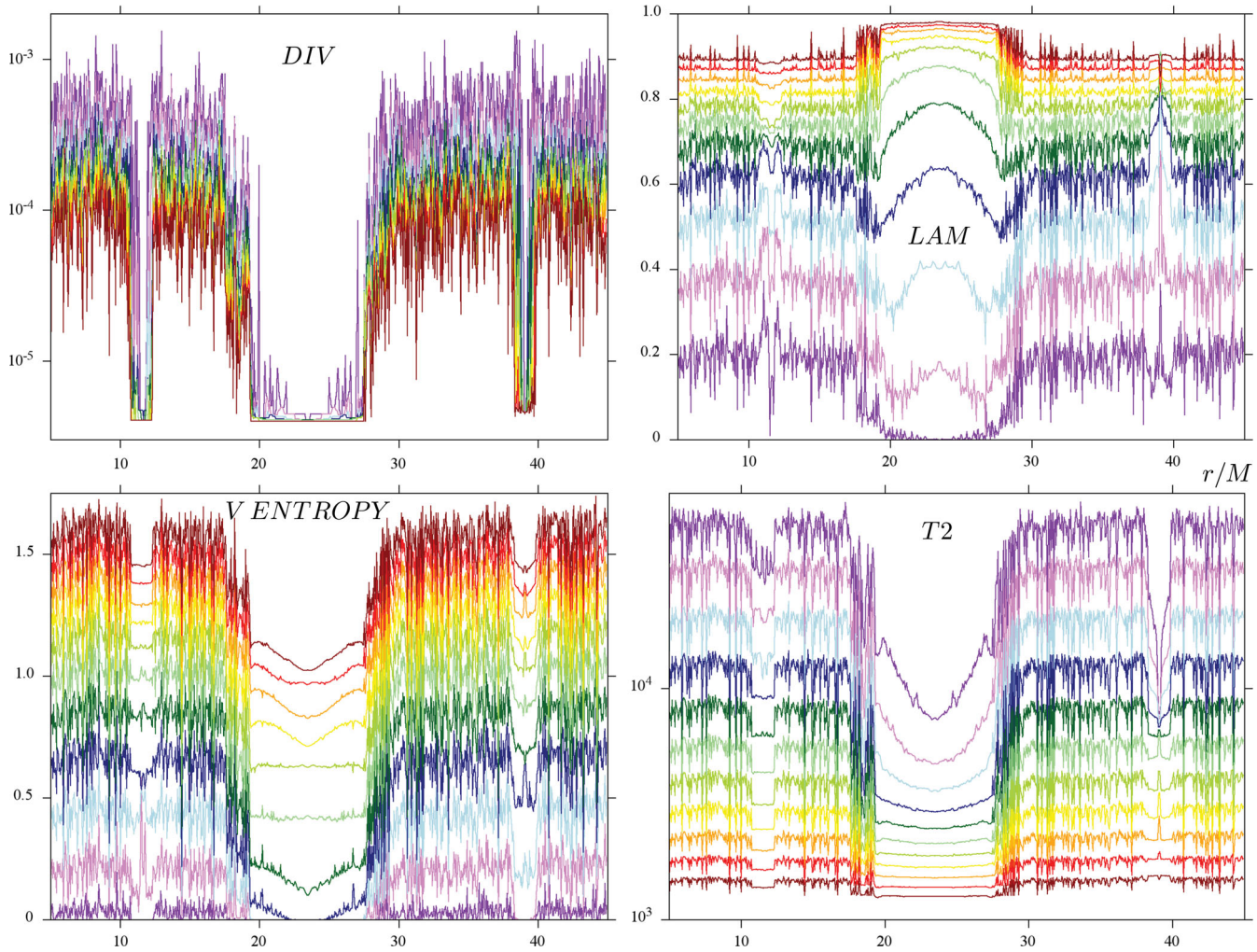


Figure 13. Dependence of four recurrence quantifiers on the choice of the threshold approach ϵ. We go through the geodesics starting with $u^r = 0$ from the radii $r = 5M$ to $45M$ from the equatorial plane of the black hole–disc system with the disc mass $\mathcal{M} = 1.3M$ and inner disc radius $r_{\rm disc} = 20M$. All the geodesics have specific energy $\mathcal{E} = 0.956$ and specific angular momentum $\ell = 4M$. Their *DIV*, *LAM*, *V ENTROPY* and $T2$ parameters are computed for 11 different values of ϵ, namely 0.50, 0.65, 0.80, 0.95, . . . , 1.85, 2.00; in this order, the line colour shifts from dark violet, violet, light blue, dark blue, . . . , to red and dark red. A primary regular island and two smaller islands aside are evident.

Besides the gravitational influence of additional matter, discussed (in a simple, static and axially symmetric case) in the present work, there would also occur *mechanical* interaction of the orbiter with that matter (see e.g. Šubr & Karas 2005). Both the compact centre and the matter around would probably have non-zero angular momentum, so dragging effects should be incorporated; actually, the orbiter may itself be endowed with spin or even higher momenta. Incoming gravitational waves can perturb the system as well as those emitted by the orbiter (back reaction).Of course, if the orbiter was charged, it would also be affected by any electromagneticfield present there.

When thinking about possible perturbations of the originally completely integrable problem of free test motion in a Schwarzschild or Kerr field, one has mainly in mind the motion of individual stars around supermassive black holes in galactic nuclei. As already stressed in Section 1, there are in fact whole *clusters* of stars in galactic nuclei; so, when solving the motion of an individual satellite, one should also take into account gravity of the whole cluster, or solve that motion right as a part of the problem of N interacting bodies. Such a problem is difficult within general relativity, mainly if the black hole centre and the disc or ring/toroid should also be taken into account, but it is being considered within Newtonian theory (see e.g. Šubr, Karas & Huré 2004; Haas, Šubr & Kroupa 2011a; Haas, Šubr & Vokrouhlický 2011b, and references therein) as well as in post-Newtonian and post-Minkowskian approximation (e.g. Chu 2009; Ledvinka, Schäfer & Bičák 2008; Hartung & Steinhoff 2011).

There are several immediate options for further work. One can of course check the results with yet other methods (Lyapunov-type coefficients, various other 'entropies', basin-boundary analysis, Melnikov integral, etc.), find and study particular significant orbits of the system (periodic and homoclinic/heteroclinic orbits) in detail, or compare the relativistic analysis with Newtonian, pseudo-Newtonian or post-Newtonian one. However, we would mainly like to focus on astrophysically more realistic situations (parameter ranges) in future. This should involve, among others, the question of whether to incorporate also other gravitating components such as spheroidal halo, disc *plus* outer ring (or thick toroid), or/and jets, and – most importantly – the question of how to account *adequately* for rotation.

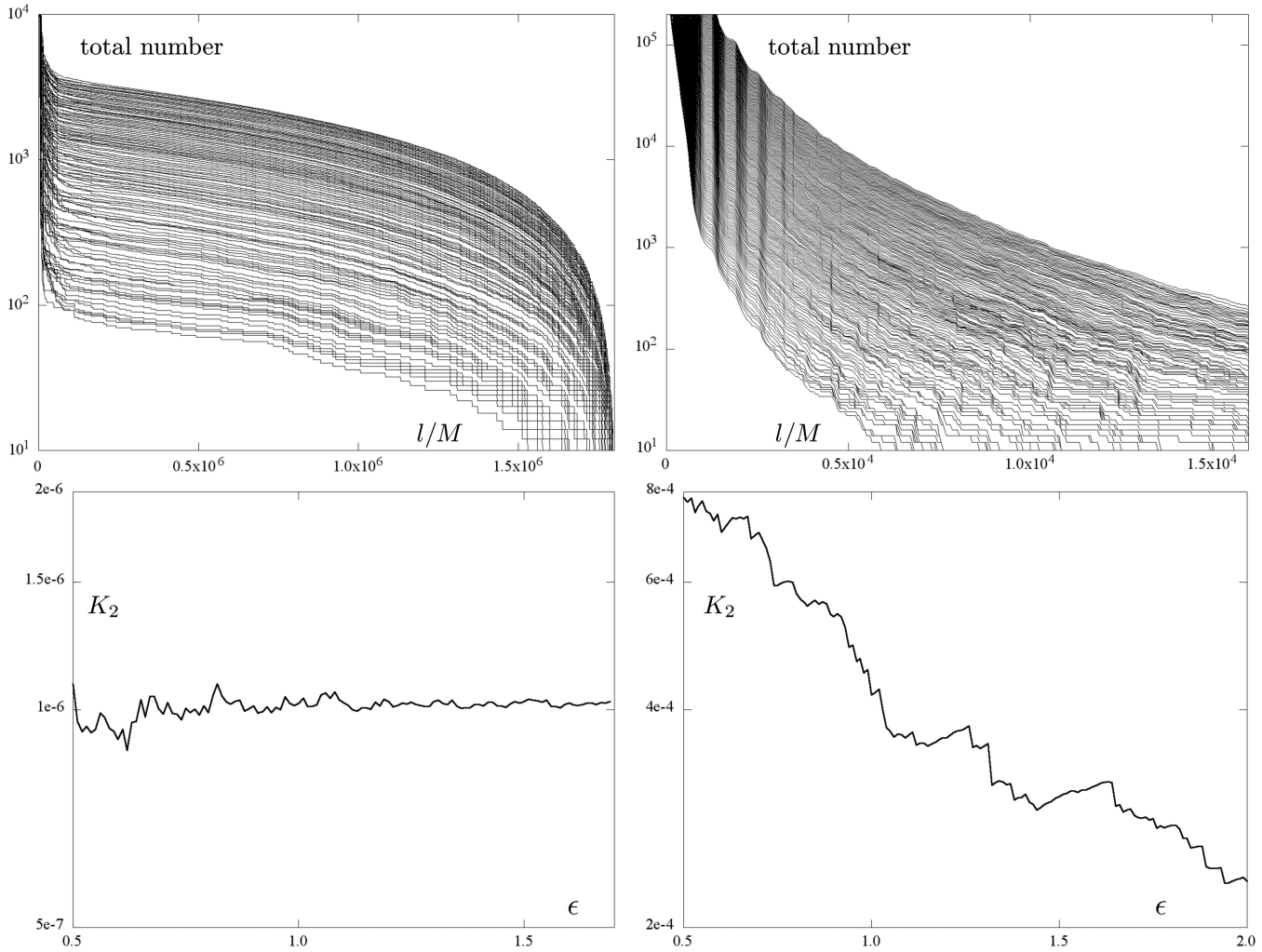


Figure 14. Dependence of the diagonal-line cumulative length histogram (top row) and of the resulting value of the correlation entropy K_2 (bottom row) on the choice of the threshold approach ϵ, plotted for a regular (left-hand column) and weakly chaotic (right-hand column) geodesics. Both geodesics have been followed for about $2 \times 10^6 M$ of proper time. Both have specific energy $\mathcal{E} = 0.956$ and specific angular momentum $\ell = 4M$ and live in a space–time of a black hole (M) surrounded by the inverted first Morgan–Morgan disc with mass $\mathcal{M} = 1.3M$ and inner radius $r_{\rm disc} = 20M$. The recurrence matrix of the chaotic geodesic has been computed using the Theiler parameter growing linearly with ϵ (from $w = 2$ to 6). The K_2 entropy of this orbit is considerably more sensitive to ϵ than that of the regular orbit on the left (the range along both K_2-axes corresponds to a change by a factor of 4); however, the two cases (regular/chaotic) are clearly distinguished as seen on the orders at the vertical axes.

ACKNOWLEDGMENTS

We are grateful to M. Žáček who provided us the numerical code developed within his diploma work on geodesic motion in Weyl space–times. The plots were produced with the help of the GNUPLOT utility (we thank K. Houfek for hints) and D. Krause's BMEPS program. For the recurrence analysis, we were using the 'COMMANDLINE RECURRENCE PLOTS' software (version 1.13z) by N. Marwan; we also thank O. Kopáček for discussions on the recurrence method. Our work has been supported by the projects GACR-202/09/0772 and MSM0021620860 (OS), GACR-205/09/H033, SVV-265301 and GAUK-428011 (PS).

REFERENCES

Bach R., Weyl H., 1922, Math. Z., 13, 134
Brink J., 2008, Phys. Rev. D, 78, 102002
Carter B., 1968, Commun. Math. Phys., 10, 280
Chu Y.-Z., 2009, Phys. Rev. D, 79, 044031
Contopoulos G., Harsoula M., Lukes-Gerakopoulos G., 2012, Celest. Mech. Dyn. Astron., preprint (arXiv:1203.1010) doi:10.1007/s10569-012-9412-4
D'Afonseca L. A., Letelier P. S., Oliveira S. R., 2005, Classical Quantum Gravity, 22, 3803
Eckmann J.-P., Oliffson Kamphorst S., Ruelle D., 1987, Europhys. Lett., 4, 973
Frolov V. P., Kubizňák D., 2008, Classical Quantum Gravity, 25, 154005
Galaviz P., 2011, Phys. Rev. D, 84, 104038
Haas J., Šubr L., Kroupa P., 2011a, MNRAS, 412, 1905
Haas J., Šubr L., Vokrouhlický D., 2011b, MNRAS, 416, 1023
Hartung J., Steinhoff J., 2011, Phys. Rev. D, 83, 044008
Igata T., Ishihara H., Takamori Y., 2011, Phys. Rev. D, 83, 047501
Judd K., Stemler T., 2009, Philos. Trans. R. Soc. A, 368, 263
Kaplan D. T., Glass L., 1992, Phys. Rev. Lett., 68, 427
Karas V., Šubr L., 2007, A&A, 470, 11
Kopáček O., Karas V., Kovář J., Stuchlík Z., 2010, ApJ, 722, 1240
Kovács T., Bene Gy., Tél T., 2011, MNRAS, 414, 2275
Koyama H., Kiuchi K., Konishi T., 2007, Phys. Rev. D, 76, 064031
Ledvinka T., Schäfer G., Bičák J., 2008, Phys. Rev. Lett., 100, 251101

© 2012 The Authors, MNRAS **425,** 2455–2476
Monthly Notices of the Royal Astronomical Society © 2012 RAS

Lemos J. P. S., Letelier P. S., 1994, Phys. Rev. D, 49, 5135
Letelier P. S., Ramos-Caro J., López-Suspes F., 2011, Phys. Lett. A, 375, 3655
Löckmann U., Baumgardt H., Kroupa P., 2009, MNRAS, 398, 429
Lukes-Gerakopoulos G., Apostolatos T. A., Contopoulos G., 2010, Phys. Rev. D, 81, 124005
Madigan A.-M., Levin Y., Hopman C., 2009, ApJ, 697, L44
Markakis C., 2012, MNRAS, preprint (arXiv:1202.5228)
Marwan N., Carmen R. M., Thiel M., Kurths J., 2007, Phys. Rep., 438, 237
Palmer K., 2000, Shadowing in Dynamical Systems. Theory and Applications. Kluwer, Dordrecht
Ramos-Caro J., Pedraza J. F., Letelier P. S., 2011, MNRAS, 414, 3105
Semerák O., 2003, Classical Quantum Gravity, 20, 1613
Semerák O., Suková P., 2010, MNRAS, 404, 545 (Paper I)
Šubr L., Karas V., 2005, A&A, 433, 405
Šubr L., Karas V., Huré J.-M., 2004, MNRAS, 354, 1177
Suková P., 2011, J. Phys. Conf. Ser., 314, 012087
Takens F., 1981, in Rand D. A., Young L.-S., eds, Lecture Notes Math. 898, Dynamical Systems and Turbulence. Springer-Verlag, Berlin, p. 366
Verhaaren C., Hirschmann E. W., 2010, Phys. Rev. D, 81, 124034
Vieira W. M., Letelier P. S., 1996, Classical Quantum Gravity, 13, 3115
Walker M., Penrose R., 1970, Commun. Math. Phys., 18, 265
Wang Y., Wu X., 2011, Commun. Theor. Phys., 56, 1045
Will C., 2009, Phys. Rev. Lett., 102, 061101

This paper has been typeset from a TEX/LATEX file prepared by the author.

C. Free motion around black holes with discs: between integrability and chaos – III

Submitted to Monthly Notices of the Royal Astronomical Society.

Mon. Not. R. Astron. Soc. **000**, 1–?? () Printed 11 July 2013 (MN LATEX style file v2.2)

Free motion around black holes with discs or rings: between integrability and chaos — III

P. Suková⋆ and O. Semerák†
Institute of Theoretical Physics, Faculty of Mathematics and Physics, Charles University in Prague, Czech Republic

ABSTRACT
We continue the study of time-like geodesic dynamics in exact static, axially and reflection symmetric space-times describing the fields of a Schwarzschild black hole surrounded by thin discs or rings. In the first paper of this series, the rise (and decline) of geodesic chaos with ring/disc mass and position and with test particle energy was revealed on Poincaré sections and on time series of position or velocity and their power spectra. In the second paper we compared these results with those obtained by two recurrence methods, focusing on "sticky" orbits whose different parts show different degrees of chaoticity. Here we complement the analysis by using several Lyapunov-type coefficients which quantify the rate of orbital divergence. After comparing the results with those obtained by the previous methods, we specifically consider a system involving a black hole surrounded by a small thin disc or a large ring, having in mind the configuration which probably occurs in galactic nuclei. Within the range of parameters which roughly corresponds to our Galactic center, we found that the black-hole accretion disc does not have a significant gravitational effect on the dynamics of free motion at larger radii, while the inner circumnuclear molecular ring (concentrated above 1 parsec radius) can only induce some irregularity in motion of stars ("particles") on smaller radii if its mass reaches 10 to 30% of the central black hole (which is the upper estimate given in the literature), if it is sufficiently compact (which does not hold but maybe for its inner rim) and if the stars can get to its close vicinity. The outer dust ring between 60 and 100 parsecs appears to be less important for the geodesic dynamics in its interior.

Key words: gravitation – relativity – black-hole physics – chaos – Galactic nucleus

1 INTRODUCTION

Black holes are the most conservative, today almost routine explanation of a whole bunch of high-energy astrophysical phenomena. Few doubt about their reality, but less certain is their accurate type. Models of accreting black holes standardly use Kerr metric for description of the gravitational field, disregarding the effect of the accreting (and any other) matter as well as possible non-stationarity and different global properties of the surrounding universe. While the main issue is still to confirm with certainty that black-hole horizons do occur in most galactic nuclei and in some X-ray binaries, it may soon become possible to test how well they correspond to what is described in general-relativity courses. It is thus desirable to discuss which effects can indicate deviations from the textbook ideal and what observational implications they may have.

One of almost unavoidable consequences of a departure from the Kerr geometry is a breakdown of the complete integrability of geodesic equations. This means, physically, that the dynamics of satellites freely orbiting astrophysical black holes should be "weakly non-integrable" and possibly prone to chaos in some regions of the phase space (Lukes-Gerakopoulos et al. 2010). In astrophysical systems with accreting black holes the matter elements have actually many reasons why to behave in a chaotic way, but we only focus on that resulting from *gravitational* influence of the accreting (or just surrounding) material. Since the latter is supposed to typically form a disc or a ring about the central black hole, it is natural to approximate the field of such a system by a suitable stationary and axially symmetric (and orthogonally transitive) space-time. Though at least outside of the sources (in a vacuum) the Einstein equations are known to be completely integrable in such a case (they are usually written and treated in the form of the Ernst equation) and "all" such space-times have actually been covered within wide families of solutions, mostly obtained by "solution-generating" techniques, these have not proved successful in describing physically reasonable fields, if having an interpretation at all.

The only case when the Einstein equations allow for a description of the composite-source field (for "superposition") which is practical for actual computations is the *static* and axially symmetric situation. Then the metric contains just two unknown functions, of which the first satisfies Laplace equation (thus adds up linearly) and the second one is obtained from the first by a suitable line in-

⋆ E-mail: lvicekps@seznam.cz
† E-mail: oldrich.semerak@mff.cuni.cz

© RAS

tegral (see e.g. Semerák & Suková 2010 for more detailed introduction and references). Needless to say, a static setting excludes rotation, which is a serious limitation concerning that the black-hole accretion systems are expected to bear a considerable angular momentum. On the other hand, the gravitational implications of rotation — the effects of rotational dragging — fall very quickly with distance from the source, so at least for satellites orbiting not so close to the centre one can assume they do not play an important role.[1]

It is a question whether some of the astrophysical black-hole–dominated systems are "clean" enough, so that the restriction to a pure gravity-driven orbital motion can be adequate. This is hardly so in the case of X-ray binaries, whose radiation itself indicates that the components interact strongly and that a corresponding amount of matter and/or fields has to be present; moreover, the geometry may be rather far from static (and even stationary) and axially symmetric in these systems. The same can generically be estimated in highly active galactic nuclei. On the other hand, in less active nuclei, with lower density of interstellar matter, the orbiting of stars around the central supermassive black hole could be well approximated by geodesic motion in the field of the hole perturbed by an accretion disc or/and by a circum-nuclear structures of colder material on larger radii.

Let us recall that in the first paper (Semerák & Suková 2010) of this series (see also Suková 2011) we considered the system of an (originally) spherically symmetric black hole surrounded by a thin disc or a ring and tried to learn how the dynamics of time-like geodesics in its field depends on parameters. More specifically, we placed the inverted 1st (and also 4th) member of the Morgan-Morgan counter-rotating disc family or the Bach-Weyl ring around the Schwarzschild hole in a concentric manner and were observing the rise (and decline) of geodesic chaos with disc/ring mass and position and with test-particle energy, as revealed on Poincaré sections and on time series of position or velocity and their power spectra. In the second paper (Semerák & Suková 2012) (see also Suková & Semerák 2012) we compared the results with those obtained by two simple and powerful recurrence methods, the method based on averaging of directions in which the system passes through a pre-defined phase-space cells, and the method of recurrence plots based on statistics over the recurrences to these cells themselves. We mainly focused there on "sticky" orbits whose different parts show different degrees of chaoticity, because such orbits, lying just between regular and strongly chaotic regime, offer the best chance to test different methods and their sensitivity to different dynamical features.

We refer to the preceding two papers for general introduction including a number of references and for details (which will not be repeated here). Let us just remind that the system we consider is fully characterised by the black-hole mass M, by the disc/ring mass $\mathcal{M}$ and by the disc inner radius $r_{\rm disc}$ or the ring radius $r_{\rm ring}$ (the radial coordinate r is of Schwarzschild type). The main parameters (constants) of geodesic motion are specific energy at infinity $\mathcal{E} \equiv -u_t$ and azimuthal angular momentum at infinity $\ell \equiv u_\phi$ (u_μ is the covariant four-velocity). The Poincaré sections show transits of the geodesics through the equatorial plane (the plane where the disc or the ring resides) in the (r, u^r) axes; regarding that the system is reflectionally symmetric with respect to the equatorial plane, we record passages in both directions.

The present paper extends the analysis by computing several Lyapunov-type coefficients which quantify the rate of orbital divergence, namely the maximal Lyapunov characteristic exponent and the computationally more suitable FLI and MEGNO indicators (they are introduced in section 2). After comparing the results with those obtained by the other methods previously (section 3), we specifically consider a system involving a black hole surrounded by a small thin "accretion" disc or a large ring (approximating the "cold" torus), having in mind the configuration which probably occurs in galactic nuclei (section 4). If choosing the parameters according to the values observed in our Galaxy, it turns out that the innermost accretion disc around the central black hole does not significantly affect the dynamics of free motion on larger radii, whereas the inner circumnuclear molecular ring can make some of the lower-radius orbits chaotic, provided that its mass is sufficiently large and compact enough and that the stars can approach it closely enough.

2 QUANTIFYING THE ORBITAL DIVERGENCE

One of the basic symptoms of chaos is a quick divergence of phase trajectories in certain directions — the well-known sensitive dependence on initial conditions. The rate of this tendency can be quantified by several coefficients whose main purpose is to distinguish between polynomial and exponential divergence. Their computation typically involves a sequence of evolutions and renormalisations of a certain relative position vector, which requires a choice of *the* time coordinate. This is of course not covariant in principle, and may even be practically ambiguous if space-time is complicated enough. Fortunately, when the space-time has a time-like symmetry (it is stationary), there does exist a privileged global time which usually is a reasonable choice for computations. Also, in agreement with the knowledge and experience that the nature of dynamics is not sensitive to the metric used in the phase space, it was shown that this also applies to the most important Lyapunov-type exponents; as quoted from Gelfert & Motter (2010): "our results show once and for all that Lyapunov exponents, entropies, and dimension-like characteristics can be used to make invariant assertions about chaos. However, the same results also show that the *values* of some quantities that have been previously conjectured to be invariant, such as the information dimension and topological entropy, are not invariant in general."

In this paper, we focus on three quantities which measure the rate of orbital divergence: the Lyapunov characteristic exponents (LCEs), the fast Lyapunov indicator (FLI) and the mean exponential growth of nearby orbits (MEGNO). (See e.g. Maffione et al. 2011 for a comparison of these quantities with several other indicators derived from deviation vectors.) The LCEs were introduced by Lyapunov in 1892 (see, e.g., Benettin et al. 1980) and are mostly computed in two different ways, namely by solving the variational equations along with the equations of motion of the given dynamical system, or by following the evolution of separation of its two nearby orbits. The variational approach is generally more accurate and reliable, but for relativistic systems it usually involves complicated equations that are very difficult to integrate; the two-particle method can be an efficient and much more convenient option which however has to be employed with caution (Tancredi et al. 2001; Wu et al. 2006). We here follow the procedure proposed by Wu & Huang (2003); Wu et al. (2006).

[1] However, in the long-term dynamics, it is difficult to estimate a priori which of the tiny effects will bring more important "perturbation", so one should definitely try to incorporate rotation in some way, if only to learn whether chaos tends to be enhanced or suppressed by the dragging effects.

The LCEs describe the rate of orbital divergence in the neighbourhood of a given trajectory. Considering the initial conditions distributed on a sphere of small radius $\mathbf{\Delta w}$ around some given point $\mathbf{w}$, the orbital flow deforms the sphere into an ellipsoid whose half-axes evolve according to $\mathrm{e}^{\lambda_i t}\mathbf{\Delta w}$, where λ_i is the LCE in the direction of the i-th axis. The orbits thus diverge exponentially in certain direction if the corresponding λ_i is positive. Though the information about phase dynamics is encoded in the whole spectrum of LCEs, it is thus most important to determine the *maximal* LCE (mLCE) (we will call it $\lambda_{\max}$) in order to decide whether the system is chaotic or not. Actually, for a randomly selected two nearby trajectories the separation vector always has some nonzero component in the direction corresponding to the mLCE and after a short time this component outweighs the others; denoting such two orbits by $\mathbf{w}(t)$ and $\mathbf{w}'$(t), the mLCE is given by the limit

$$\lambda_{\max} = \lim_{t\to\infty} \frac{1}{t} \ln \frac{\|\mathbf{\Delta w}(t)\|}{\|\mathbf{\Delta w}(0)\|} , \tag{1}$$

where $\|\mathbf{\Delta w}(t)\| \equiv \|\mathbf{w}(t) - \mathbf{w}'(t)\|$ is the norm of the displacement vector in the phase space.

LCEs belong to the quantities which do bring invariant information (it is their sign in this case) but whose *value* is coordinate dependent (Gelfert & Motter 2010). In relativity, the main issue is the choice of time t. In stationary space-times, there exists a privileged, Killing time which offers a natural option for a study of test-particle dynamics. However, Wu & Huang (2003) argued that one should examine, irrespectively of the type of space-time, the evolution of *proper* distance between the orbits in *proper* time rather than coordinate quantities. They also claim (i) that it is sufficient to follow this evolution in the configuration space (i.e. regardless of the momentum dimensions) in order to distinguish between regular and chaotic regions, and (ii) that the displacement vector need not be projected on a certain space-like hypersurface. Hence the formula

$$\tilde{\lambda}_{\max} = \lim_{\tau\to\infty} \frac{1}{\tau} \ln \frac{|\Delta\mathbf{x}(\tau)|}{|\Delta\mathbf{x}(0)|} , \tag{2}$$

$$|\Delta\mathbf{x}(\tau)| \equiv \sqrt{|g_{\mu\nu}\Delta x^\mu \Delta x^\nu|(\tau)} , \tag{3}$$

where proper time τ is the independent integration variable and $\Delta\mathbf{x}$ is the separation vector whose norm represents the momentary proper distance between the two neighbouring orbits in the configuration space. In the infinite-time limit this more convenient way of computation should coincide with the classical definition of mLCE. We have not checked this statement in detail, but will follow it, not even emphasising it in notation, so we will suppose $\tilde{\lambda}_{\max} \equiv \lambda_{\max}$ and omit the tilde hereafter. In order to keep in focus the orbital flow in the vicinity of the reference trajectory, the separation vector has to be renormalised whenever it reaches a certain prescribed value; together with the latter, the velocity deviation vector $\mathbf{\Delta u}(\tau) = \mathbf{u}(\tau) - \mathbf{u}'(\tau)$, where $\mathbf{u}$ is the four-velocity tangent to the reference world-line), has to be renormalised by the same factor $|\mathbf{\Delta x}(0)|/|\mathbf{\Delta x}(\tau)|$.

The main disadvantage of the original LCEs is their very slow convergence to the final value, which means that for weakly chaotic systems a very long integration time is often necessary to prove the nature of their orbits. Therefore, a number of related quantifiers of orbital deviation has been proposed whose computation converges faster and which thus reveal the nature of orbits in a significantly shorter integration time. Froeschlé et al. (1997) suggested the so called fast Lyapunov indicator (FLI) which is tied very straightforwardly to the idea of exponential versus polynomial grow of the separation vector: it is related to its norm by

$$\mathrm{FLI}(t) = \log_{10} \frac{\|\mathbf{\Delta w}(t)\|}{\|\mathbf{\Delta w}(0)\|} , \tag{4}$$

or, when restricting only to its configuration-space part as above,

$$\mathrm{FLI}(\tau) = \log_{10} \frac{|\mathbf{\Delta x}(\tau)|}{|\mathbf{\Delta x}(0)|} . \tag{5}$$

FLI(τ) grows considerably faster for chaotic than for regular trajectories and this trend is evident much earlier than $\lambda_{\max}$ approaches its limit value. The degree of chaoticity of different phase-space layers can thus be effectively compared according to the values of FLI($\tau_{\max}$) found for their orbits (for some suitably chosen $\tau_{\max}$), even though these values does not have an invariant meaning.

Classification of dynamics according to the rate of growth of some quantifier (FLI) is practical for a small number of orbits, but for an extensive automatic survey which should scan a large part of the phase space it is more desirable to process just *value* of some quantity, if possible a time-independent one. Such kind of quantity was proposed by Cincotta & Simó (2000): the mean exponential growth factor of nearby orbits (MEGNO), computed as the mean temporal moment of the time change of $\ln\delta(t)$, where $\delta(t)$ is the variation of trajectory, namely

$$Y(t) = \frac{2}{T}\int_0^T \frac{\dot{\delta}(t)}{\delta(t)}\, t\,\mathrm{d}t . \tag{6}$$

The authors showed that for regular orbits the value of MEGNO tends to 2 with an additional bounded oscillating term, whereas it grows linearly for chaotic orbits with a slope corresponding to the value of mLCE ($Y(\tau) \approx \lambda_{\max}\tau$ for large enough time); for a sufficiently long interval T the values clearly distinguish between the two regimes. Not long ago Mestre et al. (2011) found an analytic relation between FLI and MEGNO,[2]

$$Y(\tau) = 2\,[\mathrm{FLI}(\tau) - \overline{\mathrm{FLI}}(\tau)]\,\ln(10) , \tag{7}$$

where the FLI time average is given by

$$\overline{\mathrm{FLI}}(\tau) = \frac{1}{\tau}\int_0^\tau \mathrm{FLI}(s)\,\mathrm{d}s . \tag{8}$$

Since the value of MEGNO oscillates with the same frequency as that of FLI, we can compute its time average in the same way,

$$\overline{Y}(\tau) = \frac{1}{\tau}\int_0^\tau Y(s)\,\mathrm{d}s . \tag{9}$$

The average MEGNO $\overline{\mathrm{Y}}(\tau)$ behaves smoothly and for τ long enough clearly distinguishes between regular and chaotic motion, hence it is a most suitable indicator for automatic computations and can be easily determined from the course of FLI. Furthermore, computing the linear regression for MEGNO(τ) one infers the value of mLCE. In the literature, the MEGNO indicator has been mainly employed to study galactic and planetary dynamics. The FLI has also been computed for general-relativity problems (motion in black-hole fields), see Han (2008a,b).

In the next section, we compute the mLCE, FLI and MEGNO coefficients for our system of geodesics in the field of a static and axially symmetric (originally Schwarzschild) black hole surrounded concentrically by an inverted 1st Morgan-Morgan counter-rotating thin disc. The sources are uniquely specified by the rel-

[2] When comparing this paper with that by Cincotta & Simó (2000), mind the different definitions of FLI, with decadic logarithm in the older paper whereas with natural logarithm in the more recent one. This brings the $\ln(10)$ factor into the following relation.

ative disc mass $\mathcal{M}/M$ and by the disc's inner Schwarzschild radius $r_{\rm disc}$. The geodesics are characterised by their conserved energy and angular momentum at infinity, E and L; the role of another "integral of motion" is played by four-velocity normalisation $g_{\mu\nu}u^\mu u^\nu = -1$. The remaining freedom is exploited, in order to scan the phase space properly, by launching the particles from different points within a certain accessible domain and in different local directions. We will compare the information captured by the coefficients with each other as well as with results obtained by different methods in previous papers (Semerák & Suková 2010, 2012).

2.1 Lyapunov characteristic exponents

We will compute the mLCE by relation (2) and adopt the two-particle approach, so we will integrate two geodesics starting from slightly different initial conditions; we set the initial distance between them $|\Delta\mathbf{x}(0)|$ at $(10^{-7} \div 10^{-9})M$. The ratio of the actual to the initial separation is then recorded in some constant step of proper time τ, renormalising the deviation vector to the initial norm $|\Delta\mathbf{x}(0)|$, together with renormalising the momentum deviation by the same factor, whenever the displacement reaches $10^{-1}M$. The integration time has to be sufficient in order to reach a satisfactory convergence of mLCEs. Specifically, we follow the selected orbits for $\tau_{\rm max} = 10^7 M$ which corresponds to some $4{\cdot}10^4$ cycles abound the central black hole. We then plot the behaviour of the so-called time-dependent mLCE

$$\lambda_{\rm max}(\tau) = \frac{1}{\tau}\,\ln\frac{|\Delta\mathbf{x}(\tau)|}{|\Delta\mathbf{x}(0)|} \tag{10}$$

in a log-log scale where it decreases linearly for regular motion while it converges to some non-zero value for chaotic motion. We estimate the final value $\lambda_{\rm max} \equiv \lambda_{\rm max}(\tau \to \infty)$ by an average of the last 5% of points; for regular orbits this typically represents an upper limit on the actual mLCE value. (We also add a standard deviation of the obtained values, although this represents purely statistical error tied to a given set of points.)

Examples of $\lambda_{\rm max}(\tau)$ together with the corresponding Poincaré sections are given in figures 1 and 2. In figure 1, three different geodesics (we will call them A, B, C for later reference) with the same global parameters but different initial conditions are shown; the orbit A is regular and belongs to the primary island around the period-one orbit and the orbit B belongs to a regular island with higher period. The behaviour of $\lambda_{\rm max}(\tau)$ is somewhat more noisy for B, but in both cases it converges to zero linearly in the log-log scale, falling down to the value around $1 \cdot 10^{-6}M$ after $\tau_{\rm max} = 10^7 M$. Regarding that the reciprocal value of mLCE represents a typical time of orbital divergence (the time in which the deviation vector elongates e-times), one can just claim, after following the orbits up to $\tau_{\rm max} = 10^7 M$, that neither of them is chaotic on the time scale $\approx 10^6 M$, which is not very efficient.

The last geodesic (C) in figure 1 fills the whole chaotic layer during the integration time and the final value $\lambda_{\rm max}(\tau_{\rm max}) \approx 1.5 \cdot 10^{-3}M$ confirms that it is chaotic on time scales of a few orbital periods. Note that the given value of the maximal Lyapunov exponent characterises the whole connected region densely filled with the orbit, but finite pieces of this same trajectory may spend a substantial time in some smaller subsets of phase space, possibly in the vicinity of less unstable periodic orbits or even periodic islands ("sticky" motion), where the character of motion is determined by their stable and unstable manifolds. Symptomatically, after spending some time in a certain region, the orbit may suddenly jump to a different part of the "chaotic sea" and its local behaviour may change considerably; such a variable behaviour typically produces a ragged profile of $\lambda_{\rm max}(\tau)$, see the bottom row of figure 1. In order to better visualise this feature, we coloured the points in this chaotic orbit's Poincaré section according by their proper time: clearly the colour of chaotic layer is not homogeneous.

Figure 2 presents three orbits (D, E, F) of different levels of chaoticity; orbits E and F have the same global parameters but differ in energy. Orbit D is only slightly chaotic, filling just very thin chaotic layer which originated from a separatrix of the chain of regular islands. As it is well known, such a separatrix, representing a boundary between two different types of motion (e.g. orbits with different periods) and connecting unstable periodic points, is the seed of chaos in the non-linear system. The thin chaotic layer still contains a chain of smaller periodic islands (see the zoom of the Poincaré surface pasted inside the plot), and indeed the orbit yields quite a low value of mLCE, $\lambda_{\rm max}(\tau_{\rm max}) = 9.88(4) \cdot 10^{-5}M^{-1}$. The second orbit, E, also spends a lot of time in rather narrow layer sticked to periodic islands, but then it sets off into the wide chaotic region around; this behaviour reflects in a somewhat (roughly 4x) higher mLCE value, $\lambda_{\rm max}(\tau_{\rm max}) = 4.28(6) \cdot 10^{-4}M^{-1}$. The third orbit, F, has higher energy and is strongly chaotic — it intersects the equatorial plane quite uniformly across the surface of section; correspondingly, the mLCE tends to a much higher value $\lambda_{\rm max}(\tau_{\rm max}) = 2.250(4) \cdot 10^{-3}M^{-1}$ (note that thanks to the "clear character" of the orbit, convergence is already reached before $\tau = 10^5 M$).

2.2 Fast Lyapunov indicator

After illustrating that the mLCE behaves in an expected way for our system and, in particular, that it however requires to follow the trajectories for a very long time, let us now focus on the FLI which does not require such a long integration. First, in figures 4 and 5 we compute the FLI(τ) according to relation (5) for the above long trajectories. As expected, FLI remains below 5 for the first two regular orbits, whereas for the remaining chaotic orbits it exceeds several thousands.

We now reduce the integration time to $\tau_{\rm max} = 2.5 \cdot 10^5 M$, which allows to consider more orbits with different initial conditions and to cover the whole phase space. Three examples of such a map are given in figure 6, left column. Each of the sections shown there includes a few hundred different trajectories, which are coloured according to the final value FLI($\tau_{\rm max}$). In the first row, the same global parameters are chosen which were used for the orbits A–C in figure 1. The most chaotic trajectories of this diagram reach some FLI ≈ 300 and are clearly distinguished from the regular ones which yield FLI ≈ 3. However, some of the weakly chaotic orbits reach only FLI ≈ 10, so the distinction is quite uncertain for them. An interesting feature of the first map is the obvious split of the chaotic sea into subregions with different FLI($\tau_{\rm max}$), though we saw in figure 1 (orbit C) that the whole region is a connected chaotic layer. This can be ascribed to the shorter integration time, namely not long enough for some orbits to leave the neighbourhood of periodic islands, and it nicely illustrates the different *local* behaviour of particles within the chaotic domain.

The second and third rows in the left column of figure 6 display geodesics having the same parameters as orbits E and F in figure 2, they only differ in energy. In both cases, the phase-space structure is quite complicated. The second-row map (lower energy) shows the emergence of chaotic layers inside invariant tori, a very thin strongly chaotic region at the periphery of the accessible lobe which, however, almost borders with several higher-period regu-

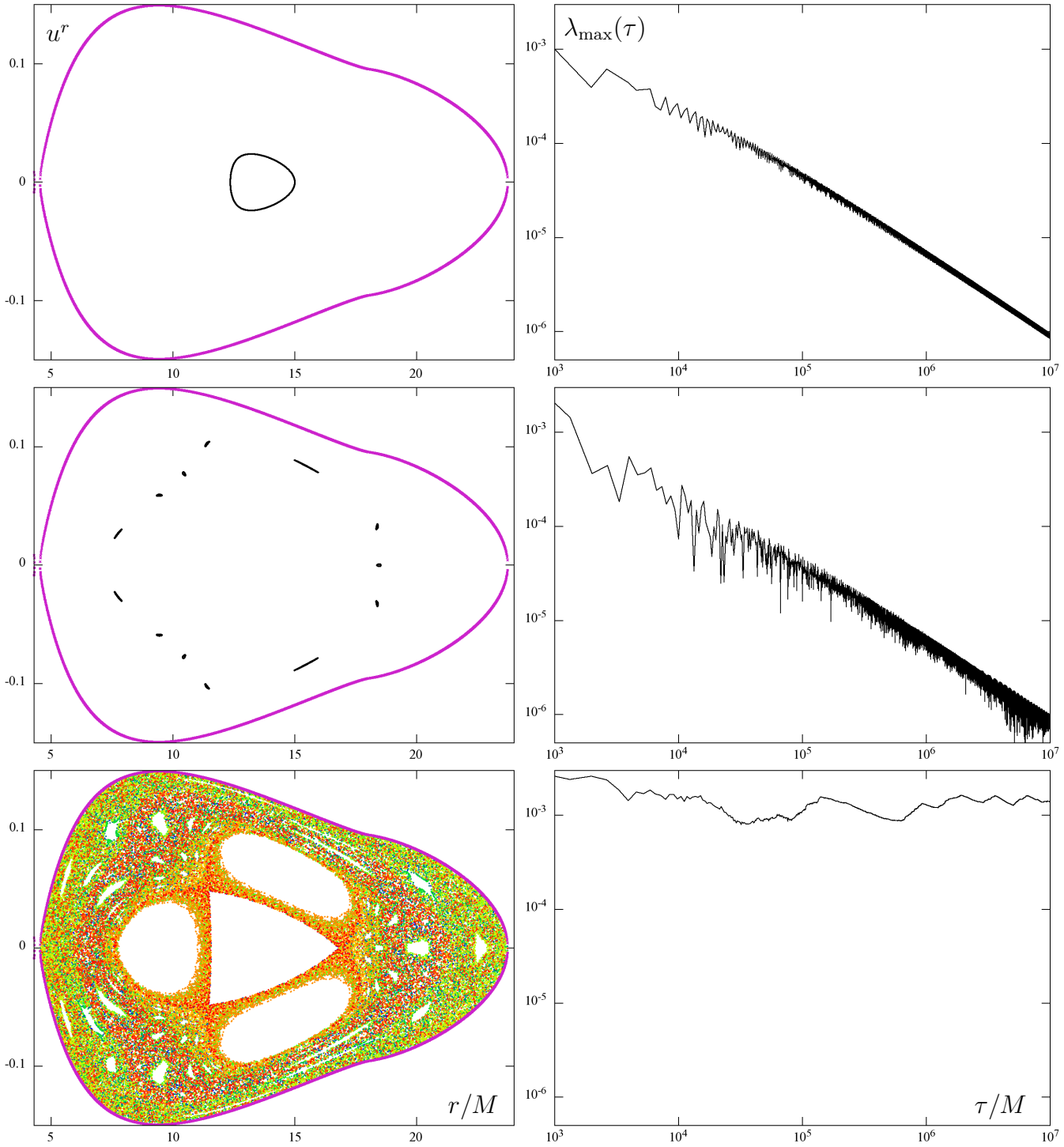


Figure 1. Poincaré sections $\theta = \pi/2$ (left) and maximal Lyapunov characteristic exponents $\lambda_{\max}(\tau)$ (mLCEs, right) for two regular (A, B) and one chaotic (C) geodesic in the field of a black hole surrounded by the inverted 1st Morgan-Morgan disc. The disc parameters are $\mathcal{M} = M/2$, $r_{\rm disc} = 18M$, and the specific energy and angular momentum of the geodesics are $\mathcal{E} \equiv -u_t = 0.9532$, $\ell \equiv u_\phi = 3.75M$. The last Poincaré section is coloured according to the proper time of the passages; the time increases from blue to red in the order of the visible-spectrum colours. Different colour tones indicate that the orbit is not distributed uniformly over the chaotic layer, but rather lingers in a specific volume for some time and then "switches" to a different one. The obtained values of $\lambda_{\max}(\tau_{\max})$ are $(9.35 \pm 0.38) \cdot 10^{-7} M^{-1}$ for the upper row (orbit A), $(8.78 \pm 0.58) \cdot 10^{-7} M^{-1}$ for the middle row (orbit B) and $(1.405 \pm 0.007) \cdot 10^{-3} M^{-1}$ for the bottom row (orbit C). The FLI and MEGNO values for the same orbits are plotted in figure 4.

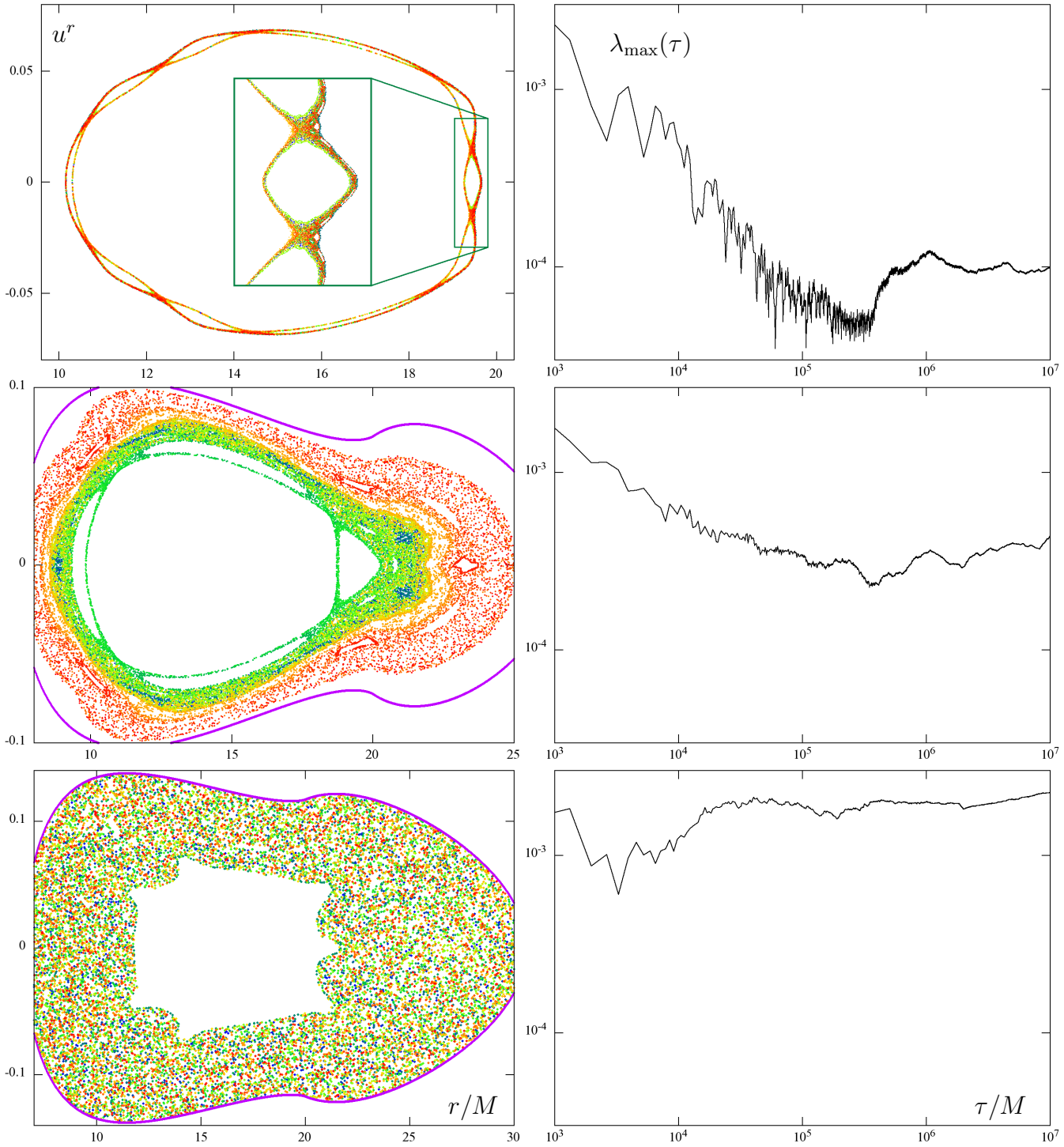


Figure 2. Poincaré sections (left) and mLCEs $\lambda_{\max}(\tau)$ (right) for three chaotic orbits (D, E, F) of different degrees of irregularity. The global parameters are $\mathcal{M} = 0.94M$, $r_{\rm disc} = 20M$, $\mathcal{E} = 0.947$, $\ell = 4M$ in the upper row (D); $\mathcal{M} = 1.3M$, $r_{\rm disc} = 20M$, $\mathcal{E} = 0.9365$, $\ell = 4M$ in the middlde row (E); and $\mathcal{M} = 1.3M$, $r_{\rm disc} = 20M$, $\mathcal{E} = 0.941$, $\ell = 4M$ in the bottom row (F). The orbits clearly fill phase-space layers of different volumes, in agreement with the obtained values $\lambda_{\max}(\tau_{\max}) = (9.88 \pm 0.04) \cdot 10^{-5} M^{-1}$ (up, D), $\lambda_{\max}(\tau_{\max}) = (4.28 \pm 0.06) \cdot 10^{-4} M^{-1}$ (middle, E) and $\lambda_{\max}(\tau_{\max}) = (2.250 \pm 0.004) \cdot 10^{-3} M^{-1}$ (bottom, F). Colouring of the passages through the Poincaré surface by proper time (it increases in the order blue $\rightarrow$ green $\rightarrow$ yellow $\rightarrow$ red) reflects that the 2nd trajectory lingers for a longer time near the periodic island and only then sets off into the outer part of the phase space, whereas the 3rd trajectory is rather uniformly distributed across the layer for all the time. Yet in a certain interval of time (around $\tau \sim 2000M$) the mLCE of the third orbit is *smaller* than the mLCE of the second one. The orbits plotted here also appear in the animations which are accessible in the online version. The same orbits D, E, F are also processed in figures 3 and 5.

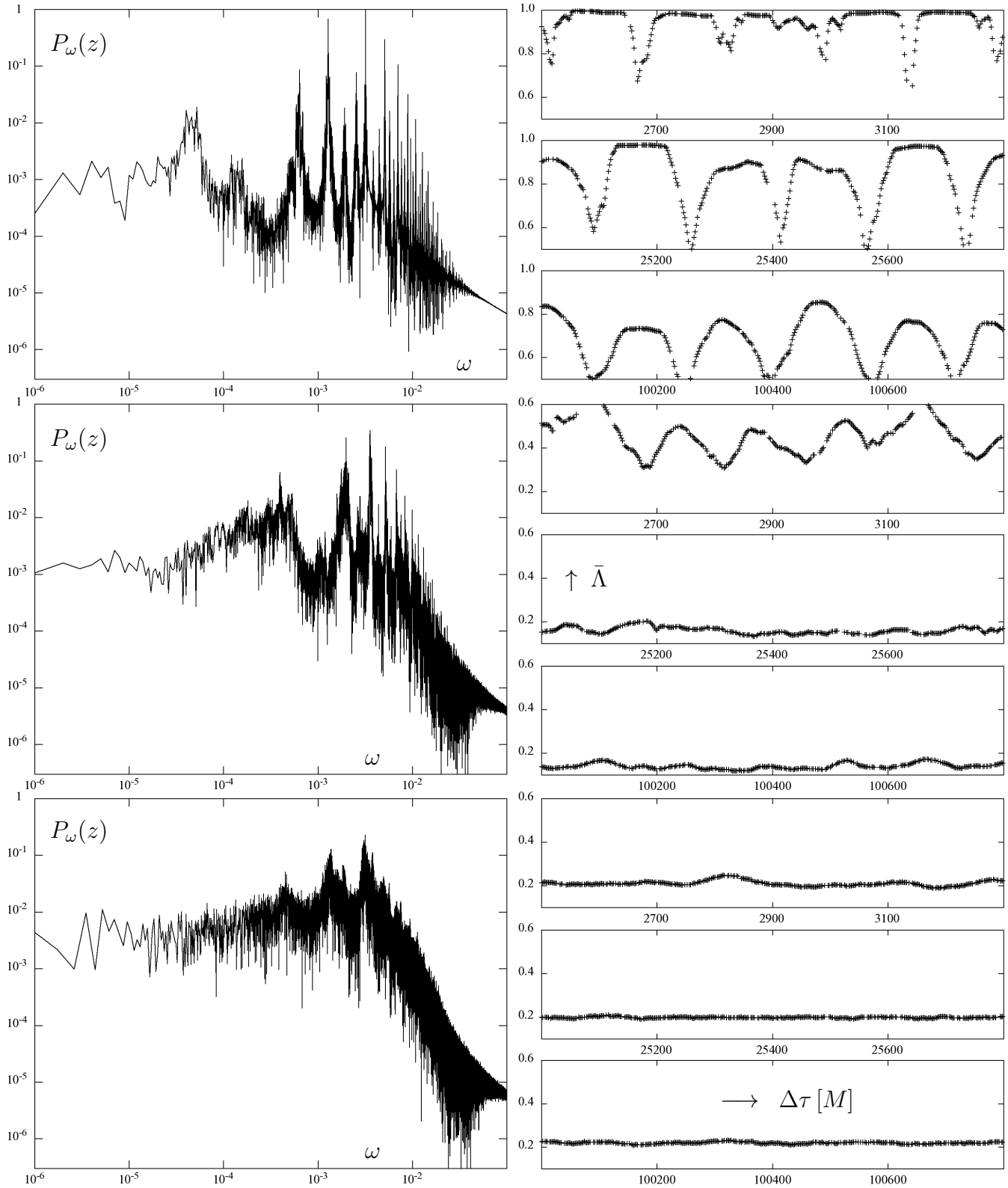


Figure 3. Power spectra of vertical position $z = r\cos\theta$ (left column) and average of the directions in which a given geodesic recurs to a prescribed phase-space mesh, $\bar{\Lambda}$ (right column), plotted for the same three orbits (D, E, F) whose Poincaré diagrams and mLCEs have been shown in figure 2. In contrast to figure 2 where the orbits were computed up to $\tau_{\max} = 10^7\,M$, here only their parts reaching to $\tau_{\max} = 10^6\,M$ have been processed. The Kaplan-Glass indicator $\bar{\Lambda}$ decreases in general (from 1 and the more the less regular is the orbit) with the time shift $\Delta\tau$ used to reconstruct a phase space from a given time series; the $\bar{\Lambda}(\Delta\tau)$ dependence for all three orbits is drawn for three separate time-shift intervals, (2500–3300)M, (25000–25800)M and (100 000–100 800)M. The first orbit is almost regular, whereas the other two are chaotic. See section 3 for more discussion. The FLI and MEGNO values for the same orbits are plotted in figure 5.

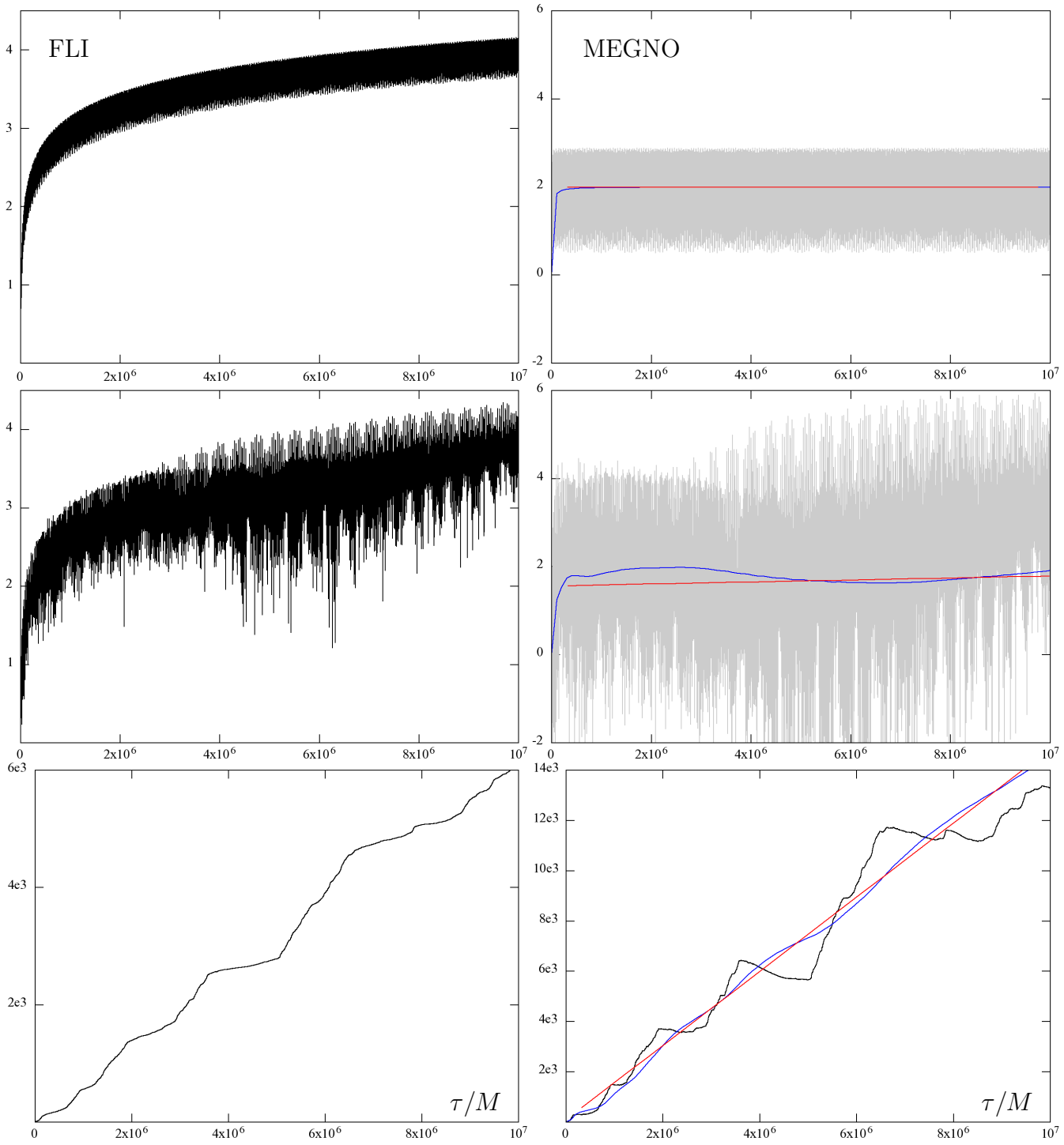


Figure 4. FLI(τ) in the left column and $Y(\tau)$ (MEGNO) in the right column for the three orbits (A, B, C) shown in figure 1. The average MEGNO $\overline{Y}(\tau)$ is drawn in blue and the linear fit of MEGNO is in red. The obtained values of $\lambda_{\max}^{\mathrm{MEGNO}}$ are $(2.12 \pm 0.01) \cdot 10^{-9} M^{-1}$ for the upper row (orbit A), $(4.50 \pm 0.08) \cdot 10^{-8} M^{-1}$ for the middle row (B) and $(1.475 \pm 0.001) \cdot 10^{-3} M^{-1}$ for the bottom row (C).

lar islands (this reminds that increasing the "distance" from the central regular island does not necessarily lead to stronger chaos). The bottom left map (higher energy) is different: regular motion is concentrated at the centre, surrounded by a large chaotic sea with quite uniformly distributed points and values of FLI($\tau_{\max}$). But neither this configuration is "stable", as inside the primary island there arises a period-three island which for higher energy breaks the surrounding tori. The last two left diagrams of figure 6 indicate that increasing the particle energy not only enlarges the accessible region but also potentiates the disc's influence on the dynamics. However, as already observed in previous papers, one cannot simply say that higher energy favours chaos; the latter is certainly true for a low end of the energy range, but the energy dependence is rather com-

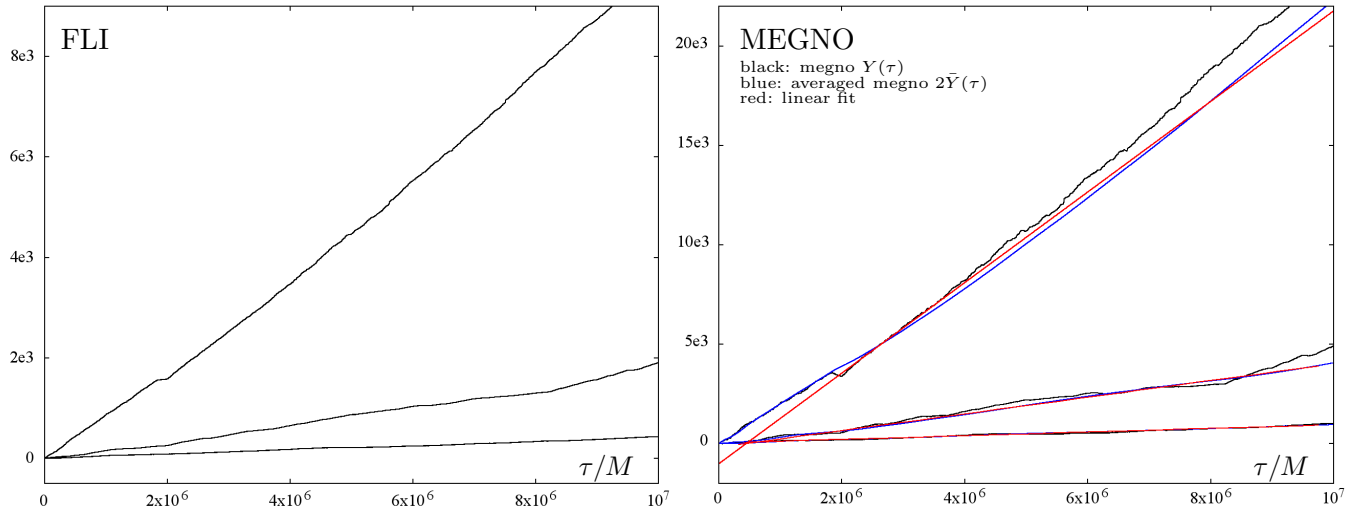


Figure 5. FLI(τ) on the left and $Y(\tau)$ (MEGNO) on the right, computed for the three orbits (D, E, F) shown in figures 2 and 3. The average MEGNO $\overline{Y}(\tau)$ is drawn in blue and the linear fit of MEGNO is in red. The obtained values of $\lambda_{\max}^{\mathrm{MEGNO}}$ are $(9.172 \pm 0.003) \cdot 10^{-5} M^{-1}$ for orbit D (the bottom one), $(4.192 \pm 0.001) \cdot 10^{-4} M^{-1}$ for orbit E (the middle one) and $(2.278 \pm 0.001) \cdot 10^{-3} M^{-1}$ for orbit F (the top one).

plicated in general, with abrupt changes around certain values, and rather typically with a regression to regularity for very large values.

2.3 Mean exponential growth factor of nearby orbits

In this section we compare the results provided by the FLI and MEGNO coefficients, as obtained from the time behaviour of FLI(τ) using the relation (7). We also estimate the mLCE from linear regression of $\bar{Y}(\tau)$, on the basis of the relation $Y(\tau) \approx \lambda_{\max}(\tau)\,\tau$; let us denote the mLCE determined in such a way λ^{MEGNO}. Note that if using the *averaged* value of MEGNO $\overline{Y}(\tau)$ for the regression, one has to bear in mind that the averaging decreases the slope of a linear function by a factor of 2. In other words, in order to get a "smooth" value of MEGNO corresponding to time τ, we have to multiply the value $\overline{Y}(\tau)$ given by relation (9) by 2 before performing the regression.

As already stressed above, the main advantage of MEGNO is a clear distinction between chaotic and regular motion, based on the fact that $\bar{Y}(\tau \to \infty) = 2$ for regular orbits regardless of the system details, and also a rather good convergence. When implementing a routine check, one chooses a certain "order-chaos" threshold μ which certainly has to be bigger than 2 (in order to include oscillations about the asymptotic value), but typically just a slight shift is sufficient. For a given μ, one can estimate how much chaotic the motion has to be in order to be able to detect its chaoticity within a given time interval. Namely, since the mLCE is deduced from the average slope of MEGNO(τ), one finds $\lambda_{\max}(\tau_{\max}) \approx \mu/\tau_{\max}$ as a rough bound on how strong chaoticity can be captured. In our computations we set $\mu \equiv 4$ and $10^5 \le \tau_{\max} \le 10^6 M$, hence we are able to "see" chaos with $\lambda_{\max}(\tau_{\max}) \gtrsim 10^{-5} M^{-1}$.

In figures 4 and 5, we plot $Y(\tau)$ and $\bar{Y}(\tau)$ (or $2\bar{Y}(\tau)$) for our selected regular and chaotic trajectories, together with the linear fit which yields the value of mLCE. The estimates of $\lambda_{\max}^{\mathrm{MEGNO}}$ for the regular orbits are in the range $10^{-8} \div 10^{-9}$, which is about two orders of magnitude below the values of $\lambda_{\max}$ obtained from the definition (2). This indicates better convergence of the present method: the values comparable to those provided by direct computation (with $\tau_{\max} = 10^7 M$) are reached now at $\tau_{\max} \approx 250\,000 M$ already. Note also that the resulting mLCEs of the chaotic trajectories are in a very good agreement for both methods, they differ only by 5% or less. The results are summarised in table 1.

Orbit	$\lambda\max(\tau_{\max})$	λ^{MEGNO}	K_2
A	$9.35 \cdot 10^{-7}$	$2.12 \cdot 10^{-9}$	$1.74 \cdot 10^{-7}$
B	$8.78 \cdot 10^{-7}$	$4.50 \cdot 10^{-8}$	$2.7 \cdot 10^{-7}$
C	$1.405 \cdot 10^{-3}$	$1.475 \cdot 10^{-3}$	$1.23 \cdot 10^{-3}$
D	$9.88 \cdot 10^{-5}$	$9.172 \cdot 10^{-5}$	$2.97 \cdot 10^{-5}$
E	$4.28 \cdot 10^{-4}$	$4.192 \cdot 10^{-4}$	$3.12 \cdot 10^{-4}$
F	$2.25 \cdot 10^{-3}$	$2.278 \cdot 10^{-3}$	$1.69 \cdot 10^{-3}$

Table 1. The values of $\lambda_{\max}(\tau_{\max})$ and K_2 for the orbits from figures 1 and 2, listed in the same order. Total integration time is $\tau_{\max} = 10^7 M$. The values were obtained by three different methods, the direct computation from definition, the estimate from linear regression on MEGNO and the estimate from K_2 provided by the recurrence analysis.

Naturally we compare now the figures where FLI and MEGNO have been used for colouring of the passage points in Poincaré diagrams. We proceed similarly as in section 2.2, recolouring the same diagrams as there according to the achieved MEGNO values $\bar{Y}(\tau_{\max})$; the maps obtained are shown in the right column of figure 6. Taking advantage of the universal small value of MEGNO for regular orbits ($\bar{Y}(\tau \to \infty) = 2$), which makes the distinction between regular and chaotic motion more reliable, we set the threshold at $\mu = 4$ and whenever $\bar{Y}(\tau_{\max})$ is found to be bigger than 4, we add 200 to its value (the added constant is optional, of course). This makes the difference between weakly chaotic and regular orbits more clear visually. (Without this adjustement, the plots would look the same as those coloured by FLI, just with a slightly different value range.) Figure 6 demonstrates that both the FLI and MEGNO capture the main features of the dynamics, with fine details better revealed by the latter thanks to having emphasised the order-chaos transition by the additional factor of 200. This is well visible in the second and third rows, where some orbits near the regular islands look rather regular in the left column, while on the right the adjusted MEGNO values reveal their chaotic nature.

In order to further support the above conclusion, we have computed another multi-orbit map spanning a significantly longer time $\tau_{\max} = 10^6 M$; it is depicted in figure 7 together with a zoom of

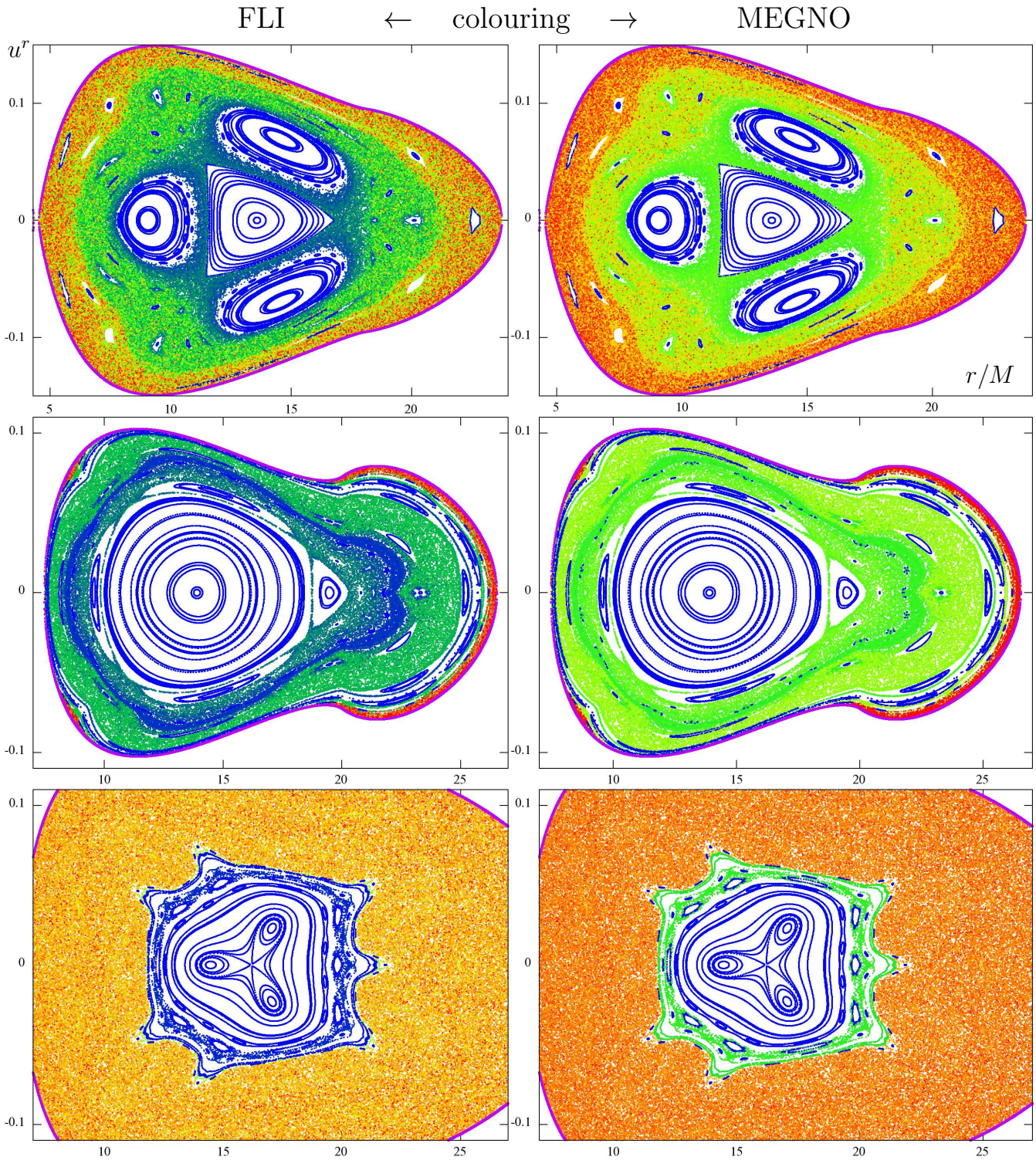


Figure 6. Poincaré surfaces of section coloured according to the value of FLI($\tau_{\max}$) (left column) and $\bar{Y}(\tau_{\max})$ (right column), where $\tau_{\max} = 250\,000M$. Choice of parameters: $\mathcal{M} = M/2$, $r_{\rm disc} = 18M$, $\mathcal{E} = 0.9532$, $\ell = 3.75M$ in the first row; $\mathcal{M} = 1.3M$, $r_{\rm disc} = 20M$, $\mathcal{E} = 0.9365$, $\ell = 4M$ in the second row; and $\mathcal{M} = 1.3M$, $r_{\rm disc} = 20M$, $\mathcal{E} = 0.941$, $\ell = 4M$ in the third row. Whenever $\bar{Y}(\tau_{\max}) > 4$, we add a constant of 200 to it $[\bar{Y}(\tau_{\max}) \to \bar{Y}(\tau_{\max}) + 200]$ in order to enhance distinction between regular and weakly chaotic regions. Such an adjusting is possible since the MEGNO indicator approaches a distinct universal value (namely 2) for regular orbits, whereas for chaotic motion it converges towards larger values (typically of the order of hundreds to thousands). This is its main advantage over the FLI, while otherwise both columns are seen to provide the same information. The colours going from blue to red in the visible-spectrum order correspond to FLI increasing in the range 0–350 (left) and to MEGNO increasing in the range 0–500 (after adding 200 to every value above 4, which makes the blue of regular islands more contrasting).

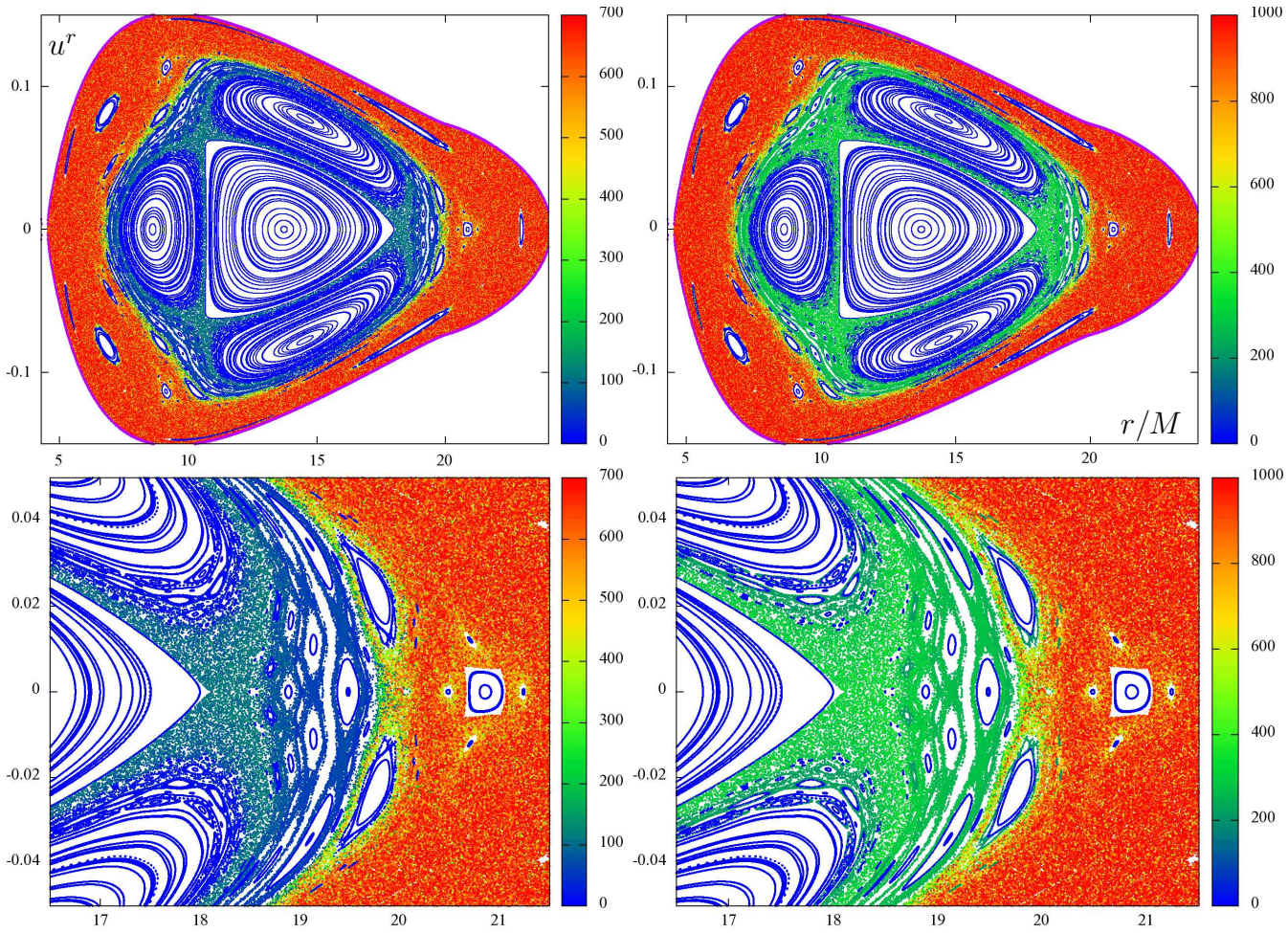


Figure 7. Poincaré surfaces of section coloured according to the value of FLI($\tau_{\max}$) (left column) and $\bar{Y}(\tau_{\max})$ (right column), where $\tau_{\max} = 10^6 M$. Zoom of the most complex regions is added in the second row. Parameters are chosen as $\mathcal{M} = M/2$, $r_{\rm disc} = 20M$, $\mathcal{E} = 0.955$, $\ell = 3.75M$. All values $\bar{Y}(\tau_{\max}) > 4$ are increased by 200 in order to better distinguish between regular and weakly chaotic regions.

the most complicated part of the phase space. The section coloured according to the adjusted average MEGNO well reveals fine structures like small periodic islands embedded inside thin chaotic layers, while the colouring by FLI (which does not enable a similar adjustement) does not render such a resolution (and the longer integration time does not improve it much).

2.4 On visualisation of chaos: animations

Chaotic dynamics yields lots of nice geometry, but it very difficult to illustrate, within finite space, its most interesting aspect, namely the *chaotic* dependence on parameters. Actually, a short series of static plots can indicate an overall tendency, but it is even more remarkable how non-monotonous, irregular these dependences often are, with sudden changes of the phase portrait occurring/disappearing within very narrow parameter ranges. In more complex systems, such features may even remain unnoticed, because numerical scanning of the phase space is performed with a certain finite "sampling step".

In order to explore more closely the role of our crucial parameters, the relative disc mass and the particle energy, we computed sequences of MEGNO-coloured Poincaré maps with gradually increasing relative-mass or energy value while leaving all the other parameters constant, and compiled animations of them. The resulting two videos are available in the online version. The first animation shows dependence of the phase portrait on particles' energy, for a system with disc mass $\mathcal{M} = 1.3M$ and inner radius $r_{\rm disc} = 20M$ and with angular momentum $\ell = 4M$. It starts from the value $\mathcal{E} = 0.931$ which is then increased by a step of 0.001; within the range $0.933 \leq \mathcal{E} \leq 0.939$ the step is only 0.0001, however, because the phase space changes quite wildly there. The accessible phase lobe emerges near the radius $r = 11M$ and contains just completely regular motion at first. Until $\mathcal{E} = 0.9331$ it grows as the particle can move regularly in larger and larger region. At $\mathcal{E} = 0.9332$ another lobe arises at higher radii, namely where the disc's density has its maximum; the motion in this new lobe is also regular. With increased energy the regular islands with higher period arise inside the primary island. First chaos is seen at $\mathcal{E} = 0.9337$, near the periphery of the secondary lobe. This secondary lobe quickly gets strongly chaotic, as indicated by very high values of FLI achieved immediately on the next snapshot ($\mathcal{E} = 0.9338$). On the following one ($\mathcal{E} = 0.9339$), the two lobes merge and the chaos breaks over the periphery of the primary lobe. The structures from the prior two lobes begin to merge, while the chaos recedes (the orbits' FLI decreases) surprisingly, and new regular tori appear which encircle both the former primary

islands and small higher-periodic islands. The strongly chaotic peripheral region remains almost untouched during this process, but when the energy reaches about 0.9362, it gets rather narrow and at $\mathcal{E} = 0.9365$ many regular islands begin to emerge within the primary island. This however brings new resonances which, as the new structures travel towards the edge of the lobe, give rise to a large chaotic sea there. At $\mathcal{E} = 0.958$ a channel in the potential well opens and the particles can fall into the black hole. For very high values of energy, the central island usually restores and spreads, as the dynamics gradually returns to a rather regular behaviour.

The second animation illustrates the dependence on relative mass of the disc with respect to the black-hole mass, $\mathcal{M}/M$, for $r_{\rm disc} = 20M$, $\mathcal{E} = 0.947$ and $\ell = 4M$. The overall tendency of evolution of the phase space is quite similar, there also first appears the primary lobe, then the secondary one around the disc's density maximum, the lobes merge and higher-periodic islands accompanied by separatrices breaking then into chaotic layers arise and shift towards the peripheral region in a complicated order. The dynamics is strongly chaotic when $\mathcal{M} \sim M$, while for very high values of the disc mass it rather returns to a more regular pattern.

3 COMPARISON WITH PREVIOUS RESULTS AND OTHER METHODS

It is interesting to compare the mLCE estimate with the value of the second-order Rényi's entropy K_2 (it reflects a certain type of correlation in the system). The latter is one of the quantifiers of chaos which can be computed from the statistics of orbital recurrences to prescribed domains in the phase/configuration space or in their subspaces; we presented the recurrence analysis of our system in previous paper (Semerák & Suková 2012). The Rényi's entropy is given by a slope of the cumulative histogram of diagonal lines of the recurrence plot and represents a lower estimate on the sum of positive Lyapunov exponents. Note that there is an important difference between recurrence quantifiers and the coefficients of orbital divergence discussed here: for obtaining LCEs etc. one has to compute two nearby trajectories (or solve the variational equation along the flow), which requires to know the underlying equations of motion, whereas the correlation entropy K_2 and similar quantifiers can be estimated from the recurrence analysis of just partial (e.g. observational) data containing only very restricted information about the system, for example, from a time series of only one dynamical variable (e.g. one coordinate). Although the computation of K_2 is quite tricky and requires some experience with recurrence analysis and tuning of its parameters, the values of mLCEs found in the present paper well agree with the estimate obtained from K_2 in the previous one. More specifically, the mLCEs computed from the MEGNO slope are slightly larger than K_2 for chaotic orbits C–F, while they are smaller than K_2 for regular orbits A, B (for which the convergence of MEGNO is better than the direct computation of $\lambda_{\rm max}$). The comparison thus confirms the results presented previously.

A more systematic test of the indicators derived from orbital-deviation evolution was carried out by Lukes-Gerakopoulos et al. (2008); their comparison with spectral methods has recently been performed by Maffione et al. (2013). Here we select figure 2 for such a comparison and add figure 3 where the same three orbits are represented (i) by power spectra of the vertical coordinate $z = r\cos\theta$, denoted $P_\omega(z)$, and (ii) by the averaged "quadratic deviations from random walk", computed from the added-up directions in which the geodesics recurrently pass through the prescribed phase-space boxes, $\bar{\Lambda}(\tau)$. This second method was originally designed by Kaplan & Glass (1992) to distinguish between deterministic and random evolutions, but we learned in the preceding paper that it can be very efficient "on the other side of the spectrum", namely in recognising tiny differences between the amount of chaos in *very weakly* perturbed systems (or rather between very weakly chaotic orbits or their parts). The rate of recurrent vanishing of a preferred local transit direction is in our case computed in a phase space spanned by a time series of the particle's $z(\tau)$ location and by its two time-delayed copies $z(\tau - \Delta\tau)$ and $z(\tau - 2\Delta\tau)$. The result depends on $\Delta\tau$ in a way that is specific for different degrees of chaoticity (or even stochasticity), while the asymptotic *value* (approached for $\Delta\tau \to \infty$) itself brings a clear information: namely, for regular motions $\bar{\Lambda}$ keeps close to unity, for chaotic motions it decreases to some smaller value and for random noise it falls towards zero.

This is an advantage over power spectra which are often hard to classify (as "more or less chaotic"), as also illustrated by figure 3. It well agrees with its counterpart 2 where Poincaré diagrams and mLCEs of the same orbits were displayed. Let us point out that $\bar{\Lambda}(\Delta\tau)$ dependences are plotted only for three selected short intervals of time delay rather than in a full available range as in preceding paper. It is worth to note the difference between the second and the third rows: in figure 2 as well as according to the left column of figure 3 (power spectra), the third-row orbit (F) is more chaotic than the second-row one (E), the only exceptions being the mLCE value around $\tau \sim 2000M$ and the low-frequency part of spectra. Correspondingly, the value of the Kaplan & Glass quantifier $\bar{\Lambda}$ (right column of figure 3) first decreases considerably more slowly for the E orbit, but for large $\Delta\tau$ it even gets *below* the value produced by the "chaotic-sea" F orbit. This confirms that orbit E involves more correlation on short time scales, but on larger scales the correlation washes away; this is consistent with the orbit's time evolution: we checked that in figure 2 it first circumscribes the regular islands (blue), then sticks to them for some time (green) and only then spreads out to a large chaotic region (red). Note that in figure 2 the maximal integration time is $\tau_{\rm max} = 10^7 M$, while in figure 3 only the first $10^6 M$ of orbital evolution is included.

It is also interesting to subject to such a comparison the quantifiers provided by the recurrence analysis. Namely, the recurrence properties are somewhat different, "more basic" in the sense that they can be inferred just from a (discrete) time series, actually even from a series bearing just partial information (like *one* coordinate), whereas the study of orbital deviation requires the knowledge of equations of motion (plus the evolution of transversal perturbation). We can, for instance, directly compare top row of figure 12 in the preceding paper (Semerák & Suková 2012) with top row of figure 6 in the present one; they both show hundreds of geodesics characterised by energy $\mathcal{E} = 0.9532$ and angular momentum $\ell = 3.75M$, scanning the phase space of the field of a black hole (M) surrounded by a disc with mass $\mathcal{M} = M/2$ and inner radius $r_{\rm disc} = 18M$. (Note that three particular trajectories occurring in these plots are shown in figure 1.) Poincaré diagrams in figure 12 of the preceding paper are coloured according to the value of DIV (left) and according to the second Renyi's entropy K_2 (right), the former being one of the simplest quantifiers of the recurrence analysis (it is the reciprocal value of length of the recurrence-plot longest diagonal), while the latter is a more sophisticated correlation indicator determined by the slope of the diagonal-line histogram. Poincaré diagrams in top row of figure 6 of the present paper are coloured according to the value of FLI (left) and MEGNO (right). Abstracting from the somewhat differ-

ent colour tones chosen, all the four plots apparently carry the same information. One possible message which stems from this comparison is a further confirmation of efficiency of the simplest recurrence quantifier DIV.

4 A SPECIFIC ASTROPHYSICAL SYSTEM: GALACTIC NUCLEUS

We have studied the geodesics in the black-hole–disc/ring system purely as a theoretical dynamical system up to now, choosing its parameters without much regarding our original astrophysical motivation. Let us focus now on "realistic" situations and ask whether pure gravity can incite a noticeable chaos in actual astrophysical systems, though approximated by a highly symmetric configuration. The given arrangement of sources may exist in galactic nuclei, namely those where a supermassive black hole is "perturbed" by an accretion disc or a ring. The current models of galactic nuclei suggest that there typically occurs an inner hot accretion disc, having radius of light days at most, not very heavy but perhaps reaching down to the vicinity of the black-hole horizon, and a much more massive molecular torus at much larger radius (50 light years, say). If the environment is sufficiently rarefied so that the physical interaction with gas and radiation is negligible, the motion of an individual star can be approximated by a geodesic in the gravitational field dominated by the black hole plus possibly the outer torus and perturbed by the accretion disc. The physical interaction is more probably relevant in nuclei displaying high activity (which is being ascribed to the presence of matter and fields interacting with the black hole), so we should rather refer to nuclei of "normal" galaxies like Milky Way.

Yet the nucleus of our galaxy is a complex region with a number of components. Considering only those which are the most important gravitationally, observations indicate the presence of a black hole with mass $M \doteq 4.3 \cdot 10^6\, M_\odot$ and of *two* molecular-gas and dust tori (usually called circumnuclear rings, CNR), one on radii $r_{\rm ring} \sim (1.2 \div 3)\,{\rm pc}$ with mass $\mathcal{M} \sim (10^4 \div 10^6)\, M_\odot$ and the other around the radius $r_{\rm ring} \sim (60 \div 100)\,{\rm pc}$ with mass $\mathcal{M} \sim 3 \cdot 10^7\, M_\odot$.[3] In terms of the black-hole parameters, the inner ring rests around the radius $r_{\rm ring} \sim 10^7\, M$ and has mass $\mathcal{M} \sim M/20$, while the outer ring is around the radius $r_{\rm ring} \sim 4 \cdot 10^8\, M$ and has mass $\mathcal{M} \sim 10M$. In comparison with the cold tori, the hot inner accretion structure around the black hole is very small (it reaches up to few hundreds or thousands Schwarzschild radii of the central hole) and bears just small fraction of the black-hole mass. Besides that, the Galaxy centre is also inhabited by stars, black holes and gas; in the central parsec, $(10^6 \div 10^7)\, M_\odot$ of such mass is supposed to be present (plus the central black hole). In other galaxies these proportions may be considerably different, however; for (extreme) example, the NGC 1277 galaxy appears to boast a black hole with $M \sim 17 \cdot 10^9\, M_\odot$ (thus with more than 10% of the whole-galaxy mass) in the centre.

We will examine which of the above structures could have some effect on particle dynamics. Approximating the centre by a static (originally Schwarzschild) black hole, the tori by the Bach-Weyl ring solution and the inner accretion disc by the inverted first Morgan-Morgan disc solution, we will ask whether some of these sources surrounding the black hole can perturb the motion of an orbiting star (treated as a test particle characterised just by mass) so as to become chaotic. The star is supposed to orbit above the inner accretion zone but below the circumnuclear rings. Note that we do *not* take the other stars into account, describing the test-star orbit as a time-like geodesic in the space-time generated by the black hole plus the surrounding ring(s) or disc alone. (Strictly speaking, the evolution of nuclear star cluster should be studied using the relativistic N-particle celestial mechanics, kinetic-theory approach or orbital-perturbation theory, for example, but the effect of "the other" stars could also be approximated by a spherical or other potential, which might be incorporated in our system quite easily. This is one of our future plans.)

Before turning to numerical results, let us at least briefly refer to the recent high activity focused on the unique black-hole laboratory of our Galactic centre Morris et al. (2012). Besides the above gaseous and dusty structures, the main attention is devoted to stars, in particular those which orbit very close to the centre (Genzel et al. 2010). One reason is of course testing of general relativity and of the precise nature of "our" supermassive black hole (Merritt et al. 2010; Sadeghian & Will 2011; Angélil & Saha 2011), while other questions are evolutionary: where and how the observed stars were born and how did they get to their present orbits (Madigan et al. 2009; Fujii et al. 2010; Haas et al. 2011). Both tasks require to evaluate properly various possible "perturbations" acting on the star motion (Iorio 2011; Psaltis 2012; Antonini & Merritt 2013). This is also our aim here, but rather than perturbations coming from fine details of the very centre (black hole plus the inner cluster) we are interested in the effect of larger circumnuclear structures (cf. Perets et al. 2007; Chang 2009, for example), namely the two rings of molecular gas and dust.

4.1 Numerical results

4.1.1 2-parsec ring

Figures 8 and 9 present a series of equatorial Poincaré sections of the geodesic dynamics in the black-hole–ring field; the former illustrates the dependence on ring's location, while the latter illustrates the dependence on its mass. In figure 8, the mass of the ring is kept at $\mathcal{M} = M$ and the ring radius is changing in the range $(2 \div 20) \cdot 10^4\, M$; therefore, as compared to the parameters of the Milky-Way inner circumnuclear ring, the above ring is about 10 times heavier and lies about 50 times closer to the centre. In other words, the above parameters do *not* correspond to actual relations in the Galactic nucleus, but they are also not orders of magnitude different. The total integration time is chosen $\tau_{\rm max} = 15 \cdot 10^9 M$ which in this case represents some 200 orbital periods. The mass of the central black hole is set at $M = 4.3 \cdot 10^6 M_\odot$, which fixes our length and time scale according to $1M \doteq 6.6 \cdot 10^6 {\rm km} \doteq 22{\rm s}$. One orbital period is thus about 50 terrestrial years and the particle/star motion is followed for about 10 000 years. The linear orbital velocity ranges from about a hundred to a few thousand km/s.

The figures show that the effect of the ring on the motion of

[3] Whereas the Sgr A* black-hole mass appears to be quite well settled, the parameters of other nuclear constituents are less certain and a considerable spread in the values of their parameters occurs in the literature. For the inner-ring mass, recent estimates range from $1.2 \cdot 10^4\, M_\odot$ (Requena-Torres et al. 2012) via $(2 \div 5) \cdot 10^5\, M_\odot$ (Oka et al. 2011) to $1.3 \cdot 10^6\, M_\odot$ (Montero-Castano et al. 2009); Haas et al. (2011) adhered to the upper estimate $\mathcal{M} = 0.3M$ when approximating the inner circumnuclear toroid by a thin ring. A thorough review of the content of the Galactic innermost region with a list and discussion of observational values has been given by Ferrière (2012). The parameters of the outer ring have notably been estimated by Molinari et al. (2011). Both rings roughly follow the galactic plane, but the outer one appears to be twisted (not planar).

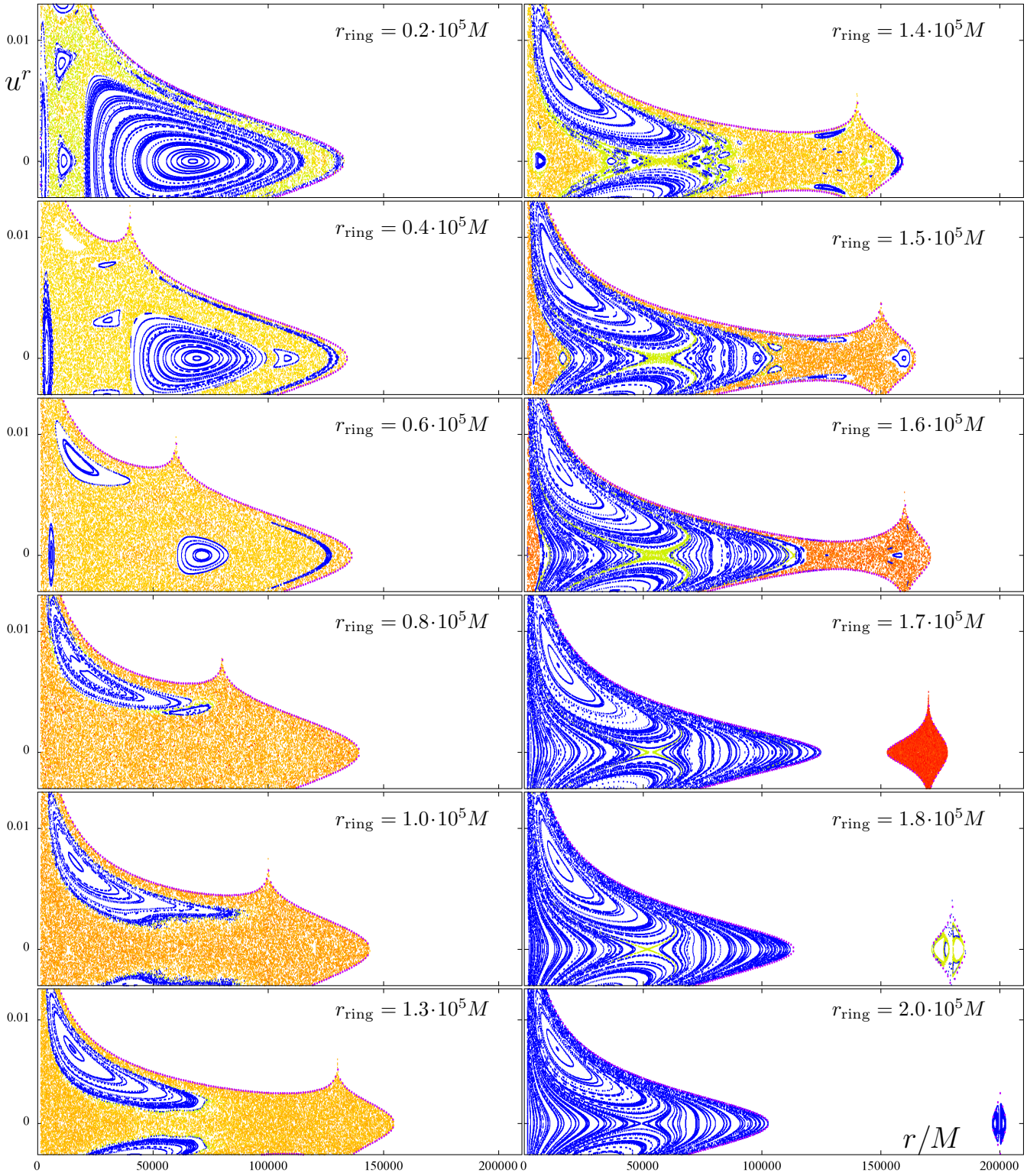


Figure 8. Geodesic dynamics in the field of a Schwarzschild black hole surrounded by a concentric Bach-Weyl thin ring with mass $\mathcal{M} = M$. Poincaré surfaces of section coloured by the value of $\bar{Y}(\tau_{\rm max})$, where $\tau_{\rm max} = 15 \cdot 10^9 M$, are shown for a sequence of space-times with changing location of the ring: from upper left to lower right (as indicated), the ring's Schwarzschild radius is $r_{\rm ring} = 2$, 4, 6, 8, 10, 13, 14, 15, 16, 17, 18 and 20 in the units of $10^4 M$. The geodesics have specific energy $\mathcal{E} = 0.999985$ and angular momentum $\ell = 50M$. Colours going from blue to red across the visible spectrum correspond to average MEGNO ranging from 0 to 200, but the values above 4 are increased by 200 in order to better distinguish between regular and chaotic regions (thus the range is expanded to 400).

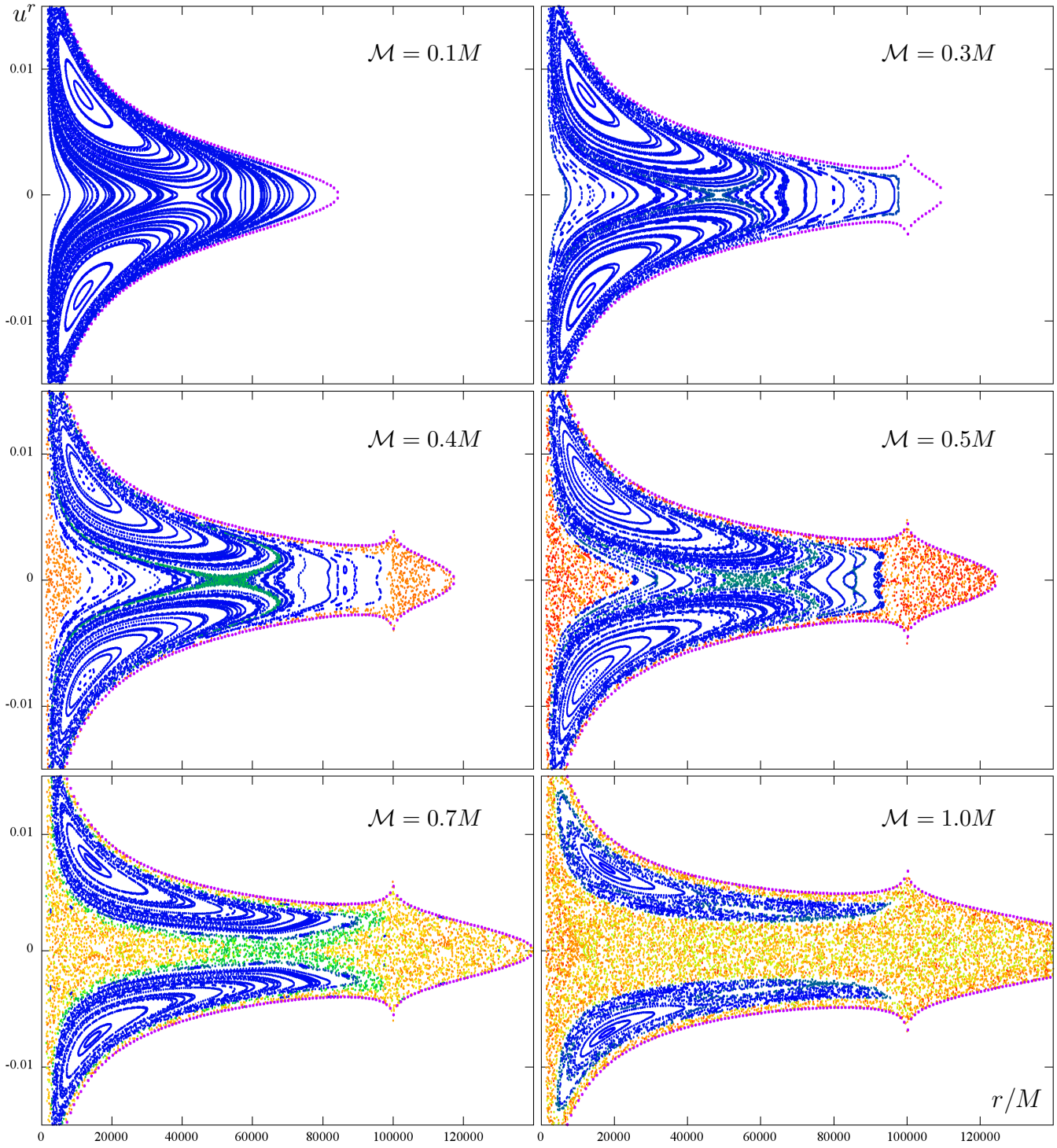


Figure 9. Poincaré sections for a sequence of black-hole & Bach-Weyl-ring space-times with changing mass of the ring: from upper left to lower right, $\mathcal{M}/M = 0.1$, 0.3, 0.4, 0.5, 0.7 and 1, while the ring's radius is kept at $r_{\rm ring} = 10^5 M$. The geodesics have specific energy $\mathcal{E} = 0.999987$ and angular momentum $\ell = 50M$. The sections are coloured by the value of $\bar{Y}(\tau_{\rm max})$, where $\tau_{\rm max} = 15 \cdot 10^9 M$. Colours going from blue to red across the visible spectrum correspond to average MEGNO ranging from 0 to 150, but the values above 4 are increased by 200 in order to better distinguish between regular and chaotic regions (thus the range is expanded to 350).

particles is quite pronounced and strongly depending on the ring location with respect to the accessible region. Generically, the ring affects mainly those orbits which pass in its vicinity. For given fixed constants of geodesic motion (energy and angular momentum at infinity), the system thus appears the most chaotic when the ring passes just through the centre of the accessible region. Then the primary island with period 1 shrinks and then disappears completely. For $r_{\rm ring} = 80\,000M$, for example, $\lambda_{\rm max}^{\rm MEGNO} \approx (5{\cdot}10^{-8} \div 5{\cdot}10^{-9})\, M^{-1}$ which confirms quite strong chaos on the time scale of only a few periods. When the ring position approaches

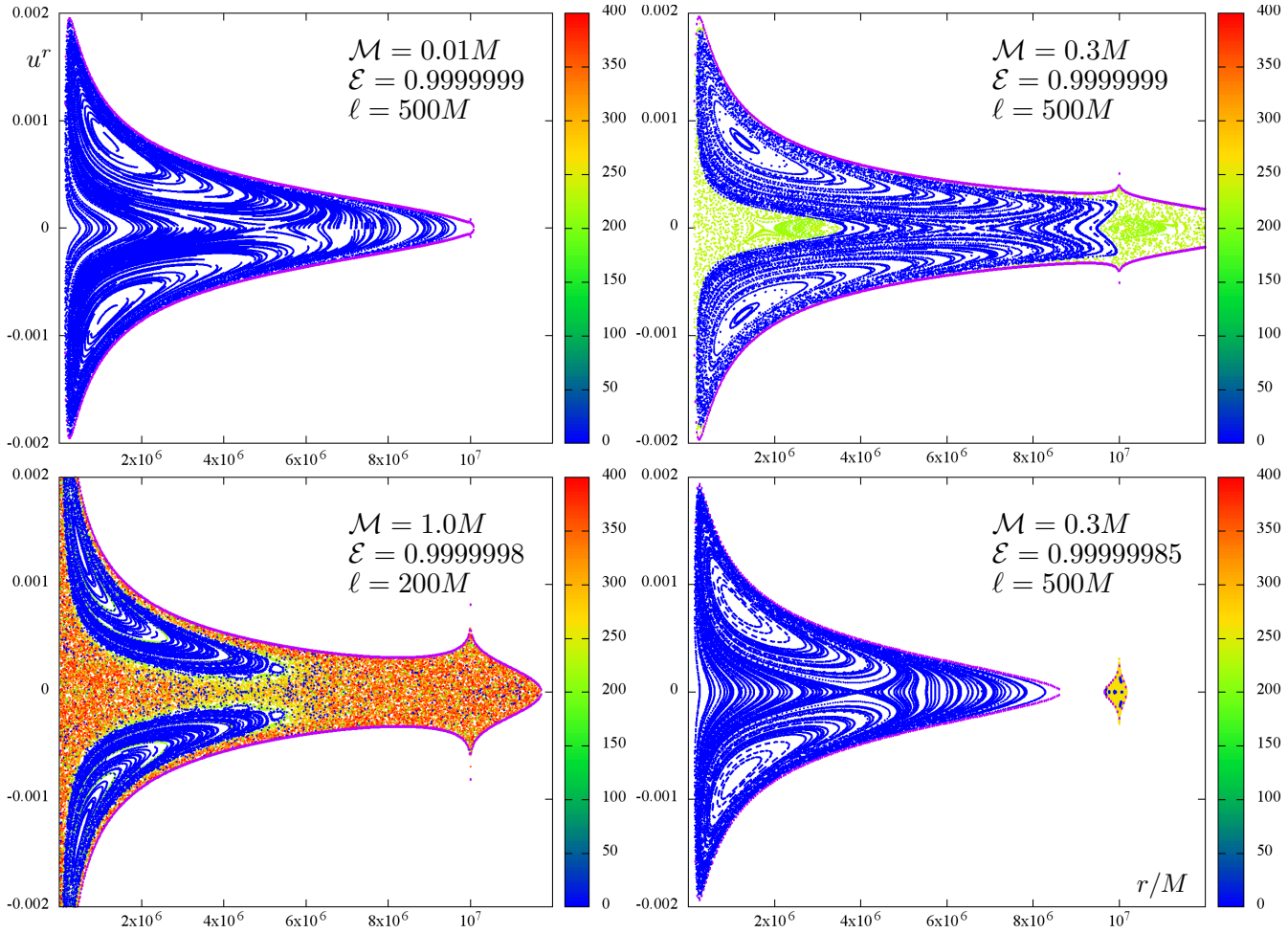


Figure 10. Poincaré sections for a sequence of black-hole & Bach-Weyl-ring space-times with parameters chosen according to the 2-parsec circumnuclear ring in our Galaxy: the ring is on radius $r_{\rm ring} = 10^7 M$ and has mass $\mathcal{M} = 0.01M$, $0.3M$ and $1.0M$ as indicated. The first two fields are probed with geodesics having specific energy $\mathcal{E} = 0.9999999$ and angular momentum $\ell = 500M$, while for the third (with the least realistic mass $\mathcal{M} = 1.0M$) the geodesic constants are chosen $\mathcal{E} = 0.9999998$, $\ell = 200M$. The last plot shows how the motion is considerably more regular when it is confined to the region not reaching up to the ring; the parameters there are $\mathcal{M} = 0.3M$, $\mathcal{E} = 0.99999985$ and $\ell = 500M$ in that case (they are the same as in the plot above, just the orbital energy is by 0.00000005 lower). The points are again coloured by the MEGNO value, with the values above 4 increased by 200.

the outer boundary of the lobe, a regular region inside grows in the form of period-two islands. Finally a secondary lobe enclosing just the ring detaches, leaving the primary lobe almost regular (except for a small territory near the separatrix between the two regions); the secondary lobe is heavily chaotic. Shifting the ring still farther, the primary lobe stabilises further, while the chaotic lobe tied to the ring gradually shrinks.

Figure 9 brings a similar sequence which demonstrates a response of the dynamics on the disc mass: the ring is kept on $r_{\rm ring} = 10^5 M$ and its mass $\mathcal{M}$ changes from $M/10$ to M. Again, if keeping the geodesics' global parameters (energy and angular momentum at infinity) constant, the dynamics is quite sensitive to the mass parameter. Namely, while varying the mass by a factor of 10, one proceeds from a completely regular to a rather chaotic system. The phase-space structures evolve in a similar way as in the preceding case.

In order to follow the actual Galactic parameters still more closely, we also analysed the case when the ring is placed at $r_{\rm ring} = 10^7 M$. Figure 10 brings three plots which mainly differ in the ring mass, $\mathcal{M} = 0.01M$, $0.3M$ and $1.0M$, respectively, and one plot where the particles/stars do not have enough energy to approach the ring. The phase spaces of the $0.3M$ and $1.0M$ cases do contain chaotic regions, but a closer look (plotting of individual trajectories) shows that only those orbits are irregular which get close to the ring. Actually, the chaotic region around the origin is connected, by these orbits and via the narrow peripheral layer, with the chaotic vicinity of the ring. This is why we also added a plot (the last one) where the motion is confined to a smaller region not reaching to the very ring. For such a motion everything is regular. More precisely, there do exist a chaotic region tied to the ring, but this is not connected with the main accessible region (and hence the latter remains regular).

4.1.2 Accretion disc

The hot accretion disc in the black-hole vicinity does not appear to have a significant gravitational effect on the dynamics of stars orbiting the centre in the distance range of the well known S-stars or somewhat farther. More specifically, we modeled the accretion structure by the inverted 1st Morgan-Morgan disc with the inner

edge on $r_{\rm disc} = 100M$ (most of its mass is concentrated close to the inner radius, say between $100M$ and $500M$ — see e.g. Semerák (2003)) and having mass $\mathcal{M} = 0.01M$. Geodesics with specific energy $\mathcal{E} = 0.99999$ and angular momentum $\ell = 50M$, launched in all possible directions and scanning the corresponding accessible phase-space region (extending roughly from $1270M$ to 10^5M), proved to be completely regular, so we do not even show the resulting Poincaré section nor the respective values of mLCE, FLI and MEGNO quantifiers. As the mass $0.01M$ is highly overshot for the actual inner accretion structure supposed to exist in the Galaxy nucleus, we can conclude that the latter does not destabilise the motion of S-type stars.

4.1.3 80-parsec ring

A similar conclusion also applies to the effect of the larger ring resting/orbiting between 60 and 100 parsecs on stars orbiting on smaller radii. We approximated the ring by the circular Bach-Weyl ring with radius $r_{\rm ring} = 4 \cdot 10^8 M$ and with mass $\mathcal{M} = 10M$, and scanned the phase space with geodesics having energy $\mathcal{E} = 0.99999993$ and angular momentum $\ell = 1000M$. All their accessible region, extending from $6 \cdot 10^5 M$ to some $2.1 \cdot 10^7 M$, proved to be regular. (We again do not attach the resulting figures and indicator values.)

5 CONCLUDING REMARKS

It is interesting and desirable to study chaotic dynamics by various methods, because different of them are sensitive to different features and they also differ in coordinate-dependence (Gelfert & Motter 2010). We have subjected to such a study the time-like geodesic dynamics in the static and axisymmetric field of a Schwarzschild black hole perturbed by the presence of a concentric thin disc or ring. After revealing basic tendencies of this system on Poincaré surfaces of section and on time-series of one of the phase-space variables and its power spectra (paper I), and after comparing the results with those provided by two effective recurrence methods while focusing on selected "sticky" orbits in more detail (paper II), we have checked in the present paper whether similar conclusions also follow by computing the basic coefficients describing the rate of orbital divergence, namely the maximal Lyapunov characteristic exponent, the fast Lyapunov indicator and the MEGNO indicator. Regarding our motivation, stemming from astrophysical systems dominated by black holes (in particular galactic nuclei with lower density of interstellar matter), we then set the system parameters at values corresponding to the structures observed/supposed in our Galactic nucleus — the central supermassive black hole, the inner hot accretion disc around it, and two circumnuclear molecular and dust rings on radii around 2pc and 80pc. Of these, only the smaller circumnuclear ring have been found to be able to partially destabilise the motion of stars (treated as test particles), but only if these can approach it closely.

We have naturally chosen our-Galaxy example for the above order/chaos test, but similar structures (discs, rings, tori) are also being observed in other galaxies, both quiet and active. Since the parameters corresponding to our Galactic nucleus are not *that* far from the range where chaos begins to occur, at least when speaking about the smaller circumnuclear ring, it is likely that in some galaxies a similar analysis of orbital dynamics would yield interesting results.

The last remark concerns the validity of exact models (exact solutions of Einstein's equations) we are using to describe the gravitational field. First, the influence of the central star cluster (of "other stars") should be incorporated. This would be rather easy if the cluster were only approximated by a kind of spheroidal potential. Second, it would certainly be more realistic to consider thick toroids instead of infinitely thin rings to model the circumnuclear galactic structures, at least if stars may get to their close vicinity. This is also a feasible task, though the metric is then much more demanding for practical computations (see e.g. Šácha & Semerák 2005 where we presented an example of a static black hole surrounded by a thick toroid). Third, a *physical* interaction of stars with circumnuclear environment should also be accounted for somehow, but it is clearly beyond our present scope to discuss it here. Finally, as relativists we would very much care for incorporating *rotation* in our black-hole–something system, both for theoretical reasons (non-linear interplay of rotational draggings from black hole and from the disc/ring) and certainly because rotation is ubiquitous in astrophysics. This turned out to be extremely difficult, unfortunately, at least within exact relativistic description; various procedures using "solution-generating techniques" have failed due to unphysical features present in the results (like in our own attempt described in Zellerin & Semerák 2000; Semerák 2002), while the outcomes of more sophisticated approaches are too complicated for inclusion as a part of some computational scheme, and even for a thorough study of their physical properties (cf. e.g. Klein & Richter (2005)).

5.1 Recent results in the field

Let us also mention several related results which have appeared in the literature recently. Wang & Wu (2011); Wu & Zhong (2011) used the FLI to study the dynamics of spinning compact binaries, analysing the effect of terms of different pN orders. Stachowiak & Szydlowski (2011) proposed a new algorithm for computing the Lyapunov exponents, not based on usual repetitive evolution and rescaling of the connecting vector. Seyrich & Lukes-Gerakopoulos (2012) developed a new integration scheme for non-integrable Hamiltonians, by combination the symmetric symplectic integrator with a new step-size controller. Lukes-Gerakopoulos (2012) demonstrated that the geodesic motion in the Zipoy-Voorhees space-time is non-integrable in general, while Kovář et al. (2013) came to the same conclusion for the motion of neutral as well as charged particles around the Bonnor's massive magnetic dipole. Contopoulos et al. (2011) and Bambi & Lukes-Gerakopoulos (2013) analysed simlilarly the geodesic dynamics in the Manko-Novikov space-time and discussed differences versus the Kerr case. Al Zahrani et al. (2013) investigated (generically chaotic) charged-particle motion around a weakly magnetised static non-rotating black hole, being mainly interested in the escape velocity of particles perturbed off the circular orbits. Very recently Brink et al. (2013) analysed, in the context of identification of the Sgr A$*$ black hole, orbital resonances in the Kerr field in order to estimate where geodesic chaos would occur in case of departure from the Kerr space-time. Finally, in connection with our plan to include rotation into the black-hole–disc/ring gravitational system and examine how dragging effects change the geodesic dynamics, we should mention that Wang & Wu (2012) considered a Kerr black hole mimicked by a pseudo-Newtonian potential and superposed it with a quadrupole halo, asking how the geodesic dynamics responds on spin of the centre and on quadrupole perturbation. They found, among others, that the black-hole rotation rather attenuates

the instability, consistently with previous experience acquired in this respect.

ACKNOWLEDGEMENTS

We used the code for geodesic motion in Weyl space-times originally written by M. Žáček and have been running it on the SNĚHURKA cluster of our faculty. The plots were produced with the help of the GNUPLOT utility and D. Krause's BMEPS program. We thank D. Heyrovský for interest and comments. Our work has been supported from the projects GACR-202/09/0772 and MSM0021620860 (O.S.); SVV-267301 and GAUK-428011 (P.S.).

REFERENCES

Al Zahrani A. M., Frolov V. P., Shoom A. A., 2013, Phys. Rev. D, 87, 084043
Angélil R., Saha P., 2011, ApJ Lett., 734, L19
Antonini F., Merritt D., 2013, ApJ Lett., 763, L10
Bambi C., Lukes-Gerakopoulos G., 2013, Phys. Rev. D, 87, 083006
Benettin G., Galgani L., Giorgilli A., Strelcyn J.-M., 1980, Meccanica, 15, 9
Brink J., Geyer M., Hinderer T., 2013, arXiv:1304.0330 [gr-qc] to appear???
Chang P., 2009, MNRAS, 393, 224
Cincotta P. M., Simó C., 2000, A&A Suppl. Ser., 147, 205
Contopoulos G., Lukes-Gerakopoulos G., Apostolatos T. A., 2011, Int. J. Bifurc. Chaos, 21, 2261
Ferrière K., 2012, A&A, 540, A50
Froeschlé C., Lega E., Gonczi R., 1997, Celest. Mech. Dyn. Astron., 67, 41
Fujii M., Iwasawa M., Funato Y., Makino J., 2010, ApJ Lett., 716, L80
Gelfert K., Motter A. E., 2010, Commun. Math. Phys., 300, 411
Genzel R., Eisenhauer F., Gillessen S., 2010, Rev. Mod. Phys., 82, 3121
Haas J., Šubr L., Vokrouhlický D., 2011, MNRAS, 416, 1023
Han W., 2008, Gen. Rel. Grav., 40, 1831
Han W., 2008, Phys. Rev. D, 77, 123007
Iorio L., 2011, Phys. Rev. D, 84, 124001
Kaplan D. T., Glass L., 1992, Phys. Rev. Lett., 68, 427
Klein C., Richter O., 2005, Ernst Equation and Riemann Surfaces: Analytical and Numerical Methods, Lect. Notes Phys. 685 (Springer, Berlin Heidelberg)
Kovář J., Kopáček O., Karas V., Kojima Y., 2013, Class. Quantum Grav., 30, 025010
Lukes-Gerakopoulos G., 2012, Phys. Rev. D, 86, 044013
Lukes-Gerakopoulos G., Apostolatos T. A., Contopoulos G., 2010, Phys. Rev. D, 81, 124005
Lukes-Gerakopoulos G., Voglis N., Efthymiopoulos C., 2008, Physica A, 387, 1907
Madigan A.-M., Levin Y., Hopman C., 2009, ApJ Lett., 697, L44
Maffione N. P., Darriba L. A., Cincotta P. M., Giordano C. M., 2011, Celest. Mech. Dyn. Astron., 111, 285
Maffione N. P., Darriba L. A., Cincotta P. M., Giordano C. M., 2013, MNRAS, 429, 2700
Merritt D., Alexander T., Mikkola S., Will C. M., 2010, Phys. Rev. D, 81, 062002
Merritt D., Gualandris A., Mikkola S., 2009, ApJ Lett., 693, L35
Mestre M. F., Cincotta P. M., Giordano C. M., 2011, MNRAS, 414, L100
Molinari S., et al., 2011, ApJ Lett., L33
Montero-Castaño M., Herrnstein R. M., Ho P. T. P., 2009, ApJ, 695, 1477
Morris M. R., Meyer L., Ghez A. M., 2012, Res. Astron. Astrophys., 12, 995
Oka T., Nagai M., Kamagai K., Tanaka K., 2011, ApJ, 732, 120
Perets H. B., Hopman C., Alexander T., 2007, ApJ, 656, 709 (erratum: 669, 661)
Psaltis D., 2012, ApJ, 759, 130
Requena-Torres M. A., et al., 2012, A&A, 542, L21
Šácha J., Semerák O., 2005, Czech. J. Phys., 55, 139
Sadeghian L., Will C. M., 2011, Class. Quantum Grav., 28, 225029
Semerák O., 2002, Class. Quantum Grav., 19, 3829
Semerák O., 2003, Class. Quantum Grav., 20, 1613
Semerák O., Suková P., 2010, MNRAS, 404, 545
Semerák O., Suková P., 2012, MNRAS, 425, 2455
Seyrich J., Lukes-Gerakopoulos G., 2012, Phys. Rev. D, 86, 124013
Stachowiak T., Szydlowski M., 2011, Physica D, 240, 1221
Suková P., 2011, Proc. Spanish Relat. Meeting ERE2010, J. Phys. Conf. Ser., 314, 012087
Suková P., Semerák O., 2012, Proc. Spanish Relat. Meeting ERE2011, AIP Conf. Proc., 1458, 523
Tancredi G., Sánchez A., Roig F., 2001, AJ, 121, 1171
Wang Y., Wu X., 2011, Class. Quantum Grav., 28, 025010
Wang Y., Wu X., 2012, Chin. Phys. B, 21, 050504
Wu X., Huang T.-Y., 2003, Phys. Lett. A, 313, 77
Wu X., Huang T.-Y., Zhang, H., 2006, Phys. Rev. D, 74, 083001
Wu X., Zhong S.-Y., 2011, Gen. Rel. Grav., 43, 2185
Zellerin T., Semerák O., 2000, Class. Quantum Grav., 17, 5103

D. Geodesic chaos around black holes with discs

Published in: Suková, P. and Semerák, O.: Geodesic chaos around black holes with discs, Proceedings of the Twelfth Marcel Grossmann Meeting on General Relativity 1, edited by T. Damour, R.T. Jantzen, R. Ruffini, World Scientific (2012), 1785

http://http://www.worldscientific.com/worldscibooks/10.1142/8316

GEODESIC CHAOS AROUND BLACK HOLES WITH DISCS

PETRA SUKOVÁ* and OLDŘICH SEMERÁK

Institute of Theoretical Physics, Faculty of Mathematics and Physics, Charles University in Prague, Czech Republic
**pet@matfyz.cz*

In the fields of isolated stationary black holes, the geodesic dynamics is regular. However, due to the presence of unstable periodic orbits, it easily becomes chaotic under various perturbations. Here we study the chaos induced by the presence of an additional source in the Schwarzschild space-time. Following the astrophysical motivation, we consider thin discs or rings lying symmetrically around the hole and describe the total fields in terms of exact static and axially symmetric solutions of Einstein's equations. The character of geodesic dynamics can be revealed by Poincaré sections, Fourier spectra of the "vertical"-position time series and evolution of the test-particle "latitudinal action".

Keywords: Black holes; exact solutions; geodesics; chaos.

"Almost all" is known about isolated and stationary black holes in asymptotically flat space-times. But "real", astrophysical black holes, assumed to play a central role in most galactic nuclei, some X-ray binaries and gamma-ray bursts, are neither isolated nor stationary, and probably not living in an asymptotically flat universe. Apropos, all the observational data about them come from their *interaction* with matter and fields around. In order to describe such processes in a consistent manner, the gravity of this matter/fields should be incorporated. Concerning the gravitational potential and its gradient ("field"), the "external" contribution is almost certainly negligible, but higher derivatives ("curvature") may be affected much more. Moreover, some features of motion of the external matter (mainly its stability) are highly sensitive to the details of the field, and thus to its own effect. Self-gravitating matter may thus settle down to a different accretion configuration than the test one.

One of indicators of the influence of additional matter should be geodesic dynamics. Namely, (uncharged) isolated stationary black holes in asymptotically flat universes are necessarily described by the Kerr metric whose geodesics are completely integrable (bound by 4 isolating integrals) [1], whereas the metric perturbed by the additional matter no longer yields "the 4th, Carter's" integral and the test motion thus may become chaotic. This is even true when the matter leaves the space-time stationary and axially symmetric, like in the case of an equatorial disc or ring. We point out such most symmetric configurations, since only they lead to a manageable form of Einstein equations. Fortunately, they are also astrophysically relevant as they may approximate a steady accretion flow onto a black hole.

This note summarises some of our results on the response of geodesic dynamics to the presence of a disc or ring, obtained within exact static and axisymmetric space-times. Restricting to the case without any EM field and with zero cosmological constant, the corresponding metric can be put into the Weyl form

$$\mathrm{d}s^2 = -\mathrm{e}^{2\nu}\mathrm{d}t^2 + \rho^2\mathrm{e}^{-2\nu}\mathrm{d}\phi^2 + \mathrm{e}^{2\lambda-2\nu}(\mathrm{d}\rho^2 + \mathrm{d}z^2),$$

where t, ϕ are tied to the symmetries and ρ, z cover isotropically the meridional plane; the functions ν and λ depend only on ρ, z. [Nevertheless, regarding the presence of the horizon, it is natural to put the results in Schwarzschild coordinates r, θ, given by $\rho = \sqrt{r(r-2M)}\,\sin\theta$, $z = (r-M)\cos\theta$.]

We specifically considered thin annular discs from the inverted counter-rotating Morgan–Morgan family and also the ("more smooth") discs whose density is power-law in Weyl radius. For such thin sources, the space-time is vacuum everywhere, with the energy-momentum tensor related to the jump of the normal derivatives of metric across the source. Einstein equations then reduce to the Laplace equation for ν and to the quadrature for λ (which in general has to be computed numerically at each point). The fields of multiple sources can thus be obtained by adding the respective component potentials ν and then integrating out λ from this "total" ν. Superpositions of both families of discs with Schwarzschild were shown to contain broad ranges of parameters where the results have reasonable physical properties.

Starting from a pure Schwarzschild field, we examined how the phase space of free test motion evolves with parameters (mass and radius) of the external source and with energy of the (massive) test particles. The results were presented in [2], together with a thorough introduction and a number of figures. We tracked the geodesic phase space of the hole+disc field by several hundreds of particles launched from a chain of relevant radii in the equatorial plane, with given energy $(-u_t)$ and angular momentum (u_ϕ) and with several different values of u^r. Using the Runge–Kutta (actually the Huťa) 6th-order method to integrate numerically the geodesic equations, the particles were followed for about $150000M$–$250000M$ of proper time (usually some 200–1000 orbital periods) and their passages across the equatorial plane $\theta = \pi/2$ (it is the plane of symmetry of our sources) were recorded in terms of r and u^r. The sequences of Poincaré sections obtained by changing the parameters revealed typical features of a "nearly integrable" ("weakly perturbed") Hamiltonian dynamical system that behaves according to the KAM theory. As expected, the degree of its stochasticity grows with compactness and relative mass of the external source and with energy of the particles. However, for large values of these parameters, the dynamics rather inclines back towards regular regime.

Besides the overall tendencies in dependence of phase portrait on parameters, it is also interesting to study particular trajectories, trying to distinguish different degrees and types of their irregularity. Various methods can be followed of which we sampled time series of phase variables and their spectra so far. For example, we plotted the time series of vertical position (z) and their Fourier image, and also the evolution of the particle's "latitudinal action" $J_\theta \equiv \frac{1}{\Delta\tau}\oint \sqrt{g_{\theta\theta}u^\theta u^\theta}\,\mathrm{d}\tau$, obtained by averaging the latitudinal four-velocity over an orbital period ($\Delta\tau$). (For these purposes, we followed the geodesics up to a coordinate time of about $10^6 M$ which typically corresponds to several thousand orbital periods.) Along regular orbits, the quantities undergo regular oscillations around certain constant mean value, so the respective Fourier spectra only contain several distinctive peaks and fall off to a flat profile at low frequencies. Chaotic orbits, on the other hand, correspond

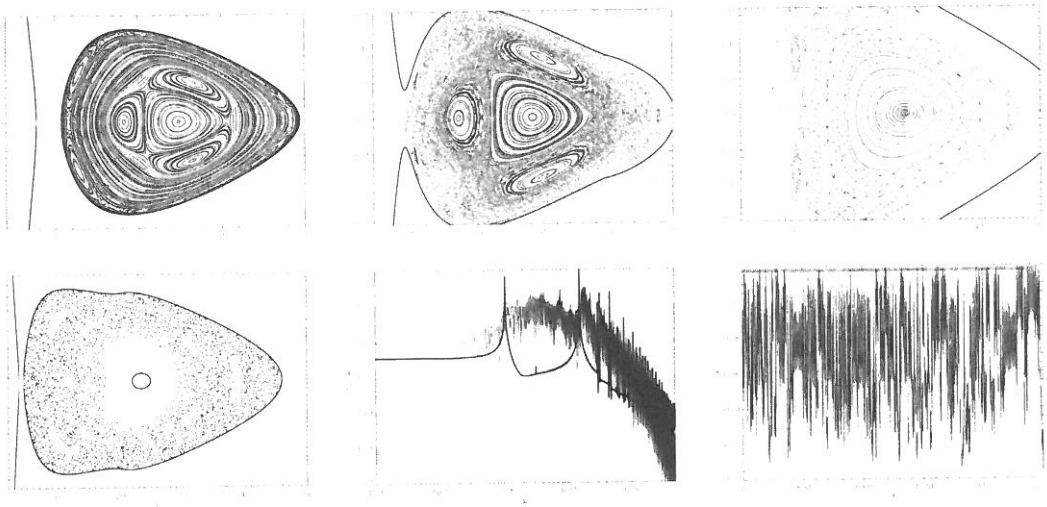


Fig. 1. Geodesic dynamics in the field of a Schwarzschild black hole (of mass M) surrounded by the inverted 1st Morgan-Morgan disc with mass $0.5M$ and inner radius $r{=}20M$. *Top row:* the dynamics changes with energy $-u_t$ from almost regular (left, $-u_t{=}0.952$) to quite chaotic (middle, $-u_t{=}0.956$) and back to more regular (right, $-u_t{=}0.975$); angular momentum is set to $u_\phi{=}3.75M$. *Bottom row:* distinguishing between regular and chaotic orbit (from left to right:) on Poincaré section (regular orbit makes a closed curve in the middle, chaotic one is filling the "sea"), on power spectrum of the z-evolution (the regular is flat at low frequencies, it is plotted thicker) and on evolution of the latitudinal action J_θ (for the regular orbit it oscillates about 0.117 evenly).

to complicated, inharmonic time series without any obvious mean value and with fuzzy Fourier spectra spanning over "all" frequencies including the low ones; the irregularity of their evolution can be detected at various scales.

Within the chaotic motions, one can further recognise those which adhere to regular orbits for most of the time and those which fill the "chaotic sea" rather uniformly. The "weakly chaotic" orbits typically produce "1/frequency" power spectrum at low frequencies (it ecreases with frequency), whereas "strongly chaotic" orbits produce "white-noise" there (fine jagged curve at rather low values). These two types of spectra, identified before on spin particles in a Schwarzschild field [3], appear in our system, too. We also confirmed that the "spectral type" is correlated with the behaviour of the latitudinal action J_θ, as suggested by [4].

Acknowledgements

We thank M. Žáček, L. Šubr and D. Heyrovský, the grants GAUK-86508 (P.S.), GAČR-202/09/0772 (O.S.) and the projects MSM0021610860 and LC06014.

References

1. B. Carter, *Phys. Rev.* **174**, 1559 (1968)
2. O. Semerák, P. Suková, *Mon. Not. R. Astron. Soc.* (2010), to appear
3. H. Koyama, K. Kiuchi, T. Konishi, *Phys. Rev. D* **76**, 064031 (2007)
4. M. Takahashi, H. Koyama, *Astrophys. J.* **693**, 472 (2009)

E. Chaotic geodesic motion around a black hole and disc

Published in: Suková, P.: Chaotic geodesic motion around a black hole and disc, Journal of Physics: Conference Series 314 (2011), 012087

http://dx.doi.org/10.1088/1742-6596/314/1/012087

IOPscience iopscience.iop.org

Home Search Collections Journals About Contact us My IOPscience

Chaotic geodesic motion around a black hole and disc

This article has been downloaded from IOPscience. Please scroll down to see the full text article.

2011 J. Phys.: Conf. Ser. 314 012087

(http://iopscience.iop.org/1742-6596/314/1/012087)

View the table of contents for this issue, or go to the journal homepage for more

Download details:
IP Address: 195.113.23.59
The article was downloaded on 12/07/2013 at 13:08

Please note that terms and conditions apply.

Journal of Physics: Conference Series **314** (2011) 012087 doi:10.1088/1742-6596/314/1/012087

Chaotic geodesic motion around a black hole and disc

Petra Suková

Institute of Theoretical Physics, Faculty of Mathematics and Physics, Charles University, V Holesovickach 2, 180 00 Praha 8, Czech Republic

E-mail: lvicekps@seznam.cz

Abstract. We study the chaotic features of time-like free motion around a Schwarzschild black hole, induced by the presence of a static, axially and reflectionally symmetric thin disc or ring. We describe the field by an exact (Weyl-type) solution of Einstein's equations and use Poincaré sections and time-series analysis in order to recognise overall tendencies in the evolution of phase portrait as well as changes that can be traced down to single orbits and their segments.

1. Introduction

Black holes assumed in galactic nuclei certainly dominate their surroundings gravitationally. However, even in non-active nuclei like that in our Galaxy, there is enough mass (in stars and gas) to influence *its own* (and each others') motion in a non-negligible way. One of tiny but robust effects is that the geodesic motion, which is integrable in the field of an *isolated* Schwarzschild or Kerr black hole, becomes chaotic when some additional matter is present. Actually, even if the additional matter does not break the space-time symmetries of the centre, the geodesic motion in the resulting field is no longer completely integrable, so it may become chaotic. This is important for the long-term evolution of the system and may have direct observational consequences, namely it can be recognised in electromagnetic and gravitational radiation emitted by the orbiting particles.

Here we consider exact static and axially symmetric space-times generated by a Schwarzschild black hole surrounded by a thin, reflectionally symmetric disc or ring, in order to show how the dynamics of free timelike motion changes from regular to chaotic (and possibly back) when parameters of the system are changed. The information revealed on Poincaré sections is supplemented by and compared with that provided by time series of phase variables. In particular, we illustrate whether and how the overall tendencies in the evolution of geodesic dynamics correspond to changes taking place on the level of individual orbits.

2. Weyl space-times

Static and axially symmetric vacuum regions of space-time can be described, in Weyl coordinates (t, ρ, z, ϕ), by the Weyl metric

$$\mathrm{d}s^2 = -\mathrm{e}^{2\nu(\rho,z)}\mathrm{d}t^2 + \rho^2\mathrm{e}^{-2\nu(\rho,z)}\mathrm{d}\phi^2 + \mathrm{e}^{2\lambda(\rho,z)-2\nu(\rho,z)}(\mathrm{d}\rho^2 + \mathrm{d}z^2)\,. \tag{1}$$

The Einstein equations yield the Laplace equation for ν, hence this function (representing gravitational potential) superposes linearly. The other unknown function λ can be obtained

Published under licence by IOP Publishing Ltd

by line integration of

$$\lambda = \int_{\text{axis}}^{\rho,z} \rho \left[(\nu_{,\rho}^2 - \nu_{,z}^2) \mathrm{d}\rho + 2\nu_{,\rho}\nu_{,z}\mathrm{d}z \right] . \tag{2}$$

We have specifically considered the superposition of an (initially) Schwarzschild black hole with three different types of additional source — the inverted Morgan-Morgan counter-rotating discs [1], the discs with power-law density profile [2] and the Bach-Weyl rings [3]. All these sources have finite mass and the disc families were shown to contain physically realistic cases within non-negligible parameter ranges. The only serious limitation of the Weyl solutions is the lack of rotation. Indeed, the systems we would like to simulate (astrophysical black holes with accretion discs or rings) are likely to rotate rapidly rather than being static. The *exact* inclusion of rotation would also be interesting because it has been indicated on approximate solutions in the literature that dragging effects can alter (probably attenuate rather than amplify) the chaotic features significantly. Unfortunately, the superposition of sources is much more difficult in a non-static (stationary) case and no solution of such a type exists that could be submitted to a similar extensive numerical study.

The Weyl space-times are stationary (even static) and axially symmetric, so the energy at infinity per unit mass $E = -g_{tt}u^t$ and the angular momentum at infinity per unit mass $L = g_{\phi\phi}u^\phi$ conserve along the geodesics. In addition, one has normalization of four-velocity, but there is no other isolating integral in general, so the (four-dimensional) motion is not completely integrable and may become chaotic.

The phenomenon of chaos has been detected and studied in many systems, notably in physics, mathematics, biology and economics. It is of special interest in systems of general relativity where the configuration space is itself described by a non-linear theory. Immediately a question thus arises whether and how general relativity contributes to chaos and whether this contribution stems mainly from special relativistic dynamics or rather from dragging effects and spatial curvature. These questions have also practical aspects, because the general relativistic description of a particular system of sources is much more difficult than in Newton's theory and it is often necessary to resort to approximations like pseudo-Newtonian potentials or weak-field limit. It has already been shown in the literature that geodesic dynamics clearly distinguishes between these approximations and full general relativistic system, which indicates that the approximations typically fail to simulate the long-term behaviour correctly.

3. Results

There are many methods how to diagnose and classify chaos. However, in general relativity the usage of some of them is not easy or does not seem to have good sense, because they are usually applied in a particular coordinate system while in relativity coordinates (time, in particular) do not have an invariant meaning. Such queries mainly occur when trying to quantify "sensitive dependence on initial conditions", namely to compare how fast nearby orbits diverge in various directions. In particular, this requires to compare certain tangent vectors (namely velocities of the neighbouring particles) at different points of the manifold which is not a unique concept as one can use different ways of how to transport the quantities to the same point. It is only to be clarified how to compute, in general relativity, correctly and efficiently the various exponents proposed as a measure of the orbital divergence. It has been proved [4], fortunately, that the sign of the mostly used *Lyapunov* exponents is independent of coordinates, although their value is otherwise not invariant. Recently several new suggestions of how to practically compute the Lyapunov exponents have appeared [5]. We plan to try them in the future.

On the other hand, some of the methods can be adopted to general relativity quite straightforwardly. In particular, the Poincaré surfaces of section are very efficient in revealing the properties of phase space for systems where one is able to find the whole trajectories. Quite naturally, we began the study of geodesics in the fields of black holes surrounded by

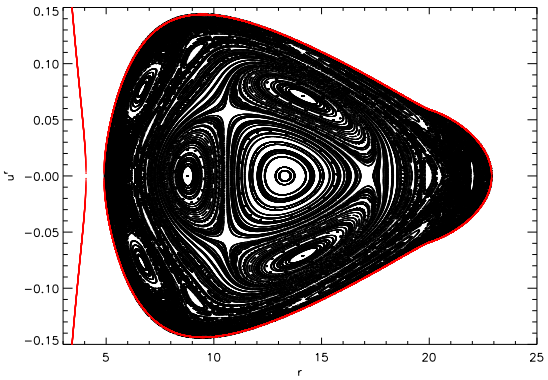


Figure 1. Poincare's surface of section (equatorial plane) for geodetic motion ($E = 0.954$, $L = 3.75M$) around BH with first iMM disc ($r = 20M$, $\mathcal{M} = 0.5M$).

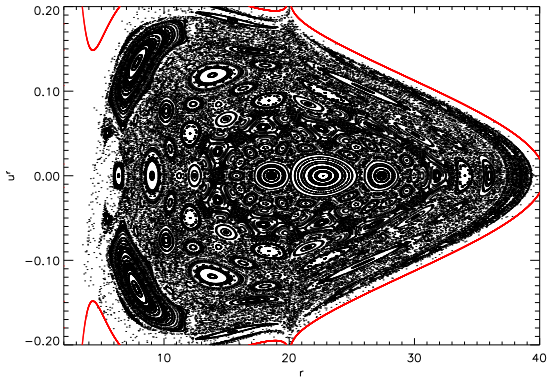


Figure 2. Poincare's surface of section (equatorial plane) for geodetic motion ($E = 0.977$, $L = 3.75M$) around BH with Bach-Weyl ring ($r = 20M$, $\mathcal{M} = 0.08M$).

discs or rings by plotting the Poincaré sections [6]; two examples for different external sources are given in figure 1 and figure 2. However, it is problematic to compare the Poincaré-section method directly with astrophysical observational data, because the latter mostly do not contain information about all three directions. The data are usually represented by time series of dynamical quantities (e.g. projection of position onto the celestial sphere). In order to decipher them, one tries to recognise their components showing different degrees of regularity, in particular, to decompose the "signal" that is probable to originate from a deterministic system from what appears to be just noise. There exist various routines that can provide the degree of regularity/stochasticity of the time series. We specifically tested the technique proposed in [7] on the data computed for our hole-disc system.

The method lies in analysis of the trajectory determined by a given time series $a(t)$ in a 3D space whose axes are $a(t)$, $a(t-\tau)$ and $a(t-2\tau)$, where $a(t-\tau)$ and $a(t-2\tau)$ are "clones" of the original series once and twice delayed by a given time shift τ. The space thus obtained is divided into m x m x m boxes and the passages of the trajectory through the boxes is recorded in terms of a normalised directional vector pointing from the point where the trajectory enters a particular box to the point where it leaves the box. The vectors provided by passages through each particular (j-th) box are then summed into a "total j-th box vector" V_j and this vector's norm is computed and divided by the number of passages through the j-th box n_j (it is assumed that the time series is long enough to yield many transits through the box). In autonomous deterministic systems the dynamics is given by equations of motion which depend on position in phase space, so when the boxes are small enough, the tangent vectors recorded for a given box point in similar directions, so their normalised sum $|V_j/n_j|$ is close to one. On the contrary, for random time series, the norm of this average tangent vector decreases with n_j as the average displacement per step for a random walk in a 3D space, i.e., for (large) n_j, as

$$\bar{R}^3_{n_j} = \frac{4}{(6\pi)^{1/2}} n_j^{-\frac{1}{2}}. \tag{3}$$

For a suitably chosen τ, a deterministic signal yields $|V_j/n_j|$ close to one for arbitrary n_j, whereas for a random signal the value falls off as $n_j^{-1/2}$.

Finally, one can compute a weighted average of $|V_j/n_j|$ over all traversed boxes for a given τ,

$$\bar{\Lambda}(\tau) = \Big\langle \frac{(V_j/n_j)^2 - (R^3_{n_j})^2}{1 - (R^3_{n_j})^2} \Big\rangle. \tag{4}$$

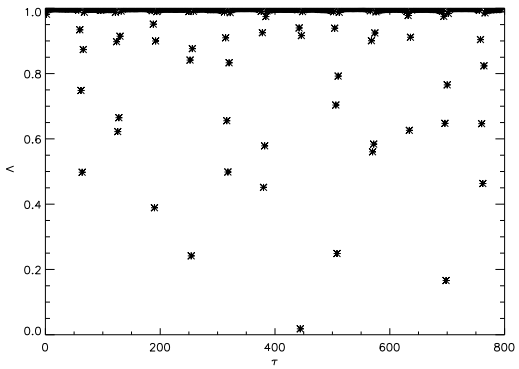


Figure 3. Weighted average of directional vectors.

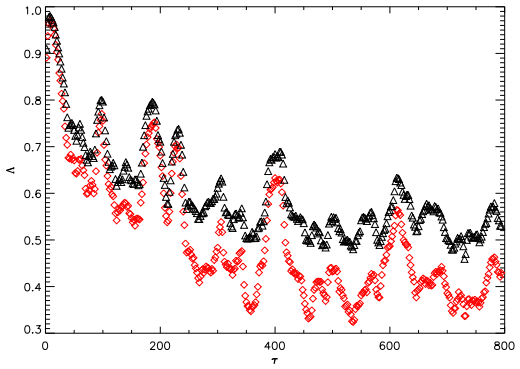


Figure 4. Weighted average of directional vectors ($m = 20$ – red, $m = 32$ – black).

The behaviour of this quantity in dependence on τ is again very different for regular and random trajectories, and we were curious to check what it does for chaotic ones. For regular trajectories the value proved to remain close to one for increasing τ except for certain specific values related to the period of motion. For chaotic trajectories the value turns out to decrease with τ, with some peaks occurring on the curve. The course of $\bar{\Lambda}$ for regular trajectory is plotted in figure 3 while for the chaotic one it is given in figure 4. Both these trajectories have the same global parameters (first inverted Morgan-Morgan disc with $r = 20M$, $\mathcal{M} = 0.5M$ and constants of the motion $E = 0.953$, $L = 3.75M$) but different initial conditions.

The value of $\bar{\Lambda}(t)$ depends on the sampling frequency of the time series (on how dense the data points are) and also on the box size, but the latter dependence (on m) is weak within the range where the elementary boxes are small enough to capture the folds of the trajectory and at the same time large enough to catch at least several points of the trajectory. This is shown in figure 4, where the red data points are computed for $m = 20$ and the black ones are computed for $m = 32$ and their behaviour is very similar.

4. Conclusions

We have shown on Poincaré surfaces of section that in the system of a static black hole surrounded by a thin static and axially symmetric dics or ring the geodesic flow could be chaotic. As usual in the weakly perturbed systems, the chaotic layers spread over the phase space from the unstable periodic points and separatrices between regular islands. We checked the degree of individual-orbit chaoticity by analysing the corresponding time series — we computed their power spectra and also applied the method of computing the weighted average of directional transit vectors suggested by [7].

Acknowledgments

The work was supported by the grants GAUK-86508, GACR-205/09/H033 and SVV 261301.

References

[1] Semerák O and Záček M 2000 *Class. Quantum Gravit.* B **17** 1613
[2] Semerák O 2004 *Class. Quantum Grav.* **21** 2203
[3] Bach R and Weyl H 1922 *Math. Zeit.* **13** 134
[4] Motter A E 2003 *Phys. Rev. Lett.* **91** 231101-1
[5] Stachowiak T and Szydlowski M 2010 *Preprint* arXiv:1008.3368v1
[6] Semerák O and Suková P 2010 *Mon. Not. R. Astron. Soc.* **404** 545
[7] Kaplan D T and Glass L 1992 *Phys. Rev. Lett.* **68** 427

F. Recurrence of geodesics in a black-hole–disc field

Published in: Suková, P. and Semerák, O.: Recurrence of geodesics in a black-hole–disc field, AIP Conference Proceedings 1458 (2012), 523

http://dx.doi.org/10.1063/1.4734475

AIP | Conference Proceedings

Recurrence of geodesics in a black-hole-disc field

Petra Suková and Oldřich Semerák

Citation: AIP Conf. Proc. **1458**, 523 (2012); doi: 10.1063/1.4734475
View online: http://dx.doi.org/10.1063/1.4734475
View Table of Contents: http://proceedings.aip.org/dbt/dbt.jsp?KEY=APCPCS&Volume=1458&Issue=1
Published by the AIP Publishing LLC.

Additional information on AIP Conf. Proc.

Journal Homepage: http://proceedings.aip.org/
Journal Information: http://proceedings.aip.org/about/about_the_proceedings
Top downloads: http://proceedings.aip.org/dbt/most_downloaded.jsp?KEY=APCPCS
Information for Authors: http://proceedings.aip.org/authors/information_for_authors

ADVERTISEMENT



Downloaded 12 Jul 2013 to 195.113.23.59. This article is copyrighted as indicated in the abstract. Reuse of AIP content is subject to the terms at: http://proceedings.aip.org/about/rights_permissions

Recurrence of geodesics in a black-hole–disc field

Petra Suková and Oldřich Semerák

Institute of Theoretical Physics, Faculty of Mathematics and Physics, Charles University in Prague

Abstract. Processes around astrophysical black holes are usually modeled with test (non-gravitating) matter and fields. However, the very fact that the holes are "visible" implies that *some* matter has to be present there. Even if very thin, it can influence the metric, mainly in higher derivatives, which should in turn affect its own behaviour, as well as motion of further (test) satellites. In particular, the geodesic dynamics, integrable in the fields of *isolated* stationary black holes, should become chaotic. Here we consider exact static, axially and reflection- symmetric space-times of a Schwarzschild black hole surrounded by a thin disc or ring, and examine how the presence of the additional source affects the dynamics of free test particles using recurence analysis.

Keywords: black holes, accretion discs, geodesic dynamics, chaos
PACS: 04.70.Bw, 04.25.-g, 05.45.Pq, 95.10.Fh

RECURRENCE ANALYSIS

Typical behaviour of a dynamical system is encoded in the pattern of its recurrences in the phase space. The pattern is different for regular, chaotic and random trajectories, so it can be used for classification of the systems and of their possible evolutions. Useful tool for visualisation of the recurrences are *recurrence plots* (RPs), developed in [1]. Recently this method was also used succesfully in general relativity, see e.g. [2] where recurrence analysis of the charged-particle motion around a magnetised rotating black hole was carried out. Here we draw RPs in order to study the geodesic dynamics in an exact static and axisymmetric space-time of a black hole surrounded by a massive thin disc, more specifically by the inverted first disc of the Morgan-Morgan family. (See [3] for details, including astrophysical motivation and analysis of the system by other methods.)

The drawing of RP requires knowledge of the test-particle phase trajectory with constant step of proper time (details are given in [4]). We find the orbits by solving numerically the corresponding geodesic equation, thus both position and velocity time series are known (in the case of just one known variable, the phase space can still be reconstructed from a sequence of its time-delayed series). The basic object of the recurrence analysis is the recurrence matrix defined by

$$\mathbf{R}_{i,j}(\varepsilon) = \Theta(\varepsilon - \| \vec{x}_i - \vec{x}_j \|), \qquad i,j = 1,...,N, \tag{1}$$

where $\vec{x}_i = \vec{x}(t_i)$ are (N) points of the phase trajectory, ε denotes a chosen threshold and Θ is the Heaviside step function. The matrix thus contains only 1's and 0's and can be easily visualised by plotting a black dot at the coordinates i, j whenever $\mathbf{R}_{i,j}(\varepsilon) = 1$. For regular orbits, the points are arranged in long diagonal lines, whereas for random behaviours they are scattered without order. Chaotic orbits yield more "artistic" plots:

Towards New Paradigms: Proceeding of the Spanish Relativity Meeting 2011
AIP Conf. Proc. 1458, 523-526 (2012); doi: 10.1063/1.4734475
© 2012 American Institute of Physics 978-0-7354-1060-2/$30.00

Downloaded 12 Jul 2013 to 195.113.23.59. This article is copyrighted as indicated in the abstract. Reuse of AIP content is subject to the terms at: http://proceedings.aip.org/about/rights_permissions

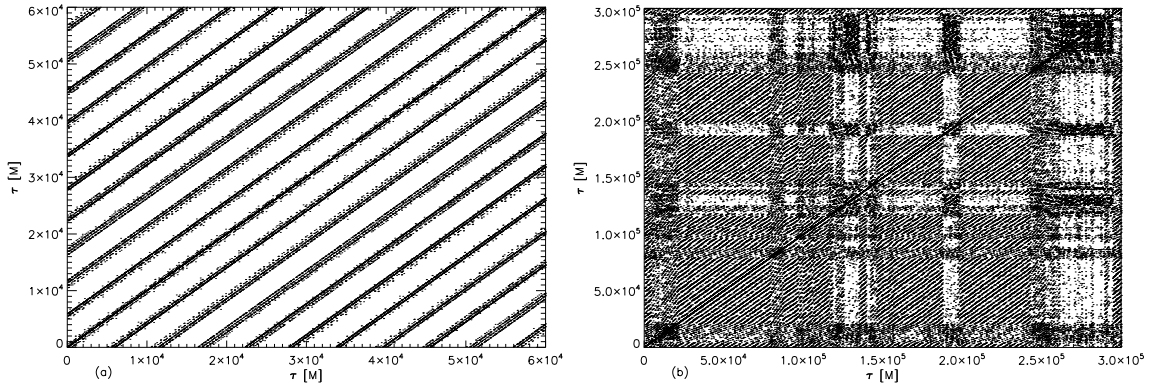


FIGURE 1. Recurrence plots for (a) regular and (b) chaotic trajectory. Note the scale change.

they contain blocks of almost-diagonal patterns as well as irregular ones, apparently placed one over another within horizontal and vertical structures. The almost-regular blocks correspond to time intervals when the trajectory sticks to some unstable periodic orbit. The more unstable this orbit is, the earlier the trajectory deviates from it and the smaller is the block in the RP. See Fig. 1 for an example of regular and chaotic RP.

Judging the degree of diagonal patterns within the RP by pure observation is of course subjective, so several quantifiers of the recurrence-matrix properties have been proposed. The simplest of them is the ratio of the recurrence points (black ones) within all points of the matrix, $RR(\varepsilon) = \frac{1}{N^2}\sum_{i,j=1}^{N} R_{i,j}(\varepsilon)$, called recurrence rate. Another, most important quantifier is the histogram of diagonal lines of a certain prescribed length l,

$$P(\varepsilon,l) = \sum_{i,j=1}^{N} (1-R_{i-1,j-1}(\varepsilon))(1-R_{i+l,j+l}(\varepsilon)) \prod_{k=0}^{l-1} R_{i+k,j+k}(\varepsilon). \tag{2}$$

Several further quantities can in turn be computed from this histogram. The one called DET is given by the ratio between all recurrence points and those of them which form a diagonal line longer than $l_{\min}$, thus $DET = \sum_{l=l_{min}}^{N} lP(l) / \sum_{l=1}^{N} lP(l)$. The length of the longest diagonal $L_{\max} = \max(\{l_i\}_{i=1}^{N})$ and its inverse $DIV = 1/L_{\max}$ are also of interest, since they are related to the rate of divergence of nearby orbits and serve as a rough estimate of the largest Lyapunov exponent. It is even possible to make this estimate more precise, because the cumulative histogram of diagonals turned out to yield the second-order Rényi's entropy K_2 which stands for a lower estimate of the sum of positive Lyapunov exponents (see [4]). Similarly, the histogram of vertical lines can be introduced,

$$P(\varepsilon,v) = \sum_{i,j=1}^{N} (1-R_{i,j}(\varepsilon))(1-R_{i,j+v}(\varepsilon)) \prod_{k=0}^{v-1} R_{i,j+k}(\varepsilon), \tag{3}$$

and also the respective measure of vertical structures $LAM = \sum_{v=v_{\min}}^{N} vP(v) / \sum_{v=1}^{N} vP(v)$. Finally, from the probabilities that some chosen diagonal/vertical line has length l,

Downloaded 12 Jul 2013 to 195.113.23.59. This article is copyrighted as indicated in the abstract. Reuse of AIP content is subject to the terms at: http://proceedings.aip.org/about/rights_permissions

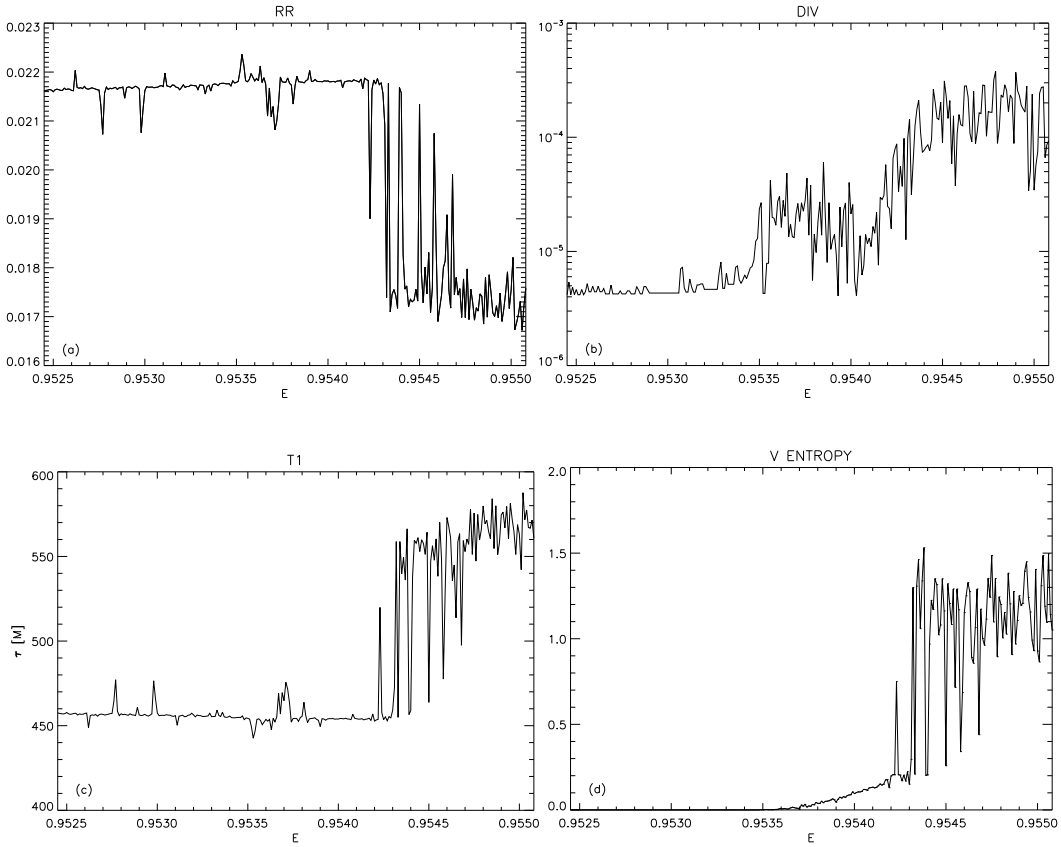


FIGURE 2. RQA measures as functions of energy: (a) the recurrence rate (RR), (b) longest-diagonal-line inverse (DIV), (c) first-type recurrence time (T1) and (d) entropy connected with the probability to find a vertical of length v (V ENTROPY).

$p(l) = P(l)/N_l$ and $p(v) = P(v)/N_v$, where N_l and N_v are the total numbers of diagonal/vertical lines, one can compute the Shannon entropies

$$ENTROPY = -\sum_{l=l_{min}}^{N} p(l)\ln p(l); \qquad VENTROPY = -\sum_{v=v_{min}}^{N} p(v)\ln p(v). \quad (4)$$

Another relevant indicator is the size of the "white gaps" between vertical lines. Namely, it is related to the recurrence times. For example, let us choose a point $\vec{x}_i$ on some trajectory and collect all the points which fall in its ε-neighbourhood, $\{\vec{x}_{j_1}, \vec{x}_{j_2}, \ldots\}$. Compute the recurrence times given by differences between serial numbers of the consecutive recurrence points $\vec{x}_{j_{k+1}}, \vec{x}_{j_k}$ multiplied by the respective proper-time steps, $\{T_k = (j_{k+1} - j_k)\Delta\tau\}$. The mean of T_k is called the recurrence time of the first type, $T1$.

Downloaded 12 Jul 2013 to 195.113.23.59. This article is copyrighted as indicated in the abstract. Reuse of AIP content is subject to the terms at: http://proceedings.aip.org/about/rights_permissions

RESULTS

We studied the behaviour of geodesics in our black-hole–disc system in dependence on their energy. In the above plots, the disc has mass $M/2$ and inner edge on $r = 20\,[M]$. The test particle is launched from $r = 6.25\,[M]$ with specific angular momentum $L = u_\phi = 3.75\,[M]$ and $u^\rho = 0$ and with specific energy $E = -u_t$ increasing from 0.951 by 0.00001 up to 0.95508 (M is the black-hole mass and u^μ is the particle's four-velocity). In each run we compute the trajectory numerically up to the time $t_{\max} = 250000\,[M]$, thus the minimal achievable DIV is 4×10^{-6}. For the recurrence analysis we use three spatial coordinates and velocities recorded with the proper-time step $\Delta\tau = 10\,[M]$. In order to be able to use the same threshold ε for different trajectories and to compare those of different extent in different directions, we normalize the series of each coordinate separately to zero mean and unit deviation. To exclude the sojourn points (the recurrence points resulting from tangential motion with ε large enough to capture more successive points of the trajectory) from the statistics, we set $l_{\min} = v_{\min} = 90\,[M]$.

For each trajectory we compute the RP and the corresponding RQA measures – see Fig. 2. The trajectory is regular initially. When the energy reaches about 0.95345, the motion becomes chaotic in a thin phase-space layer around the original regular orbit. The chaotic layer widens with increasing energy and around $E = 0.95423$ it spreads over a much larger region near the boundary of the accessible phase region. However, the process is not monotonic: for some higher energies the layer gets quite thin again, with its shape changing suddenly between these two possibilities. The computed RQA measures indicate the above behaviour in a slightly different way. Mainly, all of them clearly respond to the occurrence of a large chaotic region, but only DIV seems to be also sensitive to the thin-layer chaos. Namely, in a thin layer $DIV \simeq 3 \times 10^{-5}$ which is about ten times more than for regular motion while ten times less than in a large chaotic region. (The value 3×10^{-4} in a large chaotic region corresponds to a divergence time about several thousands $[M]$, which represents some ten cycles about the black hole.)

In the chaotic regime, the recurrence rate is lower and the vertical measures $T1$ and $VENTROPY$ grow significantly, which means that the system takes more time to get back to the chosen ε-neighbourhood.

For getting plausible results the parameters for RP (ε, $\Delta\tau$, $l_{\min}$, $v_{\min}$) have to be carefully set. More details of our results considering also this issue will be given elsewhere.

ACKNOWLEDGMENTS

The work was supported by the grants GAUK-428011, GACR-205/09/H033, SVV 263301, GACR-202/09/0772 and MSM0021610860.

REFERENCES

1. J.-P. Eckmann, S. Oliffson Kamphorst, and D. Ruelle, *EPL (Europhysics Letters)* **4**, 973 (1987).
2. O. Kopáček, V. Karas, J. Kovář, and Z. Stuchlík, *The Astrophysical Journal* **722**, 1240 (2010).
3. O. Semerák, and P. Suková, *Monthly Notices of the Royal Astronomical Society* **404**, 545 (2010).
4. N. Marwan, M. Carmen Romano, M. Thiel, and J. Kurths, *Physical Reports* **438**, 237 (2007).

Downloaded 12 Jul 2013 to 195.113.23.59. This article is copyrighted as indicated in the abstract. Reuse of AIP content is subject to the terms at: http://proceedings.aip.org/about/rights_permissions

G. Geodesic chaos in perturbed black-hole fields

To be published in the proceeding of the conference Relativity and Gravitation: 100 years after Einstein in Prague.

Geodesic chaos in perturbed black-hole fields

Petra Suková, Oldřich Semerák

Institute of Theoretical Physics, Faculty of Mathematics and Physics, Charles University in Prague, Czech Republic

E-mail: lvicekps@seznam.cz, oldrich.semerak@mff.cuni.cz

Abstract. Dynamics of time-like geodesics in the static and axially symmetric field of a black hole surrounded by a thin disc is studied by two recurrence methods, the recurrence plots (RPs) and the average of directional vectors (ADVs). Their results supplement the information obtained before from Poincaré surfaces of section and from phase-variable evolutions and the corresponding power spectra. The occurrence of chaos due to the presence of ambient matter may be important for evolution and appearance of astrophysical black-hole systems.

Inspired by models of accreting astrophysical black holes, we consider a simple, static and axisymmetric exact configuration of a black hole surrounded by a concentric thin disc or ring. Due to the presence of the additional source, the geodesic dynamics – originally completely integrable in the Schwarzschild field – generally becomes chaotic. Having illustrated this on Poincaré sections and on phase-variable time series and their power spectra [4], we have now turned to two recurrence methods which are based on statistics (i) over recurrences of the orbits to cells of the phase space (the recurrence plots [1, 3], RPs) and (ii) over direction in which the orbits recurrently pass through the cells (the average of directional vectors [2], ADVs). Here just a short glimpse on the results is given obtained for time-like geodesics in the field of a black hole (of mass M) surrounded by the inverted 1st Morgan-Morgan disc with mass $\mathcal{M} = 0.5M$ and inner Schwarzschild radius $r = 15M$; see [5, 6, 7] for details our earlier results.

RPs consist in recording the recurrence matrix whose components (zeros or units) indicate (non-)recurrences of a given orbit to selected cells. This symmetric matrix itself reveals the nature of dynamics, but

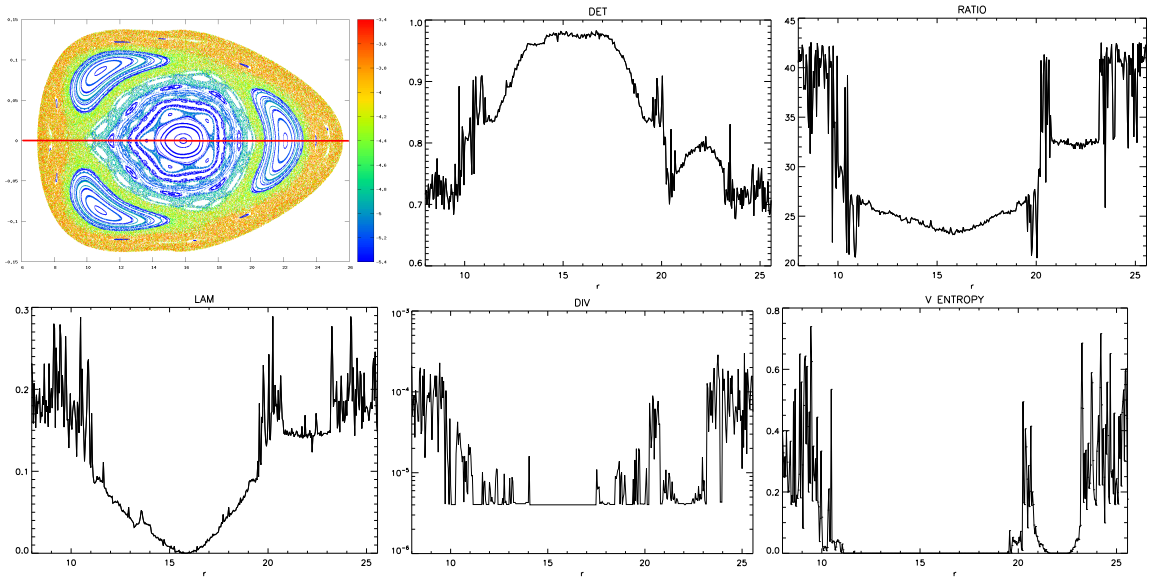


Figure 1. Poincaré section (top left) with each orbit coloured according to the value of DIV in log scale. The red line indicates starting points. The next plots show several recurrence quantifiers in dependence on initial radius of the orbits.

here we rather show several examples of useful "quantifiers" which can be computed from the recurrence data. The simplest of them is the recurrence rate RR, given by ratio of the recurrence points within all points of the matrix. Another one called DET is given by ratio of the points which form a diagonal line longer than a certain minimum $l_{\min}$ within all the recurrence points. The inverse of the longest diagonal $DIV = 1/L_{\max}$ has been shown to provide a rough estimate of the largest Lyapunov exponent. A lower estimate of the sum of positive Lyapunov exponents is given by the correlation (or Rényi's) entropy $\hat{K}_2$, determined by a slope of the cumulative histogram plotted (in log scale) against the diagonal length l (for large l). Statistics over vertical (or horizontal) lines of the matrix brings similar quantifiers, for example, LAM is a counter-part of DET and $V\,ENROPY$ is obtained from probability that a chosen vertical line has a prescribed length l. Note that the recurrence matrix and all the quantifiers of course depend on the chosen size of spatial cells and on time step with which the orbits are processed.

We launch geodesic particles with zero radial velocity from different radii between $r = 8M$ and $r = 25M$ with specific energy $E = 0.955$ and specific angular momentum $L = 4M$. Poincaré section of several hundreds of such orbits coloured according to the value of DIV is depicted in Fig. 1 together with the courses of several RP quantifiers.

The other method, ADVs, is based on monitoring the evolution of tangent to the trajectory in chosen boxes of the phase space

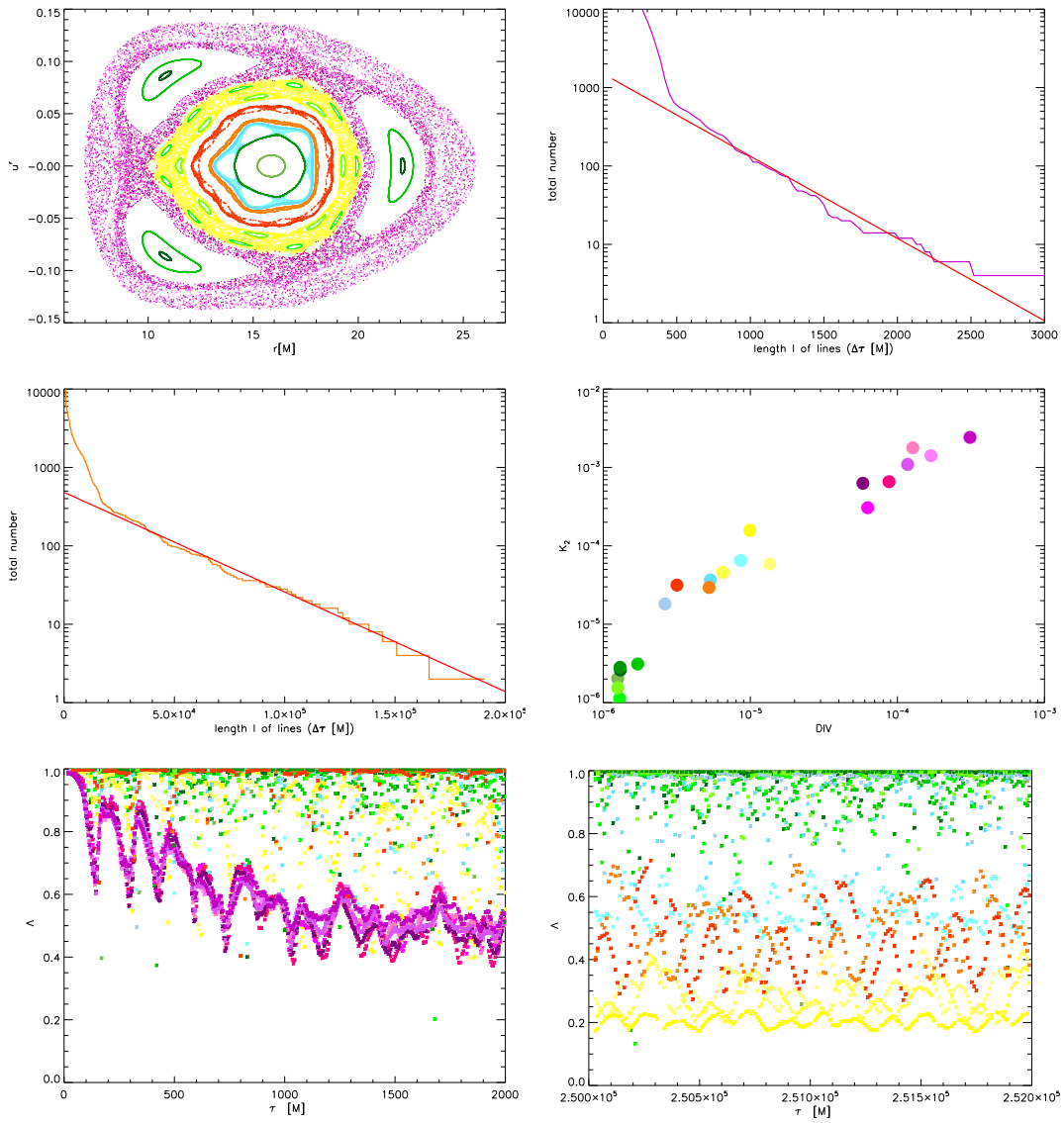


Figure 2. Poincaré surface of section with each orbit plotted in different colour (top left); cumulative histograms of diagonal lines in RP for strongly chaotic (top middle, $K_2 = 2.42 \cdot 10^{-3} M^{-1}$) and weakly chaotic (top right, $K_2 = 2.94 \cdot 10^{-5} M^{-1}$) orbit; comparison of K_2 against DIV (bottom left) and the ADV parameter $\bar{\Lambda}$ for small (bottom middle) and big (bottom right) time lags.

"reconstructed", for a given data series $x(\tau)$, by taking the delayed replicas $x(\tau)$, $x(\tau - \Delta\tau)$, $x(\tau - 2\Delta\tau)$, ..., $x(\tau - d\Delta\tau)$ as its axes, where $\Delta\tau$ is a chosen time shift. The vectors obtained for a large number of transits through the j-th box are summed, the resulting vector is normalised and the norm is averaged over all boxes which were crossed n-times. Finally, the dependence of this average on n and also of the averaged quadratic difference from random-walk case on time lag, $\bar{\Lambda}(\Delta\tau)$, are analysed. For random data the average decreases more quickly than for a deterministic

signal; for a regular orbit, it remains 1 theoretically. The ADV method was originally proposed to distinguish between deterministic and random data, but we have found it is also sensitive to different degrees of chaoticity.

The comparison of the above methods is illustrated in Fig. 2. Several trajectories have been followed there for a very long time: the most chaotic trajectories up to $\tau_{\max} = 250000M$ while other to $\tau_{\max} = 800000M$ (one orbital period represents some $300M$ of proper time). The particle position is recorded with the step $\Delta\tau = 0.25M$.[1] Each trajectory is plotted in different colour; regular orbits are green, weakly chaotic orbits range from light blue to orange and yellow and the most chaotic ones are purple. It is seen that the character of orbits is revealed by Poincaré diagram as well as by values of DIV or K_2, and also from the behaviour of $\bar{\Lambda}(\Delta\tau)$. We give particular attention to comparison of the quantities DIV or K_2 (bottom left). Namely, although K_2 is considered a more precise and reliable estimate of orbital divergence, its correct determination is tricky and less suitable for automatic procedure (see [5] for details). The DIV quantifier is obtained much more easily and reliably. The plot shows that the log values of DIV and K_2 are roughly proportional and that different types of motion (regular, weakly chaotic and strongly chaotic) yield clearly different values of both quantities.

In the last two plots of Fig. 2, the ADV main result $\bar{\Lambda}$ is shown against the time lag $\Delta\tau$. At bottom middle, the time lag ranges from $10M$ to $2000M$ (more than 6 orbital periods); $\bar{\Lambda}(\Delta\tau)$ for strongly chaotic trajectories (purples) is rapidly decreasing, while weakly chaotic and regular trajectories look quite similar. At bottom right, $\bar{\Lambda}(\Delta\tau)$ for much bigger time lags ($250000M \div 252000M$) is given; here the difference between weakly chaotic and regular orbits becomes obvious.

We would like to thank the projects GACR-205/09/H033, SVV-265301 and GAUK-428011 (PS), GACR-202/09/0772 and MSM0021620860 (OS).

References

[1] Eckmann J.-P., Oliffson Kamphorst S., Ruelle D., 1987, Europhys. Lett. **4**, 973
[2] Kaplan D. T. and Glass L., 1992, Phys. Rev. Lett. **68**, 427
[3] Marwan N., Carmen R. M., Thiel M., Kurths J., 2007, Phys. Rep. **438**, 237
[4] Semerák O. and Suková P., 2010, Mon. Not. R. Astron. Soc. **404**, 545
[5] Semerák O. and Suková P., 2012, Mon. Not. R. Astron. Soc. **425**, 2455
[6] Suková P., 2011, J. Phys. Conf. Ser. **314**, 012087
[7] Suková P. and Semerák O., 2012, AIP Conf. Proc. **1448**, 523

[1] ADVs require a sufficient number of orbital points in each phase-space box (and the boxes must be small enough), which leads to quite large data sets. In comparison, for the RPs more sparse data are sufficient (time step $30M \div 50M$).